RESPONSE ANALYSIS OF U-SHAPED REINFORCED CONCRETE WALLS

Karen Paola Gonzalez Ramirez

A Thesis Submitted to the Faculty of Graduate Studies
In Partial Fulfillment of The Requirements for the Degree of
Master of Applied Science

Graduate Program in
CIVIL ENGINEERING
York University
Toronto, Ontario

August 2026

© Karen Gonzalez, 2026

Abstract

Reinforced concrete (RC) shear walls provide critical lateral stiffness, strength, and ductility in high-seismicity zones. While commonly used around elevator shafts to enhance stability and reduce frame demands, complex section geometries, such as U-shaped walls, introduce significant uncertainties in out-of-plane buckling, torsional warping, boundary element design, and slab interactions. Current numerical tools often fail to capture these complex responses under combined bidirectional loading, creating a need for validated, practical design methodologies. This study utilizes experimental data from a half-scale, three-story U-shaped RC structure subjected to shake table testing under sequential ground motions at the National Laboratory for Civil Engineering (LNEC), Portugal. A high-fidelity finite element model was developed in ATENA and benchmarked against the experimental results. Following validation, the ATENA model was subjected to pushover analysis, and its performance was compared against the simplified section-analysis tool Response-2000 to evaluate the limits of simple engineering tools. Additionally, the validated finite element model served as the baseline for a parametric study investigating the sensitivity of U-shaped walls to variations in key geometric and material properties. Finally, the experimental and high-fidelity numerical insights were used to calibrate computationally efficient, macro-level structural models in SAP2000. The calibrated framework enables engineers to reliably estimate stiffness, strength, and ductility in practical design environments without relying solely on computationally expensive models.

To my father, Jose David Gonzalez, for your quiet strength and lifetime of guidance, and to my sister Diana Carolina Gonzalez, for your motivation, support, laughter, and lifelong friendship.
It's you and me together forever.

Acknowledgements

I want to express my deepest gratitude to my supervisor, Dr. Stavroula Pantazopoulou, for her invaluable guidance, unwavering support, and encouragement throughout this research journey. Her insights and feedback were crucial contributions to the creation of this thesis. I am profoundly grateful for the wisdom and mentorship you have so generously shared; you have significantly enhanced my professional knowledge and inspired me to push the boundaries of my understanding. With patience and dedication, you have guided me in refining my work and growing as a researcher, instilling confidence and clarity at every step. I am also grateful to my committee supervisor, Dr. Liam Butler, for his thoughtful suggestions and constructive critiques, which significantly strengthened this work. Special thanks to my colleague Farah Dameh for sharing her knowledge and support. To my father, the cornerstone of my life, whose unwavering love and tireless sacrifices have been the foundation upon which I've built my dreams. Your life is a testament to resilience, a living example of what it means to face hardship with unyielding determination and grace. Through every challenge, you've shown me that no obstacle is too significant when met with discipline, hard work, and faith. Your words of encouragement, spoken with quiet conviction, have echoed in my heart in moments of doubt, reminding me that I can achieve anything I set my mind to. Whether it was the long hours you worked to provide for us, the patience you showed in teaching me life's hard-earned lessons, or the way you led by example, by never complaining and always pushing forward, you've given me a roadmap for living with purpose and integrity. Your sacrifices were never boastful, but I see them now in the lines of your hands, the weight of your steps, and the pride in your eyes when I take a step forward towards my graduate degree. This acknowledgment is but a small reflection of the gratitude I carry for you, my father, whose love and legacy will forever live in me.

Table of Contents

Abstract ..... *ii*

Dedication ..... *iii*

Acknowledgements ..... *iv*

Table of Contents ..... *v*

List of Tables ..... *viii*

List of Figures ..... *x*

List of Notation ..... *xvi*

List of Symbols ..... *xix*

Chapter 1: Introduction *1*

1.1. Background 1

1.2. Objectives and Scope of the Thesis 3

1.3. Limitations of Research 4

1.4. Thesis Methodology 5

1.5. Thesis Outline 6

1.6. Outcomes and Contributions of Research 8

Chapter 2: Literature Review *9*

2.1 Code Provisions 9

2.2 State of the Art 20

Chapter 3: Principles of Flexural Strength for reinforced concrete walls with a U-Shaped cross-section. *25*

3.1 Analysis of a U-shaped Shear Wall Cross-Section with Concentrated Boundary Reinforcement 26

3.2 U-shaped Shear Wall Cross-Section with Concentrated Boundary Reinforcement 30

3.3 Moment-Shear Interaction Diagrams of U-shaped Shear Wall Cross-Section 33

Chapter 4: Model Verification and Experimental Benchmarking *48*

4.1 Experiment Setup 48

4.2 Experimental Material Properties 50

4.3 Static and Dynamic Loads 51

4.4 Instrumentation 58

4.5 Test Observations 59

4.6 General Assumptions of the Concrete Material Properties 60

4.6.1 Modulus of Elasticity 60
4.6.2 Modulus of Rupture 60
4.6.3 Poisson's Ratio (υ) 60
4.6.4 Fracture Energy (G_F) 60
4.6.5 Crack Model 60
4.6.6 Tension Stiffening 61
4.6.7 Onset Crushing (f'_{co}) 62
4.6.8 Critical Compressive Displacement (W_D) 62
4.6.9 Reduction of Compressive Strength due to Cracked Concrete 63
4.6.10 Compression Curve (Unconfined) 64
4.6.11 Compression Curve (Confined Sections) 64
4.7 General Assumptions of the Steel Rebar Material Properties 67
4.7.1 Menegotto-Pinto 67
4.7.2 Bond slip 67
4.8 ATENA 69
4.8.1 Concrete Model Definition 71
4.8.2 Monitor Points 75
4.8.3 Load Cases 75
4.8.4 Dynamic Response 76
4.9 SAP 2000 81
4.9.1 Loading Data 86
4.9.2 Dynamic Performance 87
Chapter 5: Push-over Analysis & Parametric Investigation *97*
5.1 Experimental Setup - ATENA 97
5.2 Experimental Setup - Response 2000 110
5.3 Parametric Study 114
5.3.1 Axial Load Ratio 117
5.3.2 Longitudinal Reinforcement (Boundary Element) 130
5.3.3 Transverse Reinforcement 140
5.3.4 Torsion 142
5.3.5 Lap Splice (ℓ_d) 144
Chapter 6: Hysteretic Response *146*
Chapter 7: Conclusions *152*

7.1 General Conclusions 152
7.2 Recommendations for Future Research 155
Bibliography *156*
Appendix A *163*
Appendix B *177*
Appendix C *183*

List of Tables

Table 2-1 NBC 2020 - Force Modification Factors 10
Table 2-2 ASCE 7 - Seismic Force Resisting Design Coefficients 10
Table 2-3 Design Requirements for shear walls-based Design Codes 11
Table 2-4 Comparative analysis of requirements for boundary element confinement based on displacement-based design 13
Table 2-5 Reduction factors to account for Effective Stiffness based on CSA A23.3 and ACI 318 14
Table 2-6 Design Requirements on Lap Splice. 19
Table 3-1 U-shaped walls neutral axis depth and flexural calculations (flange in compression) 29
Table 3-2 U-shaped walls neutral axis depth and flexural calculations (flange in tension) 32
Table 3-3 Walls Properties and Reinforcement Properties (Example 2, 3, 5, 6, and 7) 41
Table 4-1 Compressive strength of concrete at 28 days. 50
Table 4-2. Mechanical Reinforcement Properties. (from Hoult et al. 2024) 50
Table 4-3 Discretion of the specimen's total weight 51
Table 4-4 Scale factors (in percent) used for the ground motions intensity. (from Tura et al. 2025) 53
Table 4-5 Comparison of maximum experimental displacement and the pseudo-spectral displacement (3% damping) 56
Table 4-6 Confinement effectiveness in each floor. 67
Table 4-7 Parameters defining the mean bond stress-slip relationship of ribbed bars (the fib Model Code for Concrete Structures -2020) 68
Table 4-8 Progressive degradation of the fundamental natural period. 79
Table 4-9 Mass participation of each Mode 88
Table 4-10 Parametric Study of Concrete Elastic Modulus Modifications 90
Table 5-1 Numerical response parameters and damage indicators for the wall under Flanges in Compression (FC) loading 101
Table 5-2 Numerical response parameters and damage indicators for the walls reinforcement under Flanges in Compression (FC) loading 103
Table 5-3 Numerical response parameters and damage indicators for the wall under Flange in Tension (FT) loading 105
Table 5-4 Numerical response parameters and damage indicators for the walls reinforcement under Flanges in Tension (FT) loading 107
Table 5-5 Parametric matrix used for the U-shaped wall study. 116
Table 5-6 Numerical response parameters and damage indicators for the walls under axial load ratio (ν=0.20) under Flanges in Compression (FC) loading 118
Table 5-7 Numerical response parameters and damage indicators for the wall's reinforcement under axial load ratio (ν=0.20) under Flanges in Compression (FC) loading 121

Table 5-8 Numerical response parameters and damage indicators for the walls under axial load ratio (ν=0.20) under Flanges in Tension (FT) loading 122

Table 5-9 Numerical response parameters and damage indicators for the wall's reinforcement under axial load ratio (ν=0.20) under Flanges in Tension (FT) loading 124

Table 5-10 Numerical response parameters and damage indicators for the wall under Axial load ratio (ν=0.10) under Flanges in Compression (FC) loading 125

Table 5-11 Numerical response parameters and damage indicators for the wall's reinforcement under axial load ratio (ν=0.10) under Flanges in Compression (FC) loading 127

Table 5-12 Numerical response parameters and damage indicators for the wall under Axial load ratio (ν=0.10) under Flanges in Tension (FT) loading 128

Table 5-13 Numerical response parameters and damage indicators for the wall's reinforcement under axial load ratio (ν=0.10) under Flanges in Compression (FC) loading 129

Table 5-14 Numerical response parameters and damage indicators for the walls with boundary reinforcement ratios (ρ_{eb} =6%) for the flanges in Compression (FC) loading 131

Table 5-15 Numerical response parameters and damage indicators for the wall's reinforcement with boundary reinforcement ratios (ρ_{eb} =6%) for the Flanges in Compression (FC) loading 132

Table 5-16 Numerical response parameters and damage indicators for the walls with boundary reinforcement ratios (ρ_{eb} =6%) for the Flanges in Tension (FT) loading 133

Table 5-17 Numerical response parameters and damage indicators for the wall's reinforcement with boundary reinforcement ratios (ρ_{eb} =6%) for the Flanges in Tension (FT) loading 134

Table 5-18 Numerical response parameters and damage indicators for the walls with boundary reinforcement ratios (ρ_{eb} =6%) for the Flanges in Compression (FC) loading 135

Table 5-19 Numerical response parameters and damage indicators for the wall's reinforcement with boundary reinforcement ratios (ρ_{eb} =4%) for the Flanges in Compression (FC) loading 136

Table 5-20 Numerical response parameters and damage indicators for the walls with boundary reinforcement ratios (ρ_{eb} =4%) for the Flanges in Tension (FT) loading 137

Table 5-21 Numerical response parameters and damage indicators for the walls with boundary reinforcement ratios (ρ_{eb} =4%) for the Flanges in Tension (FT) loading 138

Table 5-22 Numerical response parameters and damage indicators for the walls with boundary reinforcement ratios (ρ_{eb} =4%) for the Flanges in Tension (FT) loading 139

Table 5-23 Lap splice Calculations 145

List of Figures

Figure 2-1 Governing design provisions for vertical wall segments (Table R18.10.1 ACI-318) 11

Figure 2-2 Accounting for the effective area depending on the direction of loading 16

Figure 2-3 Example configuration for a case where a special boundary element is required for a flanged wall (ACI 318-25) 16

Figure 2-4 Wall boundary regions within heights where lap splices are not permitted. (Fig. R18.10.2.3 - ACI 318-25) 17

Figure 2-5 Force and displacement levels characterize different global performances. (Garevski et al., 2010) 18

Figure 2-6 Typical building not repair probability based on residual drift ratio (FEMA P-58). 18

Figure 2-7 Longitudinal strain profile of a U-shaped RC wall under various loading directions. (Modified from Khaloo et al. 2022) 22

Figure 3-1 U-shaped cross-section under the state of equilibrium (direction of loading FC- Flanges in compression) 26

Figure 3-2 Cross-section of a 5 T-section used in examples on Response 2000 28

Figure 3-3 Assumptions at flexural strength of U-shaped shear walls (direction of loading FT-Flanges in Tension) 30

Figure 3-4 Moment-Shear Diagram (a) Direction of loading flanges in compression (b) Direction of loading flanges in tension 33

Figure 3-5 Moment Shear Diagram of Example 1 in the direction of loading Flanges in compression 36

Figure 3-6 Example 1 and 4 configurations for a T-cross section simulating a U-cross section. 37

Figure 3-7 Moment-Shear Diagram of Example 1 (a) Direction of loading flanges in compression (b) Direction of loading flanges in tension 37

Figure 3-8 Moment Shear Diagram of Example 4 (a) Direction of loading flanges in compression (b) Direction of loading flanges in tension 39

Figure 3-9 Example 2 and 3 configurations for a T-cross section simulating a U-cross section. 40

Figure 3-10 Example 5, 6, and 4 configurations for a T-cross section simulating a U-cross section. 40

Figure 3-11 Moment Shear Diagram of Examples 2 and 3 (a) Direction of loading flanges in compression (b) Direction of loading flanges in tension 42

Figure 3-12 Moment Shear Diagram of Examples 4, 5, and 6 (a) Direction of loading flanges in compression (b) Direction of loading flanges in tension 43

Figure 3-13 Comparison of Moment Shear Diagram calculations to Response 2000 45

Figure 3-14 Comparison of Moment Shear Diagram calculations to Response 2000 (continued) 46

Figure 4-1 U-shaped wall specimens (from Hoult et al. 2023) 48

Figure 4-2 Plans of the specimen a) Lateral View, b) Wall Cross-section, c) Slab plan view, and d) Collar plan view (from Hoult et al. 2023) 49

Figure 4-3 Plan of Reinforcement Details (from Hoult et al. 2023) 50

Figure 4-4 Stress- Strain curve of steel Reinforcement. 51
Figure 4-5 Large blocks section properties and self-weight (from Hoult et al. 2023) 52
Figure 4-6 Moment magnitude Mw 6.5 event from the 2016 Central Italy earthquake sequence on 30 October 52
Figure 4-7 Experimental time-histories for all ground motions for W-E Displacement and N-S Displacement at the mid-height of the collar. 53
Figure 4-8 Pseudo-spectral acceleration and pseudo-spectral displacement of 3% damped from the 2016 Central Italy earthquake, from GM1 to GM8 54
Figure 4-9 Pseudo-spectral acceleration and pseudo-spectral displacement of 3% damped from the 2016 Central Italy earthquake, from GM1 to GM8 (continued) 55
Figure 4-10 Time-history response of structural rotation (θ) across sequential ground motions (GM1 to GM8) 57
Figure 4-11 Instrumentation experimental setup 58
Figure 4-12 a) Rotated Crack Model b) Fixed Crack Model (from ATENA program Documentation - Theory) 61
Figure 4-13 Uniaxial stress-strain relationship for concrete under tension and compression (from ATENA program Documentation - Theory) 61
Figure 4-14 Characteristic concrete in tension (Modified from Dameh 2021) 62
Figure 4-15 Compressive concrete configuration (from ATENA program Documentation) 62
Figure 4-16 Compressive strength of a confined concrete model (from ATENA program Documentation - Theory) 63
Figure 4-17 Compressive strength reduction of cracked concrete (from ATENA program Documentation - Theory) 63
Figure 4-18 Unconfined concrete in compression following Hognestad's Parabola 64
Figure 4-19 Geometry of U section Wall - nomenclature of boundary elements (Modified from Hoult et al. 2023) 65
Figure 4-20 Confinement effectiveness equation by Richart et al (1928) 65
Figure 4-21 Confinement effectiveness equation by the Fib Model code 1990 65
Figure 4-22 Confinement effectiveness ratio (Pantazopoulou - Class notes CIVL 6422) 66
Figure 4-23 Stress-strain law (Modified from ATENA program Documentation) 67
Figure 4-24 Bond stress-slip relation - the fib Model Code for Concrete Structures (2020) 68
Figure 4-25 Bond stress-slip relationship 69
Figure 4-26 Mesh Configuration 70
Figure 4-27 Concrete Material Configuration 70
Figure 4-28 Elastic materials 70
Figure 4-29 Elastic material properties 70
Figure 4-30 Reinforcement model 71
Figure 4-31 Basic concrete material configuration 72

Figure 4-32 Stress-Strain Law 72
Figure 4-33 Tensile concrete configuration 72
Figure 4-34 Tensile concrete curves a) Crack opening law b) rotates, fixed model c) Tension stiffening. 72
Figure 4-35 Compressive concrete configuration 73
Figure 4-36 Compressive concrete Stress-strain Curve (peak and post-peak) 73
Figure 4-37 Compressive Concrete Stress-Strain Curve 73
Figure 4-38 Compressive concrete unconfined and confined stress-strain curve 74
Figure 4-39 Stress-strain relationship of unconfined and confined materials. 74
Figure 4-40 Monitor Points 75
Figure 4-41 Fixed surface on foundation 75
Figure 4-42 Self-weight density 75
Figure 4-43 Experimental acceleration-time history response in the West - East Seismic Excitation (Parallel to the Axis of Symmetry) 76
Figure 4-44 Experimental acceleration-time history response in the North - South Seismic Excitation (Parallel to the Web) 76
Figure 4-45 Experimental displacement time history response under West-East seismic excitation (Parallel to the Axis of Symmetry) 77
Figure 4-46 Experimental displacement time history response under North-South seismic excitation (Transverse to the Axis of Symmetry) 77
Figure 4-47 Structural Rotation (θ) time history response under sequential seismic excitation 78
Figure 4-48 Comparison of experimental W-E and N-S displacement time-histories at the collar mid-height (black line in the W-E direction and Green line in the North-South direction), with ATENA finite element model predictions (red line) across ground motions GM1 to GM3. 79
Figure 4-49 Comparison of experimental rotation time-histories at the collar mid-height (black line) with ATENA finite element model predictions (red line) across bi-axial ground motion GM2. 80
Figure 4-50 General 3D View and Mesh Discretization of the Specimen in SAP2000 (Left: Standard view, Right: Extrude view) 81
Figure 4-51 Shell layer Definition for unconfined wall section. 82
Figure 4-52 Shell layer Definition for unconfined wall section (Left: Quick Start Parameter, Right: Local axes on U-shaped wall) 82
Figure 4-53 Shell layer Definition for confined boundary element EB1. 83
Figure 4-54 Shell Section and Material Definition for the Concrete Collar. 83
Figure 4-55 Solid Steel Blocks Material Definition. 84
Figure 4-56 Material Discretization of Boundary Confinement Elements (Eb1, Eb2) and Unconfined Concrete for the U-Shaped Shear Wall Cross-Section. 84
Figure 4-57 Material Definition for Unconfined Concrete 85
Figure 4-58 Material Definition for Confined Concrete Zone Eb1 (1st floor) 85
Figure 4-59 Material Definition for Confined Concrete Zone Eb2 (1st floor) 85

Figure 4-60 Material Definition for 12mm rebar 86
Figure 4-61 Concrete material definition - Sap2000 86
Figure 4-62 Dynamic Time History Load Case defined in Sap2000 87
Figure 4-63 Mass Source Data 87
Figure 4-64 Dynamic Mode Shapes and Natural Periods of the Structure; Mode 1: Lateral Displacement (Y-direction), Mode 2: Translational Displacement (X-direction), Mode 3: Pure Torsional/Warping Displacement (Z-direction), units in meters 88
Figure 4-65 Comparison of experimental W-E and N-S displacement time-histories at the collar mid-height (black line in the W-E direction and Green line in the North-South direction), with ATENA finite element model predictions (red line) and SAP2000 model predictions (blue line) across ground motions GM1 to GM3 89
Figure 4-66 Nomenclature of the four corner nodes of the C-shaped section wall 90
Figure 4-67 Deformation Shape Mode 1 (Left: Lateral deformation, Right: Transverse deformation) 91
Figure 4-68 Deformation Shape Mode 2 - Transverse deformation 91
Figure 4-69 Deformation Shape Mode 3 (Left: Lateral deformation, Right: Transverse deformation) 92
Figure 4-70 Pseudo-spectral acceleration of 3% damped from the 2016 Central Italy earthquake, from GM 7(Left), Experimental time-histories for GM 7 for W-E Displacement (Right). 92
Figure 4-71 Modal participation factors and modal mass coefficients (ATC-40, 1996) 93
Figure 4-72 Lateral View of the U-shaped Wall 93
Figure 4-73 Pseudo-spectral acceleration of 3% damped from the 2016 Central Italy earthquake, from GM 8(Left), Experimental time-histories for GM 8 for W-E Displacement in mm (Top Right), Experimental time-histories for GM 8 for N-S Displacement in mm (Bottom Right). 95
Figure 5-1 Pushover - Experiment Setup 98
Figure 5-2 Lateral displacement profiles 99
Figure 5-3 Principal Strain (compression) at 2.FC marker at a 0.5m height 100
Figure 5-4 Bond Slip under Flanges in Compression (FC) 104
Figure 5-5 Principal Strain (web in compression) 108
Figure 5-6 Moment-Shear interaction curves 109
Figure 5-7 T-Cross-sectional details and geometric properties of the experiment on Response 2000. 110
Figure 5-8 Pushover - Parametric study of Axial Load Ratio (ν) 111
Figure 5-9 Crack patterns and crack width contours (mm) in Response2000. 112
Figure 5-10 Response-2000, member response profiles showing bending moment, curvature distribution, and shear strain distribution at final force control stage. 113
Figure 5-11 Pushover - Parametric study of Axial Load Ratio (ν) 117
Figure 5-12 Bond Slip reinforcement under Flanges in Compression (FC) 122
Figure 5-13 Strain of Reinforcement under axial load ratio (ν=0.10) 130
Figure 5-14 Pushover - Parametric study of Boundary Element Reinforcement Ratio 130

Figure 5-15 Pushover - Parametric study of Transverse Reinforcement spacing 141
Figure 5-16 Pushover - Parametric study of Torsion with Tributary Load in the Collar 143
Figure 5-17 Pushover - Lateral load-rotation response perpendicular to the axis of the three-floor level of loading 143
Figure 5-18 Lateral Rotation profiles (a) for an axial load of 90 kN and (b) for an axial load of 180 kN 144
Figure 5-19 Pushover - Parametric study of Lap splice in plastic Hinge region 145
Figure 6-1 Lateral Load vs. Top Displacement / Drift Ratio curves for U-shaped reinforced concrete shear wall under cyclic loading, a) Hysteresis flanges in compression first b) Hysteresis flanges in Tension first. 146
Figure 6-2 Plastic Hinge displacement and reinforcement strain 147
Figure 6-3 Marker 2 wall behavior a) Crack width b) Reinforcement strain c) Concrete principal strain 147
Figure 6-4 Marker 3 wall behavior a) non-linear displacement (x-axis) b) Concrete principal strain 148
Figure 6-5 Marker 1 wall behavior, a) Reinforcement strain b) Crack width 148
Figure 6-6 Marker 2 wall behavior: a) Crack width; b) Reinforcement strain; c) Concrete principal strain; d) Plastic strain in the Z direction. 149
Figure 6-7 Marker 3 walls behavior a) Crack width b) Reinforcement strain c) Reinforcement strain for next step d) Concrete plastic stain 149
Figure 6-8 Marker 3 wall behavior, out-of-plane displacement (x-axis) 150
Figure 6-9 Marker 4 walls behavior a) Reinforcement train b) Concrete principal strain c) Concrete plastic stain 150
Figure 6-10 Marker 4 walls behavior a) out of plane displacement (y-axis) b) out of plane displacement (x-axis) 151
Figure A-1 Rectangular cross-section under the state of equilibrium (Uniformly distributed reinforcement). 163
Figure A-2 Rectangular cross-section under the state of equilibrium (without considering reinforcement in compression). 165
Figure A-3 Rectangular cross-section under the state of equilibrium (considering 70% reinforcement in Tension). 166
Figure A-4 Five Rectangular cross-section used in example on Response 2000. 167
Figure A-5 Rectangular wall (uniform reinforcement distribution) neutral axis depth and flexural calculations. 169
Figure A-6 Rectangular cross-section under the state of equilibrium (Concentrated Boundary Reinforcement). 170
Figure A-7 Rectangular cross-section under the state of equilibrium (Concentrated Boundary Reinforcement in Tension only) 172
Figure A-8 Rectangular cross-section under the state of equilibrium considering 70% reinforcement in Tension (Concentrated Boundary Reinforcement in Tension only). 173
Figure A-9 Rectangular cross-section under the state of equilibrium considering 70% reinforcement in Tension (Concentrated Reinforcement Boundaries). 174

Figure A-10 Four rectangular cross-sections with boundary reinforcement (Ex6 to Ex9) on Response 2000. 175
Figure A-11 Rectangular wall (boundary elements) neutral axis depth and flexural calculations. 176
Figure A-12 Response 2000 - Rectangular wall (boundary elements) Example 6. 183
Figure A-13 Response 2000 - Rectangular wall (boundary elements) Example 7 184
Figure A-14 Response 2000 - Rectangular wall (boundary elements) Example 8 185
Figure A-15 Response 2000 - Rectangular wall (boundary elements) Example 9 186
Figure A-16 Response 2000 - T-shaped wall (boundary elements) Example 1..... 187
Figure A-17 Response 2000 - T-shaped wall (boundary elements) Example 2..... 188
Figure A-18 Response 2000 - T-shaped wall (boundary elements) Example 3..... 189
Figure A-19 Response 2000 - T-shaped wall (boundary elements) Example 4..... 190
Figure A-20 Response 2000 - T-shaped wall (boundary elements) Example 5..... 191

List of Notation

A_b	Cross-sectional area of one longitudinal bar.
A_{cv}	Represents the net-gross cross-sectional area of a structural element resisting shear,
A_{cw}	Area of concrete section of an individual pier, horizontal wall segment resisting shear.
A_{cx}	Area of concrete section A_{cx} or A_{cw}, where applicable.
A_g	Cross-sectional area of the column
A_{sb}	Area of the longitudinal reinforcement in the boundary element
A_{sf}	Area of the longitudinal reinforcement in the Flange excluding the boundary element
A_{sl}	Total area of the longitudinal reinforcement
A_{sw}	Area of the longitudinal reinforcement in the Web
A_{xe}	Effective axial cross-section area to be used for analysis
b	Cross section width
b_c	Concrete core section width from center to center of transverse reinforcement.
b_f	Effective flange width
b_i	Clear distance between adjacent longitudinal bars that are laterally restrained by a tie corner or crosstie leg.
c	Distance from extreme compression fiber to neutral axis (Subscripts 1, 2 depend on the direction of lateral loading in the asymmetric U-shaped wall cross section)
C_{b1}	Compression forces from steel in the boundary element compression zone
C_c	Concrete compressive resultant Force
C_s	Compression forces from steel in the compression zone
d	Distance from extreme compression fiber to centroid of longitudinal tension reinforcement
d_b	Longitudinal reinforcement bar diameter
d_{cs}	The smaller of a) the distance from the closest concrete surface to the center of the bar being developed; or b) two-thirds of the center-to-center spacing of the bars being developed.
E_c	Modulus of Elasticity of Concrete
E_s	Modulus of Elasticity of non-prestressed reinforcement
f'_c	Compressive strength of concrete cylinder at 28 days
f'_{cc}	Compressive strength of concrete in columns, or confined section of a wall
$f'_{cc,\,res}$	Residual stress capacity of confined concrete compressive strength
f_y	Yield strength of the longitudinal reinforcement steel
f_{yw}	Yield strength of the transversal reinforcement steel
G	Elastic shear modulus after cracking (Cervenka et al. 2020).

G_F	Energy fracture (Cervenka et al. 2020)
h	Depth of the gross cross-section
h_c	Confined concrete core section depth from center to center of transverse reinforcement
h_w	Clear height
I	Moment of inertia of the section about the centroidal axis.
I_{cr}	Moment of inertia of the cracked section transformed to concrete
I_e	Effective moment of inertia
I_g	Moment of inertia of gross concrete section about the centroidal axis, neglecting reinforcement
J_o	Polar Mass Moment of Inertia
K	Strength enhancement factor for concrete confinement
K_e	The effectiveness coefficient of the confinement pressure produced by the transverse reinforcement.
k_e	Confinement effectiveness coefficient
K_{tr}	Transverse reinforcement index
ℓ_{be}	Boundary element length
ℓ_d	Development length
ℓ_f	Flange length
ℓ_{if}	Flange length excluding the boundary element length
ℓ_p	Plastic hinge length
ℓ_w	Wall length
M	Nominal flexural moment capacity (Subscripts 1, 2 depend on the direction of lateral loading in the asymmetric U-shaped wall cross section)
$\bar{M}$	Normalized nominal flexural strength limit
m^*	Equivalent Mass
MCE_R	Maximum Considered Earthquake
M_u	Factored Moment at the section
n	number of bars or wires being spliced or developed along the potential plane of bond splitting / constant normalizing factor for moment and shear strength
P_o	Nominal axial strength at zero eccentricity
P_u	factored permanent load perpendicular to the shear plane
R	Response Modification Coefficient
R_d	Response Modification Coefficient due to Ductility
R_o	Response Modification Coefficient due to Overstrength
$s\,;\, s_h$	Center-to-center spacing of transverse reinforcement measured along the longitudinal axis of the structural member

$\overline{S_1}$	Upper flexural-dominated Boundary Slope
$\overline{S_2}$	Lower shear-dominated boundary slope
S_a	Spectral Acceleration: The maximum acceleration experienced by a single-degree-of-freedom (SDOF) when subjected to ground motion.
S_d	Spectral Displacement: The peak relative deformation and drift demand experienced by the equivalent SDOF system.
T	Tensile force by the longitudinal reinforcement in the flange segment outside the boundary elements / Structures Period
T_b	Tensile force by the longitudinal reinforcement in the boundary element.
t_f	Thickness of flange/web
T_w	Tensile force by the longitudinal reinforcement in the Web.
$\bar{V}$	Normalized shear force demand
V_c	Concrete shear contribution
V_s	Transverse steel shear reinforcement contribution
V_u	Factored shear force
V_y	Base shear at yield
w_w	Descending slope of stress-strain relation of concrete (CEB-FIP Model Code 1990)
$\bar{y}$	Distance from centroidal axis of gross section to tension face.
Z	Descending slope of the stress-strain relation of concrete proposed by Kent and Park (1971)

List of Symbols

α	Concrete stress block intensity factor; Modal Mass Coefficient
α_c	Coefficient defining the relative contribution of concrete strength to nominal wall shear strength. where α_c=0.25 for $h_w/l_w \leq 1.5$ and αc=0.17 for $h_w/l_w \geq 2.0$. Defined in ACI318-25 section 11.5.4.3
α_{sh}	Shape factor to define the shear stress limit for walls
α_w	Section property reduction factor used for the wall's effective stiffness properties
β	Stress block depth factor for the equivalent rectangular stress block
Γ	Modal Participation Factor
δ	Displacement
δ_{el}	Elastic displacement
δ_{pl}	Plastic displacement
δ_u	Ultimate displacement
δ_u	Inelastic displacement
ε	Strain
ε_c	Concrete strain
$\varepsilon_{c,\,85}$	Strain at 85% of unconfined strength on the descending branch
$\varepsilon_{cc,\,50}$	Strain at 50% of peak confined strength on the softening curve
$\varepsilon_{cc,\,85}$	Strain at 85% of confined strength on the descending post-peak branch
$\varepsilon_{cc,u}$	Ultimate axial compressive strain of confined concrete
ε_{cm}	Strain at the extreme concrete compression fiber of the wall
$\varepsilon_{co}; \varepsilon_o$	Unconfined Concrete strain at peak strength.
ε_{cp}	Concrete plastic strain
ε_{cu}	Maximum usable strain at extreme concrete compression fiber
ε_{cy}	Expected yield strain in the extreme concrete compression fiber
ε_{el}	Concrete elastic strain
ε_{sh}	Steel strain during hardening
ε_{su}	Steel strain at Ultimate
ε_{sy}	Steel strain at yield
ε_{sy}	Expected yield strain in the extreme layer of longitudinal tension reinforcement
ε_y	Strain at yield
θ	Rotation
θ_p	Plastic Rotation
θ_m	Max Maximum rotation

λ	modification factor to reflect the reduced mechanical properties of lightweight concrete relative to normal weight concrete.
λ_k	Slenderness Ratio factor
$\lambda_{M,v}$	Axial load flexural correction factor
$\lambda_{M,\rho}$	Longitudinal reinforcement ratio correction factor
λ_s	factor used to modify shear strength based on the effects of member depth, commonly referred to as the size effect factor
$\lambda_{v,1}$;$\lambda_{v,2}$	Axial load factor
ρ	ratio of non-prestressed tension reinforcement, equal to A_s / b d
ρ_I	Longitudinal reinforcement ratio
ρ_w	Transversal reinforcement ratio
ρ_w	Transversal reinforcement ratio
σ_c	Concrete stress
σ_{lat}	Effective lateral confinement pressure exerted by transverse steel at yielding
φ	strength reduction factor
φ_p	Plastic curvature
Ψ	Normalized mode shape profile
ω'	Normalized flange length ratio
ω''	Normalized material strength and sectional geometry ratio
ω_w	Mechanical volumetric ratio of transverse reinforcement
κ	Normalized constant factor
κ'	Geometric effective area factor

Chapter 1: Introduction

1.1. Background

In contemporary high-rise construction, Reinforced Concrete (RC) structural walls, also known as shear walls, are the primary lateral-load-resisting system and are essential for maintaining structural integrity under wind and seismic forces. In these structures, shear walls are often arranged in U-shaped (or channel-shaped) configurations to wrap around service cores, such as elevator shafts and stairwells. This geometry introduces complex structural behavior because concentrating a building's lateral stiffness into a single, open-section U-shaped elevator core induces high geometric eccentricities between the center of mass and the center of rigidity. Under multidirectional seismic excitation, this eccentricity triggers severe torsional warping and intense biaxial cyclic bending, ultimately leading to premature, brittle concrete crushing in the wall's boundary elements.

Field data from the 2023 Turkey earthquakes indicate that even buildings with a reasonable global wall density index, including newer structures designed in accordance with modern seismic provisions, still suffered severe damage or collapse when they used concentrated, non-planar geometries (Kazaz, 2024). These unexpected, severe structural failures, along with documented damage from the 2010 Chile and 2011 New Zealand earthquakes, highlight an urgent need to re-examine the performance and current design methodologies of shear walls, particularly those with non-planar configurations. A critical combination of intense flexural and axial actions drove most of the shear wall damage recorded during these global seismic events. This severe demand was concentrated primarily within the plastic hinge regions of the lower stories, culminating in premature failure of the moderately or poorly confined boundary elements of the wall sections.

The complex seismic behavior of these non-planar systems remains an active area of investigation because design standards such as ASCE 7-10, ACI 318-25, and CSA A23.3:24 fail to capture important response characteristics of U-shaped walls, including nonlinear shear/flexural/torsional interaction, nonlinear shear behavior, the significant effects of torsional warping of the cross-section, and out-of-plane deformations in individual wall segments. These standards fail to reflect actual dynamic behavior, which is substantially more complex than that observed in typical planar walls.

The complex geometry of U-shaped walls does not obey the fundamental Bernoulli-Euler hypothesis (plane sections remain plane) due to shear lag and torsional warping. Experimental work (e.g., Constantin and Beyer 2016) showed that non-linear strain profiles indicate an additional compression zone at the web-flange intersections. Because the web and flanges do not deform in unison, this non-linear strain distribution causes the flanges to lag behind the web, resulting in significant cross-sectional warping rather than maintaining a planar

profile. Consequently, conventional design codes rely on linear strain models, which may significantly underestimate critical stress concentrations at wall corners and potentially lead to premature material failure.

While most historical research and experimental programs have focused on rectangular shear wall sections, there has been recent progress in investigating the behavior of reinforced concrete (RC) U-shaped walls (Ile and Reynouard 2005; Beyer et al. 2008; Lowes et al. 2013; Constantin and Beyer 2016; Behrouzi et al. 2020; Hoult et al. 2020). However, the existing body of work has primarily focused on quasi-static experimental testing under combined axial and flexural loading along in-plane paths, largely neglecting torsional effects. Consequently, a critical knowledge gap remains regarding how these open-section configurations transfer complex torsional warping stresses under multidirectional seismic loading, underscoring the need for advanced nonlinear numerical modeling to benchmark practical engineering design tools.

Dynamic shake-table tests on structural walls are limited in the industry. Despite the critical importance of large-scale testing for characterizing the behavior of non-planar reinforced concrete (RC) walls, such programs remain scarce due to high costs and extensive time requirements. Dr. Nicolas Ile conducted the first landmark shake-table test on U-shaped walls in 2002, using a 0.6-scale model subjected to unidirectional seismic action parallel to the axis of symmetry. While this study successfully evaluated dynamic amplification factors and the progressive degradation of translational stiffness under real-world acceleration records, the specimen was constrained to uniaxial excitation. Consequently, the experiment could not capture the highly complex, coupled flexural-axial-torsional response and multidirectional warping behavior that naturally occur in non-planar core walls during real-world, bidirectional earthquake shaking.

Because physical experimental data for non-planar cross-sections are scarce, complementary computational simulations have become increasingly vital. Accurate numerical modeling reduces reliance on costly physical testing when evaluating novel design concepts. Additionally, the industry's shift toward performance-based seismic design (PBSD) requires analytical tools that are computationally efficient and can capture complex nonlinear behavior. Although several modeling frameworks for planar and non-planar walls have been proposed, the demand for an optimal balance between computational efficiency and nonlinear accuracy continues to drive innovation in structural engineering.

To evaluate these intricate nonlinear responses in open-section geometries, this study draws on data from a recent, state-of-the-art large-scale experimental program (Hoult et al., 2023b). The ERIES-ALL4wALL 2023 Blind Prediction Competition involved shake-table testing of a 40-tonne RC U-shaped wall with an additional 25-tonne collar mass at the National Laboratory for Civil Engineering (LNEC) in Lisbon, Portugal. To simulate realistic seismic demands, the specimen was subjected to both uniaxial and bidirectional torsional excitation. Organized by UCLouvain and funded by Engineering Research Infrastructures for European Synergies (ERIES), the program aimed to characterize the coupled dynamic, structural, and seismic performance of U-shaped wall configurations.

The test unit, denoted UWS1, represents a half-scale wall subjected to increasing-intensity input motions that induce both pure unidirectional flexure and bidirectional torsional responses. Experimental results served as a reference for validating a detailed ATENA finite element model. The numerical model was designed to replicate the complex nonlinear behavior observed during testing, ensuring the simulation accurately reflects the wall's structural integrity and damage progression.

By benchmarking a finite element (FE) model against experimental data, this study established a validated baseline model in ATENA to investigate the nonlinear response of U-shaped reinforced concrete (RC) walls. The calibrated model subsequently served as the foundation for a comprehensive parametric analysis designed to evaluate how key structural characteristics influence overall performance. The parameters investigated included axial load ratios, longitudinal and transverse reinforcement ratios, and the effects of lap splices, among other critical variables.

Building on this validated baseline, the research extends its scope to evaluate the nonlinear response of U-shaped RC walls by benchmarking the high-fidelity ATENA FE model against a streamlined yet robust fiber analysis model in Response2000 and a macro-model in SAP2000. This comparative analysis aims to bridge the gap between complex continuum mechanics and practical engineering applications. By validating an efficient modeling approach that maintains high accuracy in performance-based seismic evaluation, this work ultimately contributes to the broader effort to refine regional seismic design standards for non-planar structural systems.

1.2. Objectives and Scope of the Thesis

This thesis aims to provide a robust modeling framework in Response2000 to estimate the strength and deformation capacity of U-shaped walls and to analyze them in SAP2000. The study uses a detailed ATENA model, calibrated against experimental benchmarks, to verify the accuracy of the streamlined SAP2000 approach. Ultimately, this work establishes a practical path for structural engineers to simulate complex non-planar behavior with high confidence and reduced computational overhead.

By accurately predicting strain patterns and stress gradients, the model facilitates a detailed assessment of critical failure modes, including concrete crushing, cover spalling, and longitudinal reinforcement buckling. Furthermore, the proposed strategy provides essential insights into the optimal reinforcement distribution needed to mitigate localized and global instabilities, bridging the gap between theoretical analysis and resilient structural detailing.

Furthermore, the study offers specific design recommendations for detailing longitudinal and transverse reinforcement, establishing confinement requirements for boundary elements at section extremities and geometric intersections (junctions), optimizing longitudinal reinforcement distribution across confined and unconfined sections, and refining transverse detailing. By analyzing these critical zones, the research provides

a framework for achieving superior structural performance and resilience in non-planar reinforced concrete systems.

Ultimately, this research aims to accurately model the critical behavior of complex structural systems under seismic action. By precisely determining the location, extent, and severity of structural damage, engineers can proactively strengthen the most vulnerable components of a building, minimize structural damage, and ensure the safety and resilience of non-planar RC structures.

1.3. Limitations of Research

While this study provides valuable insights into the non-linear response and seismic performance of U-shaped reinforced concrete shear walls, several computational and analytical limitations warrant acknowledgment.

First, the high-fidelity 3D non-linear finite element models (NLFEA) implemented in ATENA require fine spatial discretization and small time-stepping to reliably capture concrete cracking, crushing propagation, and multidirectional warping. Running full non-linear dynamic time-history simulations across multiple ground motion suites is exceptionally time-intensive, often requiring several months of continuous processing. Additionally, these high-fidelity simulations generate massive volumes of output data, demanding extensive high-capacity storage infrastructure to archive output metrics such as strain tensors, stress fields, and crack propagation histories at every iteration step. Consequently, full dynamic evaluations were restricted to select critical ground motion records, while broad structural sensitivity was primarily evaluated using non-linear static (pushover) analyses.

Streamlined engineering tools (e.g., SAP2000 macro-models and Response-2000 sectional analysis) rely on simplified mechanics assumptions (such as plane sections remaining plane or simplified shell element formulations). While computationally efficient, these tools cannot fully capture micro-level localized failure modes, including non-linear shear lag, complex torsional warping stresses, and dynamic bar buckling as effectively as high-fidelity continuum FE models.

Physical experimental datasets for non-planar (U-shaped) reinforced concrete shear walls subjected to multidirectional dynamic loading remain extremely scarce in the literature. Most existing experimental programs are constrained to quasi-static, cyclic in-plane loading on planar or rectangular wall sections. While this study utilizes high-quality data from the recent ERIES-ALL4wALL 2023 shake-table test, the limited availability of diverse dynamic testing datasets restricts the broader validation of non-linear finite element models across a wider spectrum of wall geometries, scale factors, aspect ratios, and dynamic excitation protocols.

1.4. Thesis Methodology

This research follows an integrated methodology, combining nonlinear finite element analysis in ATENA with rigorous analytical tools and evaluation of experimental datasets. By using these complementary tools, the study aims to refine seismic evaluation standards for non-planar structural systems and capture the complex behavior of U-shaped wall geometries. These methods will include:

First, a comprehensive literature review synthesizes data from various experimental programs by documenting key structural parameters, including longitudinal and transverse reinforcement ratios, axial load ratios, lateral loading protocols, and aspect ratios. This systematic data collection allows for an empirical evaluation of the deformation capacity of U-shaped RC walls and provides a foundational understanding of characteristic failure modes unique to non-planar cross-sections, such as shear-flexure interaction and torsional instability. Additionally, this study focuses primarily on a recent large-scale shaking table experiment (wall UWS1) from the ERIES-ALL4wALL 2023 Blind Prediction Competition (Hoult et al., 2023b) as a benchmark to investigate the behavior of reinforced concrete walls under lateral seismic loading and to validate the numerical framework through a systematic comparison of predicted analytical responses with the experimental dataset. By benchmarking the simulation results against measured global and local deformations, the study ensures that the nonlinear modeling strategy can replicate the observed structural behavior.

Secondly, the structural response is evaluated using analytical formulations based on equilibrium and stress-strain compatibility. This phase rigorously assesses the neutral-axis depth under lateral loading by defining the ultimate limit state in terms of the concrete cover's compressive strain capacity. The investigation further evaluates the effective depth to determine the wall's internal stress state and moment capacity to sustain high-intensity seismic demands. These parameters are primarily governed by cross-sectional geometry, the compressive strength of the concrete (f'_c), the area and yield strength of the reinforcement steel (f_y) and the axial forces acting on the wall. These first-order estimates establish a theoretical baseline for the wall's nonlinear behavior and serve as a critical verification step in the initial stages of the computational modeling process. Moreover, to achieve high-fidelity modeling of the wall's response, a variety of material characteristics were analyzed. This included evaluating compression curves and stress-strain relationships, distinguishing between the enhanced performance of confined regions and that of unconfined sections, and applying the bond-slip analytical models prescribed by the fib Model Code (2020).

Thirdly, the global structural capacity is quantified through nonlinear pushover analyses conducted primarily in ATENA and on two other platforms (Response-2000 and SAP2000). Comparing these outputs ensures that structural strength and nonlinear response are accurately captured across different levels of discretization. This multi-level validation framework provides rigorous checks of convergence and accuracy, establishing a reliable baseline for subsequent parametric studies.

The pushover analysis along the axis of symmetry used a displacement-control method, applying displacement increments at the collar's mid-height until collapse. Conversely, the pushover analysis perpendicular to the axis of symmetry required a different methodology because the wall's asymmetric shape makes it difficult to identify a single control point for displacement application. Therefore, the analysis adopted a hybrid approach, applying an incremental gravitational field until peak strength was reached. To fully capture the subsequent post-peak nonlinear response, displacement-controlled loading was then implemented while maintaining the established displacement response shape. To evaluate how progressive damage degrades the system, a cyclic pushover procedure was introduced to compare structural behavior under cyclic lateral reversals (hysteresis analysis) with the standard monotonic pushover response.

Once validated, the finite element model is used to conduct an extensive parametric study evaluating how wall geometry and reinforcement detailing affect structural performance. Key parameters include transverse and longitudinal steel distribution, lap splice characteristics, and cross-sectional geometry. The study evaluates stiffness, lateral load-carrying capacity, and deformation limits at key limit states.

The next phase of the study involves developing a simplified numerical strategy in SAP2000 that effectively captures the nonlinear mechanisms observed in the experiment and in ATENA simulations. By calibrating constitutive inputs and structural characteristics, this approach realistically represents wall behavior while significantly reducing the computational demand of performance-based seismic evaluation. This methodology enables a more rigorous and accurate design process, which is essential for ensuring the structural reliability of non-planar walls. Ultimately, this approach is a valuable tool for refining boundary-element specifications in U-shaped and other complex sections, where intricate stress distributions often challenge standard design assumptions.

1.5. Thesis Outline

Chapter 1: Introduction - This chapter lays the research foundation by defining the core problem and identifying open issues in current engineering practice. It also outlines the research objectives, the scope of the investigation, and the theoretical background, and concludes with a detailed overview of the thesis methodology.

Chapter 2: Literature Review - This chapter reviews existing research on the behavior of reinforced-concrete shear walls, focusing on thin-walled U-shaped sections, and traces the evolution of standard analytical procedures from simplified 2D models to complex 3D interaction frameworks.

Chapter 3: Principles of Flexural Strength for reinforced walls with a U-Shaped cross-section - This chapter evaluates the nominal moment capacity (M_n) by first analyzing the sectional behavior of the U-shaped cross-section. By treating the section as a single plane, the analysis enforces the fundamental principles of Strain Compatibility and Internal Force Equilibrium, which are traditionally applied to rectangular sections and reinforced concrete beams. The study then extends this sectional approach to a member-level evaluation to determine how flexural capacity and demand vary along the wall height.

Chapter 4: Model Verification and Experimental Benchmarking - This chapter presents an experimental benchmark to validate the nonlinear response of U-shaped shear walls. It outlines the specimen geometry, material properties, and key experimental observations from the ERIES-ALL4wALL dynamic test. It also details the development of a high-fidelity Nonlinear Finite Element Model (NLFEA) using the ATENA software environment. The numerical framework is validated by comparing the simulated response with the experimental load-displacement envelope and displacement-time histories, thereby ensuring the model's accuracy before proceeding with the parametric study. This chapter further focuses on translating the complex nonlinear behavior of U-shaped walls into a simplified SAP2000 framework. It discusses selecting and calibrating shell sections to reflect the multi-axial interactions identified in ATENA.

Chapter 5: Pushover Analysis and Parametric Investigation - This chapter presents a comprehensive parametric investigation, using pushover analysis, to capture the complex, nonlinear interactions among flexure, shear, and torsion inherent in U-shaped cross-sections. The parametric study varies model loading conditions and reinforcement detailing and evaluates the critical transition from ductile flexural response to brittle, stability-governed failure mode. The objective is to quantify the sensitivity of the wall's ultimate capacity to effects such as torsional warping and tension shift, which standard design codes often simplify or neglect.

Chapter 6: Hysteretic Response- This chapter evaluates how the U-shaped shear wall dissipates energy under cyclic, reversed lateral loading. The analysis provides deep insights into the complex interactions governing concrete cracking, crushing, reinforcement yielding, and bond-slip mechanisms. It also identifies critical failure modes, including localized rebar buckling and global instability of the thin-walled section. The resulting hysteretic loops capture progressive stiffness and strength degradation, critical cyclic phenomena that conventional nonlinear static pushover analysis cannot account for.

Chapter 7: Conclusions and Future Work - This final chapter synthesizes findings from the numerical investigation and the parametric study of U-shaped reinforced-concrete shear walls. It highlights the critical influence of multi-axial interactions, including the complex coupling of shear, flexure, and torsion, on the wall's

ultimate capacity and failure mechanisms. Design recommendations are proposed. The chapter concludes by identifying current limitations and suggesting directions for future research to further refine the seismic assessment of U-shaped shear walls.

1.6. Outcomes and Contributions of Research

This research aims to further characterize the nonlinear behavior and deformation capacity of U-shaped RC sections under lateral loads. The non-linear response is driven by concrete cracking, steel yielding, and, ultimately, confined-core crushing. By accurately predicting strain patterns and stress gradients, a finite element model enables a detailed assessment of critical failure modes, specifically concrete crushing, cover spalling, and longitudinal reinforcement buckling. Furthermore, the proposed strategy provides essential insights into the optimal reinforcement distribution required to mitigate localized and global instabilities, bridging the gap between theoretical analysis and resilient structural detailing.

Additionally, this study provides actionable design recommendations for boundary element confinement at section extremities and geometric intersections (junctions), optimal distribution of longitudinal steel across confined and unconfined zones, and transverse reinforcement detailing. By analyzing these critical regions, the research establishes a robust framework for enhancing the structural performance and seismic resilience of non-planar reinforced concrete systems.

Moreover, this study advances understanding of the complex seismic response of U-shaped RC walls. Beyond numerical validation, it aims to develop a simplified analytical framework to more accurately determine the neutral axis depth, effective depth, and confinement requirements. These findings help evaluate the applicability of current building codes to non-rectangular sections and identify potential gaps in standard design practices. A central part of this research is an extensive finite element (FE) investigation and the development and calibration of nonlinear models against experimental data from U-shaped RC wall tests to accurately capture hysteresis and complex failure modes. These advanced models serve as benchmarks for evaluating simplified modeling approaches in SAP2000. This validation ensures that practitioners can accurately incorporate complex seismic behaviors, including flexural-torsional coupling and concrete crushing, using standard commercial software. The research is expected to highlight specific areas where these standards may require adjustments to better represent the behavior of non-planar reinforced concrete structures.

Chapter 2: Literature Review

This chapter presents a comprehensive review of the literature on the behavior, analysis, and design of U-shaped reinforced concrete shear walls. First, it examines current code provisions, including specific guidelines, limitations, and recommendations, to assess the effectiveness of standard methodologies for this unique cross-section geometry. Second, this chapter reviews historical experimental data, focusing on how different loading combinations influence structural behavior, ultimate load capacity, and distinct failure modes of these sections. Through this systematic evaluation, the chapter identifies current research gaps and provides the foundation for the subsequent numerical and parametric investigations.

2.1 Code Provisions

Code provisions for reinforced concrete shear wall design aim to provide adequate reinforcement details and concrete strength to allow inelastic response during major earthquakes without reaching a critical damage state.

Shear walls act as vertical cantilevers that primarily resist lateral forces through flexural action. The reinforcement cage effectively confines the concrete, ensuring the wall reaches its flexural plastic capacity while avoiding brittle shear failure under cyclic seismic loading. This design, however, depends on the required ductility level of the shear wall; design standards such as CSA A23.3 and ACI 318 mandate specific seismic detailing to achieve different levels of energy-dissipation capacity.

Seismic codes establish design-level lateral force requirements that represent the expected inertial demands on a structure during an earthquake. The Canadian Building Code (NBCC 2020) classifies seismic detailing and ductility into (i) Ductile Shear Walls, (ii) Moderately Ductile, and (iii) Conventional Construction. In the American Society of Civil Engineers (ASCE 7) standard, these are grouped by structural system, based on the participation of structural elements designed to resist both gravity and lateral loads. These are (i) Bearing Walls, (ii) Building Frame system, and (iii) Dual system. These are then subdivided into Special structural walls and Ordinary walls, which differ in their detailing and ductility.

Defining these systems is essential for determining the Response Modification Coefficient (R), a factor used in seismic design to reduce the elastic forces an earthquake would theoretically impose on a structure, accounting for the expected inelastic behavior or ductility the structure can undergo under lateral loading. These definitions vary by code, as shown in Table 2-1 and Table 2-2.

In contrast to the U.S. approach of using a single R value, the National Building Code of Canada (NBC) divides this concept into two distinct factors: R_d (Ductility) and R_o (Overstrength). In the Canadian Code, the total reduction is the product of these two factors.

System Type	R_d	R_o	$R_d R_o$
Ductile shear walls	3.5	1.6	5.6
Moderately ductile shear walls	2	1.4	2.6
Conventional construction (Shear Walls)	1.5	1.3	1.95

Table 2-1 NBC 2020 - Force Modification Factors

System Type	Wall Detail Level	R
Bearing Wall System	Special Structural Wall	5
	Ordinary Structural Wall	4
Building Frame System	Special Structural Wall	6
	Ordinary Structural Wall	5
Dual System	Special Structural Wall	7
	Ordinary Structural Wall	6

Table 2-2 ASCE 7 - Seismic Force Resisting Design Coefficients

A comparison of these two codes shows that the seismic force-reduction factors are remarkably similar for high-ductility systems. Specifically, the NBC 2020 'Ductile Shear Wall', which uses a combined factor ($R_d R_o$) of 5.6, aligns closely with the ASCE 7-22 'Special Structural Wall' within a bearing wall system, which is assigned an R-factor of 5. These factors, derived from experimental data, influence the economy and structural performance of optimized shear walls.

Both standards define the maximum hazard, the Maximum Considered Earthquake (MCER), based on a 2% probability of exceedance in 50 years, corresponding to a 2475-year return period. However, a key difference lies in the design basis: whereas the Canadian NBC 2020 design assumes the full intensity of this event, the American ASCE 7-22 defines the Design Earthquake as two-thirds (2/3) of the MCER intensity before applying the R coefficient.

This study evaluates the design of reinforced concrete shear walls in accordance with updated Canadian (CSA A23.3-24) and American (ACI 318-25) standards. Both standards use a Limit States Design framework to ensure structural integrity and seismic resilience, providing a margin of safety against collapse and ensuring the building lasts its intended lifespan while remaining functional under everyday loads.

Because many requirements in CSA A23.3 are displacement-based, it is important to reasonably estimate the expected maximum displacement due to the design earthquake. The codes impose varying constraints on lateral flexibility to protect non-structural components in typical residential, commercial, and office buildings; the allowable story drift is limited to 2.0% of the story height in ASCE 7-22. In contrast, the NBC 2020 allows a slightly larger maximum lateral displacement of 2.5% of the story height. Regarding residual story drift, ASCE 7-22 Section 16.4.1.3 restricts the maximum drift to 1% for structures at rest in buildings exceeding 73 m in height.

Building codes are organized into chapters by element type and further subdivided into seismic and ordinary requirements. When designing shear walls subjected to seismic forces, the design must primarily comply with the provisions for Intermediate or Special Structural Walls. Because these seismic provisions impose more stringent design criteria than standard rules, satisfying them inherently meets the general ordinary requirements. The specific chapters focused on in this study for shear wall design are listed in Table 2-3.

	CSA A23.3:24	ACI 318-25
General Requirements	Clause 14	Chapter 11
Seismic Design	Clause 21	Chapter 18.10
Detailing Reinforcement	Clause 12	Chapter 25

Table 2-3 Design Requirements for shear walls-based Design Codes

For standard reinforced concrete walls, thickness is determined primarily by slenderness and reinforcement requirements. For bearing walls, CSA A23.3 (Clause 14.1.7) sets the minimum thickness to the greater of the ratios $l_w/25$ or $h_w/25$ (unsupported length or clear height), but not less than 150 mm. In seismic design, the minimum thickness depends on ductility (R_d) and whether the segments are within a plastic hinge region. According to Clause 21.5.3.2, the thickness within a plastic hinge is limited to $l_w/14$ or $l_w/10$ (for ductile walls), while regions outside the plastic hinge are limited to $l_w/20$ or $l_w/14$.

In comparison, ACI 318 (Chapter 11.3) limits the minimum thickness to $l_w/25$ or $h_w/25$ but not less than 100 mm. However, these values apply only to walls designed under the simplified design method in Section 11.5. When designing for seismic demand, these restrictions become significantly stricter to prevent out-of-plane buckling.

The dimensional boundary requirements for classifying vertical wall segments and wall piers according to ACI 318 are summarized in Figure 2-1. The structural classification depends on two geometric ratios: the aspect ratio (h_w/l_w), and the section slenderness ratio (l_w/b_w). For low aspect ratios ($h_w/l_w < 2.0$), the element is classified strictly as a wall regardless of section slenderness. Conversely, for taller segments ($h_w/l_w \geq 2.0$), the element behaves as a wall pier when the section slenderness is limited ($l_w/b_w > 6.0$). Otherwise, the segment must satisfy specified column seismic design provisions (Section 18.10.8.1). Only when the length-to-thickness ratio exceeds 6.0 ($l_w/b_w > 6.0$) does the slender element qualify as a standard structural wall.

Clear height of vertical wall segment/length of vertical wall segment (h_w/ℓ_w)	**Length of vertical wall segment/wall thickness (ℓ_w/b_w)**		
	(ℓ_w/b_w) ≤ 2.5	**2.5 < (ℓ_w/b_w) ≤ 6.0**	**(ℓ_w/b_w) > 6.0**
$h_w/\ell_w < 2.0$	Wall	Wall	Wall
$h_w/\ell_w \geq 2.0$	Wall pier required to satisfy specified column design requirements; refer to 18.10.8.1	Wall pier required to satisfy specified column design requirements or alternative requirements; refer to 18.10.8.1	Wall

[1] h_w is the clear height, ℓ_w is the horizontal length, and b_w is the width of the web of the wall segment.

Figure 2-1 Governing design provisions for vertical wall segments (Table R18.10.1 ACI-318)

For a Special Structural Wall, thickness is governed by the requirement for two curtains of reinforcement and the stability requirements of Section 18.10.1 (Table R18.10.1). According to Section 18.10.2.2, two layers of reinforcement are mandatory if shear forces exceed $V_u > 0.17\lambda\sqrt{f'}_c\, A_{cv}$ or if the wall has an aspect ratio. However, walls requiring special boundary elements, as suggested in Chapter 18.10.6.4, should have a width of at least $h_w/16$ and, in some cases, 300mm.

The maximum reinforcement ratio in walls depends on the wall system's ductility level. In general wall design, the maximum is $0.08A_g$. In high-ductility walls, such as those in the Canadian Standard (CSA A23.3:24, Clause 21.5.4.4), the limit is stricter, capped at $0.06\ A_g$, including lap splices. Similarly, ACI 318 establishes an absolute maximum of $0.08A_g$ for longitudinal reinforcement, including splice regions. To remain compliant with the absolute 8% cap in lap splice regions, engineers typically limit the 'base' reinforcement to 4%. This ensures that when bars overlap, and the steel area doubles, the total ratio does not exceed the code-mandated limit.

According to CSA A23.3, Clause 14.1.8.2.4, the minimum area of distributed vertical reinforcement is $0.0015A_g$ for standard shear walls, increasing to $0.002A_g$ for squat shear walls and $0.0025A_g$ for ductile shear walls (Clause 21.5.5.1). In contrast, ACI 318-25 Section 11.6 for general cast-in-place structural walls requires a minimum longitudinal reinforcement ratio of $0.0012A_g$ when using bars smaller than No. 16. However, under high shear demand, defined as $V_u > 0.5\,\phi\,\alpha_c\,\lambda\,\sqrt{f'c}\,A_{cv}$, the minimum longitudinal reinforcement ratio is increased to $0.0025A_g$. Furthermore, for Special Structural Walls, ACI 18.10.2.4 mandates a more rigorous minimum ratio of $0.5\sqrt{f'_c}\,/f_y$ at the wall ends to ensure proper ductility and the distribution of secondary flexural cracks, assuming the inelastic response is dominated by flexural yielding at the critical section.

According to CSA A23.3, Clause 14.1.8.4, for standard walls, vertical and horizontal bars shall not be spaced farther apart than the lesser of three (3) times the wall thickness or 500 mm. However, for seismic design, Clause 21.5.5.2 reduces the maximum spacing of horizontal reinforcement in ductile and moderately ductile shear walls from 400 mm to 300 mm, thereby improving crack control and concrete confinement within the plastic hinge region.

In ACI 318-25, Sections 11.7.2 and 18.10.2.1, limit the longitudinal spacing for general structural walls to the lesser of three (3) times the wall thickness or 450 mm. For special structural walls designed for seismic demand, transverse reinforcement spacing is stricter around boundary elements; evaluate these in accordance with 18.10.6.2 to 18.10.6.5. Two design approaches are presented. The first is a displacement-based design based on the wall's expected lateral displacement. This approach assumes that the wall's inelastic response is dominated by flexural action. It compares the wall's curvature demand to its compression capacity, up to a maximum strain of 0.003. Under the assumption that plastic deformations are isolated within a defined plastic hinge length of $l_p = 0.5\ l_w$, the plastic rotation demand (θ_p) concentrated within this hinge can be approximated as the ratio of the design displacement demand to the effective wall height.

This approach directly establishes the need for localized boundary confinement when the neutral axis depth exceeds $c \geq \frac{l_w}{600\left(1.5\frac{\delta_u}{h_w}\right)}$, ensuring that the concrete's strain capacity can safely accommodate the global drift demands.

The second approach is known as the stress-based approach. It is based on the maximum extreme fiber compressive stress. If this stress exceeds 0.2 f'_c under factored load combinations (including earthquake effects), Special Boundary Elements are required. The Boundary element can be discontinued at the height where the calculated compressive stress drops below 0.15 f'_c.

The Canadian code also uses a displacement-based design approach that relies on the wall's expected lateral inelastic displacement. It compares the estimated inelastic rotation demand to the inelastic rotation capacity, with a maximum strain of 0.0035 and a yield strain of 0.002. The Canadian code also assumes a plastic hinge length of $l_p = 0.5\ l_w$. Based on clauses 21.5.7.2 and 21.5.7.3, boundary element confinement is required when the neutral axis depth $c \geq \frac{l_w}{570\left(\frac{\delta_{in}}{2h-l_w}+0.002\right)}$. The comparative analysis of the CSA A23 and ACI 318 codes is shown in Table 2-4.

	CSA A23.3:24	ACI 318-25
Curvature	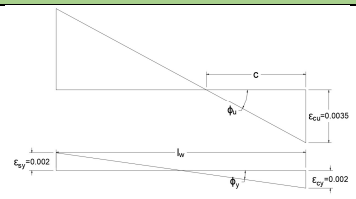 $\phi_p = \phi_u - \phi_y$ $\phi_p = \frac{\varepsilon_{cu}}{c} - \frac{\varepsilon_{sy}+\varepsilon_{cy}}{l_w}$	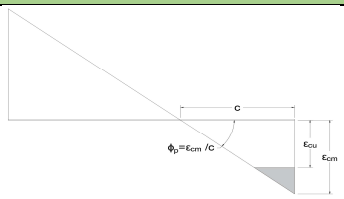 $\phi_p = \frac{\varepsilon_{cm}}{c}$
Displacement	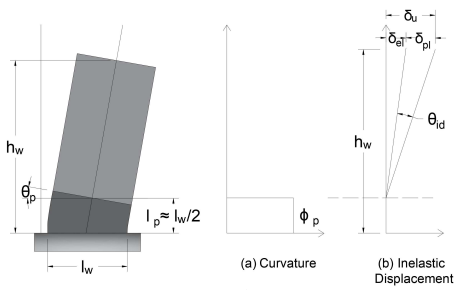 $\theta_{id} = \frac{\delta_{pl}}{h_w - l_p}$ $\emptyset_p = \frac{\theta_{ic}}{l_p} \rightarrow \frac{\theta_{ic}}{l_p} = \frac{\varepsilon_{cu}}{c} - \frac{\varepsilon_{sy}+\varepsilon_{cy}}{l_w}$ $\theta_{ic} = \frac{l_w}{2}\left(\frac{\varepsilon_{cu}}{c} - \frac{\varepsilon_{sy}+\varepsilon_{cy}}{l_w}\right)$ $\theta_{ic} = \left(\frac{l_w\ \varepsilon_{cu}}{2\ c} - 0.002\right)$ $\theta_{ic} \geq \theta_{id} \rightarrow \frac{l_w\ \varepsilon_{cu}}{2\ c} - 0.002 \geq \frac{\delta_{pl}}{h_w - l_w/2}$ $c \geq \frac{l_w\ \varepsilon_{cu}}{2\left(\frac{\delta_{pl}}{h_w - \frac{l_w}{2}} + 0.002\right)}$ $\frac{\varepsilon_{cu}}{2} \approx 0.00175\ or \frac{1}{570}$	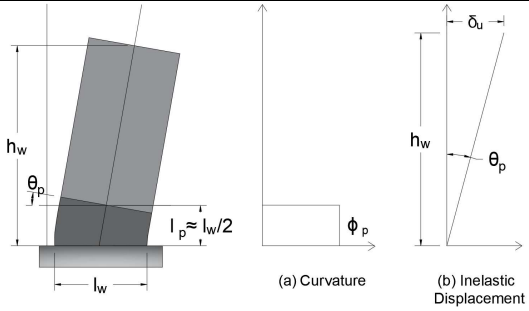 $\theta_p = \frac{\delta_u}{h_w}$ $\emptyset_p = \frac{\theta_p}{l_p} \rightarrow \emptyset_p = \frac{\left(\frac{\delta_u}{h_w}\right)}{\left(\frac{l_w}{2}\right)} = \frac{\varepsilon_{cm}}{c}$ $\frac{\varepsilon_{cm}}{c} = \frac{2\left(\frac{\delta_u}{h_w}\right)}{(l_w)} \rightarrow c = \frac{\varepsilon_{cm}}{2} \cdot \frac{l_w}{\left(\frac{\delta_u}{h_w}\right)}$ $\frac{\varepsilon_{cm}}{2} \approx 0.0015\ or \frac{1}{660} \approx \frac{1}{600}$

Table 2-4 Comparative analysis of requirements for boundary element confinement based on displacement-based design

	CSA A23.3:24	ACI 318-25
neutral axis depth	$c \geq \frac{l_w}{570\left(\frac{2\delta_{pl}}{2h_w - l_w} + 0.002\right)}$ Where is express as $\delta_{pl} = (\Delta_f R_d R_o - \Delta_f \gamma_{wd})$ from the code Clause 21.5.7.2	$c \geq \frac{l_w}{600\left(1.5\frac{\delta_u}{h_w}\right)}$

Table 2-4 Comparative analysis of requirements for boundary element confinement based on displacement-based design (Continued)

Furthermore, for a flanged cross-section such as a U-shaped wall, Section 18.10.5.2 of ACI 318 defines the effective flange width as extending from the face of the web by a distance equal to the lesser of one-half the distance to an adjacent wall web and 25% of the total wall height above the section under consideration. For a U-shaped wall, this limit applies when the flanges are exceptionally long (deep channel) relative to the structure's total height. In contrast, Clause 10.3.3 of the Canadian standard (CSA A23.3) limits the effective overhanging flange width for general flexural T-beams to 12 times the flange thickness or, in a U-section, the web thickness ($12\ t_w$). Other specific provisions are tailored primarily to beam geometry rather than to structural walls.

Both the American Concrete Institute (ACI 318-25) and the Canadian Standards Association (CSA A23) define Effective Stiffness (EI_{eff}) to account for the reduction in a wall's rigidity caused by concrete cracking and reinforcement yielding during a seismic event (see Table 2-5). ACI 318 offers a simplified approach, using $0.35\ I_g$ recommended for walls expected to crack and $0.70\ I_g$ for uncracked walls. An alternative, more detailed expression for the moment of inertia is available via a formula that accounts for the contribution of axial compression, which increases the stiffness by delaying the onset of cracking $\left(I_e = \left(0.80 + 25\frac{A_{st}}{A_g}\right)\left(1 - \frac{M_u}{P_u\, h} - \frac{P_u}{P_o}\right) I_g\right)$; This value is constrained between $0.35 I_g$ and $0.875 I_g$.

Similarly, the Canadian standard (CSA A23.3) uses a specific reduction factor $\left(I_e = \left(1 - 0.35\left(\frac{R_d R_o}{\gamma_w} - 1\right)\right) I_g\right)$, based on the anticipated seismic demand (R_d R_o) and the wall's overstrength (γ_w). The resulting effective stiffness is limited to a minimum of $0.5\ I_g$ and a maximum of $1.0\ I_g$.

	CSA A23.3:24	ACI 318-25
Simplified Method	Moment of inertia: Beams $0.35I_g$ Columns $0.70I_g$ Walls — Uncracked $0.70I_g$ Walls — Cracked $0.35I_g$ Flat plates and flat slabs $0.25I_g$	**Member and condition** / **Moment of inertia** Columns: $0.70I_g$ Walls — Uncracked: $0.70I_g$ Walls — Cracked: $0.35I_g$ Beams: $0.35I_g$ Flat plates and flat slabs: $0.25I_g$

Table 2-5 Reduction factors to account for Effective Stiffness based on CSA A23.3 and ACI 318

<table>
<tr><th></th><th>CSA A23.3:24</th><th>ACI 318-25</th></tr>
<tr><td>Detailed Method</td><td>
<table>
<tr><th>Element type</th><th>Effective property</th></tr>
<tr><td>Beam</td><td>$I_e = 0.4\,I_g$</td></tr>
<tr><td>Column</td><td>$I_e = \alpha_c I_g$</td></tr>
<tr><td>Coupling beam (Clause 21.5.8.1)</td><td>$A_{ve} = 0.15A_g$; $I_e = 0.4\,I_g$</td></tr>
<tr><td>Coupling beam (Clause 21.5.8.2)</td><td>$A_{ve} = 0.45\,A_g$; $I_e = 0.25\,I_g$</td></tr>
<tr><td>Slab frame element</td><td>$I_e = 0.2\,I_g$</td></tr>
<tr><td>Wall</td><td>$A_{ve} = \alpha_w A_g$; $I_e = \alpha_w I_g$</td></tr>
</table>
$\alpha_w = 1.0 - 0.35\left(\frac{R_d R_o}{\gamma_w} - 1.0\right) \geq 0.5$ and ≤ 1.0
</td><td>
<table>
<tr><th>Member</th><th>Alternative Value for I for elastic analysis (I_e)</th></tr>
<tr><td>Columns and walls</td><td>$\left(0.80 + 25\frac{A_{st}}{A_g}\right)\left(1 - \frac{M_u}{P_u\,h} - \frac{P_u}{P_o}\right) I_g$</td></tr>
<tr><td>Beams, flat plates, and flat slabs</td><td>$(0.10 + 25\rho)\left(1.2 - 0.2\frac{b_w}{d}\right) I_g$</td></tr>
</table>
Notes: For continuous flexural members, I shall be permitted to be taken as the average of values obtained for the critical positive and negative moment sections P_u. and M_u shall be calculated from the load combination under consideration, or the combination of P_u. and M_u that produces the least value of I.
</td></tr>
<tr><td>Range constraints (Shear walls)</td><td>$0.5\,I_g < I_e < 1.0\,I_g$</td><td>$0.35\,I_g < I_e < 0.875\,I_g$</td></tr>
</table>

Table 2-5 Reduction factors to account for Effective Stiffness based on CSA A23.3 and ACI 318 (Continued)

ACI 318-25 has recently added Section 18.10.4.4, which establishes new shear strength provisions for non-planar walls. Because shear stress distribution is non-uniform in non-planar geometries, the factor $\propto_{sh}$ was introduced to account for the increased shear strength observed in flanged wall tests compared with simple rectangular sections.

The code states that the total shear capacity V_n must not exceed $V = \propto_{sh} 0.66\sqrt{f_c'}\,A_{cv}$ across all vertical wall segments sharing a common lateral force. Additionally, for any single vertical segment, V_n shall not be taken greater than $V = \propto_{sh} 0.83\sqrt{f_c'}\,A_{cw}$, where A_{cw} represents the cross-sectional concrete area of that specific segment. The term is $\propto_{sh}$ a shape factor that defines the shear stress limit for walls, and is given by the equation:

$$\propto_{sh} = 0.7\left(1 + \frac{b_f\,t_f}{A_{cx}}\right)^2 \leq 1.2 \qquad \textit{Eq. 2-1}$$

Where $b_f\,t_f$ is the total area of the effective flange width and b_f can be determined in accordance with Section 18.10.5.2 as $b_f = \min(0.5\,L_{adj}, 0.25\,h_w)$.

As illustrated in Figure 2-2, the effective depth depends on the orientation and direction of the lateral loading, resulting in different calculated values for $\propto_{sh}$. The term A_{cx} always represents the combined concrete area of the wall segments oriented parallel to the applied lateral force. Conversely, $b_f\,t_f$ captures the area of the perpendicular geometric components acting as flanges.

When the direction of loading places the flanges in compression, the effective flange width is minimized, and $b_f\,t_f$ is taken as the localized intersection area between the web and the flanges. But when the loading direction is reversed, subjecting the flanges to flexural tension and the web to compression, a significantly greater effective flange length b_f is considered. This methodology is calibrated against a database of 340 symmetrical wall cross-sections (including rectangular, barbell, and H-shapes) compiled by Rojas-León (2022) and Rojas-León et al. (2024).

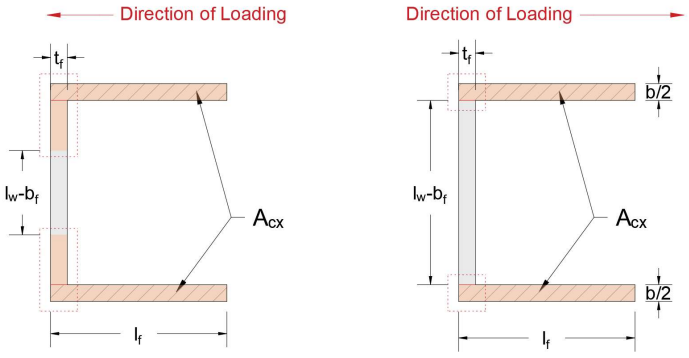

(a) Web in compression *(b) Web in tension*

Figure 2-2 Accounting for the effective area depending on the direction of loading

In terms of the code, the term $\propto_{sh}$ must be between 0.9 and 1.2, inclusive. However, Rojas-León et al. (2024) originally proposed an upper limit of 1.5.

In addition to effective flange widths, design codes provide specific recommendations for detailing reinforcement at the intersections of interconnected shear walls. CSA A23.3 Clause 21.5.10.6 requires a minimum of four longitudinal bars at the ends and intersections of all wall flanges; if the factored shear force exceeds a specific threshold, these four bars must be at least 15M in size and enclosed by ties configured as a compression member. Regarding the stirrups, Clause 14.8.5 stipulates that horizontal reinforcement must not terminate at the inside corner interface. Still, it must instead fully extend into the flange or be anchored within regions of concentrated reinforcement at the ends of the wall. In relatively thin walls, these intersections often become heavily congested, creating significant constructability challenges that require careful detailing review.

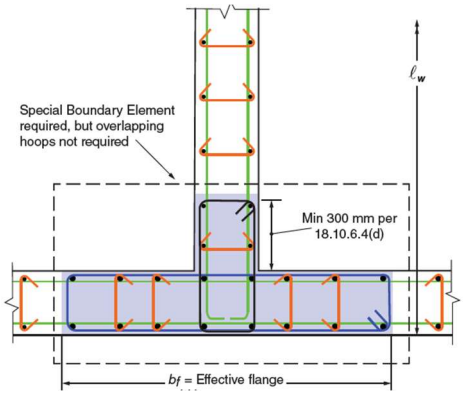

Figure 2-3 Example configuration for a case where a special boundary element is required for a flanged wall (ACI 318-25)

ACI Section 18.10.6.4(d) establishes additional detailing requirements. For flanged sections, the confined concrete zone must fully cover the effective width of the flange in compression and anchor itself deeply into the stem (web) by at least 300 mm (for detailed representation, refer to the example configuration of Figure

2-3). This development is necessary because severe stress concentrations at the web-to-flange interface make it highly susceptible to local concrete crushing.

Clause 21.5.6.5 of the Canadian Standard (CSA A23.3) prohibits lap splices in ductile walls over at least one-half of the story height to avoid placing them within plastic hinge regions. In contrast, ACI 318-19 takes a more localized approach for special structural walls; Section 18.10.2.3 prohibits lap splices of longitudinal reinforcement within confined boundary elements over a height equal to the floor level (h) and the wall length (l_w), as illustrated in Figure 2-4. Although the Canadian code enforces this restriction across the entire wall cross-section at every floor level for all longitudinal reinforcement, ACI limits it strictly to confined boundary elements and to a minimum height of 6 meters. Consequently, a lap splice is permissible at the base of the adjacent floor, as shown in Figure 2-4, a detail commonly adopted in the United States to facilitate construction.

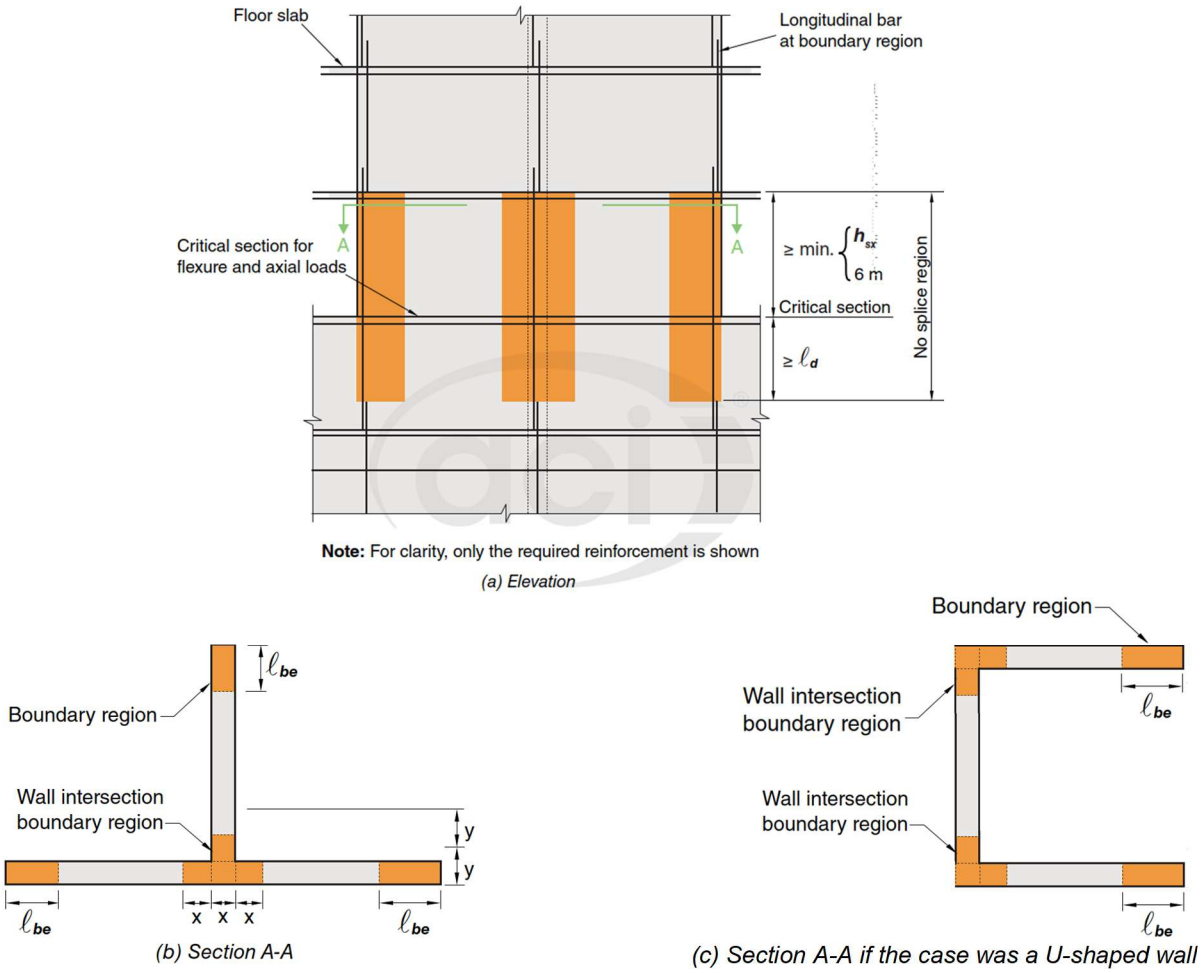

Figure 2-4 Wall boundary regions within heights where lap splices are not permitted. (Fig. R18.10.2.3 - ACI 318-25)

The primary objective of current design standards is to prevent collapse under the design earthquake. These standards target a Life Safety performance level, as illustrated in Figure 2-5. Buildings are expected to sustain extensive damage during a major seismic event, resulting in loss of operational function and lengthy repair

or replacement timelines. Because immediate occupancy is not the objective, re-occupancy typically requires extensive structural retrofitting or, in the worst case, complete demolition and reconstruction.

According to recent studies (FEMA, 2018), a major seismic event could leave up to 40% of modern US code-compliant buildings unoccupiable and in need of substantial repair, while roughly 20% would be uneconomical to repair.

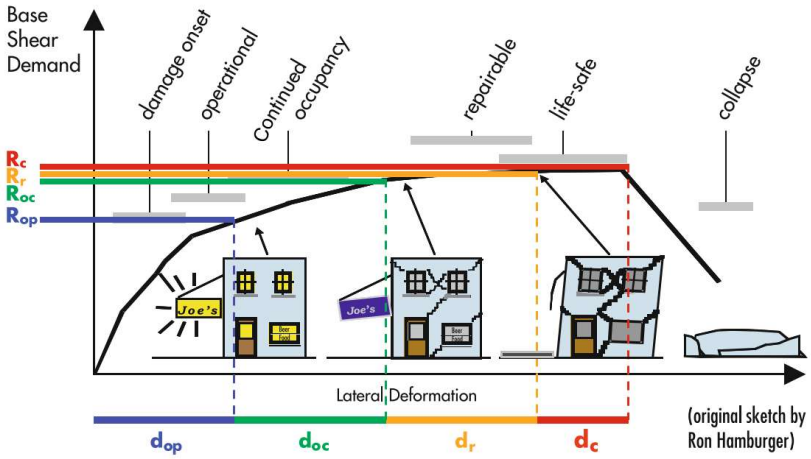

Figure 2-5 Force and displacement levels characterize different global performances. (Garevski et al., 2010)

Modern engineering philosophies recommend designing new buildings for recovery-based objectives, such as functional recovery, in addition to traditional safety-based objectives. The Functional Recovery Structural Limit (FRSL) is a component-based deformation limit state targeting a sufficient margin of residual capacity to withstand future events safely. It sets specific limits such that a component's structural damage (e.g., crack widths, concrete crushing, or residual drift) is mild enough to allow the building to maintain or quickly restore its primary functions.

Guidelines such as FEMA P-58 estimate the maximum residual drift ratio, used to determine whether a building is repairable and practicable, at about 0.5%, as shown in Figure 2-6. The residual drift ratio is plotted against a structure's repair viability. Variables such as repair cost, repair time, and environmental impacts are considered.

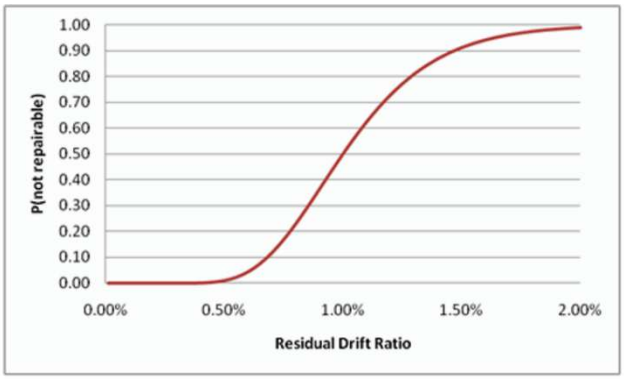

Figure 2-6 Typical building not repair probability based on residual drift ratio (FEMA P-58).

This study evaluates the post-earthquake condition of U-shaped reinforced concrete (RC) walls under various seismic intensities to determine whether the structure remains serviceable after subsequent, or even stronger, seismic events.

Lap splices within structural walls are critical components that significantly influence overall seismic behavior and lateral strength. Historically, these splices are considered weak links, particularly in high-tension regions. The plastic hinge zone is the most critical location for lap splices due to severe cyclic flexural demands. However, to maximize construction efficiency, it is common to terminate foundation reinforcement and initiate lap splices directly within this critical hinge region; extending long, continuous longitudinal bars vertically from the foundation during early construction poses significant logistical challenges and on-site hazards. To address this vulnerability, Aaleti et al. (2013) concluded that lap splices should be strictly avoided within plastic hinge zones and recommended using mechanical couplers instead.

The development length (l_d) provisions in both the Canadian Standard (CSA A23.3, Clause 12.2.2) and the American Code (ACI 318, Chapter 25.4.2 follow similar methodologies. However, the Canadian Standard provides a slightly more detailed approach regarding concrete density and reinforcement grade. While ACI 318 incorporates reinforcement yield strength directly as a variable in its fundamental equations, CSA A23.3 accounts for different steel grades through discrete, predefined values. Additionally, both standards impose a strict lower limit, stating that the development length must not be less than 300 mm. Ultimately, the required length is governed by the bar diameter, the concrete compressive strength ($f_c'$and other modification factors specified in Table 2-6.

	CSA A23.3:24
	Clause 12.2.2
Development length (l_d)	$l_d = \left(0.9 \frac{f_y}{\sqrt{f_c'}} \frac{k_d\ k_l\ k_c\ k_s\ k_g}{\left(\frac{d_{cs}+K_{tr}}{d_b}\right)} \right) d_b$
	$\left(\frac{d_{cs}+K_{tr}}{d_b}\right) \leq 2.5$
	$K_{tr} = \frac{40\ A_{tr}}{sn}$

Table 2-6 Design Requirements on Lap Splice.

For modification factors $k_d\ \ k_l\ k_c\ k_s\ k_g$ refer to Table 12.2 of CSA A23.3:24

$k_d = 1$ for Normal-density concrete

$k_l = 1$ for Vertical Reinforcement

$k_c = 1$ for Uncoated Reinforcement

$k_s = 0.8$ for 20M and smaller bars

$k_g = \frac{f_y}{900} + 0.56$ for $f_y > 400\ MPa$ Reinforcement Grade

For the vertical reinforcement of the experimental shear wall, the validated nonlinear model described in Chapter 5.2.5 included a lap splice at the base of the RC wall to analyze the effects under lateral loading. A minimum development length of 300 mm was applied to both the 6 mm and 8 mm diameter bars. For the 12 mm longitudinal reinforcement, a lap splice length of 730 mm was used. The calculated development length is strongly influenced by the clear concrete cover, which is set at 15 mm for this case study. This relatively shallow concrete cover imposes stricter design constraints, necessitating a longer development length to ensure adequate bond performance. Detailed calculations for these reinforcement metrics are provided in Table 5-23, and their application within the broader parametric study is detailed in Chapter 5.2.5, Lap splice (l_d).

2.2 State of the Art

Paulay and Priestley (1992) laid the groundwork for establishing the capacity design philosophy for flanged shear walls, including U-Shaped walls under seismic performance conditions. Their work prioritized ductile, flexural failure over brittle, shear failure, which can be avoided through rational quantification of appropriate detailing.

Chadchart Sittipunt and Sharon L. Wood first conducted an experimental study of U-shaped walls in 1993. The primary focus was on using finite element analysis (FEA) to model and understand the behavior of reinforced concrete shear walls, particularly the role of web reinforcement. Validation of the FEA model against experimental work is relevant for analyzing complex geometries such as a U-shaped wall. The experimental specimens were subjected to lateral loads in the pushing and pulling directions along the wall's symmetry axis at the top. The experimental failure mode resulted from concrete crushing and buckling of the longitudinal reinforcement in a boundary element. Two models were considered: one using shell elements and the other using two-dimensional plane-stress elements. The analysis concluded that both element types produced nearly identical results, likely because of the slender, 3-inch wall section. This investigation developed material models that represent the cyclic response of concrete and reinforcing steel in shear walls. The concrete model adopted a smeared-crack model with fixed orthogonal cracks. The model captured inelastic bar buckling and boundary-element crushing. The analytical results overestimated the drift at which failure would occur and also predicted web crushing; this failure wasn't present in the experimental results.

Ile & Reynouard (2005) were the first to study the behavior of a U-shaped wall under extreme biaxial cyclic loading (quasistatic cyclic). They evaluated eight U-shaped wall specimens and reported that, under low axial load and low steel ductility, the failure mechanism is dominated by concrete cracking and major steel tensile yielding, with limited concrete crushing due to steel bar fracture. With high axial load and high steel ductility, the specimens failed in flexure and exhibited a ductility of approximately 6. When loaded along the

axis of symmetry at a 1% drift ratio, the longitudinal steel bars at the flange boundaries initiated buckling, and the failure was ultimately caused by the buckling of bars at the corner of the wall web.

Beyer et al. (2008) also investigated the bidirectional quasi-static performance of U-shaped wall sections and observed that shear deformations in non-planar geometries are significantly larger than in typical rectangular walls. Their research demonstrated that standard plastic hinge analyses overestimate flexural moment capacities compared to experimental results. Furthermore, they showed that conventional macro-modeling techniques, which rely on an elastic, uncracked shear stiffness calculated from the gross concrete cross-section, are fundamentally flawed for seismic analysis. While modifying modeling parameters such as shear stiffness, rotational spring stiffness, and link shear flexibility altered the simulated stiffness, unloading loops, and internal force distribution, the ultimate capacity reached in a pushover analysis remained unaffected. This indicates that the maximum capacity is strictly governed by cross-sectional flexural mechanics. Ultimately, the authors concluded that neglecting shear-flexure interaction (SFI) leads to highly inaccurate and potentially dangerous structural designs, a consequence of the flawed practice of assigning a fixed, constant value to shear stiffness. Because shear deformations continue to grow drastically even after a stable flexural hinge formation at the base of the wall, they proposed mitigating this issue by decoupling the shear stiffness ($G \cdot A$) into distinct values before and after flexural yielding.

The paper by Constantin and Beyer (2016) focused on bi-directional seismic behavior; it addressed failure modes, displacement limits, and the development of plastic hinge length for U-shaped wall cross sections. They highlighted that diagonal loading direction is more critical, causing the intersection of the web and flange to become a deep, concentrated compression zone, producing anticipated concrete crushing and triggering rapid buckling of the vertical reinforcement. Another common failure noted was the ends of the flanges. Due to their thin, unconfined regions near the free ends of the flanges, these are highly prone to lateral instability and buckling upon the reversal of large tensile strains. When the U-shaped walls were bent parallel to the flanges (forcing the web into deep compression), the vertical reinforcement at the free ends of the flanges experienced large tensile strains, causing wide, continuous horizontal cracks to open. When the loading path reversed, these open cracks had to close. However, because the free ends were thin and often lacked the heavy confinement found at the main corners, the section struggled to transfer the compressive force uniformly. Before the cracks could completely close to re-establish aggregate interlock, the flange would undergo out-of-plane displacement, triggering lateral instability (out-of-plane wall buckling). This paper also found that longitudinal reinforcement distribution influences the failure modes. The more the longitudinal reinforcement was concentrated in the boundary elements, the more susceptible the boundary element was to failure due to out-of-plane bending. The authors also proved that the physical length of the plastic zone changes with the loading direction because the depth of the compression zone (c) shifts. The authors successfully modified the L_p equations to account for these

multidirectional variations, not only in the walls' web length and height but also in shear stress and the axial load ratio.

Blandon et al. (2024) focused their research on thin shear walls (thickness less than 150 mm). Their experimental program tested a half-scale U-shaped wall specimen under multidirectional lateral loading, reinforced primarily with a single layer of welded wire mesh (WWM), a common construction method used for low-cost government housing programs in Latin America. In these programs, non-planar walls are frequently arranged in multiple geometric configurations to define the layout of the housing units.

The experimental results showed severely limited displacement capacity, with a maximum lateral drift ratio of approximately 1.15%. Ultimate failure was highly brittle, governed by abrupt concrete crushing at the unconfined flange boundaries. Furthermore, the wall exhibited an exceptionally rapid loss of stiffness during the very early stages of loading, losing 50% of its initial gross stiffness at just 0.3% drift when loaded parallel to the flanges. Because incorporating proper concrete confinement at the wall boundaries poses a significant constructability challenge in such thin sections, a reliable approach to ensure the structural safety of these walls is to restrict design parameters so concrete compressive strains remain strictly below their crushing limits. Another recommendation is to apply a severe stiffness-reduction factor below 0.4, given the rapid degradation observed.

The most recent findings of Hoult and Almeida (2023b) indicated shear lag (a structural phenomenon characterized by a non-uniform stress distribution across a member's cross-section). They demonstrated, by analyzing experimental strain data captured via dense instrumentation, that the strain profile across the web and flanges is highly nonlinear, curving sharply near the intersections and concentrating immense demand at the web-flange corner junctions (see Figure 2-7). Because linear design methods do not account for this phenomenon, they overpredict the U-shaped shear wall's actual initial stiffness and ultimate in-plane bending capacity.

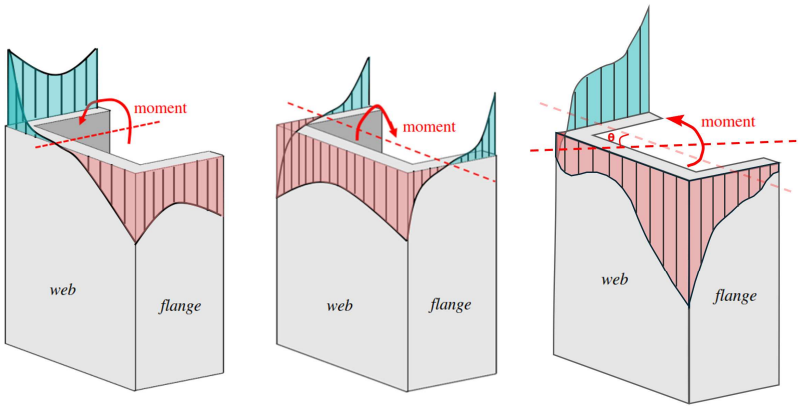

Figure 2-7 Longitudinal strain profile of a U-shaped RC wall under various loading directions. (Modified from Khaloo et al. 2022)

In typical high-rise building design, torsion is frequently treated as a secondary effect or assumed to be resisted through pure shear. However, for an open, non-planar profile such as a U-shaped core, Hoult and Almeida (2024) noted that torque is resisted almost exclusively by warping torsion rather than by circulatory torsion. Crucially, they discovered that the longitudinal normal stresses generated by these warping actions are of the same order of magnitude as those caused by primary lateral building flexure. Consequently, the combination of flexure and warping torsion introduces a highly non-linear strain gradient. This results in intense localized strain concentrations at the web-flange junctions, accelerating concrete crushing and reinforcing bar buckling well before traditional macro-models predict. When the structure experiences torsion and lateral drift simultaneously, the overlapping stresses drastically reduce the in-plane bending moment capacity.

Most existing experimental programs on reinforced concrete (RC) U-shaped core walls have evaluated their structural performance under combined axial and flexural forces. These investigations typically subject the non-planar cross-sections to unidirectional in-plane bending, bidirectional diagonal actions, or multidirectional quasi-static reversed-cyclic loading paths. However, the most realistic experimental configurations that represent actual seismic events use shaking table tests. A prominent example is the study by Hoult et al. (2025), which tested a slender, 40-ton, 0.5-scale RC U-shaped wall specimen (designated USW1) under simulated ground motions based on the 2016 Italian earthquake. The USW1 specimen was fully reinforced using conventional structural steel to evaluate its dynamic behavior. Under a high-intensity unidirectional earthquake applied parallel to the flanges, the structure developed widespread flexural cracking at the extreme ends of the flange boundaries, with cracks worsening at the foundation bed. Under the sequential excitation GM6, the wall experienced combined flexure, shear, and torsion, resulting in extreme compressive stresses concentrated at the corner junction and visible concrete crushing. In the final earthquake motion, the main longitudinal reinforcement buckled; one flange experienced local out-of-plane buckling, kneeling inward toward the wall interior.

After Hoult et al. (2025) release the detailed report on this experiment, a refined 3D finite element model will be developed, and material parameters will be calibrated to improve model accuracy. The results and conclusions of these analyses are also presented, verifying performance under earthquake motion. Subsequently, parametric studies on the influence of axial load ratio, longitudinal and transverse reinforcement ratios, and lap splice locations will be conducted to evaluate the wall's ultimate strength, stiffness, ductility, and the occurrence of local failures.

Despite recent advances in non-linear finite element modeling, current analytical approaches for U-shaped reinforced concrete shear walls exhibit noticeable limitations under complex seismic demands. Standard design codes (e.g., ACI 318, CSA A23.3) and conventional macro-modeling tools frequently neglect coupled shear-flexure-torsional interactions and post-yield shear stiffness decay, often leading to inaccurate design predictions. Crucially, there remains a need to explicitly evaluate how torsional warping stresses distribute

across open sections and to determine the extent to which axial compressive loading affects warping deformation through compressive pre-stressing effects. Furthermore, comprehensive parametric studies are necessary to evaluate global wall behavior, systematically mapping key structural parameters against key drift limit states to establish safety margins. Addressing these combined analytical, behavioral, and experimental shortfalls is essential to establishing reliable non-linear modeling workflows and targeted detailing guidelines for non-planar shear wall systems.

Chapter 3: Principles of Flexural Strength for reinforced concrete walls with a U-Shaped cross-section.

Research on high-rise shear walls with rectangular cross-sections indicates that their strength is primarily governed by flexure rather than shear. Consequently, flexural strength can be accurately determined using the same fundamental assumptions employed in reinforced concrete beam design (per ACI 318-25):

1. Strain Compatibility: Strain in the reinforcement and concrete is assumed to be directly proportional to the distance from the neutral axis.
2. Concrete Strain Limit: The maximum usable strain at the extreme concrete compression fiber is assumed to be 0.003 in the US practice, 0.0035 in the Canadian and European practice.
3. Neglecting Tension: The tensile strength of concrete is neglected in flexural calculations.
4. Stress Distribution: For practical design, an equivalent rectangular concrete stress block (defined by factors such as α_1 for the intensity and β_1 for the effective height of the stress block) represents the concrete compressive stress distribution.

In shear wall design, the compression depth (c) It is the most critical factor because it defines the position of the neutral axis, the boundary separating the wall regions in tension from those in compression. Determining c is the essential first step in calculating the wall's ultimate flexural capacity.

Cárdenas and Magura's (1972) research showed that calculating the compression depth for a slender shear wall relies on equilibrium and strain compatibility. For a rectangular wall with uniformly distributed vertical reinforcement, the sum of internal forces, comprising the concrete compression resultant and the forces in the distributed longitudinal steel, must equal the external design axial load (P).

While the initial calculations focused on walls with rectangular cross-sections and uniformly distributed vertical reinforcement, it is well established that concentrating reinforcement near the wall boundaries (edges) yields superior structural performance. Specifically, concentrated reinforcement enhances moment capacity and improves ultimate curvature, which significantly increases ductility. Consequently, the following subsections review the Cárdenas and Magura (1972) equations and extend their application to walls with concentrated edge reinforcement.

Furthermore, these principles will be adapted to derive equations for U-shaped cross-sections. To validate these analytical methods, the results will be compared with numerical data from Response2000, a reinforced concrete sectional and member analysis program that allows detailed prediction of the load-deformation behavior of sections under combined axial load, moment, and shear.

3.1 Analysis of a U-shaped Shear Wall Cross-Section with Concentrated Boundary Reinforcement

Following the methodology of Cárdenas and Magura (1972), this study analyzes a U-shaped cross-section with a central web and two orthogonal flanges. The section is subjected to combined positive flexure and axial loading, with the analysis aligned along the axis of symmetry. Under this loading condition, the compression block develops within the flanges, while the web reinforcement primarily sustains tensile stress. The wall has distributed vertical reinforcement (A_{sw}) in the web, the flange (A_{sf}), and distinct boundary elements (A_{sb1}, A_{sb2}) at the flange corners. This localized reinforcement configuration significantly enhances flexural capacity compared to a uniform distribution. Consequently, a series of formulations was derived to determine the ultimate moment capacity (M_u) specifically for this reinforcement layout.

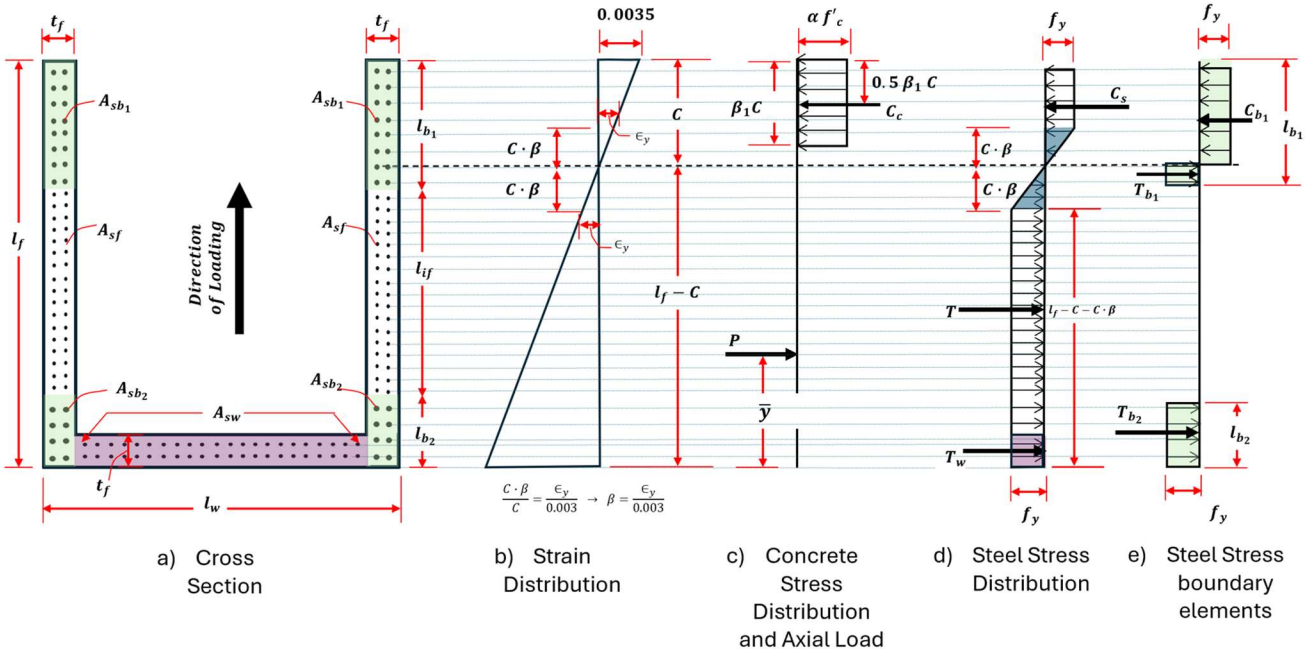

Figure 3-1 U-shaped cross-section under the state of equilibrium (direction of loading FC- Flanges in compression)

The distance to the centroid is defined relative to the extreme bottom fiber of the web as:

$$\bar{y} = \frac{(l_w - 2t_f)\left(\frac{t_f^2}{2}\right) + l_f^2\, t_f}{(l_w - 2t_f)(t_f) + 2\, l_f\, t_f} \qquad \textit{Eq. 3-1}$$

Axial force equilibrium is established by balancing the internal forces acting normal to the cross-section against the external axial load. This equilibrium is expressed as follows:

$$T_w + 2T_{b2} + 2T + 2T_{b1} + P = 2C_c + 2C_s + 2C_{b1} \qquad \textit{Eq. 3-2}$$

By substituting each internal force term based on the section geometry and material properties, the detailed axial force equilibrium equation is obtained:

$$A_{sw}\,f_y + 2\,A_{s,b_2}\,f_y + 2\left(\frac{l_f - c_1 - c_1\,\beta}{l_{If}}\right)A_{sf}\,f_y + 2\left(\frac{l_{b_1} - c_1}{l_{b_1}}\right)A_{sf}\,f_y + P = 2\left(\alpha\,f_c'\,\beta_1\,c_1\,t_f\right) +$$

$$2\,\frac{(c_1 - c_1\,\beta)}{l_{if}}\,A_{sf}\,f_y + 2\left(\frac{c_1}{l_{b_1}}\right)A_{s,b_1}\,f_y \qquad \textit{Eq. 3-3}$$

Isolating the depth of the compressive zone as from Equation 3-3 gives:

$$c_1 = \frac{A_{sw}\,f_y + 2\,A_{s,b_2}\,f_y + 2\,A_{s,b_1}\,f_y + \frac{2\,l_f\,A_{sf}\,f_y}{l_{if}} + P}{2\left(\alpha\,f_c'\,\beta_1\,t_f\right) + \frac{4\,A_{sf}f_y}{l_{if}} + \frac{4\,A_{s,b_1}f_y}{l_{b_1}}} \qquad \textit{Eq. 3-4}$$

Note that c is the depth of the compression zone. Since this value depends on the direction of loading, a subscript "1" (c_1) was added to evaluate the depth of the compressive zone when the direction of loading places the flanges in compression; in the opposite direction, the depth of the compression zone has the nomenclature of c_2.

$$c_1 = \frac{A_{sw}\,f_y + 2\,A_{s,b_2}\,f_y + 2\,A_{s,b_1}\,f_y + \frac{2\,l_f\,A_{sf}\,f_y}{l_{if}} + P}{2\left(\alpha\,f_c'\,\beta_1\,t_f\right) + \frac{4\,A_{sf}f_y}{l_{if}} + \frac{4\,A_{s,b_1}f_y}{l_{b_1}}} \qquad \textit{Eq. 3-5}$$

$$c_1 = \frac{l_{b_1}l_{if}\;f_y(0.5A_{sw} + A_{s,b_2} + A_{s,b_1}) + l_{b_1}l_f\left(A_{sf}\,f_y + 0.5\,P\frac{l_{if}}{l_f}\right)}{(\alpha\,f_c'\,\beta_1\,t_f)l_{b_1}l_{if} + 2\,f_y\,(A_{sf}l_{b_1} + A_{s,b_1}\,l_{if})} \qquad \textit{Eq. 3-6}$$

Dividing both the numerator and denominator by the concrete compressive strength (f_c'), the wall thickness (t_f), the length of the boundary confinement elements at the flange tip (l_{b_1}), and the internal flange length excluding the boundary confinement elements (l_{if}), the following expression is obtained:

$$\frac{c_1}{l_f} = \frac{\frac{f_y}{f_c'\,t_f}(0.5A_{sw} + A_{s,b_2} + A_{s,b_1}) + \frac{1}{f_c'\,t_f}\cdot\frac{l_f}{l_{if}}\left(A_{sf}\,f_y + 0.5\,P\frac{l_{if}}{l_f}\right)}{(\alpha\,\beta_1)\,l_f + \frac{2\,f_y}{f_c'\,t_f\,l_{b_1}}\cdot\frac{l_f}{l_{if}}(A_{sf}l_{b_1} + A_{s,b_1}\,l_{if})} \qquad \textit{Eq. 3-7}$$

Defining terms as:

$$\omega' = \frac{l_{if}}{l_f} \qquad \kappa = \frac{1}{f_c'\;t_f}$$

It follows that the normalized depth of compression zone is:

$$\frac{\boldsymbol{c_1}}{\boldsymbol{l_t}} = \frac{\boldsymbol{f_y\,\kappa\left(0.5A_{sw} + A_{s,b_2} + A_{s,b_1}\right) + \frac{\kappa}{\omega'}\left(A_{sf}\,f_y + 0.5\,P\,\omega'\right)}}{\boldsymbol{(\alpha\,\beta_1)\,l_f + \frac{2\,\kappa\,f_y}{\omega'}\left(A_{sf} + A_{s,b_1}\frac{l_{if}}{l_{b_1}}\right)}} \qquad \textit{Eq. 3-8}$$

By taking the moments about the wall's centroid ($\bar{y}$), the equilibrium equation incorporates the concrete compressive resultant (C_c), the force couples generated by the concentrated boundary reinforcement (T_{b2} and C_{b1}), and the resultant of the distributed web reinforcement (T_w). A negative moment component is included to

account for the boundary reinforcement located beyond the neutral axis depth (c_1), where the stress distribution shifts.

On the other hand, the distributed reinforcement located in the immediate vicinity of the centroid (T) is neglected in the moment summation. This is justified by two factors: first, the minimal lever arm of these bars results in a negligible moment contribution. Second, because some of the bars are distributed symmetrically about the centroidal axis, the opposing positive and negative moments generated by bars above and below the axis effectively cancel each other out. By multiplying each force by its respective lever arm, the ultimate flexural strength capacity M is derived as,

$$M_1 = 2\,C_c\left(l_f - \bar{y} - 0.5\beta_1 c_1\right) + 2\,C_{b1}\left(l_f - \bar{y} - 0.5\,l_{b1}\right) + 2\,T_{b2}\left(\bar{y} - \frac{l_{b2}}{2}\right) + T_w\left(\bar{y} - \frac{t_f}{2}\right) - 2\cdot 2\,T_{b1}\left(l_f - \bar{y} - c_1 - \left(\frac{l_{b_1} - c_1}{2}\right)\right) \quad \textit{Eq. 3-9}$$

$$M_1 = 2(\alpha_1\, f'c\, \beta_1 c_1\, t)\left(l_f - \bar{y} - 0.5\beta_1 c_1\right) + 2\,A_{sb1}\,f_y\left(l_f - \bar{y} - 0.5\,l_{b1}\right) + 2\,A_{sb2}\,f_y\left(\bar{y} - \frac{l_{b2}}{2}\right) + A_{sw}\,f_y\left(\bar{y} - \frac{t_f}{2}\right) - 4\left(\left(\frac{l_{b_1} - c_1}{l_{b_1}}\right)A_{sb1}\,f_y\right)\left(l_f - \bar{y} - c_1 - \left(\frac{l_{b_1} - c_1}{2}\right)\right) \quad \textit{Eq. 3-10}$$

$$\boldsymbol{M_1 = 2(\alpha_1\, f'c\, \beta_1 c_1 t)\left(l_f - \bar{y} - 0.5\beta_1 c_1\right) + 2\,A_{sb1}\,f_y\left(l_f - \bar{y} - 0.5\,l_{b1}\right) + 2\,A_{sb2}\,f_y\left(\bar{y} - \frac{l_{b2}}{2}\right) + A_{sw}\,f_y\left(\bar{y} - \frac{t_f}{2}\right) - 4\left(\left(1 - \frac{c_1}{l_{b_1}}\right)A_{sb1}\,f_y\right)\left(l_f - \bar{y} - 0.5\,l_{b_1} - 0.5c_1\right)} \quad \textit{Eq. 3-11}$$

Five T-shaped sections (labeled Example 1 through 5) were evaluated; notably, these are equivalent to U-shaped cross-sections when analyzed for bending along the axis of symmetry. This geometry was selected because Response-2000 cannot model U-shaped cross-sections directly. The cross-sections were analyzed with boundary elements at the corners and flange edges. To validate the derived equations, the analytical results were compared against outputs from Response-2000, a recognized industry benchmark for sectional and member analysis. This comparison validates the derived equations and ensures they accurately capture the wall's ultimate strength.

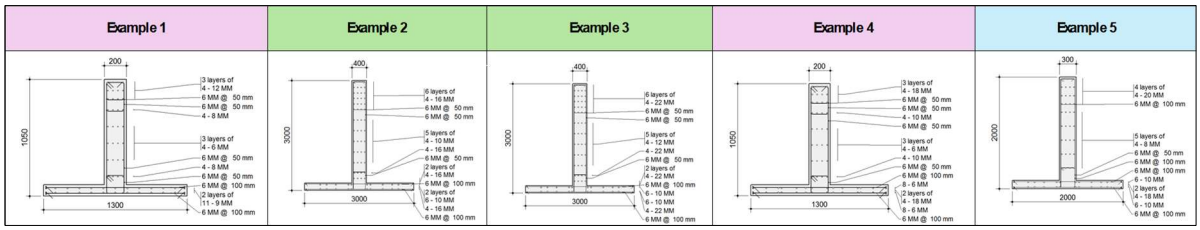

Figure 3-2 Cross-section of a 5 T-section used in examples on Response 2000

Examples 1 and 4 maintain identical cross-sectional geometry while varying the reinforcement ratios to isolate the impact of steel density on capacity. Similarly, Examples 2 and 3 utilize consistent geometric

parameters with varying reinforcement configurations. This approach allows direct evaluation of how reinforcement ratios affect the flexural performance of walls with boundary elements.

The study evaluates the neutral axis depth (C_1) and nominal moment capacity (M) for each wall specimen using an analytical approach and a computational benchmark. The organization of the comparative data is as follows:

I. Equations 3-8 and 3-11: Derived using the fundamental principles established in the Cárdenas and Magura formulations. The primary distinction in this approach lies in the explicit separation of the boundary elements from the flange reinforcement, allowing their unique contribution to be integrated directly into the flexural strength formulation.

II. Response 2000 (flexural) analysis: To establish a reference point for wall strength, results were obtained from Response-2000 software (Depicted in red).

III. Response 2000 + Shear: For a comprehensive view of nonlinear behavior, additional software runs were performed to account for shear-flexure interaction at specific shear spans (L= 2 m and L= 4.02 m).

		f_y	f'_c	L_f	L_{if}	$L_{b,1}$	$L_{b,2}$	t_f	L_w	$\bar{y}$	A_{sw}	A_{sf}	$A_{sb,1}$	$A_{sb,2}$	A_{st}	P	ω'	κ	α_1	β_1	β	$\rho_{v\,Lb,1}$	$\rho_{v\,Lb,2}$	ρ_{sw}	ρ_{sf}	ρ_v	v	c / L_T	c	Error	M	Error
		Mpa	Mpa	mm	mm	mm	mm	mm	mm	mm	mm^2	mm^2	mm^2	mm^2	mm^2	N		mm/N											mm		kN*m	
Example 1	EQ . 3-8 & EQ . 3-11	550	27	**1050**	600	275	175	100	**1300**	361.7	896	268	678	356	3500	244858	0.571	0.00037	0.81	0.90	1.0	0.025	0.020	0.008	0.004	**1.09%**	**0.028**	0.220	231	-2%	1100	-1%
	Resp. 2000 (flexural)																											0.225	236		1114	
	Resp. 2000 + Shear (L= 2 m)																											**0.197**	**207**	-13%	**1030**	-8%
	Resp. 2000 + Shear (L= 4.02 m)																											**0.247**	**260**	9%	**1049**	-6%
Example 2	EQ . 3-8 & EQ . 3-11	550	27	**3000**	1690	800	510	200	**3000**	1077	942.5	785	2412	1608	10553	244858	0.563	0.00019	0.81	0.90	1.0	0.015	0.016	0.002	0.002	**0.61%**	**0.005**	0.144	432	-10%	8706	-7%
	Resp. 2000 (flexural)																											0.159	478		9359	
	Resp. 2000 + Shear (L= 2 m)																											**0.052**	**156**	-67%	**5173**	-45%
	Resp. 2000 + Shear (L= 4.02 m)																											**0.115**	**346**	-28%	**8444**	-10%
Example 3	EQ . 3-8 & EQ . 3-11	550	27	**3000**	1700	800	500	200	**3000**	1077	942.5	1131	4562	3041	18410	244858	0.567	0.00019	0.81	0.90	1.0	0.029	0.030	0.002	0.003	**1.07%**	**0.005**	0.172	517	-10%	13319	-4%
	Resp. 2000 (flexural)																											0.192	577		13841	
	Resp. 2000 + Shear (L= 2 m)																											**0.079**	**238**	-59%	**6607**	-52%
	Resp. 2000 + Shear (L= 4.02 m)																											**0.170**	**510**	-12%	**10032**	-28%
Example 4	EQ . 3-8 & EQ . 3-11	550	27	**1050**	600	275	175	100	**1300**	361.7	452.4	327	1527	1175	6509	244858	0.571	0.00037	0.81	0.90	1.0	0.056	0.067	0.004	0.005	**2.03%**	**0.028**	0.225	236	-2%	1692	-3%
	Resp. 2000 (flexural)																											0.230	241		1750	
	Resp. 2000 + Shear (L= 2 m)																											**0.267**	**281**	14%	**1370**	-22%
	Resp. 2000 + Shear (L= 4.02 m)																											**0.219**	**230**	-5%	**1643**	-6%
Example 5	EQ . 3-8 & EQ . 3-11	550	27	**2000**	1100	500	400	150	**2000**	724.1	942.5	503	2513	1018	9010	244858	0.550	0.00025	0.81	0.90	1.0	0.034	0.017	0.004	0.003	**1.05%**	**0.011**	0.157	314	-13%	4086	-9%
	Resp. 2000 (flexural)																											0.180	359		4490	
	Resp. 2000 + Shear (L= 2 m)																											**0.128**	**256**	-29%	**3022**	-33%
	Resp. 2000 + Shear (L= 4.02 m)																											**0.151**	**302**	-16%	**4166**	-7%

Table 3-1 U-shaped walls neutral axis depth and flexural calculations (flange in compression)

Under pure flexural conditions, the analytical predictions derived from equations 3-8 and 3-11 demonstrate a strong correlation with the Response-2000 benchmarks. Notably, the analytical approach consistently yields conservative results for both the neutral axis depth (C) and the nominal moment capacity (M) when compared to the Response-2000 data, ensuring a reliable margin of safety in the design.

Moment strength drops significantly when considering shear-flexure interaction. For 2m high walls, moment capacity drops by up to 52%, while 4m high walls show a maximum reduction of 28% compared to pure flexural benchmarks. This trend is particularly evident in the 3m long flanges and webs, where shear significantly reduces the predicted analytical capacity. These findings validate the governing equilibrium equations as a robust baseline for member analysis under standard loading. With flange compression validated, the investigation can proceed to analyze the cross-section under reversed loading conditions. In these cases, the web is subjected to compression while the flanges are in tension.

3.2 U-shaped Shear Wall Cross-Section with Concentrated Boundary Reinforcement

Following the same U-shaped cross-section and reinforcement configuration detailed in the previous chapter, the analysis was extended to the reverse orientation along the axis of symmetry. In this case, the section is subjected to combined negative flexure and axial loading. Under this loading sense, the compression block develops within the web, while the flange reinforcement, including the boundary elements, primarily sustains tensile stress. Consequently, a series of formulations was derived to determine the ultimate moment capacity (M_u) specifically for this reinforcement layout.

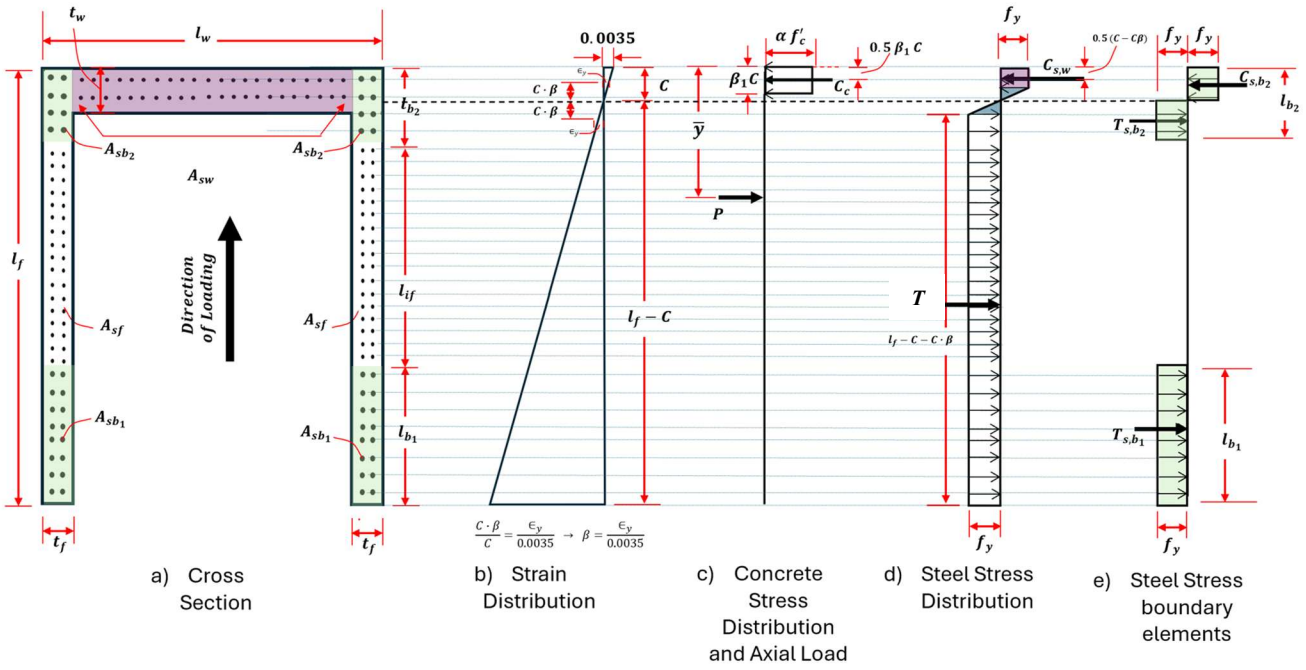

Figure 3-3 Assumptions at flexural strength of U-shaped shear walls (direction of loading FT-Flanges in Tension)

$$2T_{s,b_1} + 2T_{s,b_2} + 2T + P = C_c + 2C_{s,w} + 2C_{s,b_2} \qquad \textit{Eq. 3-12}$$

$$2\,A_{s,b_1}\,f_y + 4\left(\frac{l_{b_2}-c_2}{l_{b_2}}\right)A_{s,b_2}\,f_y + 2\left(\frac{l_f-c_2-c_2\,\beta-l_{b_1}}{l_{If}}\right)A_{sf}\,f_y + P = \alpha\,f_c'\,\beta_1\,c_2\,l_w + \frac{(c_2-c_2\,\beta)}{t_f}\,A_{sw}\,f_y + 2\,A_{s,b_2}\,f_y \qquad \textit{Eq. 3-13}$$

Note that c is the depth of the compression zone. Since this value depends on the direction of loading, a subscript "2" (c_2) was added to evaluate the depth of the compressive zone when the direction of loading places the web in compression. The normalized depth of the compression zone is:

$$\frac{c_2}{l_f} = \frac{2\,f_y\left[A_{s,b_1}+A_{s,b_2}+A_{sf}\left(\frac{l_f-l_{b_1}}{l_{if}}\right)\right]+P}{(\alpha\,f_c'\,\beta_1)l_w l_f + f_y\,l_f\left[\frac{A_{sw}(1-\beta)}{t_f}+\frac{4\,A_{s,b_2}}{l_{b_2}}+\frac{2\,A_{sf}(1+\beta)}{l_{if}}\right]} \qquad \textit{Eq. 3-14}$$

Divide the numerator and denominator by: $f'_c\, l_w\, l_f$

$$\frac{C_2}{l_f} = \frac{2\frac{f_y}{f'_c\, l_w\, l_f}\left[A_{s,b_1} + A_{s,b_2} + A_{sf}\left(\frac{l_f - l_{b_1}}{l_{if}}\right)\right] + \frac{P}{f'_c\, l_w\, l_f}}{(\alpha\, \beta_1) + \frac{f_y}{f'_c\, l_w\, l_f} l_f \left[\frac{A_{sw}\, l_{b_2} l_{if}\, (1-\beta)}{t_f\, l_{b_2}\, l_{if}} + \frac{4\, t_f\, l_{if}\, A_{s,b_2}}{t_f\, l_{b_2}\, l_{if}} + \frac{2\, t_f\, l_{b_2}\, A_{sf}(1+\beta)}{t_f\, l_{b_2}\, l_{if}}\right]} \qquad \textit{Eq. 3-15}$$

And after algebraic simplifications, the following is obtained:

$$\frac{C_2}{l_f} = \frac{2\,\frac{f_y}{f'_c\, l_w\, l_f}\cdot\left[A_{s,b_1} + A_{s,b_2} + A_{sf}\left(\frac{l_f - l_{b_1}}{l_{if}}\right)\right] + \frac{P}{f'_c\, l_w\, l_f}}{(\alpha\, \beta_1)\frac{(t_f\, l_{b_2}\, l_{if})}{(t_f\, l_{b_2}\, l_{if})} + \frac{f_y}{f'_c\, l_w\, l_f}\cdot\frac{l_f}{(t_f\, l_{b_2}\, l_{if})}\left[A_{sw}\, l_{b_2} l_{if}\, (1-\beta) + 4\, t_f\, l_{if}\, A_{s,b_2} + 2\, t_f\, l_{b_2}\, A_{sf}(1+\beta)\right]} \qquad \textit{Eq. 3-16}$$

$$\frac{C_2}{l_f} = \frac{2\,\frac{f_y}{f'_c\, l_w\, l_f}(t_f\, l_{b_2}\, l_{if})\left[A_{s,b_1} + A_{s,b_2} + A_{sf}\left(\frac{l_f - l_{b_1}}{l_{if}}\right)\right] + \frac{P\,(t_f\, l_{b_2}\, l_{if})}{f'_c\, l_w\, l_f}}{(\alpha\, \beta_1)(t_f\, l_{b_2}\, l_{if}) + \frac{f_y}{f'_c\, l_w\, l_f} l_f \left[A_{sw}\, l_{b_2} l_{if}\, (1-\beta) + 4\, t_f\, l_{if}\, A_{s,b_2} + 2\, t_f\, l_{b_2}\, A_{sf}(1+\beta)\right]} \qquad \textit{Eq. 3-17}$$

By introducing the following parameters,

$$\boldsymbol{\omega'' = \frac{f_y}{f'_c\, l_w\, l_f}} \qquad \boldsymbol{\kappa' = t_f\, l_{b_2}\, l_{if}}$$

It follows:

$$\frac{\boldsymbol{C_2}}{\boldsymbol{l_f}} = \frac{\boldsymbol{2\omega''(\kappa')\left[A_{s,b_1} + A_{s,b_2} + A_{sf}\left(\frac{l_f - l_{b_1}}{l_{if}}\right)\right] + \alpha'\kappa'}}{\boldsymbol{(\alpha\, \beta_1)\kappa' + \omega'' l_f\left[A_{sw}\, l_{b_2} l_{if}\, (1-\beta) + 4\, t_f\, l_{if}\, A_{s,b_2} + 2\, t_f\, l_{b_2}\, A_{sf}(1+\beta)\right]}} \qquad \textit{Eq. 3-18}$$

By taking moments about the wall's centroid ($\bar{y}$), the equilibrium equation includes the concrete compressive resultant (C_c) and the force couples generated by the concentrated boundary reinforcement ($C_{sb,2}$ and $T_{s,b1}$).

The distributed reinforcement located in the immediate vicinity of the centroid (T) is neglected in the moment summation. This is justified by two factors: first, the minimal lever arm of these bars results in a negligible moment contribution. Second, because some of the bars are distributed symmetrically about the centroidal axis, the opposing positive and negative moments generated by bars above and below the axis effectively cancel each other out. By multiplying each force by its respective lever arm, the ultimate flexural strength (M) is derived as

$$M_2 = C_c\,(\bar{y} - 0.5\beta_1 C_2) + 2\,T_{s,b1}\left(l_f - \bar{y} - 0.5\,l_{b1}\right) + 2\,C_{s,b2}\left(\bar{y} - \frac{l_{b2}}{2}\right) + C_{s,w}\left(\bar{y} - \frac{C_2 - C_2\,\beta}{2}\right) \qquad \textit{Eq. 3-19}$$

$$\boldsymbol{M_2 = (\alpha_1\, f'c\, \beta_1 C_2 l_w)\,(\bar{y} - 0.5\beta_1 C_2) + 2\,A_{sb1}\, f_y\left(l_f - \bar{y} - 0.5\,l_{b1}\right) + 2\,A_{sb2}\, f_y(\bar{y} - 0.5\,l_{b2}) + A_{sw} f_y\left(\frac{C_2 - C_2\beta}{t_w}\right)(\bar{y} - 0.5C_2 - 0.5C_2\beta)} \qquad \textit{Eq. 3-20}$$

Building on the previous study, the same five T-shaped profiles were re-evaluated by reversing the analysis direction along the axis of symmetry. As with the prior cases, results were compared with Response-2000 outputs. This step is critical to ensuring that the derived equation maintains the predictive accuracy for flexural strength across different analysis directions.

This approach allows for a direct evaluation of how reinforcement ratios influence the flexural performance of walls with boundary elements. The study evaluates the neutral axis depth (C_2) and nominal moment capacity (M) for each wall specimen using an analytical approach and a computational benchmark. The organization of the comparative data is as follows:

I. Equations 3-18 and 3-20: Derived using the fundamental principles established in the Cárdenas and Magura formulations. The primary distinction in this approach lies in the explicit separation of the boundary elements from the flange reinforcement, allowing their unique contribution to be integrated directly into the flexural strength formulation.

II. Response 2000 (flexural) analysis: To establish a reference point for wall strength, results were obtained from Response-2000 software (Depicted in red)

III. Response 2000 + Shear: For a comprehensive view of nonlinear behavior, additional software runs were performed to account for shear-flexure interaction at specific shear spans (L= 2 m and L= 4.02 m)

		F_y	F'_c	L_f	L_{if}	$L_{b,1}$	$L_{b,2}$	t_f	L_w	$\bar{y}$	A_{sw}	A_{sf}	$A_{sb,1}$	$A_{sb,2}$	A_{st}	P	ω''	α'	κ'	α_1	β_1	β	$\rho_{v\ Lb,1}$	$\rho_{v\ Lb,2}$	ρ_{sw}	ρ_{sf}	ρ_v	v	c / L_f	c	Error	M	Error
		Mpa	Mpa	mm	mm	mm	mm	mm	mm	mm	mm^2	mm^2	mm^2	mm^2	mm^2	N	mm^2		mm^3													kN*m	
Example 1	EQ 3-18 & EQ 3-20	550	27	**1050**	600	275	175	100	**1300**	361.7	896	268	678	356	3500	244858	1E-05	0.007	10500000	0.81	0.90	1.0	0.025	0.020	0.008	0.004	**1.09%**	**0.028**	0.054	57	-2%	1007	-11%
	Resp. 2000 (flexural)																												**0.055**	**58**		**1137**	
	Resp. 2000 + Shear (L= 2 m)																												**0.060**	**63**	8%	**991**	-13%
	Resp. 2000 + Shear (L= 4.02 m)																												**0.056**	**59**	1%	**1056**	-7%
Example 2	EQ 3-18 & EQ 3-20	550	27	**3000**	1690	800	510	200	**3000**	1077	942	785	2412	1608	10553	244858	2E-06	0.001	172380000	0.81	0.90	1.0	0.015	0.016	0.002	0.002	**0.61%**	**0.005**	0.029	86	-22%	10794	8%
	Resp. 2000 (flexural)																												**0.037**	**111**		**9977**	
	Resp. 2000 + Shear (L= 2 m)																												**0.026**	**79**	-28%	**5133**	-49%
	Resp. 2000 + Shear (L= 4.02 m)																												**0.055**	**164**	32%	**7613**	-24%
Example 3	EQ 3-18 & EQ 3-20	550	27	**3000**	1700	800	500	200	**3000**	1077	942	1131	4562	3041	18410	244858	2E-06	0.001	170000000	0.81	0.90	1.0	0.029	0.030	0.002	0.003	**1.07%**	**0.005**	0.046	138	-4%	18697	4%
	Resp. 2000 (flexural)																												**0.048**	**144**		**18004**	
	Resp. 2000 + Shear (L= 2 m)																												**0.042**	**127**	-12%	**6966**	-61%
	Resp. 2000 + Shear (L= 4.02 m)																												**0.070**	**209**	31%	**10853**	-40%
Example 4	EQ 3-18 & EQ 3-20	550	27	**1050**	600	275	175	100	**1300**	361.7	452	327	1527	1175	6509	244858	1E-05	0.007	10500000	0.81	0.90	1.0	0.056	0.067	0.004	0.005	**2.03%**	**0.028**	0.084	88	0%	2010	-7%
	Resp. 2000 (flexural)																												**0.084**	**88**		**2153**	
	Resp. 2000 + Shear (L= 2 m)																												**0.143**	**150**	41%	**1463**	-32%
	Resp. 2000 + Shear (L= 4.02 m)																												**0.085**	**89**	1%	**1877**	-13%
Example 5	EQ 3-18 & EQ 3-20	550	27	**2000**	1100	500	400	150	**2000**	724.1	942	503	2513	1018	9010	244858	5E-06	0.002	66000000	0.81	0.90	1.0	0.034	0.017	0.004	0.003	**1.05%**	**0.011**	0.053	106	9%	6252	-3%
	Resp. 2000 (flexural)																												**0.048**	**96**		**6436**	
	Resp. 2000 + Shear (L= 2 m)																												**0.063**	**126**	24%	**3468**	-46%
	Resp. 2000 + Shear (L= 4.02 m)																												**0.046**	**92**	-5%	**5316**	-17%

Table 3-2 U-shaped walls neutral axis depth and flexural calculations (flange in tension)

Under pure flexural conditions, the analytical predictions from Equations 3-18 and 3-20 agree well with the Response-2000 benchmarks. Notably, the analytical approach consistently yields conservative results for both the neutral axis depth (C_2) and the nominal moment capacity (M). The calculated negative error values reflect analytical estimates that are lower than the Response-2000 results, ensuring a reliable margin of safety in the design.

In this orientation, the section exhibits higher flexural strength than the opposite direction analyzed previously. While the wall shows superior compressive performance when the web is in compression, concurrent shear forces can alter this behavior. Consequently, the analysis was expanded into a parametric investigation varying key design variables, including axial load ratios and reinforcement ratios, to further validate the analytical model across diverse load combinations.

3.3 Moment-Shear Interaction Diagrams of U-shaped Shear Wall Cross-Section

An analysis of varying wall height aspect ratios demonstrates that flexural behavior governs the design of slender walls, whereas shear effects predominate in the design of squat walls.

Structural analysis of the wall sections reveals a distinct performance asymmetry based on loading orientation. When analyzing the flexural response in the direction of symmetry, where the web is in tension and flanges are in compression, the shear-moment (V-M) interaction follows a non-linear, elliptical profile. Conversely, when the loading is reversed to place the web in compression, the interaction exhibits a more linear trend. This behavior aligns with the patterns shown in the images below: the images on the left illustrate the flexural direction with the web in tension, while the images on the right depict the behavior with the web in compression and the flanges in tension.

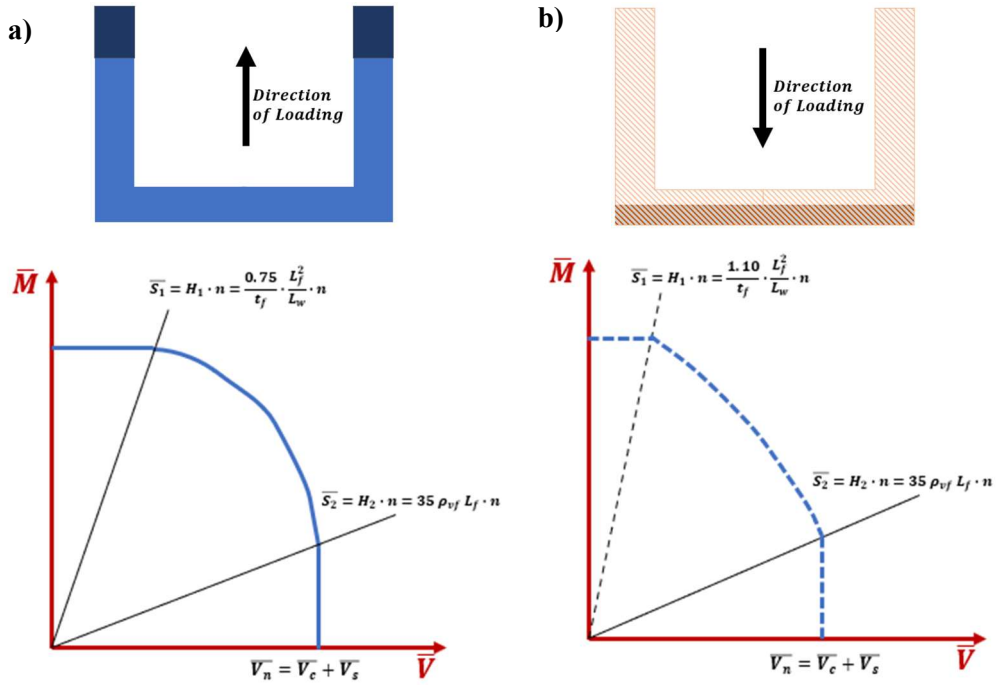

Figure 3-4 Moment-Shear Diagram (a) Direction of loading flanges in compression (b) Direction of loading flanges in tension

To enable a generalized comparison across wall configurations, both flexural and shear strengths have been normalized. The normalized moment is defined as $\bar{M}$, while the normalized shear is expressed as $\bar{V}$.

$$\bar{M} = \frac{M}{\alpha_1\, f_c'\, l_w\, l_f^2} \qquad \textit{Eq. 3-21}$$

$$\bar{V} = \frac{V}{0.083\,\sqrt{f_c'}\,A_g} \qquad \textit{Eq. 3-22}$$

Analysis indicates that the flexural strength of tall, slender walls reaches its peak when the height-to-length ratio reaches $\frac{H_1}{L_f} = \frac{0.75}{t_f} \cdot \frac{L_f}{L_w}$ (when the U-section web is in tension) or $\frac{H_1}{L_f} = \frac{1.10}{t_f} \cdot \frac{L_f}{L_w}$ (in the reversed direction).

Note that the constants 0.75 and 1.10 are expressed in meters (m) to ensure the resulting equation is dimensionless. The slope defining peak flexural strength for tall walls is defined by the product of these expressions and $L_f \cdot n$, where n represents the constant normalizing factor for moment and shear strength, with units of m^{-1}.

(reminder of $\alpha_1 = 0.85 - 0.0015\, f_c'$).

$$n = \frac{0.083\sqrt{f_c'}\, A_g}{\alpha_1\, f_c'\, l_w\, l_f^2} \qquad \textit{Eq. 3-23}$$

Similarly, the shear strength remains constant for squat walls until the height-to-length ratio reaches $\frac{H_2}{L_f} = 35\,\rho_{vf}$ where ρ_{vf} denotes the vertical reinforcement ratio of the flanges.

In the established literature, the ultimate shear strength is defined as the sum of the nominal contribution of the concrete (V_c) and the contribution of the reinforcing steel (V_s). In ACI 318, the steel contribution is expressed as $V_s = \frac{A_t\, f_y\, d\, \cot\emptyset}{s}$ or $V_s = \rho_t f_y\, bd\, \cot\emptyset$, while the concrete contribution is defined by $V_c = \beta\lambda\sqrt{f_c'}\, bd$.

Notably, while ACI 318 specifies a constant coefficient of β= 0.17 (in SI units), the Canadian standards (CSA A23.3) treat this value as a variable, which depends on aggregate size, effective crack spacing, and the longitudinal strain of the reinforcement. This transition from a constant to a variable coefficient reflects the Canadian standard's emphasis on the sectional state of strain and crack geometry. However, despite these differing analytical approaches, the concrete contribution remains largely a semi-empirical value in both standards.

In this study, a parametric analysis of a U-shaped cross-section was conducted using Response-2000. The wall was initially modeled without horizontal reinforcement to evaluate its inherent concrete shear strength (V_c) and was analyzed under zero axial load. The results concluded that the basic concrete contribution for a U-shaped section is:

$$V_c = 0.23\,\lambda\sqrt{f_c'}\,(2t)L_f \qquad \textit{Eq. 3-24}$$

The assessment further indicates that increasing axial loads significantly augments both the shear and flexural capacity of the section. This enhancement occurs because the axial force compresses and closes concrete cracks, a mechanism fundamentally similar to the principles governing prestressed or post-tensioned concrete.

According to ACI 318-25, Section 22.5.5, the contribution of axial load is integrated into the concrete shear capacity proportional to axial load through the term $\frac{P}{6\,A_g} b_w d$. Additionally, the longitudinal reinforcement ratio is accounted for in the determination of shear strength via the expression $0.66\lambda_s\lambda\,(\rho_v)^{1/3}\sqrt{f_c'}\, b_w d$. This formulation captures the influence of reinforcement density and the resulting dowel action (capacity of longitudinal bars to resist shear across a crack), which significantly enhances the overall shear resistance of the member.

Consequently, it is justifiable to state that the concrete's contribution to shear strength is a function of the material's mechanical properties and the section's geometric configuration, further augmented by the effects of axial loading. Regarding reinforcement, while the primary shear resistance is provided by the transverse steel, the contribution of the longitudinal reinforcement must not be ignored. Ultimately, the total nominal shear strength (V_n) of a U-shaped wall is determined by the summation of these components:

$$V_n = V_c + V_s \qquad \textit{Eq. 3-25}$$

The nominal shear contributions of the concrete (V_c) and the reinforcement (V_s) are determined as follows:

$$V_c = \left(0.23\,\lambda\sqrt{f_c'} + \lambda_v\,\frac{P}{6\,A_g}\right) 2t\,L_f \qquad \textit{Eq. 3-26}$$

$$V_s = \left(\rho_{tr} f_y + 0.66\,\lambda_v\,\lambda_k\,(\rho_{v,f})^{1/3}\sqrt{f_c'}\right)\,2t\,d \qquad \textit{Eq. 3-27}$$

The effective depth of the cross-section is defined as $d = 0.80\,L_f$ consistent with established practices for the analysis of structural wall components.

An axial load factor influences the concrete and steel contributions to the ultimate shear strength λ_v and a slenderness ratio factor λ_k.

$$\lambda_{v,1} = \sqrt{\frac{1}{1+\frac{v}{0.60}}} \le 1$$

Analytical results indicate that the shear strength enhancement attributed to axial load does not increase in direct proportion with the load magnitude; rather, the relative benefit diminishes as the axial load increases. Furthermore, this load factor is highly dependent on the loading orientation. When the loading direction places the web in tension, the factor is defined as $\lambda_{v,1}$ whereas in the reversed direction, it is defined as $\lambda_{v,2}$.

$$\lambda_{v,2} = \sqrt{\frac{1}{1+\frac{v}{0.30}}} \le 1$$

$$\lambda_k = \frac{t_f \cdot 10}{L_f} \le 1$$

This differentiation reflects the observation that the diminishing benefits of axial load occur much faster when the web is in compression. Importantly, neither factor may exceed 1.0, establishing an upper bound on the beneficial influence of axial compression. Finally, the longitudinal reinforcement contribution includes a slenderness-ratio factor; when the wall is slender, this longitudinal contribution decreases.

Having established the upper limits for both shear and flexural contributions, a governing equation can be developed to construct a Moment-Shear (M-V) interaction diagram. This formulation defines the section strength as a function of the U-shaped wall's height, geometric properties, and specific reinforcement design.

However, a phenomenon observed in Response 2000 occurs when loading places the flanges in compression. Specifically, when the wall height-to-length ratio reaches approximately 200 (implying a wall height of 200 m, roughly 70 stories), the moment-to-shear diagram exhibits a drastic jump that becomes more pronounced as the axial load increases (see Figure 3-5). Because this study focuses on realistic wall behavior up

to 60 m, this jump is outside our scope. Therefore, in the comparative analysis, the flexural strengths from the analytical moment strengths calculated using the fundamental equations from Chapter 3.1 (represented by the horizontal dotted lines) are generally higher than the values from Response-2000 (represented by the solid lines in Figure 3-5).

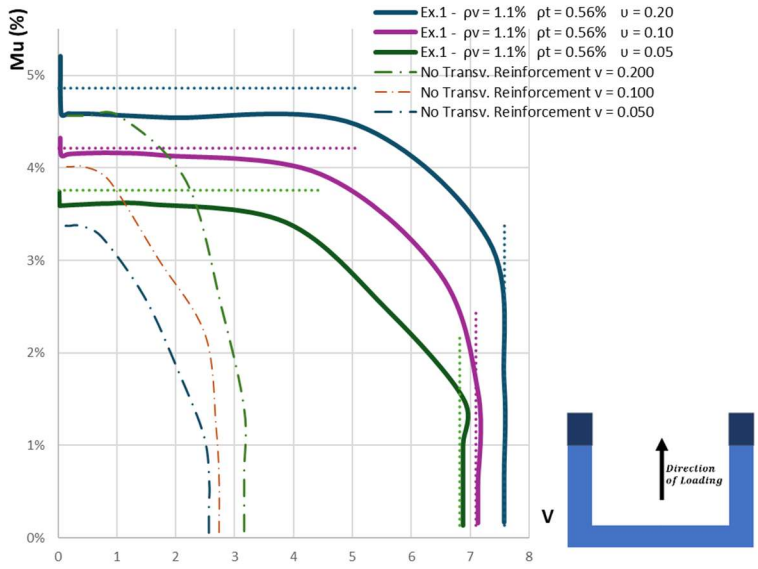

Figure 3-5 Moment-Shear Diagram of Example 1 in the direction of loading Flanges in compression

This specific behavior can be attributed to the limitations of Bernoulli's hypothesis of linear strains, which assumes that plane sections remain plane after loading. This phenomenon is highly dependent on the axial load ratio and the longitudinal reinforcement density; specifically, in walls with high axial loads or heavy longitudinal reinforcement ($\rho_{v,f} > 2\%$), the expected flexural strength is influenced by a nonlinear strain distribution. To bridge the gap between theoretical models and standard wall configurations, this nonlinear effect was incorporated into the flexural strength formulation through a correction factor $\boldsymbol{\lambda_{M,v}}, \boldsymbol{\lambda_{M,\rho}}$ defined as:

$$\lambda_{M,v} = \sqrt{\frac{1}{0.93\ \frac{v}{0.90}}} \leq 1 \qquad \lambda_{M,\rho} = \sqrt{\frac{2}{1+\frac{100\cdot\rho_{v,f}}{1.60}}} \leq 1$$

Were, $\boldsymbol{M_{u,2} = \lambda_{M,v} \cdot \lambda_{M,\rho} \cdot M_2}$ ***Eq. 3-28***

These factors were applied to the flexural equation only when the web is in tension; in the reversed orientation (web in compression), the standard flexural formulations tended to slightly underestimate the section capacity. This discrepancy is attributed to specific simplifications in the flexural strength calculation, which neglected the contribution of distributed reinforcement within the flanges. This assumption was based on the premise that reinforcement situated closer to the plastic centroid provides a significantly reduced lever arm, resulting in a marginal contribution to the total moment resistance. These approximations are currently being validated against a benchmark set of seven wall specimens, categorized as follows:

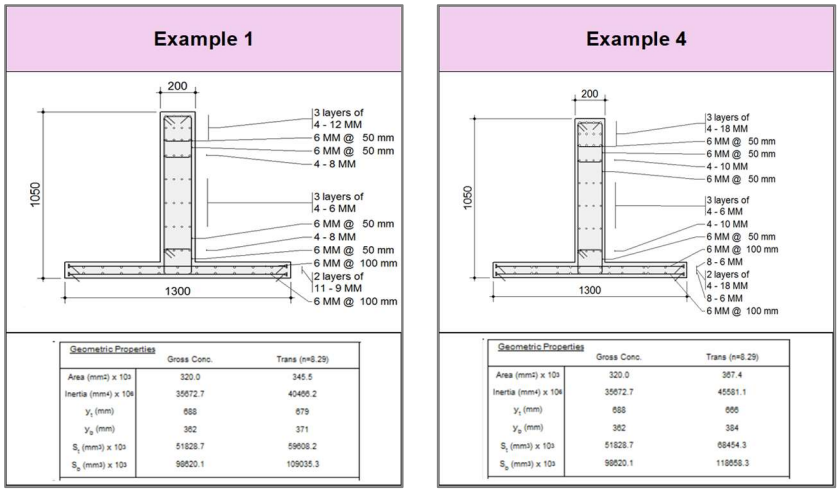

Figure 3-6 Example 1 and 4 configurations for a T-cross section simulating a U-cross section.

Examples 1 and 4 share identical geometric and material properties, featuring flange lengths (L_f) of 1050 mm and a web length (L_w) of 1300 mm, with a uniform section thickness of 100 mm. In Example 1, the longitudinal reinforcement ratio is established at 1.09%, consistent with a recent large-scale experimental program (Hoult et al. 2023b).

a)

		Ex. 1		
		υ = 0.05	υ = 0.1	υ = 0.2
F_y	Mpa	550		
F'_c	Mpa	27		
L_f	mm	1050		
L_{lf}	mm	600		
$L_{b,1}$	mm	275		
$L_{b,2}$	mm	175		
t_f	mm	100		
L_w	mm	1300		
$\overline{y}$	mm	361.7		
A_{sw}	mm^2	896		
A_{sf}	mm^2	268		
$A_{sb,1}$	mm^2	678		
$A_{sb,2}$	mm^2	356		
A_{st}	mm^2	3500		
ω'		0.571		
κ	mm/N	0.00037		
α_1		0.81		
β_1		0.90		
$\rho_{v\ sb,1}$		2.47%		
$\rho_{v\ sb,2}$		2.03%		
ρ_{sw}		0.81%		
ρ_{sf}		0.45%		
ρ_v		1.09%		
$\rho_{v,f}$		1.24%		
A_g	m2	0.32		
P	N	428501	866959	1724009
υ		0.05	0.10	0.20

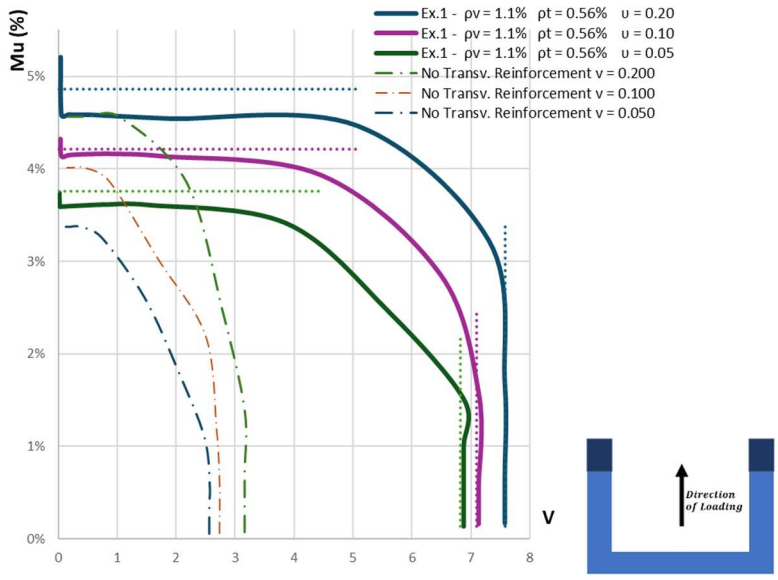

Figure 3-7 Moment-Shear Diagram of Example 1 (a) Direction of loading flanges in compression (b) Direction of loading flanges in tension

b)

		Ex. 1		
		υ = 0.05	υ = 0.1	υ = 0.2
C_1 / L_f		0.237	0.277	0.356
C_1	mm	249	291	374
M_1	kN*m	1176	1347	1633
$\overline{M_1}$		3.75%	4.21%	4.86%
C_2 / L_f		0.060	0.073	0.099
C_2	mm	63	77	104
β		0.23	0.23	0.23
M_2	kN*m	1054	1162	1359
$\overline{M_2}$		3.36%	3.71%	4.34%
ρ_{tr}			0.565%	
$\beta \sqrt{f'_c}\, 2t\, L_f$	kN		251	
$\rho_{tr} F_y\, 2t\, d$	kN		523	
$P/6A_g\, 2t\, L_f$	kN	47	95	189
λ_k			0.952	
$0.66 \lambda_v \lambda_k \rho v,f$	kN		127	
V_c	kN	296	339	414
V_s	kN	645	640	633
$V_{n,1}$	kN	940.6	978.8	1046.9
$\overline{V_{n,1}}$		6.82	7.09	7.59
$V_{n,2}$	kN	934.6	965.5	1018.0
$\overline{V_{n,2}}$		6.77	7.00	7.38
$\lambda_{v,1}$		0.96	0.93	0.87
$\lambda_{v,2}$		0.93	0.87	0.77
$\lambda_{M,\rho}$		1.00	1.00	1.00
$\lambda_{M,v}$		1.00	0.98	0.93
$\lambda_{M,\rho} \lambda_{M,v}$		1.00	0.98	0.93

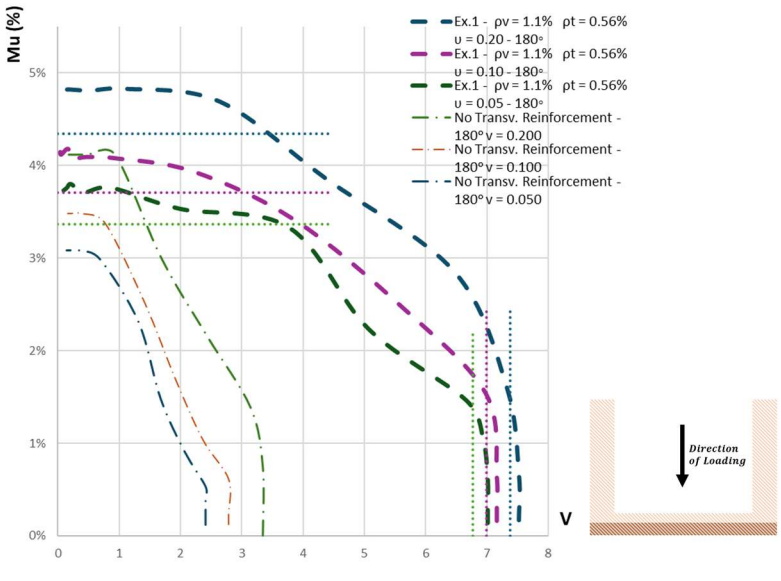

Figure 3-7 Moment-Shear Diagram of Example 1 (a) Direction of loading flanges in compression (b) Direction of loading: flanges in tension (continued)

The figures below illustrate the calculated maximum flexural and shear strength for Example 1 under three distinct axial load ratios: 0.05, 0.10, and 0.20. In these plots, the x-axis represents normalized shear strength values, while the y-axis depicts the normalized flexural strength. The dotted horizontal and vertical lines denote the theoretical maximum moment and shear limits, respectively.

The continuous and dashed curves represent the Response-2000 results for maximum strength across varying wall heights. When the web is in tension, the interaction diagram follows a smooth, quasi-elliptical failure envelope. Conversely, under reversed loading (web in compression), the behavior shows a linear trend, and the flexural calculations appear to underestimate the capacity due to the simplifications discussed earlier. Additionally, the curves exhibiting lower shear strength represent models without horizontal reinforcement. These cases were analyzed to isolate and evaluate the primary influence of transverse steel on the overall shear resistance of the U-section.

Furthermore, Figure 3-8 highlights a distinct jump in flexural capacity for high-aspect-ratio walls as the shear force approaches zero. This discontinuity becomes more pronounced as the axial load ratio increases, suggesting a high sensitivity to axial-flexure interaction in extremely slender members.

When the geometric and material properties are held constant while increasing the longitudinal reinforcement ratio (as demonstrated in example 4), the following behavioral shifts are observed:

a)

		Ex. 4		
		υ = 0.05	υ = 0.1	υ = 0.2
F_y	Mpa	550		
F'_c	Mpa	27		
L_f	mm	1050		
L_{tf}	mm	600		
$L_{b,1}$	mm	275		
$L_{b,2}$	mm	175		
t_f	mm	100		
L_w	mm	1300		
$\bar{y}$	mm	361.7		
A_{sw}	mm^2	452.4		
A_{sf}	mm^2	326.7		
$A_{sb,1}$	mm^2	1526.8		
$A_{sb,2}$	mm^2	1175.0		
A_{st}	mm^2	6509.4		
P	N	428501	868959	1724009
ω'		0.571	0.571	0.571
κ	mm/N	0.00037	0.00037	0.00037
α_1		0.8		
β_1		0.9		
$\rho_{v\,sb,1}$		5.55%		
$\rho_{v\,sb,2}$		6.71%		
ρ_{sw}		0.41%		
ρ_{sf}		0.54%		
ρ_v		2.03%		
$\rho_{v,f}$		2.88%		
A_g	m^2	0.32		
P	N	428501	868959	1724009
υ		0.05	0.10	0.20

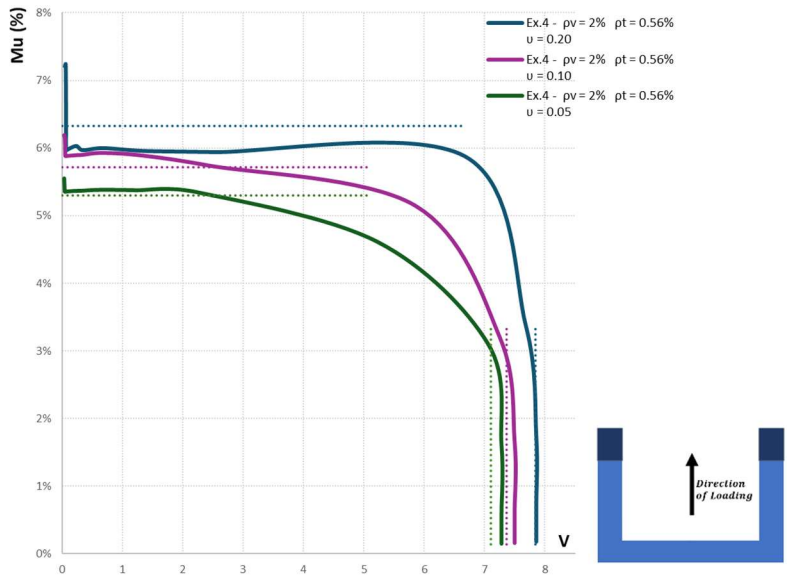

b)

		Ex. 4		
		υ = 0.05	υ = 0.1	υ = 0.2
C_1 / L_f		0.235	0.259	0.306
C_1	mm	246	272	321
M_1	kN*m	1769	1947	2265
$\overline{M_1}$		5.30%	5.71%	6.32%
C_2 / L_f		0.088	0.098	0.118
C_2	mm	93	103	124
β		0.23	0.23	0.23
M_2	kN*m	2041	2115	2252
$\overline{M_2}$		6.52%	6.75%	7.19%
ρ_{tr}		0.565%	0.565%	0.565%
$\beta \sqrt{f'_c}\, 2t\, L_f$	kN	251	251	251
$\rho_{tr} F_y\, 2t\, d$	kN	523	523	523
$P/6A_g\, 2t\, L_f$	kN	47	95	189
λ_k		0.952	0.952	0.952
$0.66\, \lambda_v \lambda_k \rho_{v,f}$	kN	168	168	168
V_c	kN	296	339	414
V_s	kN	684	678	668
$V_{n,1}$	kN	980.3	1017.0	1082.6
$V_{n,1}$		7.10	7.37	7.84
$V_{n,2}$	kN	972.8	1001.2	1050.0
$V_{n,2}$		7.05	7.25	7.61
$\lambda_{v,1}$		0.96	0.93	0.87
$\lambda_{v,2}$		0.93	0.87	0.77
$\lambda_{M,\rho}$		0.94	0.94	0.94
$\lambda_{M,v}$		1.00	0.98	0.93

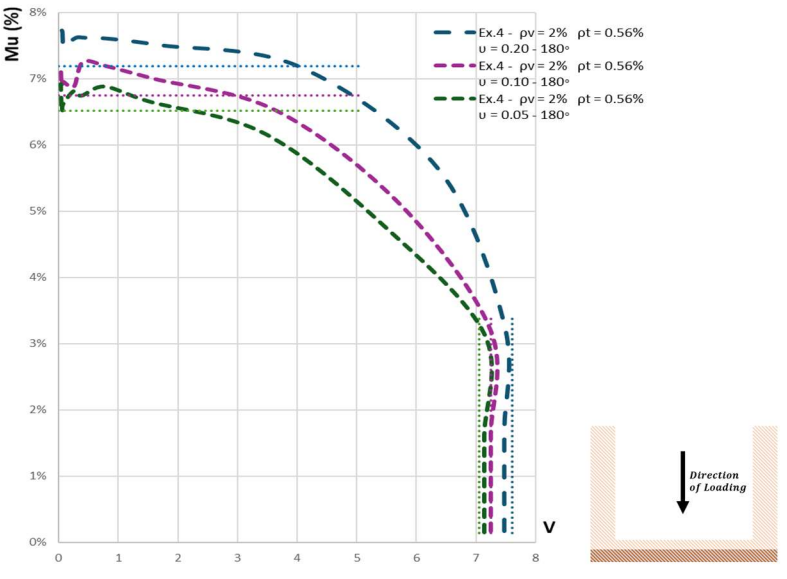

Figure 3-8 Moment-Shear Diagram of Example 4 (a) Direction of loading flanges in compression (b) Direction of loading flanges in tension

Comparing Example 4 to Example 1, the increased longitudinal reinforcement ratio results in the expected enhancement of the flexural strength, while the ultimate shear strength remains relatively consistent. Graphically, the failure envelopes for Specimen 4 transition from a quasi-elliptical form toward a more rectangular edge, a trend that is particularly pronounced at higher axial load ratios.

This behavior suggests that as reinforcement density and axial load increase, the interaction between shear and moment becomes less coupled. Consequently, any proposed moment-shear interaction formulation must incorporate the wall's aspect ratio and the specific distribution of longitudinal reinforcement along the flange's length to capture these boundary transitions accurately.

A second set of examples with varying reinforcement ratios is shown in examples 2 and 3 of Figure 3-9. These feature a distinct geometric profile compared to the previous cases, with flange lengths (L_f) of 3000 mm, a web length (L_w) of 3000 mm, and an overall thickness of 200 mm.

The analysis of these specimens focuses on longitudinal reinforcement ratios of 0.6% and 1.1%.

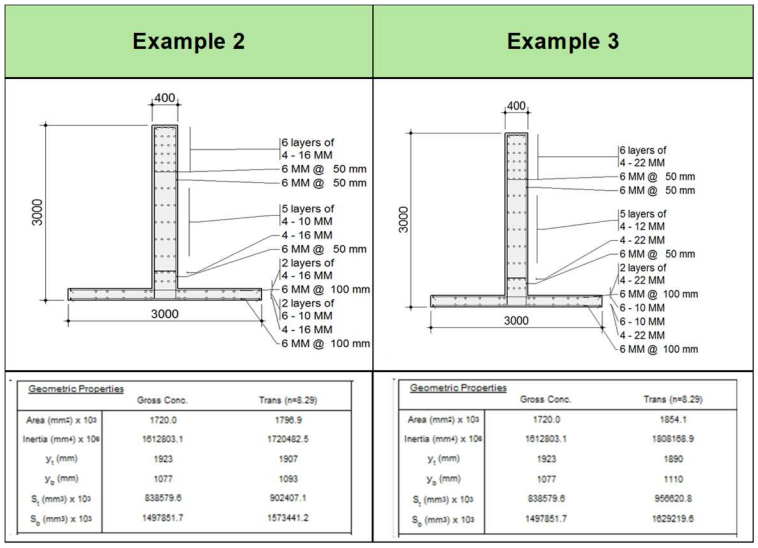

Figure 3-9 Example 2 and 3 configurations for a T-cross section simulating a U-cross section.

Finally, a third set of examples (5, 6, and 7) is presented in Figure 3-10. These walls possess flange and web lengths of 2000 mm with a reduced thickness of 150 mm. The longitudinal reinforcement ratios for these cases are 1.05% for Specimen 5, 2.15% for Specimen 6, and 0.62% for Specimen 7. Comprehensive geometric and material properties for all specimens are detailed in the figures below:

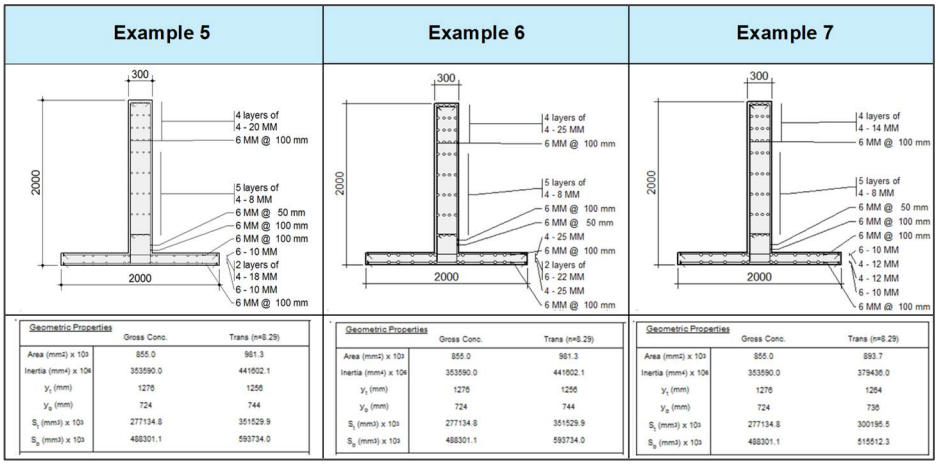

Figure 3-10 Example 5, 6, and 4 configurations for a T-cross section simulating a U-cross section.

The table is organized by example case number and further subdivided by three Axial Load Ratios (0.05, 0.10, and 0.20) to demonstrate the U-shaped section's sensitivity to axial-flexure-shear interaction.

The green headers identify the larger geometries (Specimens 2 and 3), while the blue headers denote the intermediate geometries. Material properties are held constant across all specimens, with a yield strength (f_y) of 550 MPa and a compressive strength (f'_c) of 27 MPa.

		Ex. 2			Ex. 3			Ex. 5			Ex. 6			Ex. 7		
		υ = 0.05	υ = 0.1	υ = 0.2	υ = 0.05	υ = 0.1	υ = 0.2	υ = 0.05	υ = 0.1	υ = 0.2	υ = 0.05	υ = 0.1	υ = 0.2	υ = 0.05	υ = 0.1	υ = 0.2
F_y	Mpa	550			550			550			550			550		
F'_c	Mpa	27			27			27			27			27		
L_f	mm	3000			3000			2000			2000			2000		
L_{if}	mm	1690			1690			1100			1100			1100		
$L_{b,1}$	mm	800			800			500			500			500		
$L_{b,2}$	mm	510			510			400			400			400		
t_f	mm	200			200			150			150			150		
L_w	mm	3000			3000			2000			2000			2000		
$\bar{y}$	mm	1076.7			1076.7			724.1			724.1			724.1		
A_{sw}	mm^2	942.5			942.5			942.5			942.5			942.5		
A_{sf}	mm^2	785.4			1131.0			502.7			1131.0			502.7		
$A_{sb,1}$	mm^2	2412			4561.6			2513.274123			4561.592533			1231.5		
$A_{sb,2}$	mm^2	1608			3041.1			1017.87602			3041.061689			452.4		
A_{st}	mm^2	10553.3			18410			9010.1			18409.7			5315.6		
ω'		0.563			0.563			0.550			0.550			0.550		
κ	mm/N	0.00019			0.00019			0.00025			0.00025			0.00025		
α_1		0.81			0.81			0.81			0.81			0.81		
β_1		0.90			0.90			0.90			0.90			0.90		
$\rho_{v\ sb,1}$		1.51%			2.85%			3.35%			6.08%			1.64%		
$\rho_{v\ sb,2}$		1.58%			2.98%			1.70%			5.07%			0.75%		
ρ_{sw}		0.18%			0.18%			0.37%			0.37%			0.37%		
ρ_{sf}		0.23%			0.33%			0.30%			0.69%			0.30%		
ρ_v		0.61%			1.07%			1.05%			2.15%			0.62%		
$\rho_{v,f}$		0.80%			1.46%			1.34%			2.91%			0.73%		
A_g	m^2	1.72			1.72			0.86			0.86			0.86		
P	N	2326147	4652294	9304589	2326147	4652294	9304589	1150831	2301661	4626339	1150831	2301661	4626339	1150831	2301661	4626339
υ		0.050	0.100	0.200	0.050	0.100	0.200	0.050	0.100	0.200	0.050	0.100	0.200	0.050	0.100	0.200

Table 3-3 Walls Properties and Reinforcement Properties (Example 2, 3, 5, 6, and 7)

The flange and web lengths are defined by L_f and L_w, while the boundary element dimensions are denoted by $L_{b,1}$ and $L_{b,2}$. The parameter $\bar{y}$ represents the distance to the centroid, the reference point for all lever arm calculations. Finally, the reinforcement distribution across the U-section is categorized by the steel areas in the web and flanges, A_{sw} and A_{sf}, and by the boundary elements, $A_{sb,1}$ and $A_{sb,2}$, with the total longitudinal steel area denoted as A_{st}.

The data is divided into two primary groups based on the loading direction: web in compression and web in tension. For each case, the neutral axis depth (c) and its ratio to the flange length (c/L_f) are calculated using equations expressed in Chapters 1.4 and 1.5. The nominal moment capacity (M) and total nominal shear capacity (Vn) are determined for both directions. Furthermore, the normalized moment and shear values ($\underline{M}$ and $\underline{V_n}$) highlighted in green represent the upper limits in the following interaction diagrams.

The curves illustrate the Response-2000 results, depicting the maximum flexural and shear strengths across varying wall heights. The diagrams on the left show behavior when the web is in tension, while those on the right show moment-shear interaction when the web is in compression.

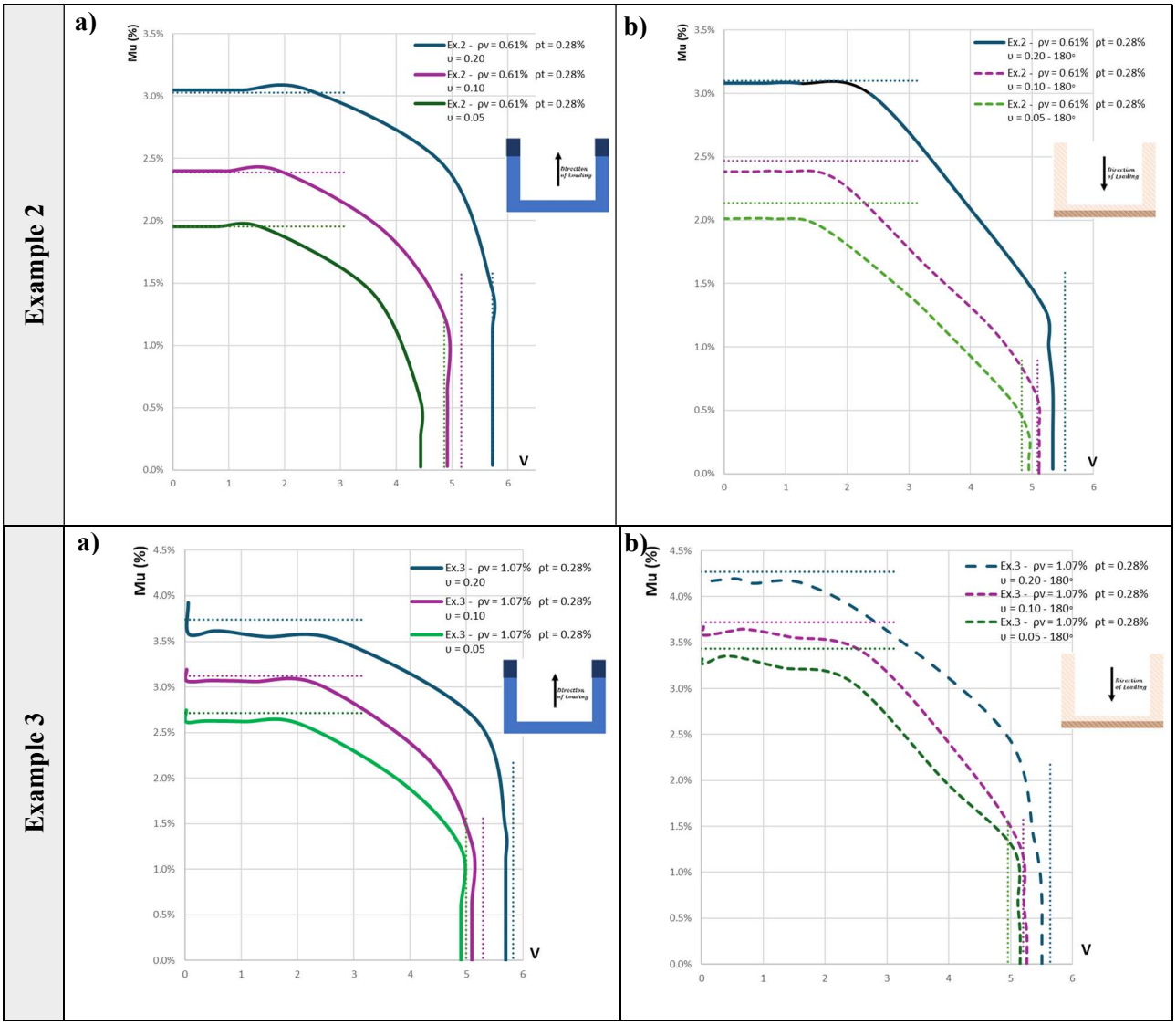

Figure 3-11 Moment Shear Diagram of Examples 2 and 3 (a) Direction of loading flanges in compression (b) Direction of loading flanges in tension

In the web-compression orientation, the wall's behavior closely matches the theoretical moment equations without additional correction factors. Conversely, in the web-tension direction, a distinct jump in flexural strength occurs as the shear force approaches zero. This phenomenon is most pronounced in example 6, which features the highest longitudinal reinforcement ratio in this study at 2.15%. Such high reinforcement density is atypical for standard structural design, as reinforced concrete shear walls are generally designed with much lower ratios to ensure ductile behavior and economic efficiency.

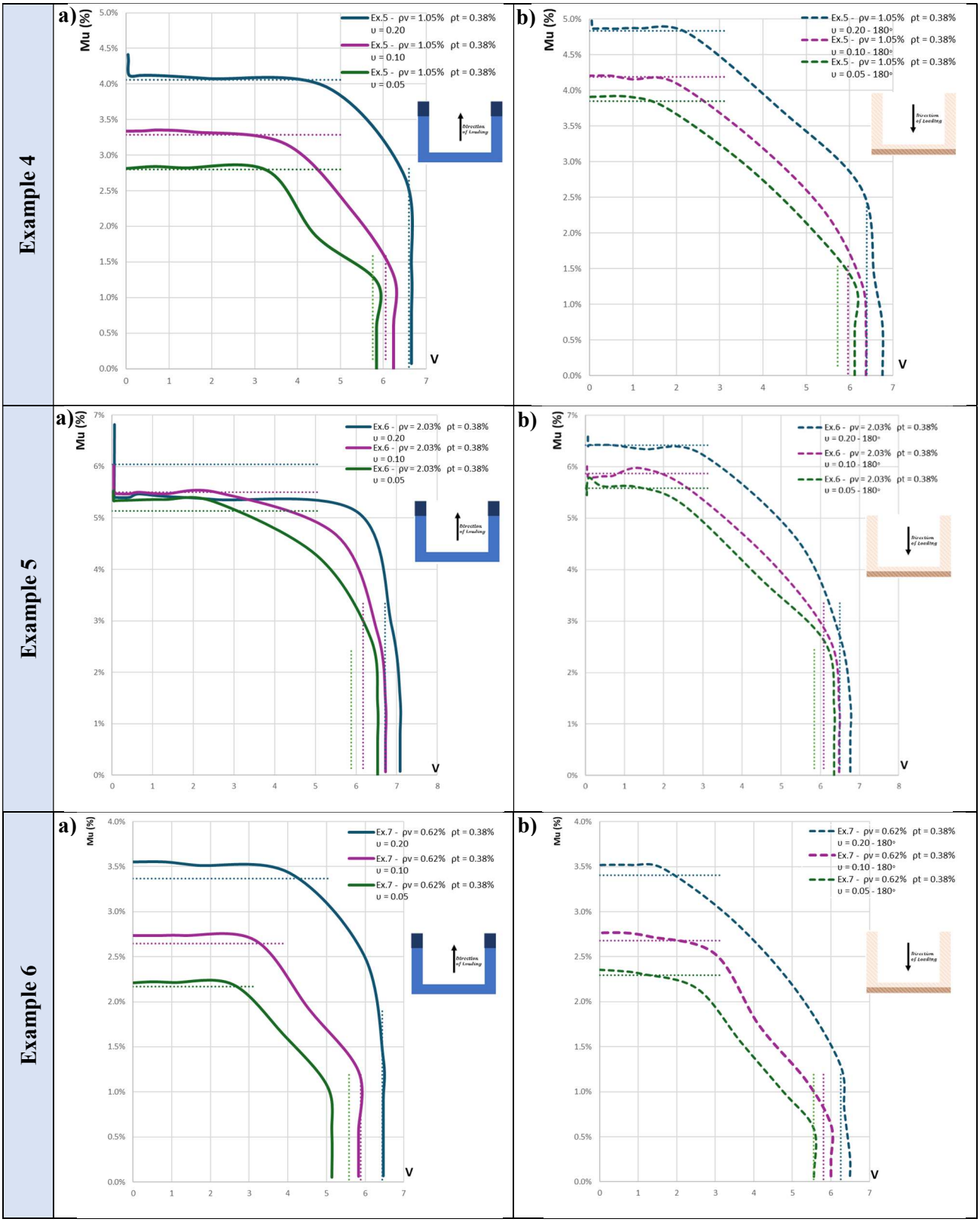

Figure 3-12 Moment Shear Diagram of Examples 4, 5, and 6 (a) Direction of loading flanges in compression (b) Direction of loading flanges in tension

A valid approximation is that the wall maintains relatively constant flexural strength when shear demands are low (typical of tall buildings) until it reaches a critical point at which the strength begins to decrease nonlinearly. This transition point is established where the slope is $S = H \cdot n$ of the interaction curve changes at a height of $H_1 = \frac{0.75}{t_f} \cdot \frac{L_f^2}{L_w}$ this is the case where the U-section web is in tension. This limit changes in the reversed direction to a height of $H_1 = \frac{1.10}{t_f} \cdot \frac{L_f^2}{L_w}$ (Note that the constants 0.75 and 1.10 have a unit length in meters) Similarly, the shear capacity remains constant for squat walls until the height reaches the transition limit, with a height of $H_2 = 35\ \rho_{vf}\ L_f$. The following relationship establishes the elliptical curve representing the interaction between these two regimes:

$$\bar{\bar{M}} = \overline{\overline{(M_n}} - S_2\ \bar{\bar{V}_n}) \sqrt{1 - \left(\frac{\bar{\bar{V}} - \frac{\overline{\overline{M_n}}}{S_1}}{\bar{\bar{V}_n} - \frac{\overline{\overline{M_n}}}{S_1}} \right)^{\varphi_w}} + S_2\ \bar{\bar{V}_n} \qquad \textit{Eq. 3-29}$$

Where:

- S_1 is the slope defining the limit of constant flexural capacity, established as $S_1 = H_1 \cdot n$
- S_2 is the slope defining the limit of constant shear capacity, established as $S_2 = H_2 \cdot n$
- $\overline{\overline{M_n}}$ and $\bar{\bar{V}_n}$ represent the maximum normalized flexural and shear strength, respectively, as determined by the previously established equations.
- $\bar{\bar{M}}$ and $\bar{\bar{V}}$ establish a normalized shear and moment interaction curve that determines the wall's strength within the studied height range of 2 m to 60 m.
- φ_w is the curvature factor that dictates the non-linearity of the interaction envelope. This factor is sensitive to the loading orientation (web in tension vs. compression) and the axial load factor ν. The value of φ_w is constrained between a lower limit of 1 and an upper limit of 5, and is expressed as:

$$\varphi_w = \delta\ \nu \left(1 + \frac{1}{L_f}\right) \qquad \textit{Eq. 3-30}$$

The curvature parameter δ depends on the load direction. If the web is in tension $\delta = 9$, however, when the load is reversed, and the web is in compression, this value changes to $\delta = 4$. This parameter dictates the interaction envelope profile: a lower value results in a more linear transition, and a higher value produces a sharper corner or a more rectangular profile. These coefficients provide the closest approximation of the non-linear behavior predicted by Response-2000. The comparative results are summarized in the following graphs:

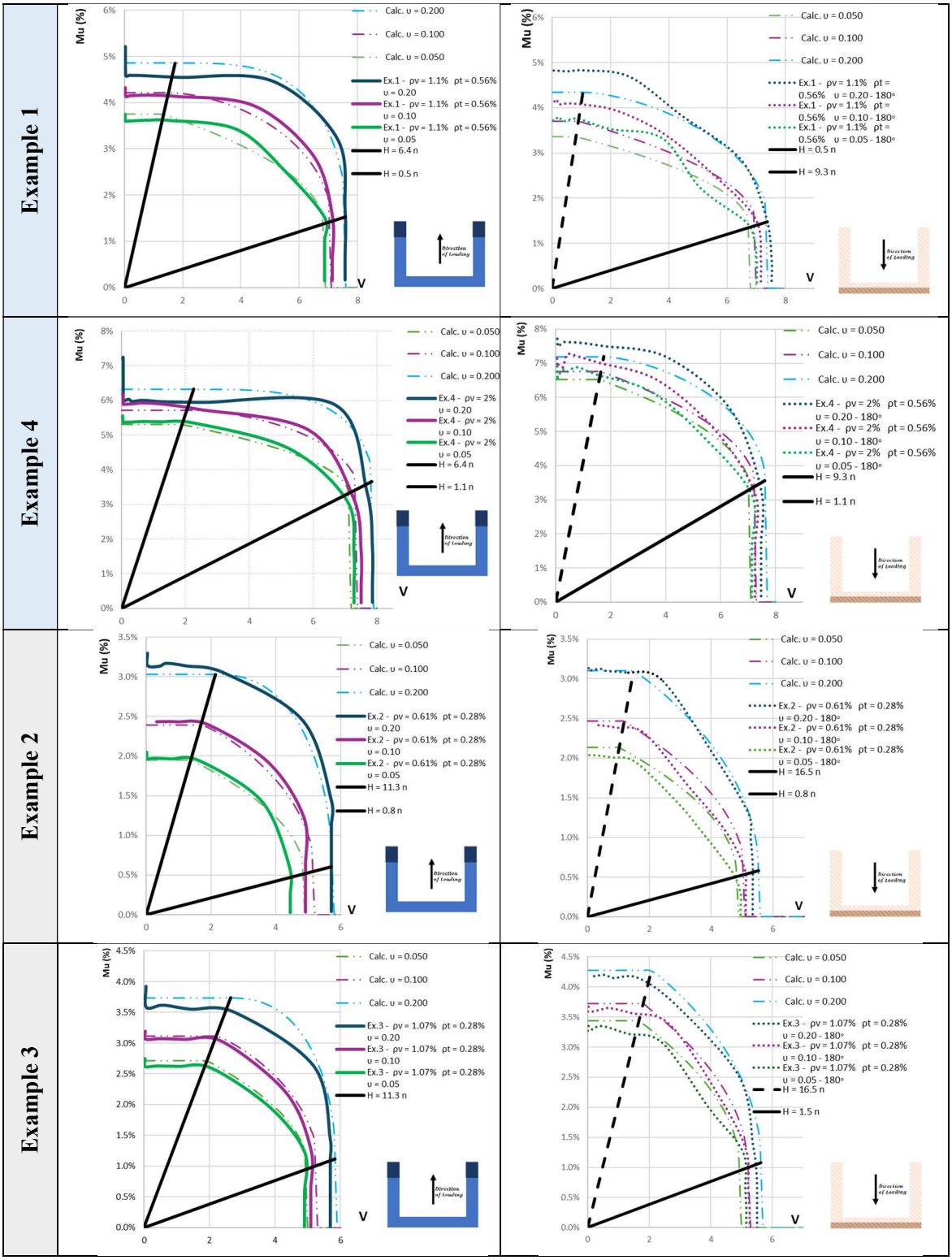

Figure 3-13 Comparison of Moment Shear Diagram calculations to Response 2000

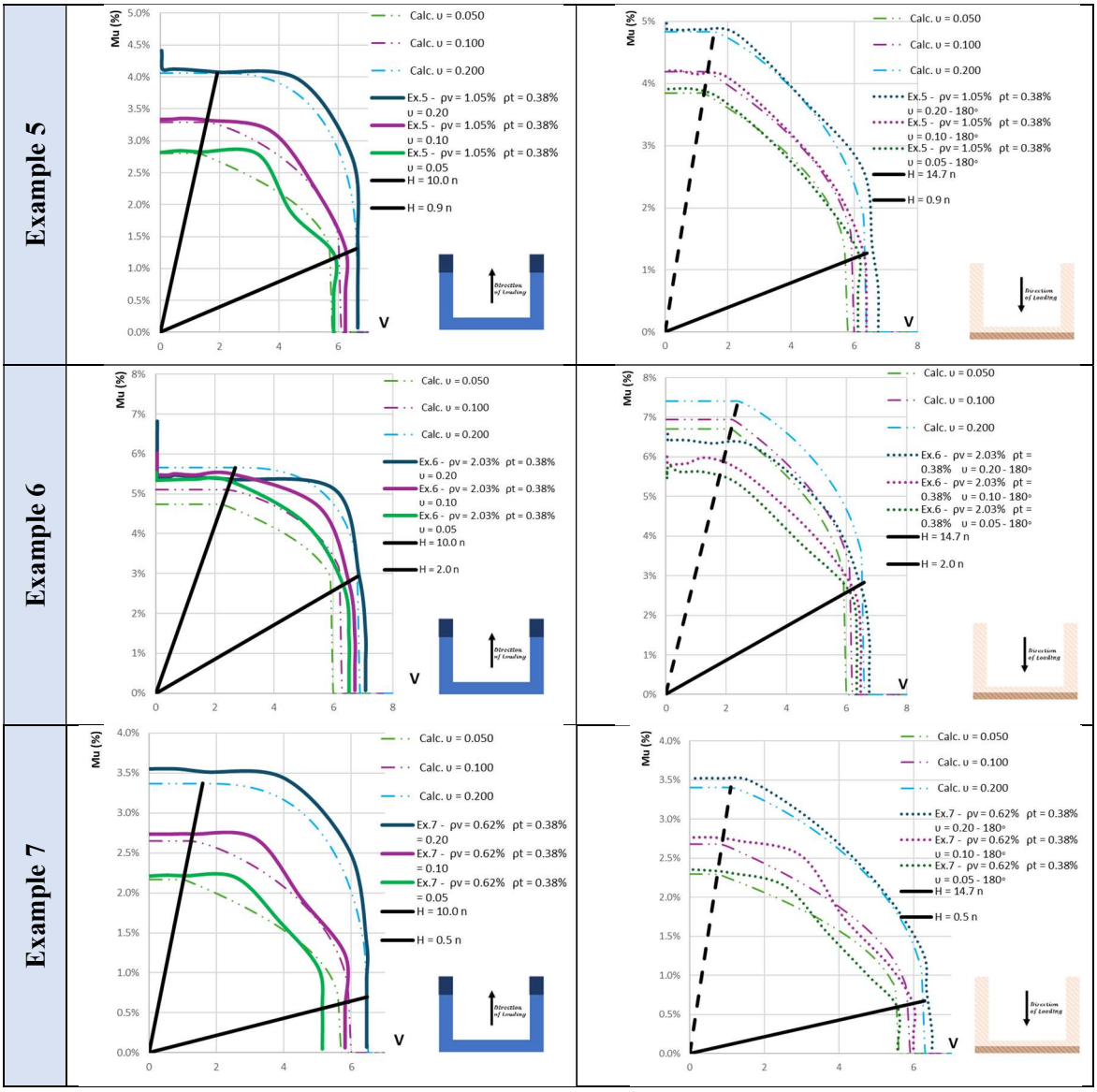

Figure 3-14 Comparison of Moment Shear Diagram calculations to Response 2000 (continued)

The interaction diagrams compare the analytical model with the formulated equations. The double-dashed lines represent the capacities derived from the proposed equations, while the continuous and dotted lines denote the results generated by Response-2000. In regions dominated by flexural behavior, wall strength varies only slightly; a similar trend is observed for squat walls, where shear strength remains relatively stable. Consequently, assuming constant strength in these regions is a valid and practical approximation.

The flexural strength is notably higher when the web of the U-section is subjected to compression, as evidenced in examples 3 through 6. In these cases, the interaction curves show a nonlinear progression toward the maximum flexural strength. Conversely, under reversed loading (web in tension), the behavior follows a plateau-like trend, characterized by an abrupt jump in flexural strength for high aspect ratio (very tall) walls. This behavior is considered a numerical inconsistency rather than a realistic physical response. Consequently,

for the purposes of this study, this sudden increase in strength is not attributed to the section's actual flexural strength.

The analysis shows that the plateau defining the constant shear strength of squat walls remains valid regardless of the loading orientation. However, the transition point separating flexural dominance varies with load direction. Specifically, when the web is in compression, the region of constant flexural strength extends to a higher aspect ratio than under reversed loading. This suggests that the orientation of the U-section significantly influences the threshold at which flexure governs failure modes.

The analytical results show a strong correlation with the derived numerical equations, with errors within acceptable engineering limits. However, to further validate these findings, a finite element analysis (FEA) is required. This advanced modeling approach will provide a more detailed characterization of the localized failure modes inherent to U-shaped walls, thereby confirming the accuracy of the established data.

Chapter 4: Model Verification and Experimental Benchmarking

This chapter validates the nonlinear numerical modeling framework against experimental benchmarks of reinforced concrete shear walls. The model is calibrated by incorporating concrete softening, tension stiffening, confinement effects within critical boundary elements, and an explicit steel-concrete bond-slip model relationship. This process verifies the modeling approach's ability to capture stable plastic hinge formation, cyclic degradation, and flexure-shear interactions, providing the calibration foundation needed to ensure the fidelity of the structural simulations.

4.1 Experiment Setup

Serving as a continuation of UCLouvain's prior experimental program, the ERIES-ALL4wALL dynamic tests complement earlier quasi-static tests on two reinforced concrete U-shaped core walls subjected to axial-flexural and axial-torsional loading (Hoult et al., 2023b). The experiment reviewed here was a Blind Prediction Competition (2023), principally organized by UCLouvain with LNEC's assistance, specifically targeting response prediction of the initial wall specimen.

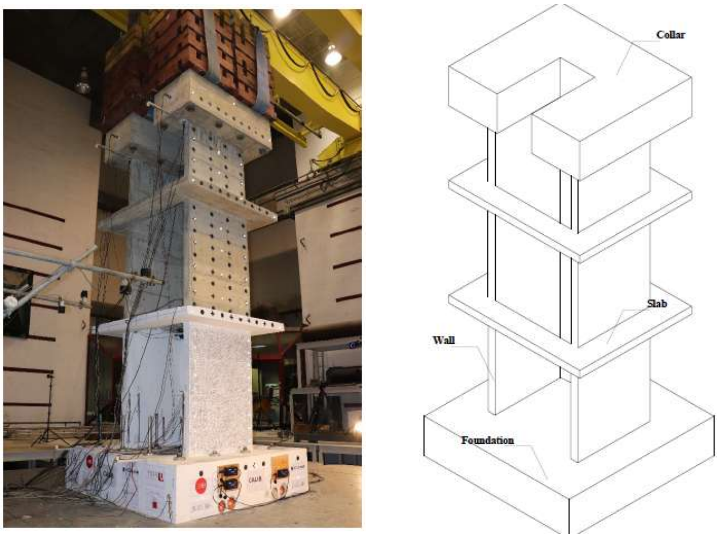

Figure 4-1 U-shaped wall specimens (from Hoult et al. 2023)

The experimental setup consists of a half-scaled, three-story reinforced concrete structure. As illustrated in Figure 4-1, the structure incorporates two intermediate slabs, each with a central opening matching the interior perimeter of the wall cross-section. A 500mm thick, U-shaped reinforced concrete collar beam is integrated into the top story to support concentrated mass blocks. The foundation, measuring 2100 mm × 2100 mm × 500 mm,

was securely fastened to the shake table using 16 threaded bars, spaced at 500 mm intervals across its entire area. The wall's foundation and collar were heavily reinforced to remain elastic throughout testing.

The structure consists of a three-story, U-shaped reinforced concrete wall with a net height of 4040 mm (excluding the foundation and collar). It incorporates two intermediate slabs, each 100 mm thick. The U-shaped wall's cross-sectional dimensions include a flange length (L_f) of 1050 mm and a web length (L_w) of 1300 mm, with a uniform wall thickness of 100 mm. Refer to the annotated views in Figure 4-2 for a visual representation.

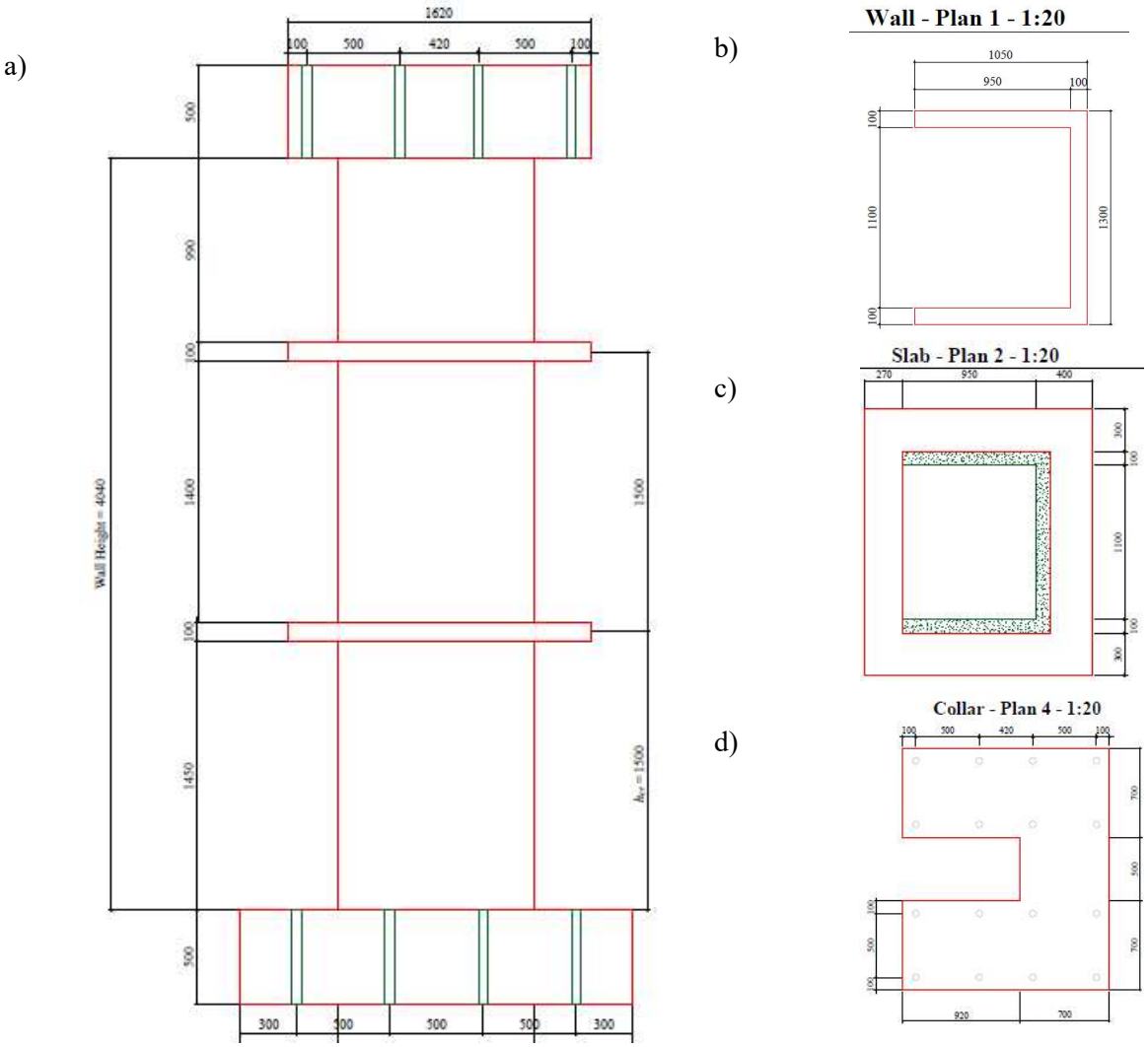

Figure 4-2 Plans of the specimen a) Lateral View, b) Wall Cross-section, c) Slab plan view, and d) Collar plan view (from Hoult et al. 2023)

The unit UWS1 features a classical RC design in accordance with Eurocode 8 (CEN 2004b) to meet the requirements of ductility class high (DCH). This ensures the wall can develop a stable plastic hinge at its base, dissipating seismic energy through large inelastic flexural deformation without brittle shear or stability failures.

As shown in the cross-sectional view (Figure 4-3), the wall specimen features four dense confined boundary regions: two at the flange-free ends and two at the web-flange intersections. The spacing of the 6 mm

diameter confining stirrups is 50 mm on the first floor, which then doubles to 100 mm on the second floor and 200 mm on the top floor. To accommodate the higher strains expected in these critical zones, the extreme ends are more heavily reinforced, utilizing longitudinal bars with diameters of 12 mm and 8 mm.

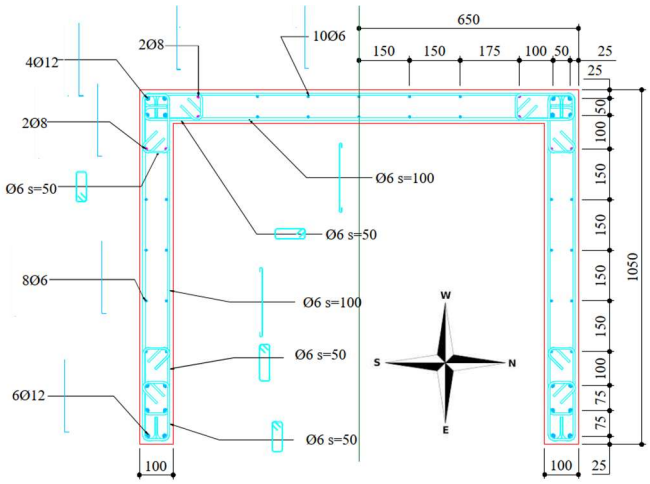

Figure 4-3 Plan of Reinforcement Details (from Hoult et al. 2023)

4.2 Experimental Material Properties

The average concrete strength of the wall, defined at 28-day cylinder strength, is 27 MPa. Table 4-1 depicts the compressive strength development of the various structural components at early stages. Additionally, the mechanical properties of the three different rebar sizes are presented in Table 4-2, which lists the yield strength (f_y), ultimate strength (f_u), yield strain (ε_{sy}), strain on the onset of hardening (ε_{sh}) (this represents the end of the yield plateau), the ultimate strain (ε_{su}) and the Modulus of Elasticity (E_s).

						Cylinder 1	Cylinder 2	Cylinder 3	Average
Day	3	4	6	7	14	28			
Foundation	17.1	-	22.4	-	-	29.7	29.4	29.6	29.6
Wall	-	19.4	-	22.2	24.6	27.4	27.5	26.2	27.0
Collar	-	-	-	-	-	-	-	-	-

Table 4-1 Compressive strength of concrete at 28 days.

d_{bl}	f_y	f_u	ε_{sy}	ε_{sh}	ε_{su}	E_s
[mm]	[MPa]	[MPa]	[mm/mm]	[mm/mm]	[mm/mm]	[GPa]
6	550	676	0.0027	0.010	0.095	207
8	538	664	0.0027	0.024	0.120	196
12	580	690	0.0029	0.021	0.101	199

Table 4-2. Mechanical Reinforcement Properties. (from Hoult et al. 2024)

Figure 4-4 displays the tensile stress-strain behavior of the three different reinforcement bar diameters (6 mm, 8 mm, and 12 mm) used in the validation structure.

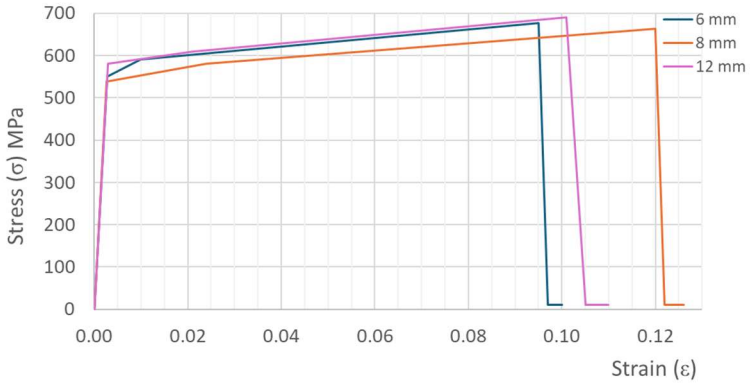

Figure 4-4 Stress- Strain curve of steel Reinforcement.

4.3 Static and Dynamic Loads

Experimental analysis includes two main loads: dead load (self-weight) and dynamic load. These are explained below:

Self-Weight: There were several mass blocks connected to the top Collar (1.13 ton and 0.59-ton mass blocks); these mass blocks were 840 mm x 840 mm in cross-section, and 250 mm or 130 mm thick (see Figure 4-5). The applied mass of each tower is 6.24 tons, and the total mass (4 towers) above the collar is 24.96 tons. A breakdown of the self-weight on the structure is depicted in Table 4-3. (Assuming a reinforced concrete density of 2500 kg/m^3)

	Area (m^2)	**Height (m)**		**Weight (ton)**
Blocks			(4) [0.59+5(1.13)]	24.96
"U" Wall concrete	0.32	4.04	(0.32) (4.04) (2.4 Ton/m^3)	3.1027
Collar	2.618	0.50	(2.618) (0.50) (2.4 Ton/m^3)	3.1416
Slab	1.713	0.10	(1.713) (0.10) (2.4 Ton/m^3)	0.411
Foundation	4.41	0.5	(4.41) (0.50) (2.4 Ton/m3)	5.292
			Total =	**36.907**

Table 4-3 Distribution of the specimen's total weight

To accurately evaluate how a real-world, full-scale structural shear wall behaves under extreme loads, the laboratory scaled-down model must experience the same normal and shear stress fields. Therefore, 30-ton blocks were placed on top of the collar to ensure the wall reached the scaled unit's flexural strength. Excluding the foundation structure, the total weight subjected to seismic excitation is 31.62 tons.

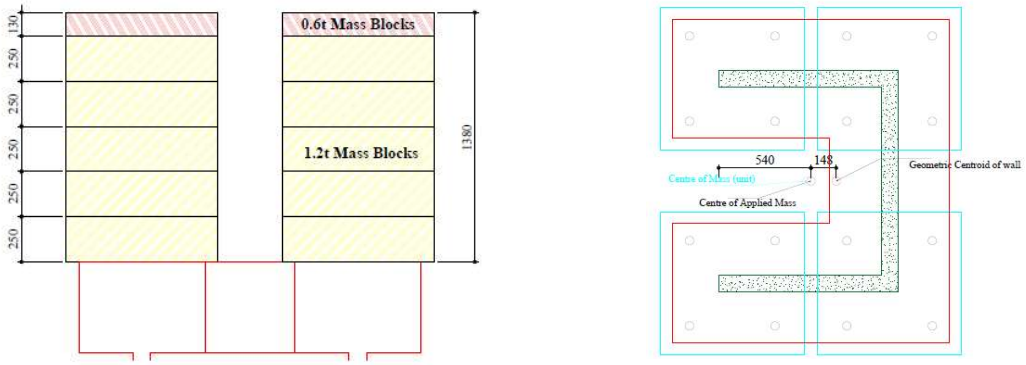

Figure 4-5 Large blocks section properties and self-weight (from Hoult et al. 2023)

Dynamic Load: The dynamic test was conducted based on the 2016 Central Italy earthquake, the most significant Italian seismic event recorded by modern geodetic measurements (Cheloni et al., 2017). According to Hoult (2025), the peak ground acceleration (PGA) was approximately 0.645g and 0.808g in the respective directions; Figure 4-6 shows the corresponding 5% damped pseudo-spectral acceleration (PSA) response recorded by seismometer station MZ04 in the east-west and north-south directions.

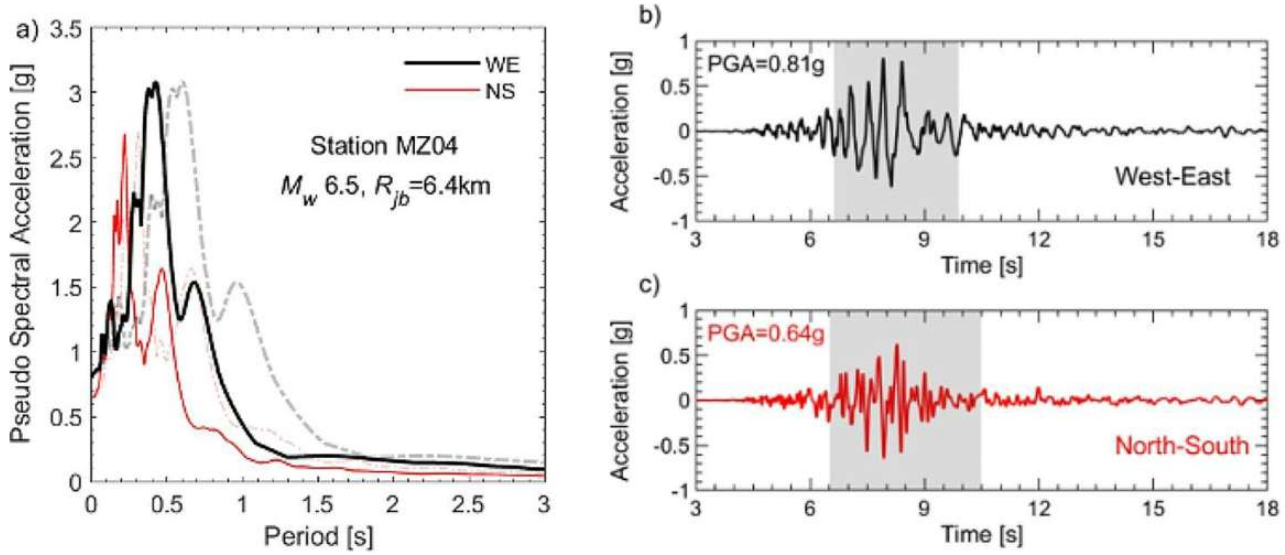

Figure 4-6 Moment magnitude Mw 6.5 event from the 2016 Central Italy earthquake sequence on 30 October (a) 5% damped pseudo-spectral acceleration; the translucent dashed lines represent the original (uncorrected) response captured by MZ04 using a time-step interval of 0.005s, whereas the opaque lines represent the corrected response using a scaled time-step (b) acceleration-time history in the west-east (c) acceleration-time history in the north-south (from Hoult et all, 2025)

The experiment was subjected to eight distinct ground motion (GM) levels, ranging from GM0 to GM8. Each GM level corresponds to a unique scaling combination. The test began with GM0, representing 10% of the east-west ground motion (along the axis of symmetry), and progressively increased in intensity with each subsequent step until it reached 100% of the simulated earthquake, as shown in Table 4-4. The paired ground

motions (GM2, GM4, GM6, and GM8) also include north-south ground motion. This shift from uniaxial response to a biaxial cyclic configuration was intended to induce torsional behavior in the wall.

	GM0	*GM1*	*GM2*	*GM3*	*GM4*	*GM5*	*GM6*	*GM7*	*GM8*
E-W direction	10%	25%	25%	50%	50%	75%	75%	100%	100%
N-S direction	-	-	25%	0	50%	0	75%	0	100%

Table 4-4 Scale factors (in percent) used for the ground motions intensity. (from Tura et al. 2025)

The experimental time histories for the different-scale ground motions, showing the W-E and N-S displacements at the mid-height of the collar, are presented in Figure 4-7. The black line represents the axis of symmetry (W-E displacement), while the green line represents the direction parallel to the web (N-S displacement).

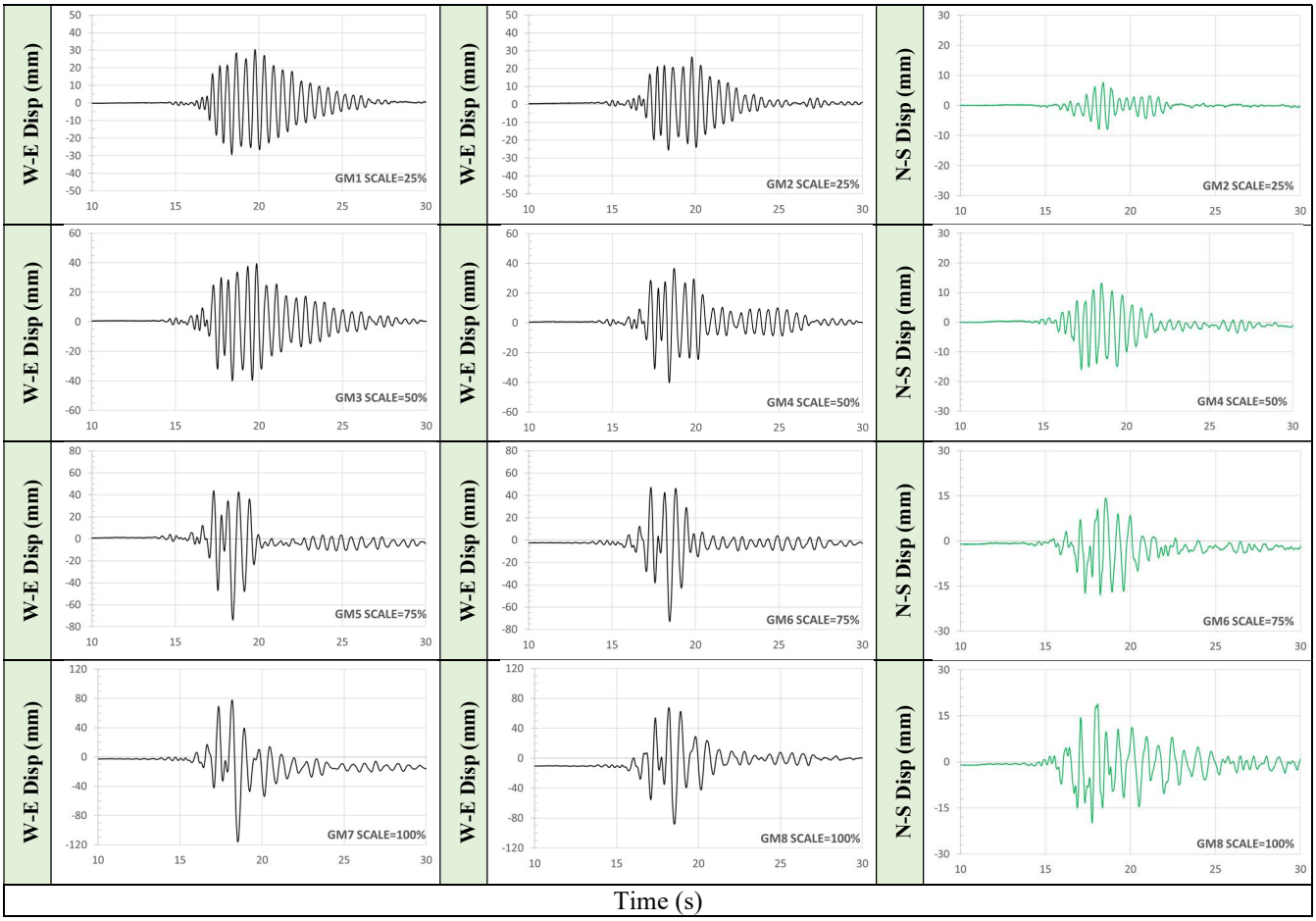

Figure 4-7 Experimental time-histories for all ground motions for W-E Displacement and N-S Displacement at the mid-height of the collar.

Figure 4-7 displays the 3% damped acceleration and displacement response spectra for each scaled ground motion from the 2016 Central Italy earthquake. The solid black line signifies the axis of symmetry (W-E displacement), whereas the dotted line denotes the direction parallel to the web (N-S displacement).

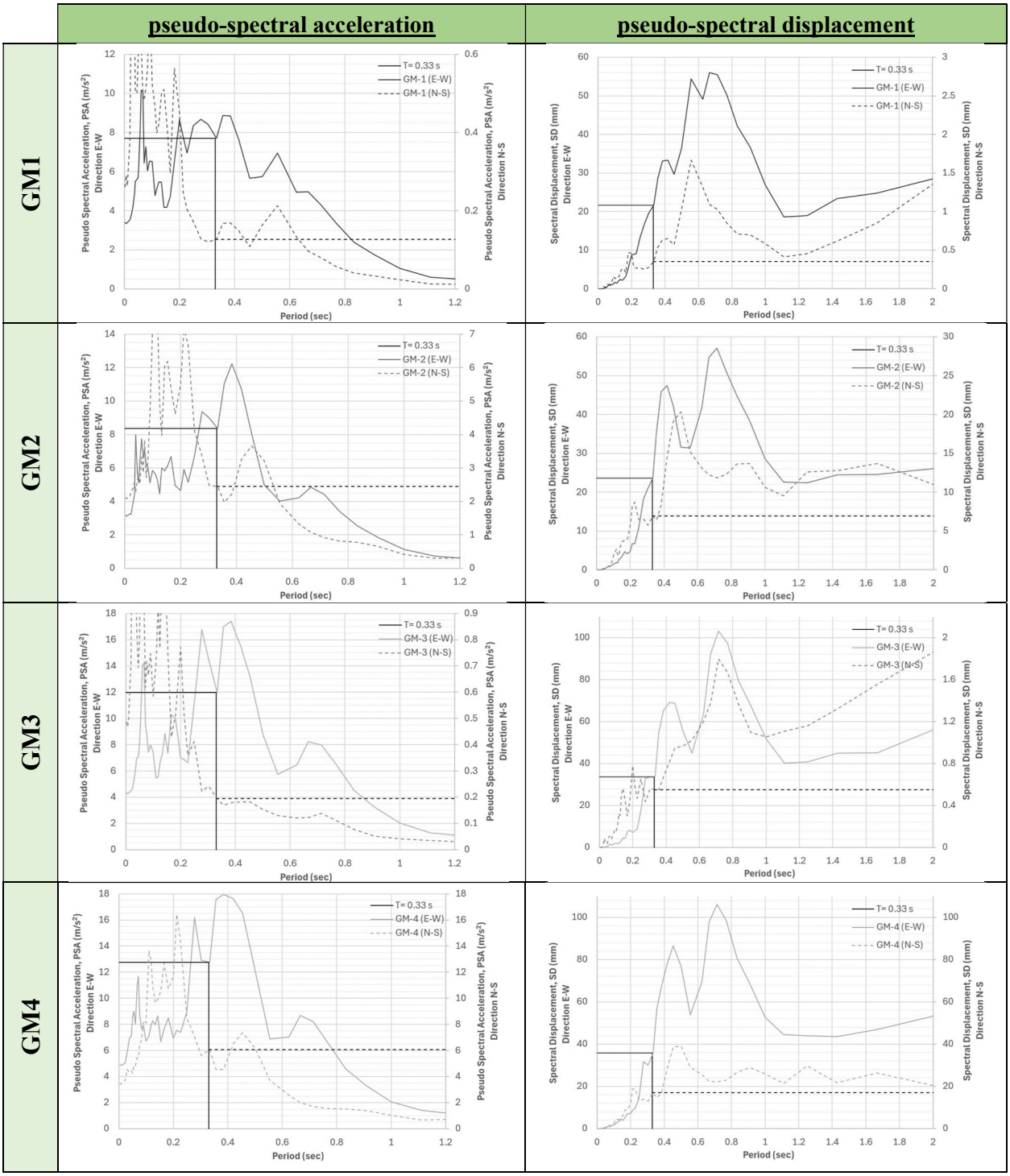

Figure 4-8 Pseudo-spectral acceleration and pseudo-spectral displacement of 3% damped from the 2016 Central Italy earthquake, from GM1 to GM8

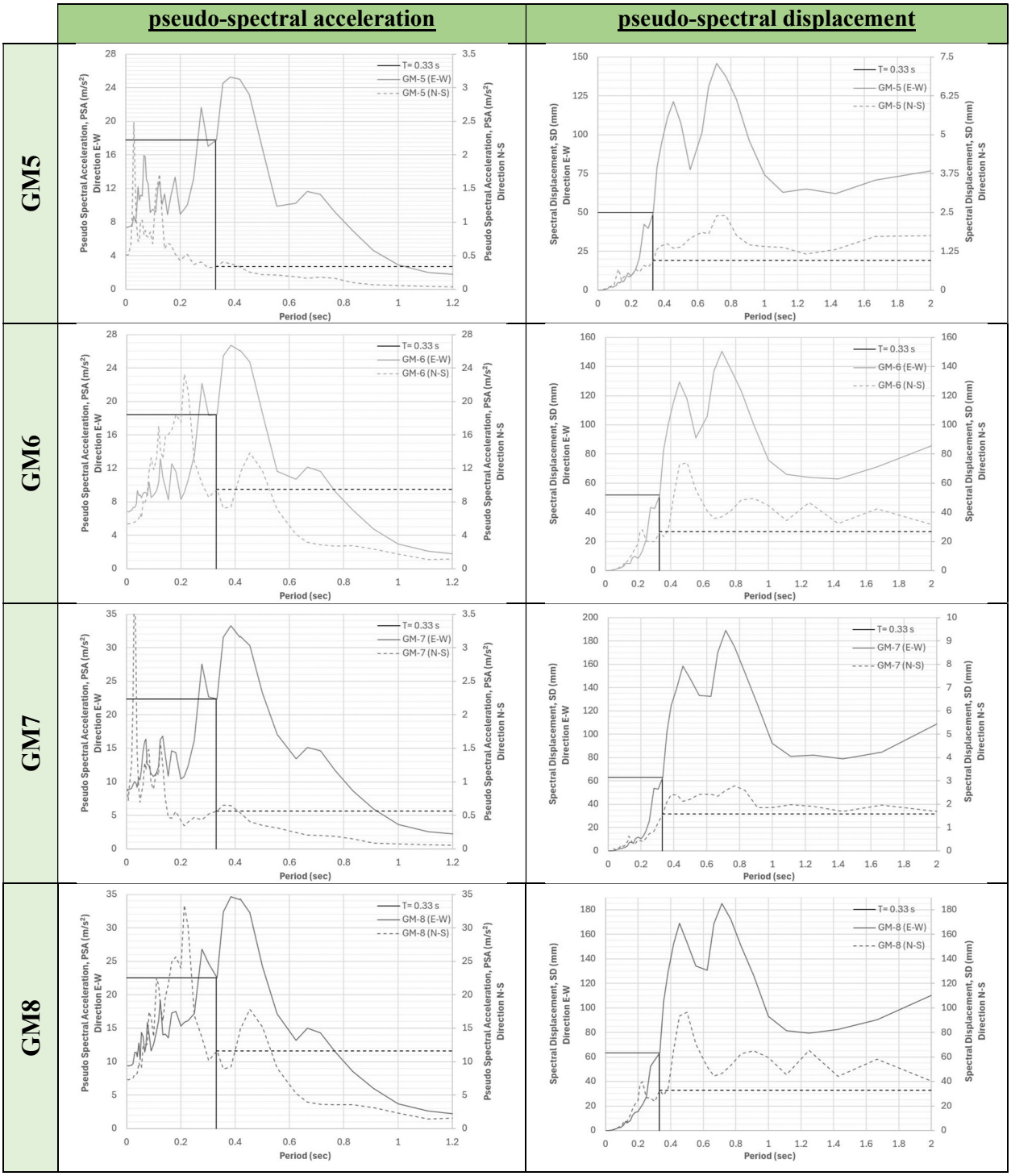

Figure 4-9 Pseudo-spectral acceleration and pseudo-spectral displacement of 3% damped from the 2016 Central Italy earthquake, from GM1 to GM8 (continued)

Using the pseudo-spectral acceleration, pseudo-spectral displacement, total structural weight, and natural period, the maximum displacement that the experimental specimen will experience can be estimated;

these values are summarized in Table 4-5 for a natural period of T=0.33s (taken from Hoult, 2025) and compared with the experimental displacement in mm (maximum and minimum displacements).

	Spectral Acceleration (m/s^2)		Spectral Displacement (mm)		Experimental Displacement (mm)		Experimental Lateral Inertia Force (kN)
Direction	**E-W**	**N-S**	**E-W**	**N-S**	**E-W**	**N-S**	**E-W**
GM1	7.71	–	21.7	–	30.38	–	-127.4
GM2	8.37	2.45	23.57	6.91	26.66	7.97	-135.7
GM3	11.98	–	33.73	–	-39.98	–	168.1
GM4	12.76	6.06	35.93	17.07	- 40.25 + 36.67	16	173.8
GM5	17.77	–	50.02	–	-73.84 +43.81	–	243.3
GM6	18.44	9.51	51.9	26.77	-72.91 +47.18	18	-194.3
GM7	22.35	–	62.92	–	-116.14 +77.88	–	-228.2
GM8	22.51	11.62	63.36	32.72	-88.07 +67.62	19.9	274

Table 4-5 Comparison of maximum experimental displacement and the pseudo-spectral displacement (3% damping)

As shown in Table 4-5, the displacements derived from the elastic response spectra closely correlate with the experimental displacements in the negative direction during initial loading phases. However, the experimental and spectral values begin to diverge drastically starting from ground motion GM5. This divergence is attributed to accumulated non-linear damage and period elongation in the test specimen, as the structure likely experienced significant concrete cracking, rebar yielding, and bond degradation from the previous ground motions (GM1 through GM4), which the idealized elastic spectrum cannot capture.

The rotation time-histories recorded during the sequential application of ground motions (GM1 to GM8) are presented in Figure 4-10. As illustrated, the highest rotation demands systematically occur during the biaxial loading phases (GM2, GM4, GM6, GM8). As the seismic intensity is increased to 50%, a significant escalation in rotation demand occurs, particularly during GM4, where peak rotations reach nearly $22 \times 10^{-3}\ rad$. This concentration of high-amplitude cycles indicates the onset of widespread concrete cracking and longitudinal reinforcement yielding within the highly stressed critical regions.

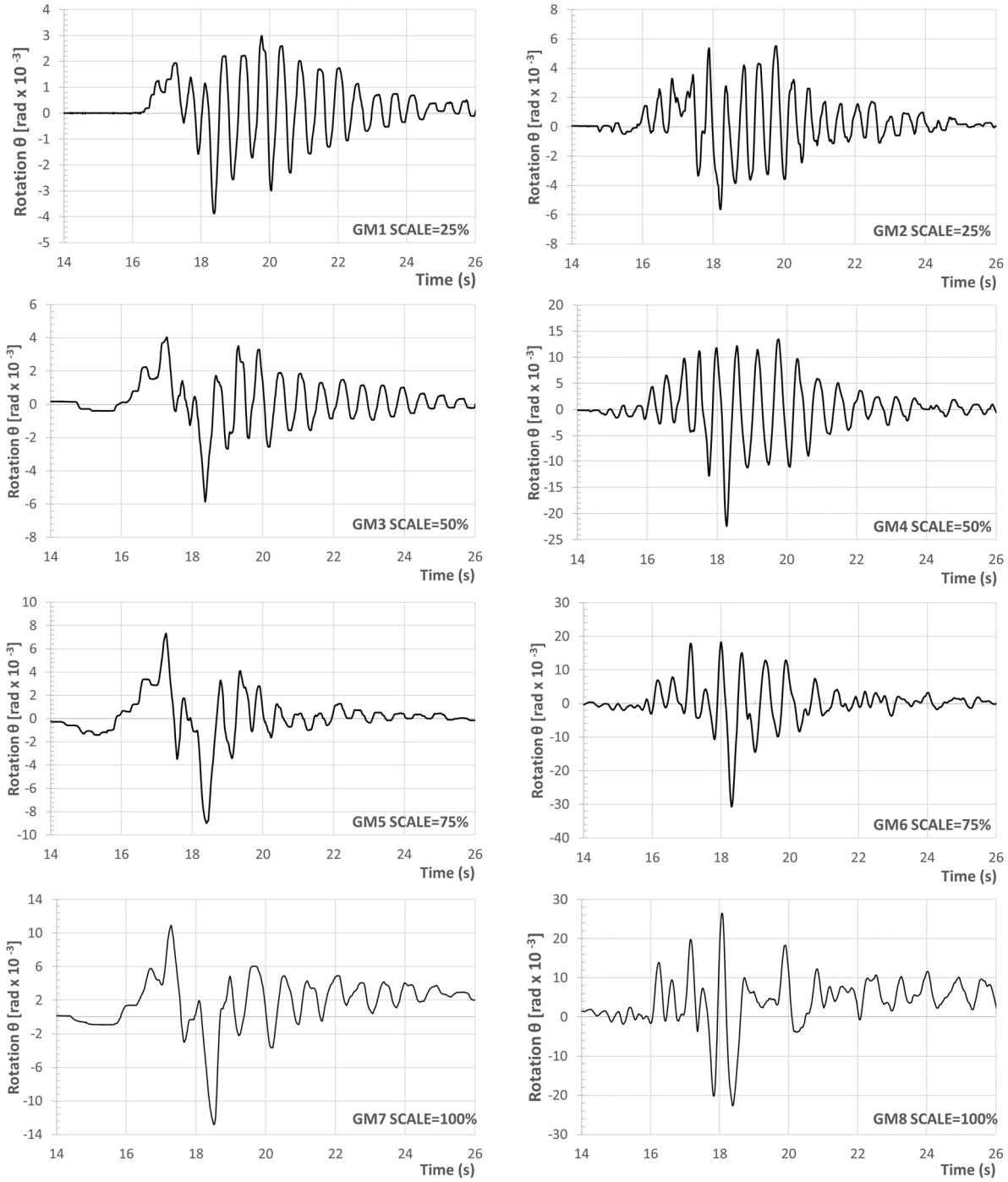

Figure 4-10 Time-history response of structural rotation (θ) across sequential ground motions (GM1 to GM8)

4.4 Instrumentation

The experimental tracking setup for the 40-ton U-shaped wall integrates external macro-displacement sensors, internal discrete transducers, and triaxial accelerometers. While the displacement potentiometers and accelerometers are positioned at the mid-height of the collar, several horizontal displacement gauges are located below it at the wall ends. Figure 4-11 illustrates these instrument layouts.

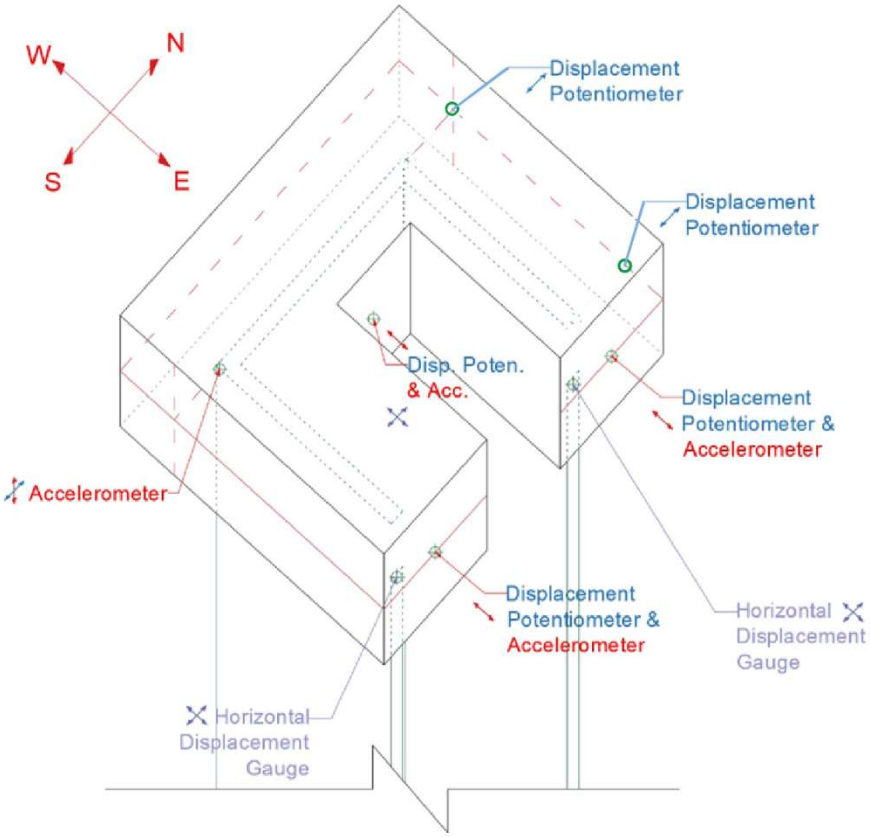

Figure 4-11 Instrumentation experimental setup

In Figure 4-11, the instrumentation is color-coded for clarity, with displacement potentiometers in blue, accelerometers in red, and horizontal gauges in purple. Their respective reading directions are marked adjacent to each notation. A single accelerometer captures vertical acceleration at mid-height on the collar at the wall's southwest corner.

The experimental time histories for East-West displacement shown in Figure 4-7, were calculated by averaging the readings from two potentiometers located at collar mid-height at the flange tips. In contrast, North-South displacements were measured at collar mid-height above the intersection of the north flange and web. The torsional rotations shown in Figure 4-10 were derived from measurements from the two potentiometers on the north flange, spaced 1.05 m apart.

4.5 Test Observations

In the U-shaped shear experiment, failure modes shifted from standard flexural cracking to highly complex failures driven by combined multidirectional bending and dynamic torsion.

The wall initially began in an uncracked state. Low-amplitude ground motions (GM1 and GM2) initiated fine horizontal hairline cracks exclusively along the construction cold joint at the foundation interface. As seismic demands slightly increased during GM3 and GM4, these horizontal cracks propagated from the flange tips inward toward the web. Throughout these early runs (GM1-GM4), the wall exhibited a cracked-elastic response characterized by negligible residual displacements, keeping the localized steel reinforcement well within its elastic limits. High-resolution data confirmed that vertical tension strains did not spread upward into the first story; instead, they formed sharp, narrow peaks strictly at the foundation interface joint. This strain localization indicates that the wall behaved essentially as a rigid elastic block rotating slightly about its cracked base boundary.

At GM5, a high-intensity unidirectional earthquake applied parallel to the flanges of the structure generated a maximum drift of 1.74%, causing widespread flexural cracking at the extreme ends of the flange boundaries and worsening of the cracks at the foundation bed. At GM6, the wall sustained a peak drift of 1.65% parallel to the axis of symmetry and 0.65% perpendicular to it; it also underwent a massive torsional rotation of 25.4 mrad. The massive combination of flexure, shear, and torsion concentrated extreme compressive stresses at the corner junction, inducing visible concrete crushing. GM7 reached its highest in-plane drift of 2.71%, crushing the boundary edge of the flange and both corner intersections heavily.

Finally, at GM8, the wall exhibited highly flexural damage distribution, reaching a maximum drift 2.05% in the direction parallel to the axis of symmetry and a 0.46% drift perpendicular to the axis of symmetry. The wall also increased the torsion rotation to 27.4 mrad. In this final earthquake motion, severe concrete crushing was evident at the boundary ends of the flanges, causing longitudinal rebar buckling. One flange experienced local out-of-plane buckling, kneeling inward toward the interior of the wall. Localized boundary flange failure was mainly driven by intense strain reversals. Evidence also showed sliding shear displacement along the foundation base joint.

4.6 General Assumptions of the Concrete Material Properties

The following chapter details the material assumptions and code-prescribed formulations adopted to define the advanced concrete properties required for the nonlinear finite element analysis in ATENA:

4.6.1 Modulus of Elasticity

The modulus of elasticity (E) was determined in accordance with CSA A23.3-24 Clause 8.6.2.3, based on the concrete's specified compressive strength ($f'c$) of 27 MPa.

$$E = 4500\sqrt{f'c}$$

$$E = 4500\sqrt{27} = 23\,383\ MPa = 23\,383\,000\ Kn/m^2$$

4.6.2 Modulus of Rupture

The modulus of rupture, f_r Shall be taken as stated in the code (CSA A23.3-24 Clause 8.6.4) where $\lambda = 1.0$ for normal density concrete

$$f_r = 0.6\,\lambda\sqrt{f'c}$$

$$f_r = 0.6\ (1.0)\sqrt{27} = 3.12\ Mpa$$

4.6.3 Poisson's Ratio (υ)

The fib Model Code for Concrete Structures (2020), Clause 14.6.1.4.3, states that Poisson's ratio for concrete varieties is between 0.14 and 0.26 for an array of stresses. "The influence of crack formation at the limit state (ULS), the estimation of $\upsilon = 0.20$ meets the required accuracy"

4.6.4 Fracture Energy (G_F)

Defined from the *fib* Model Code for Concrete Structures (2020) as the energy required to propagate a tensile crack of unit area. It's calculated to be

$$G_F = 85\ {f_c'}^{0.15}$$

$$G_F = 85\ (27)^{0.15} = 139.35\ N/m\ \approx 140\ N/m$$

4.6.5 Crack Model

The Rotated Crack coefficient (0= Rotated) assumes that the directions of the principal stresses continuously coincide with the principal strain axes, meaning no shear strains or stresses occur on the crack plane (Cervenka et al., ATENA Documentation). Although a rotating crack formulation can capture realistic structural behavior by tracking shifting stress fields under monotonic loading, this approach typically introduces severe numerical convergence difficulties, especially in dynamic models subjected to large strains.

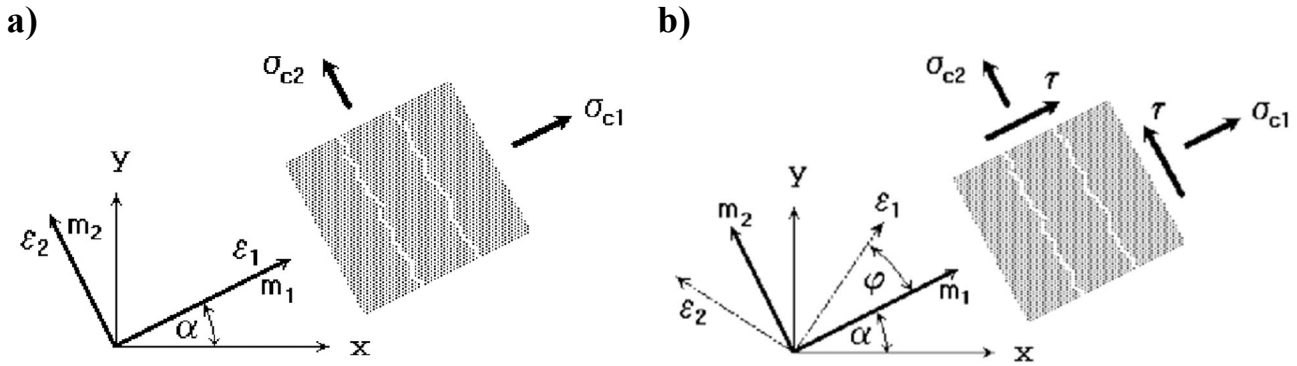

Figure 4-12 a) Rotated Crack Model b) Fixed Crack Model (from ATENA program Documentation - Theory)

Under the Fixed Crack configuration (1 = Fixed), the crack orientation becomes locked in place immediately upon exceeding the concrete's tensile strength, which subsequently induces shear stresses along the crack plane as the external loading directions shift. Consequently, a Fixed Crack formulation was considered to resolve specific numerical convergence issues encountered during the modeling phase.

4.6.6 Tension Stiffening

In general, it is common knowledge that the design of a reinforced concrete structure is such that the tension forces occurring in a crack must be absorbed by the reinforcement only. However, bond transfers tension stresses from the embedded steel reinforcement into the concrete. The concrete also participates in absorbing internal tension forces, which increases structural component stiffness. This stiffness comes from uncracked concrete or partially open cracks and is generally due to strain localization.

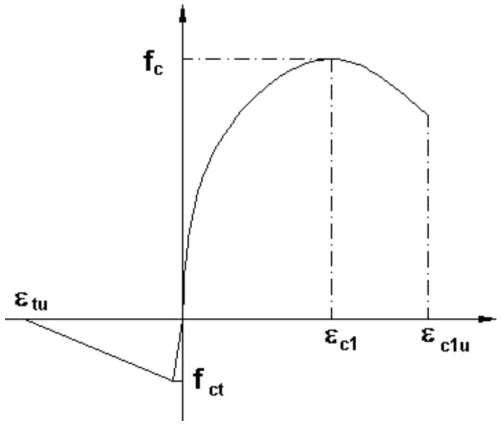

Figure 4-13 Uniaxial stress-strain relationship for concrete under tension and compression (from ATENA program Documentation - Theory)

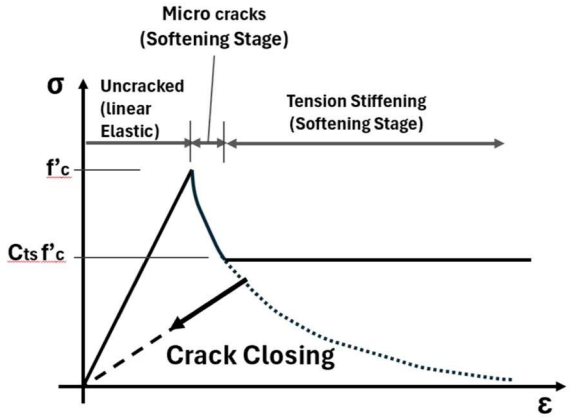

Figure 4-14 Characteristic concrete in tension (Modified from Dameh 2021)

Tension stiffening and effect can be simulated by specifying a tension stiffening factor c_{ts} this factor represents the relative limiting value of tensile strength in the tension softening diagram. The minimum tension stress cannot be below the value given by the product of $c_{ts}\ f_t$. The recommended default value for c_{ts} is 0.4 as recommended by CEB-FIP Model Code 2020. However, a factor of 0.5 was adopted to better account for confinement provided by the dense horizontal reinforcement and to improve numerical stability and reduce convergence errors during cyclic load reversals.

4.6.7 Onset Crushing (f'_{co})

As shown in Figure 4-36, this limit defines the onset of non-linear behavior in compression. It marks the stress level at which the concrete deviates from its linear-elastic response and begins to experience irreversible plastic deformation, micro-cracking, and macroscopic spalling of the concrete cover before reaching peak compressive strength. This linearity limit is estimated to be $f'_{c0} = 0.40\ f'_c = 10.8\ MPa$.

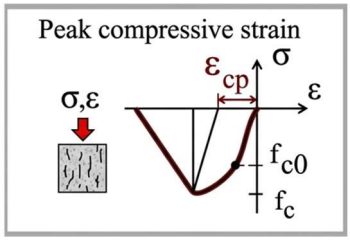

Figure 4-15 Compressive concrete configuration (from ATENA program Documentation)

4.6.8 Critical Compressive Displacement (W_D)

Crushing Compressive Displacement after which the compressive stress drops to zero. This typically goes with the crush band length in which the compressive test is executed (cylinder of a longitude of 300 mm)

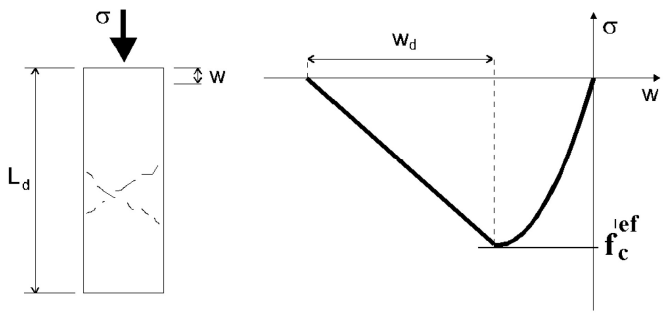

Figure 4-16 Compressive strength of a confined concrete model (from ATENA program Documentation - Theory)

From the experiments of Van MIER (1986), the value of w_d=0.5mm for normal concrete. For the concrete in the unconfined section of the wall, and aligning with the compression curve from the model of Hognestad's Parabola illustrated in Figure 4-18, the ultimate strain is estimated as $\varepsilon_u = 0.0044$, which defines the critical compressive displacement W_d as:

$$W_d = (\varepsilon_u - \varepsilon_o)\, L_d = (0.0044 - 0.0022)\, 300mm = 0.66\, mm \approx 0.0007\, m$$

4.6.9 Reduction of Compressive Strength due to Cracked Concrete

The reduction of compressive strength parallel to the cracks due to transverse tensile straining is based on experimental data. The constant c represents the maximum strength reduction under large transverse strain. According to Cervenka et al. 2021 a value of $r_c = 0.45$ was derived for concrete reinforced experiments with a fine mesh. Conversely, other researchers (e.g., Dyngeland, 1989) found that the reduction did not exceed $r_c = 0.8$. In this study, the value of r_c is assumed to be $r_c = 0.60$, an intermediate value between these two experimental limits.

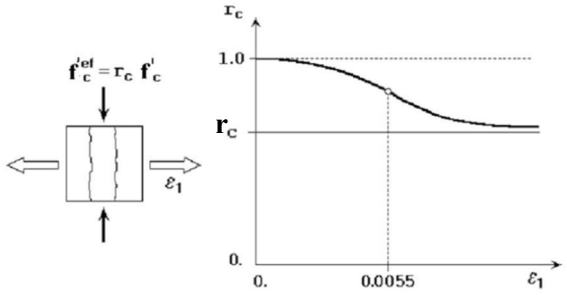

Figure 4-17 Compressive strength reduction of cracked concrete (from ATENA program Documentation - Theory)

4.6.10 Compression Curve (Unconfined)

The compressive curve of the concrete in the unconfined section of the wall is defined up to the maximum compressive stress. $f_c' = 27\ Mpa$. As shown in Figure 4-18, the stress-strain relationship follows Hognestad's Parabola (Hognestad, 1951), following the equation:

$$\sigma_c = f_c \left[\frac{2\ \varepsilon_c}{\varepsilon_o} - \left(\frac{\varepsilon_c}{\varepsilon_o} \right)^2 \right]$$

Where $\varepsilon_o = \frac{2\ f_c}{E_0} = \frac{2\ (27)}{23\ 383} = 0.00231\ \approx\ \varepsilon_o = 0.0022$ (for common strength concrete)

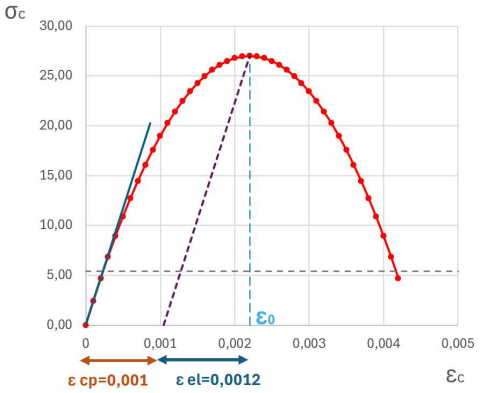

Figure 4-18 Unconfined concrete in compression following Hognestad's Parabola

Figure 4-18 shows an elastic strain of $\varepsilon_{el} = 0.0012$ and a plastic strain of $\varepsilon_{cp} = 0.001$. Adding these two components defines the total peak compressive strain $\varepsilon_o = 0.0022$ at the maximum unconfined compressive stress of $f_c' = 27\ Mpa$ before the curve enters its descending branch.

4.6.11 Compression Curve (Confined Sections)

The U-shaped wall used in the parametric study features boundary elements confined with transverse reinforcement throughout its height, using variable spacings: 50 mm on the ground floor, 100 mm on the second floor, and 200 mm on the top floor. The boundary elements are divided into two designations: EB-1 refers to the boundary elements at the ends of the flanged sections, and EB-2 refers to those located at the web-flange intersections, as shown in Figure 4-19.

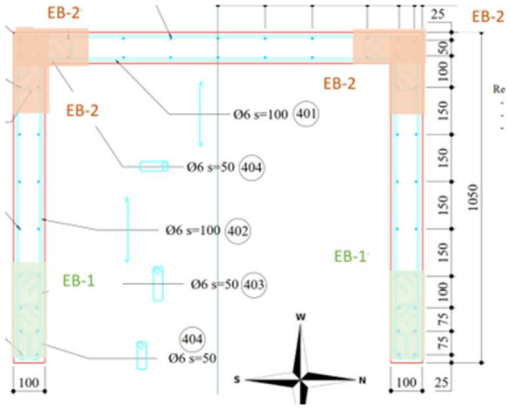

Figure 4-19 Geometry of U section Wall - nomenclature of boundary elements (Modified from Hoult et al. 2023)

Confinement within reinforced concrete walls enhances the material's energy dissipation capacity by increasing both the compressive strength and ductility of the concrete core. Several constitutive models define this enhanced stress-strain behavior. Richart et al. (1928) were the first to study confined concrete through extensive experimental testing, establishing the foundational equations specified below:

$$f'_{cc} = f'_c + 4.1\sigma_{lat} \approx f'_c\left(1 + 2k_e\rho_w \frac{f_{yw}}{f'_c}\right)$$

$$\varepsilon_{cc,u} = \varepsilon_{co}\left(1 + 5\left(\frac{f'_{cc}}{f'_c} - 1\right)\right) = \varepsilon_{co}\left(1 + 10k_e\rho_w \frac{f_{yw}}{f'_c}\right) = \varepsilon_{co}\left(1 + 20k_e\rho_w \frac{f_{yw}}{f'_c}\right)$$

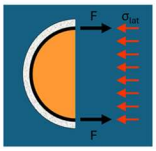

σ_{lat} = 2F/D for spiral confinement. The highest value of σ_{lat} occurs at the onset of stirrup yielding :

F = $f_{yw}A_{sw}$/s (kN per leg per 1 m length)

σ_{lat} = 2$f_{yw}A_{sw}$/D·s (internal pressure)

Figure 4-20 Confinement effectiveness equation by Richart et al (1928)

Another widely accepted formulation is established by the fib Model Code, which defines the enhanced compressive strength of confined concrete using the following relationships:

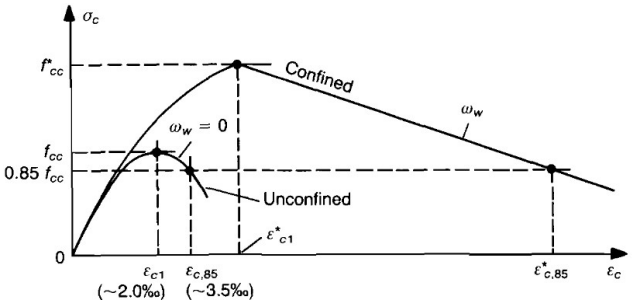

$$f_{cc} = f_c(1 + 2.5k_e\omega_w) \qquad (k_e\omega_w \le 0.1);$$

$$f_{cc} = f_c(1.125 + 1.25k_e\omega_w) \qquad (k_e\omega_w \le 0.1);$$

$$\varepsilon_{cc,o} = \varepsilon_{co}\left(\frac{f_{cc}}{f_c}\right)^2; \qquad \varepsilon_{cc,85} = \varepsilon_{c,85} + 0.1k_e\omega_w$$

Figure 4-21 Confinement effectiveness equation by the Fib Model code 1990

Alternatively, the Park and Priestley (1982) model describes the behavior of confined concrete. Based on experimental analysis, they developed the following governing equations:

$$f'_{cc} = f'_c + \rho_w f_{yw} = K f'_c; \quad K = 1 + \rho_w \frac{f_{yw}}{f'_c}$$

$$f_{cc,res} = 20 - 30\% f_{cc}$$

$$Z = \frac{0.5}{\varepsilon_{cc,50} - \varepsilon_{cc,o}}$$

$$\varepsilon_{cc,50} = \frac{3 + 0.29 f'_c}{145 f'_c - 1000} + 0.75\rho_w \left(\frac{b_c}{s}\right)^{1/2}$$

Where: ρ_w is the ratio of lateral steel to the concrete core.

Z is a constant controlling the slope of descending portion.

To quantify the efficiency of the transverse ties, the Mander et al. (1988) model introduces a confinement effectiveness coefficient (k_e). As illustrated in Figure 4-22, this coefficient reduces the total volumetric ratio of transverse reinforcement to an effective volumetric ratio. The value of k_e accounts for both the vertical arching action between hoop layers and the horizontal arching action between longitudinal bars, governed by the following expression:

$$k_e = \underbrace{\left(1 - \frac{s_h}{2b_c}\right)\left(1 - \frac{s_h}{2h_c}\right)}_{\text{Effect of the height-wise arrangement}} \underbrace{\left(1 - \frac{\sum b_i^2}{6b_c h_c}\right)}_{\text{Effect of cross-sectional pattern}}$$

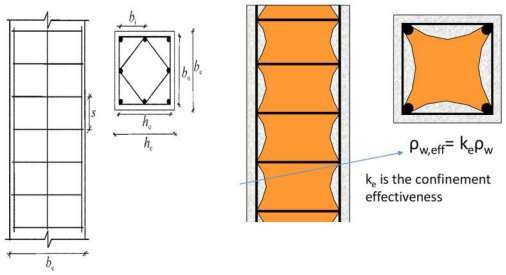

Figure 4-22 Confinement effectiveness ratio (Pantazopoulou - Class notes CIVL 6422)

The geometric parameters defining the confinement effectiveness factor include s_h as center-to-center vertical spacing of transverse hoop ties/stirrups along the member height; b_c, defined as the core section width measured centerline-to-centerline of the outermost peripheral hoop; h_c, representing the corresponding core depth measured along the orthogonal axis and b_i denotes the clear horizontal distance between adjacent, laterally supported longitudinal reinforcement bars along the section perimeter, where parabolic arching action develops between cross-ties.

These confinement models are applied to the distinct boundary element zones of the U-shaped wall. Because stirrup spacing varies by floor (50 mm, 100 mm, and 200 mm), confinement effectiveness varies accordingly. This variation requires calculating distinct localized stress-strain curves for the concrete core at each floor level, as presented in Appendix B.

Based on this comparative evaluation, the Park and Priestley (1982) model was selected to simulate concrete confinement. For the third-floor structural elements featuring a stirrup spacing of 200 mm, the CEB-fib Model Code equations mathematically generated a confined compressive strength lower than that of the unconfined concrete, which is physically unrealistic. Similarly, at the same 200 mm spacing, the Richart et al. (1928) model predicted a negligible confinement-stress contribution of less than 1 MPa. Consequently, the more robust and versatile Mander, Priestley, and Park (1988) formulation was adopted for the non-linear finite element analysis in ATENA. A summary of the resulting confinement parameters is presented in Table 4-6.

	Confined compressive stress (MPa)	
Direction	**EB 1**	**EB-2**
1st Floor	38.19	39.55
2nd Floor	32.60	33.27
3nd Floor	29.80	30.14

Table 4-6 Confinement effectiveness in each floor.

4.7 General Assumptions of the Steel Rebar Material Properties

Building upon the concrete material models presented in the previous chapter, this chapter details the mechanical assumptions and code-prescribed formulations used to define the constitutive properties of the reinforcing steel.

4.7.1 Menegotto-Pinto

To accurately capture the cyclic response and hysteretic behavior of the reinforcement under seismic loading, the Menegotto-Pinto model is implemented within the ATENA finite element framework. The input parameters and the governing stress-strain relationships are detailed below:

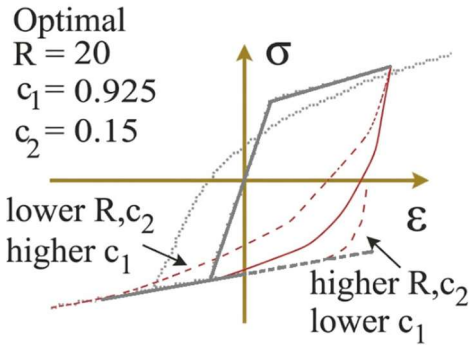

Figure 4-23 Stress-strain law (Modified from ATENA program Documentation)

4.7.2 Bond slip

To accurately capture the interaction between the steel reinforcement and the surrounding concrete mixture, a nonlinear bond-slip relationship is implemented. In the finite element model, it was implemented using distributed interfacial bond springs. Bond strength-slip relations adopted from the fib Model Code (2020) are quantified on the degree of confinement, the concrete compressive strength, and the concrete bond condition to the longitudinal steel reinforcement.

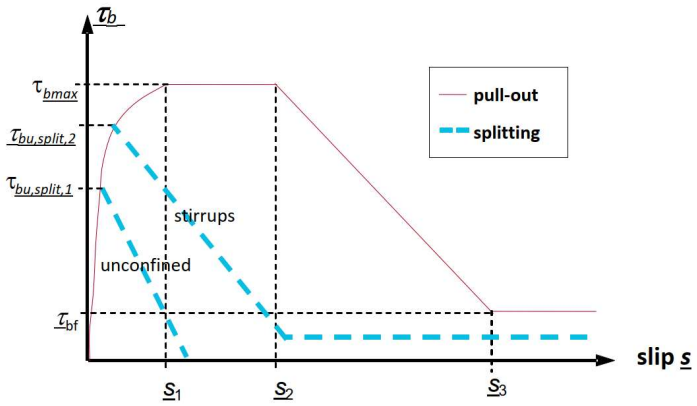

Figure 4-24 Bond stress-slip relation - the fib Model Code for Concrete Structures (2020)

Two primary bond-slip failure mechanisms are anticipated: pull-out and splitting. As shown in Figure 4-24, a ductile pull-out failure develops when heavy confinement prevents splitting of the concrete cover. Under these conditions, bond stress develops along the solid envelope curve, reaches a peak, then remains constant across a slip-rate plateau before descending to a residual frictional value. Conversely, if the cover lacks sufficient lateral restraint, a premature splitting failure occurs along the dashed trajectories. Consequently, these unconfined sections exhibit highly brittle splitting failures, occurring at significantly lower slip and bond stress thresholds than their heavily confined counterparts.

	1	2	3	4	5	6
	Pull-out (PO)		Splitting (SP)			
	$\varepsilon_s < \varepsilon_{s,y}$		$\varepsilon_s < \varepsilon_{s,y}$			
	Good bond cond.	All other bond cond.	Good bond cond.		All other bond cond.	
			Unconfined	Stirrups	Unconfined	Stirrups
τ_{bmax}	$2.5\sqrt{f_{cm}}$	$1.25\sqrt{f_{cm}}$	$2.5\sqrt{f_{cm}}$	$2.5\sqrt{f_{cm}}$	$1.25\sqrt{f_{cm}}$	$1.25\sqrt{f_{cm}}$
$\tau_{bu,split}$	—	—	$7.0\cdot\left(\frac{f_{cm}}{25}\right)^{0.75}$	$8.0\cdot\left(\frac{f_{cm}}{25}\right)^{0}$	$5.0\cdot\left(\frac{f_{cm}}{25}\right)^{0.75}$	$5.5\cdot\left(\frac{f_{cm}}{25}\right)^{0.75}$
s_1	1.0 mm	1.8 mm	$s(\tau_{bu,split})$	$s(\tau_{bu,split})$	$s(\tau_{bu,split})$	$s(\tau_{bu,split})$
s_2	2.0 mm	3.6 mm	s_1	s_1	s_1	s_1
s_3	c_{clear} [1)]	c_{clear} [1)]	$1.2s_1$	$0.5c_{clear}$ [1)]	$1.2s_1$	$0.5c_{clear}$ [1)]
α	0.4	0.4	0.4	0.4	0.4	0.4
τ_{bf}	$0.40\,\tau_{max}$	$0.40\,\tau_{max}$	0	$0.4\,\tau_{bu,split}$	0	$0.4\,\tau_{bu,split}$

[1)] c_{clear} is the clear distance between ribs

	1	2	3	4	5	6
	Pull- Out (PO)		Splitting (SP)			
	$\varepsilon_s < \varepsilon_{s,y}$		$\varepsilon_s < \varepsilon_{s,y}$			
	Good bond cond.	All other bond cond.	Good bond cond.		All other bond cond.	
			Unconfined	Stirrups	Unconfined	Stirrups
τ_{bmax} (MPa)	12.99	6.50	12.99	12.99	6.50	6.50
			7.0	*8.0*	*5.0*	*5.5*
$\tau_{bu,split}$	-	-	7.14	8.16	5.10	5.61
s_1 (mm)	1.00	1.80	0.22	0.31	0.98	1.25
s_2 (mm)	2.00	3.60	0.22	0.31	0.98	1.25
s_3 (mm)	6.00	6.00	1.20	3.00	2.16	3.00
α	0.40	0.40	0.40	0.40	0.40	0.40
τ_{bf} (MPa)	5.20	2.60	0.00	3.26	0.00	2.24

Table 4-7 Parameters defining the mean bond stress-slip relationship of ribbed bars (the fib Model Code for Concrete Structures -2020)

The bond stress-slip relationships for both pull-out and splitting failure modes are generated using the experimental concrete compressive strength $f_c = 27\ Mpa$ and a rebar rib spacing of 6 mm. The analytical curves assume a 'good bond' condition, as illustrated in Figure 4-25. Within the ATENA finite element model, bond behavior was explicitly defined for both the vertical and horizontal reinforcement. However, while the end nodes of the horizontal reinforcement are modeled as "fixed" with respect to the concrete (preventing slip at this node), the longitudinal reinforcement remains unfixed, requiring it to comply with the defined bond slip-stress curve.

For the 6 mm diameter longitudinal bars under a splitting failure mechanism (depicted by the black dashed lines), a semi-confined model was assumed. This intermediate state bridges unconfined and stirrup-confined splitting behavior, since these 6 mm bars lie between boundary zones that lack reinforcement confinement yet benefit from the overall presence of transverse reinforcement. Conversely, a full pull-out model was applied to the 6 mm bars embedded in the foundation and collar (depicted by the continuous black line), where they reach their maximum bond stress capacity of $\tau_{bmax} = 12.99\ Mpa$.

For the 8 mm and 12 mm bars, the splitting models are represented by purple dashed lines, while their respective pull-out envelopes are shown as continuous purple lines. Because reinforcement bars in ATENA can only be assigned a single local bond-slip constitutive curve, the splitting relationship was chosen as the default baseline. To account for pull-out failures where necessary, a scaled-up version of this splitting envelope was defined and assigned to those specific regions. This was implemented by activating ATENA's location-dependency feature, which scales bond-strength magnitude along the embedded length of the bar to reflect local confinement conditions.

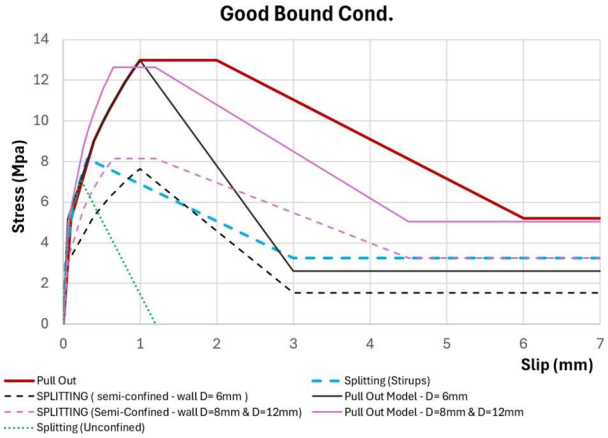

Figure 4-25 Bond stress-slip relationship

4.8 ATENA

This chapter outlines the geometric definitions, material configurations, boundary conditions, and loading protocols applied to simulate the nonlinear behavior of the U-shaped reinforced concrete shear wall using the finite element software ATENA. Figure 4-26 illustrates the mesh configuration, with a maximum element size of 0.1 m. Furthermore, the concrete material definitions are presented in Figure 4-27, where the confined concrete within the boundary elements has different material properties and exhibits enhanced compressive strength and higher ductility. Appendix B details the specific localized stress-strain relationships for each distinct material zone.

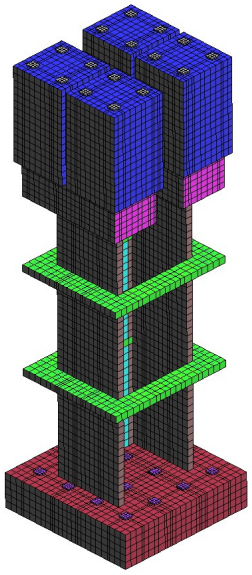

Figure 4-26 Mesh Configuration

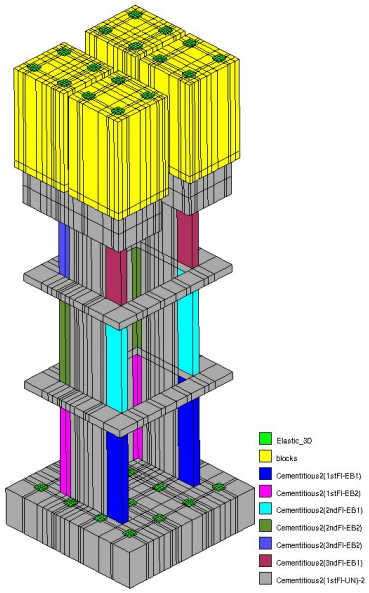

Figure 4-27 Concrete Material Configuration

The 30-ton loading blocks are modeled as elastic using the steel modulus of elasticity. Similarly, the 40 mm diameter circular bolts used within the foundation and the collar to secure the assembly are defined using the elastic modulus of structural steel. To accommodate the geometric constraints of the numerical model while ensuring structural equivalence, these circular bolts were modeled as rectangular sections possessing an identical gross cross-sectional area. These rods connect to the concrete via steel plates at the top and bottom of the assembly, which act as clamping devices analogous to a bolt head and nut anchor. Additionally, the steel rods within the foundation are fixed at the bottom surface. These boundary conditions closely replicate the experimental setup. Figure 4-28 and Figure 4-29 illustrate the elastic material configuration and properties.

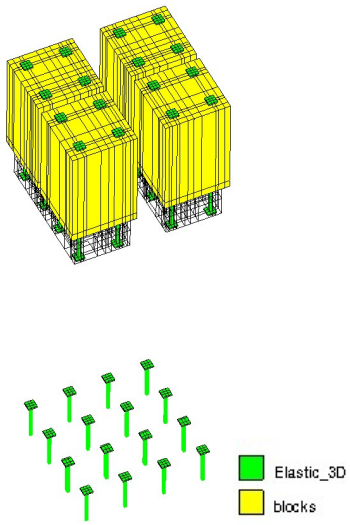

Figure 4-28 Elastic materials

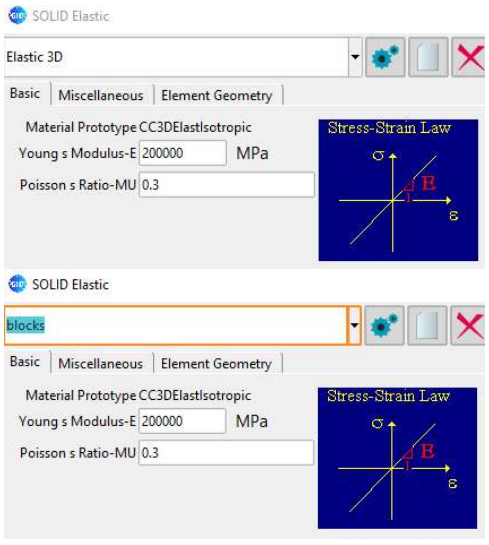

Figure 4-29 Elastic material properties

The reinforcement configurations are modeled as discrete 1D line elements embedded within the concrete mesh, as illustrated in Figure 2-1. The constitutive steel material properties match the experimental data outlined in Section Chapter 4.2 Experimental Material Properties, while the cyclic hysteretic behavior follows the Menegotto-Pinto parameter formulation detailed in Section 4.7.1 To capture the localized interaction between the steel and concrete, non-linear bond-slip interface elements (utilizing a discrete bond spring model with material memory) are distributed along the length of the reinforcing bars, these were defined for both the vertical and horizontal reinforcement. However, while the end nodes of the horizontal reinforcement are modeled as 'fixed' with respect to the concrete, the longitudinal reinforcement remains unfixed, requiring it to fully comply with the defined bond stress-slip constitutive relationship defined in Chapter 4.7.2.

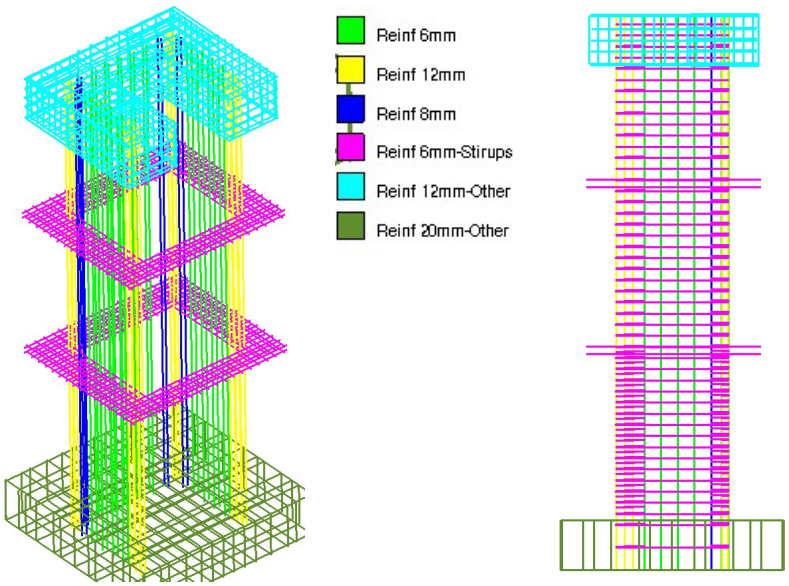

Figure 4-30 Reinforcement model

4.8.1 Concrete Model Definition

This section details the concrete constitutive models and advanced material parameters provided within the ATENA software environment.

Unconfined concrete

The concrete modulus of elasticity (E) was reduced to 50% of the value reported in Section 4.2 to calibrate the numerical model's effective stiffness. Initial simulations using the full, unreduced elastic modulus produced an overly stiff global response compared with the experimental data. Dynamically, the physical test specimen exhibited a fundamental natural period of T=0.33s, whereas the initial uncracked numerical model yielded a shorter period of T=0.283s. By reducing the concrete modulus (E) by 50% to account for early microcracking from temperature strains and boundary flexibility, the numerical model achieved a calibrated natural period of T=0.387 s, closer to the specimen period for the subsequent nonlinear analysis.

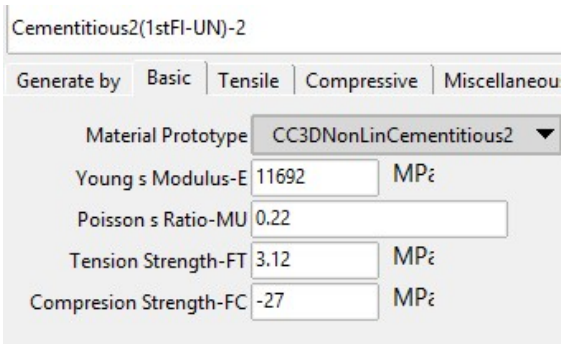

Figure 4-31 Basic concrete material configuration

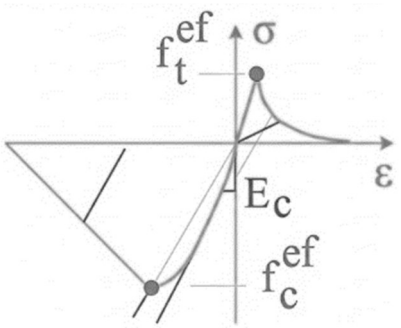

Figure 4-32 Stress-Strain Law

The concrete tension strength and Poisson's ratio are established in accordance with standard design code recommendations.

As illustrated in Figure 4-33, the tension stiffening factor is defined as 0.5 ft. This parameter implies that, after cracking initiates and the initial softening phase stabilizes, the concrete blocks between macroscopic cracks are modeled to maintain an average continuous residual tensile stress equal to 50% of the peak tensile strength, as shown schematically in Figure 4-34c. Furthermore, a strictly fixed, smeared-crack approach (1 = Fixed) was implemented to enhance numerical stability and ensure model convergence under dynamic cyclic loading. Additionally, a minimum crack spacing of 50mm was enforced to prevent the localized generation of an unrealistic cluster of micro-cracks within a single high-stress region.

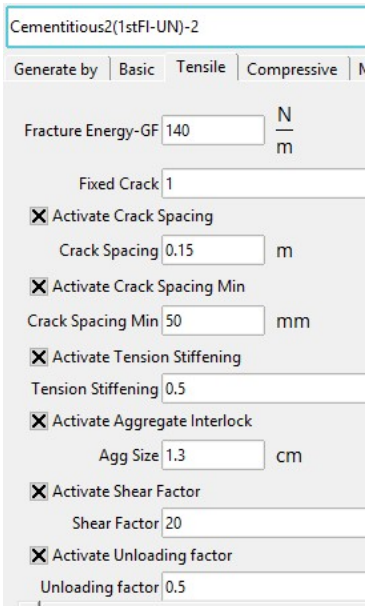

Figure 4-33 Tensile concrete configuration

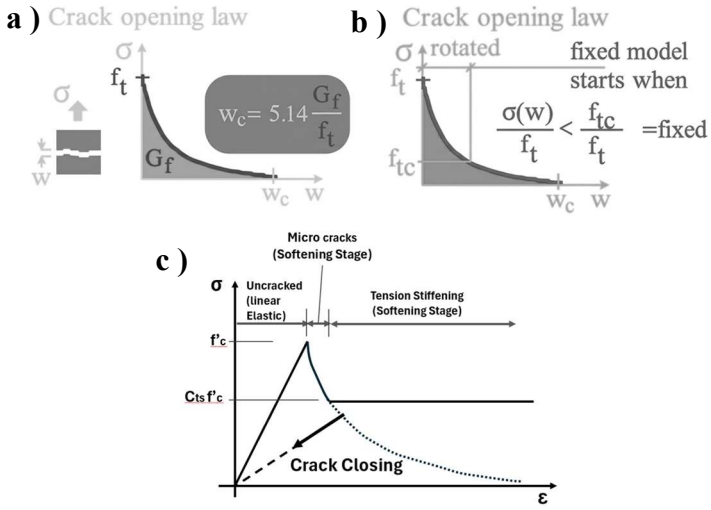

Figure 4-34 Tensile concrete curves a) Crack opening law b) rotates, fixed model c) Tension stiffening

Furthermore, the specific compressive stress-strain behavior defined for concrete is presented below:

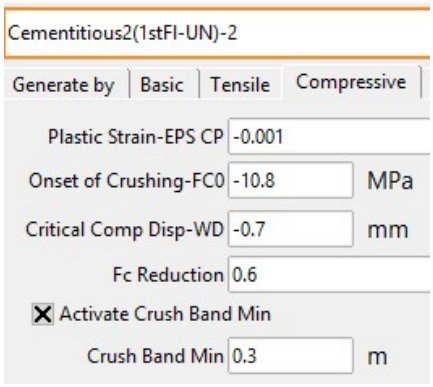

Figure 4-35 Compressive concrete configuration

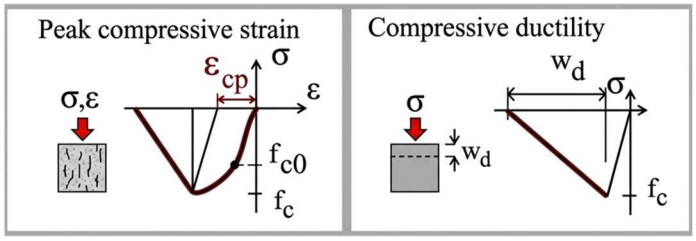

Figure 4-36 Compressive concrete Stress-strain Curve (peak and post-peak)

Figure 4-35 and Figure 4-36 show that ATENA modeled the compressive behavior of unconfined concrete; the plastic strain capacity increases significantly when the confinement effectiveness factor is incorporated to account for triaxial compressive stress states.

The compressive stress-strain relationship for the unconfined concrete material is defined using a piecewise constitutive model divided into ascending and descending branches. The ascending branch is governed by the Hognestad parabola, which captures the initial elastic and pre-peak non-linear hardening response up to the peak compressive strength. Conversely, the post-peak softening behavior along the descending branch is modeled in accordance with the modified Park & Kent formulation to represent the strain-softening response of unconfined concrete.

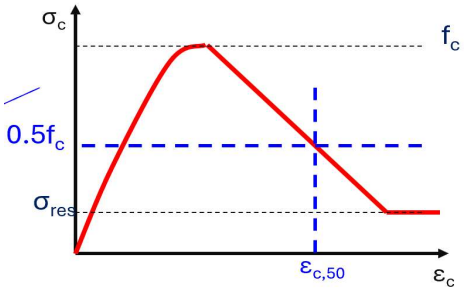

Figure 4-37 Compressive Concrete Stress-Strain Curve

$$f'_{cc} = f'_c + \rho_w f_{wy} = K\, f'_c \;;\; K = 1 + \rho_w \frac{f_{wy}}{f_c'}$$

$$Z = \frac{0.5}{\epsilon_{cc,50} - \epsilon_{cc,0}}$$

$$\epsilon_{cc,50} = \frac{3 + 0.29\, f'_c}{145\, f'_c - 1000} + 0.75\, \rho_w \left(\frac{b_c}{s}\right)^{1/2}$$

$$f'_{cc,res} \approx 20\ to\ 30\%\ f'_{cc}$$

Figure 4-37 illustrates the non-linear compressive stress-strain constitutive relationship adopted for concrete, incorporating the beneficial effects of lateral confinement. The peak confined compressive strength, f_{cc}', is calculated using a confinement enhancement factor K, which accounts for the volumetric ratio ρ_w and yield strength f_{wy} of the transverse reinforcement. The non-linear response features an initial ascending branch up to peak stress, followed by a linear softening post-peak branch governed by the slope parameter Z. This post-peak degradation is defined by $\epsilon_{cc,50}$, the strain corresponding to a 50% reduction in peak stress ($0.5\, f'_{cc}$). At

large plastic deformations, a residual compressive stress plateau ($f'_{cc,res}$) equal to 20% to 30% of f'_{cc} is maintained.

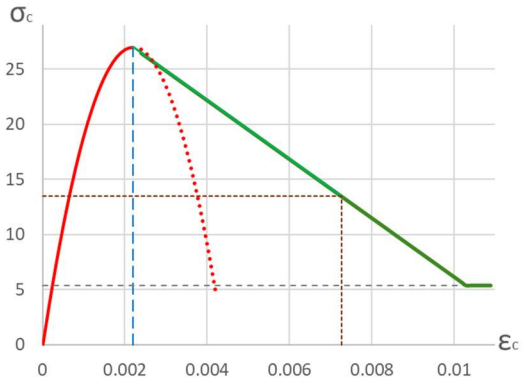

Figure 4-38 Compressive concrete unconfined and confined stress-strain curve

The compressive stress-strain relationships assigned to the confined concrete zones within the ATENA model are illustrated in Figure 4-39. As shown, the first-floor boundary elements (yellow and green curves) exhibit higher peak compressive strength and greater ductility, reaching residual capacity at significantly higher strains due to dense confinement. Interestingly, the baseline unconfined concrete model (red curve) shows slightly higher ductility than the top-floor boundary elements, which have a wide stirrup spacing of S = 200mm. This behavior occurs because the concrete designated as 'unconfined' in the wall actually represents a semi-confined environment benefiting from overall transverse web reinforcement spaced at S = 100mm, thereby outperforming the sparsely tied boundary zones at the top of the structure.

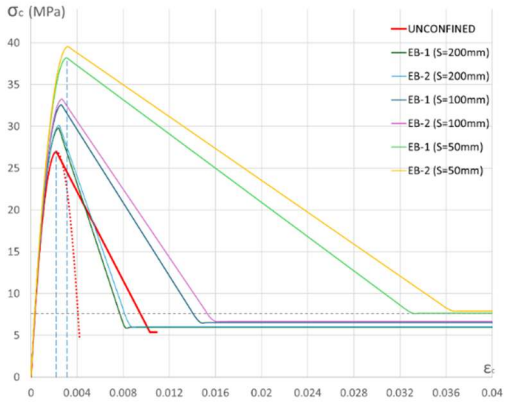

Figure 4-39 Stress-strain relationship of unconfined and confined materials.

4.8.2 Monitor Points

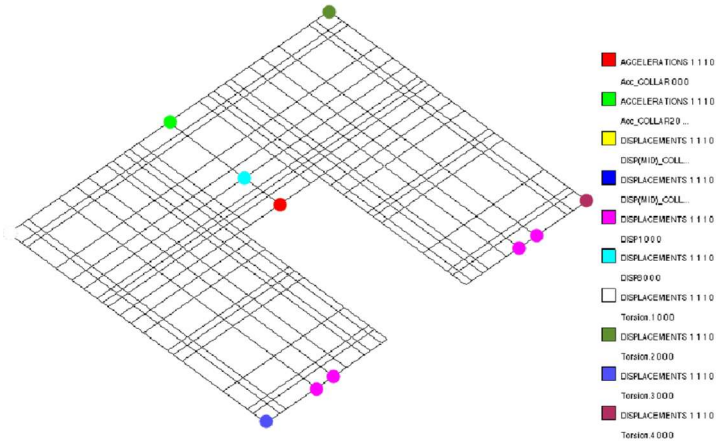

Figure 4-40 Monitor Points

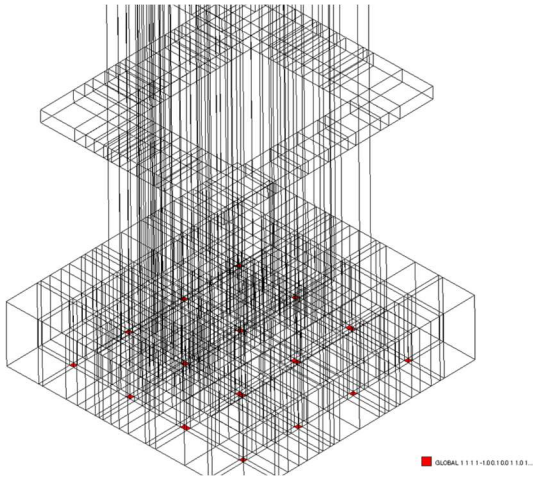

Figure 4-41 Fixed surface on foundation

The boundary conditions on the foundation are situated in the bottom surfaces of the foundation steel bolts. The monitor points for displacement and acceleration are shown in Figure 4-40 and correspond to the displacement potentiometers and accelerometers used in the experiment described in Chapter 4.5.

4.8.3 Load Cases

Prior to dynamic cyclic loading, the structural specimen is subjected to its self-weight and initial gravity loads. Consequently, the first load step in the finite element model applies this dead load for 2.0 seconds. To simulate the target axial load, the reinforced concrete U-shaped shear wall, intermediate slabs, and foundation block were assigned a standard concrete unit weight of 24 kN/m^3, whereas the four loading blocks at the top collar were assigned an increased equivalent unit weight of 62.86 kN/m^3 (Figure 4-42). This self-weight distribution corresponds directly to the detailed specimen weight breakdown presented in Table 4-3, resulting in a total vertical reaction of 368 kN.

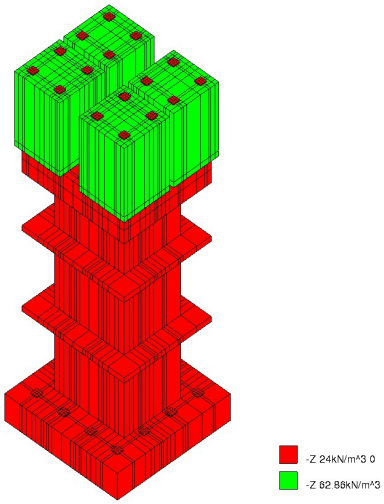

Figure 4-42 Self-weight density

The subsequent dynamic protocol comprises eight sequential ground motions (GM1-GM8). Each ground motion record spans a duration of 32.0 seconds and is evaluated using a time-integration increment of 0.005 seconds. Between consecutive seismic events, a zero-acceleration rest interval is introduced (maintaining only gravity loads) to allow the structural model to decay into free vibration and approach static equilibrium before initiating the next ground-motion phase.

4.8.4 Dynamic Response

Direct time-step integration for the dynamic cyclic loading was performed using the Newmark method (Using standard unconditionally stable parameters $\gamma = 0.5$ and $\beta = 0.2505$). Structural damping was modeled at 1% of the critical damping ratio ($\zeta = 1\%$) to represent the baseline energy dissipation of the reinforced concrete assembly prior to severe damage and cracking. With these input parameters defined, the time-history records were simulated consecutively. The experimental acceleration time-history responses represent the specimen's actual motion, provided by the Université Catholique de Louvain (UCLouvain) on their website [39] and graphed in sequence order (see Figure 4-43 and Figure 4-44).

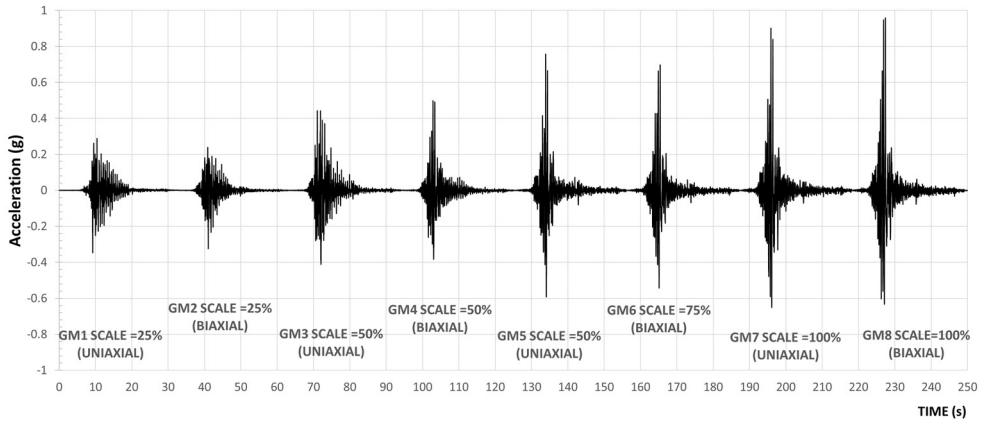

Figure 4-43 Experimental acceleration-time history response in the West - East Seismic Excitation (Parallel to the Axis of Symmetry)

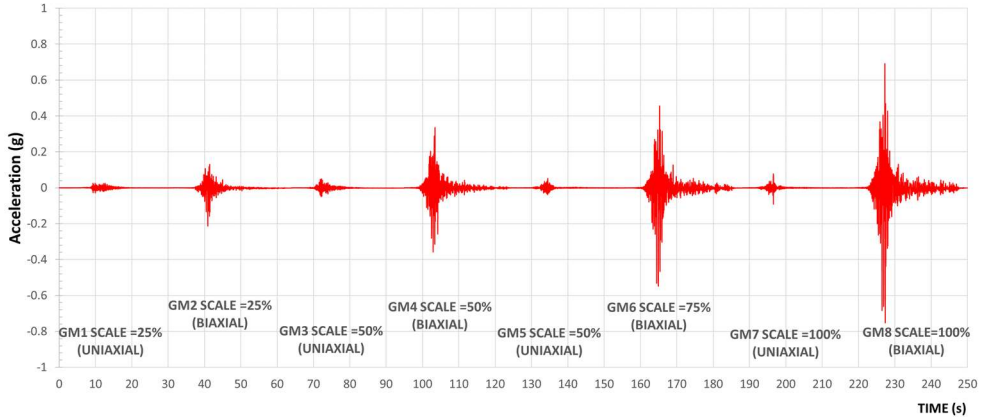

Figure 4-44 Experimental acceleration-time history response in the North - South Seismic Excitation (Parallel to the Web)

Potentiometers measured experimental displacements at mid-height on the top collar throughout the continuous ground-motion sequence (GM1 to GM8). Figure 4-45 illustrates the displacement along the axis of symmetry (East-West direction), while Figure 4-46 presents the transverse displacement relative to the axis of symmetry (North-South direction).

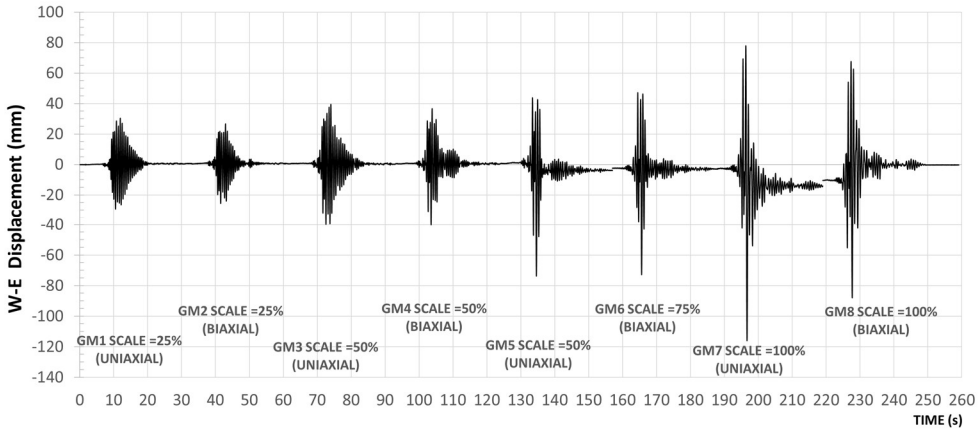

Figure 4-45 Experimental displacement time history response under West-East seismic excitation (Parallel to the Axis of Symmetry)

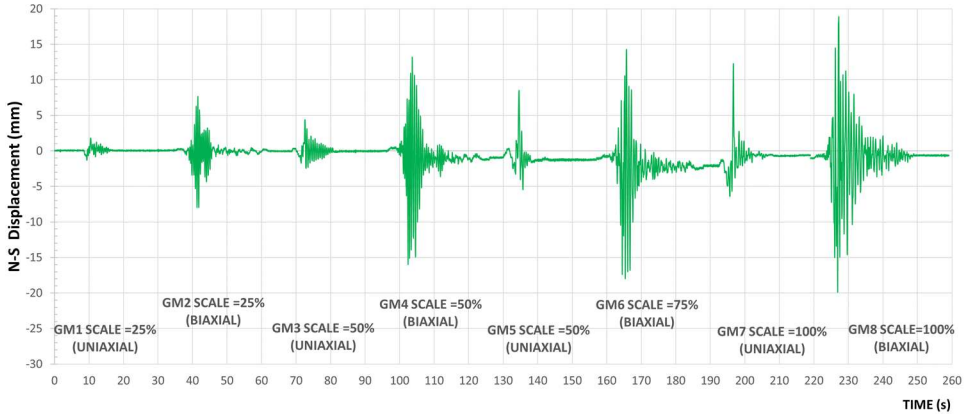

Figure 4-46 Experimental displacement time history response under North-South seismic excitation (Transverse to the Axis of Symmetry)

The rotation time-history responses at the collar's mid-height across successive ground motion records are shown in Figure 4-45. Peak rotations are evident during ground motion GM4, indicating the onset of widespread concrete cracking and highly stressed critical regions.

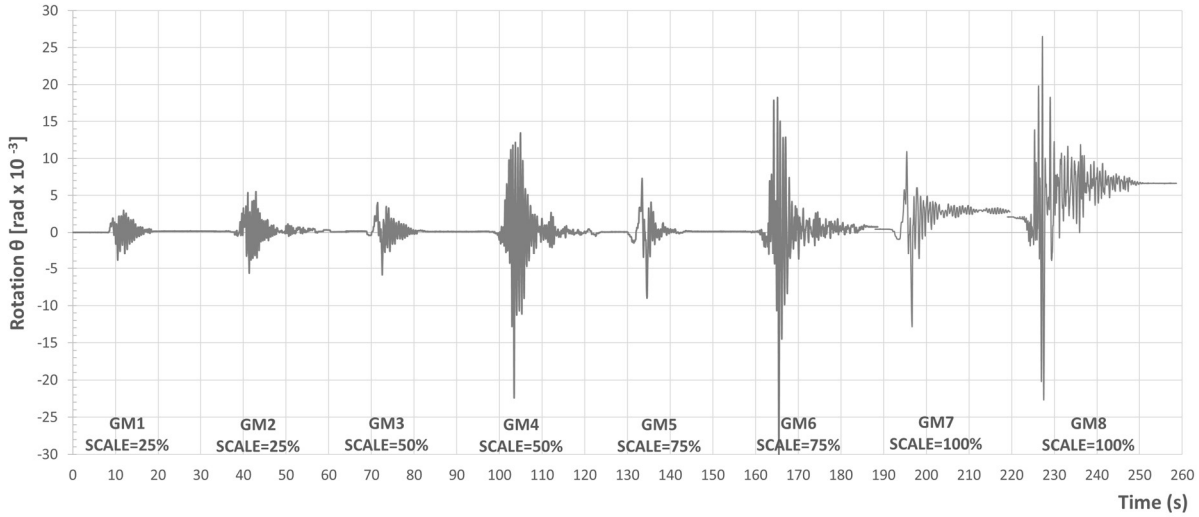

Figure 4-47 Structural Rotation (θ) time history response under sequential seismic excitation

The comparison on a larger scale is shown in Figure 4-48. The experimental response is plotted as a solid black line for the axis of symmetry (East-West direction) and green for the direction parallel to the web (North-South direction), while the finite element model predictions are shown in red. During the initial phase (GM1-GM2), the numerical model demonstrates excellent phase correlation and closely matches the experimental peak-displacement demands. However, in GM1, a notable divergence in peak amplitudes is observed after the peak value, suggesting that the finite element model exhibits higher effective damping because it attenuates more rapidly.

An alternative explanation for this amplitude modulation is a structural beating effect observed in the experiment, triggered by the inertial mass blocks attached to the top collar. If the connection interface between these inertial mass blocks and the collar has localized flexibility (rather than acting as a single perfectly rigid body), the mass blocks can behave as an independent oscillator with a distinct natural period. This creates a multi-degree-of-freedom system in which the mass blocks and the primary shear wall have closely spaced frequencies. The resulting coupled response causes energy to alternate between the wall and the top masses, producing the distinct expanding and contracting displacement envelope shown in ground motion GM1. This phenomenon is also observed to a lesser degree in GM2, which exhibits the same intensity as GM1 along the axis of symmetry and in the perpendicular direction, thereby inducing torsional effects in the structure.

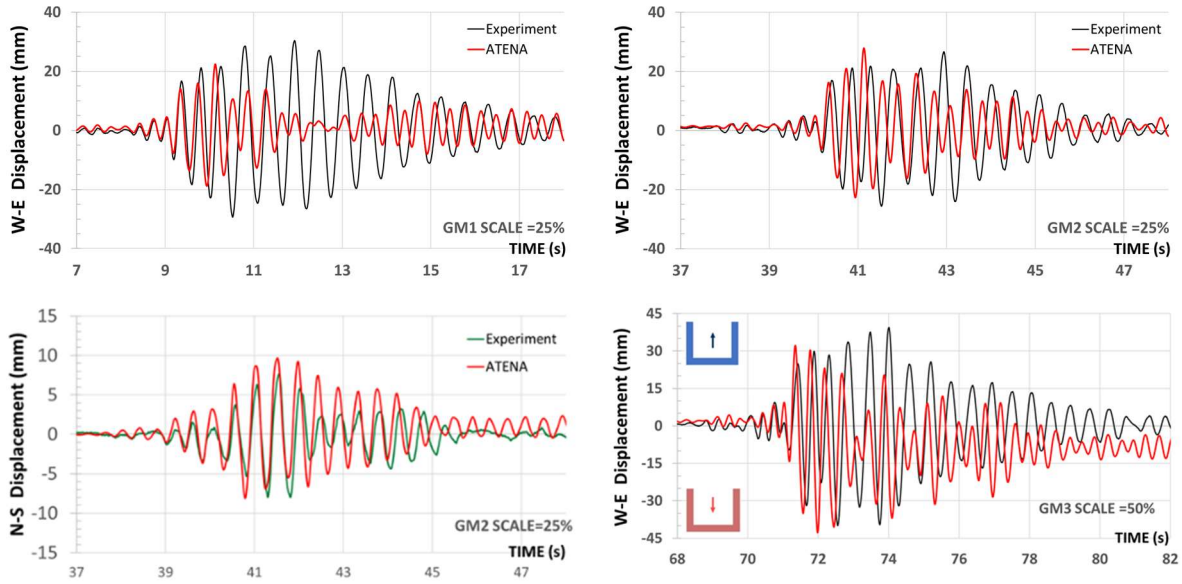

Figure 4-48 Comparison of experimental W-E and N-S displacement time-histories at the collar mid-height (black line in the W-E direction and Green line in the North-South direction), with ATENA finite element model predictions (red line) across ground motions GM1 to GM3.

In the North-South direction, the displacement response aligns periodically during the initial phase of the GM2 time history. Overall, the finite element model accurately tracks the experimental response, predicting a peak displacement of 6.7 mm compared to the measured maximum of 8.0 mm. While the period matches closely at the start of loading, the experimental response exhibits period elongation after reaching peak displacement compared to the numerical prediction. This difference highlights the software's capability and limitations in capturing real structural degradation.

As stated earlier, the finite element model included a 1-second window of zero ground-motion excitation between sequential earthquake records. By evaluating the structural response during this free-vibration phase in the absence of external lateral forces, the fundamental period could be isolated and measured after each seismic event. This approach allows quantification of structural stiffness degradation, which manifests as a progressive elongation of the fundamental period with each subsequent ground-motion application. These recorded values are summarized below:

	GM1 - GM2 (32-33s)	GM2 - GM3 (63-34s)
Fundamental period	0.36 s	0.37 s

Table 4-8 Progressive degradation of the fundamental natural period.

The rotation response under biaxial ground motion (GM2) is shown in Figure 4-49, which shows excellent phase correlation between the ATENA model and the experimental results. However, the finite element model appears to overestimate the rotation relative to the experimental data.

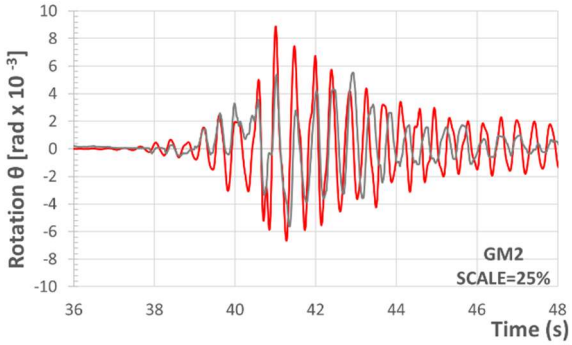

Figure 4-49 Comparison of experimental rotation time-histories at the collar mid-height (black line) with ATENA finite element model predictions (red line) across bi-axial ground motion GM2.

Furthermore, when the specimen was excited only unidirectionally along the axis of symmetry, a loss of symmetric structural response was observed after prior biaxial loading cycles, resulting in noticeable transverse displacements. This behavior is attributed to asymmetric material degradation, which created an eccentricity between the loading axis and the degraded shear center, thereby triggering transverse drift.

4.9 SAP 2000

The experimental data were validated using another, more industry-friendly software, SAP2000, by running a nonlinear model to compare the global cyclic response, lateral strength capacity, and overall displacement ductility under cyclic loading. By utilizing appropriate modeling tools, this study aims to accurately simulate the behavior of U-shaped reinforced concrete walls under cyclic loading, capturing both plastic deformation mechanisms and localized failure modes, while highlighting current modeling limitations.

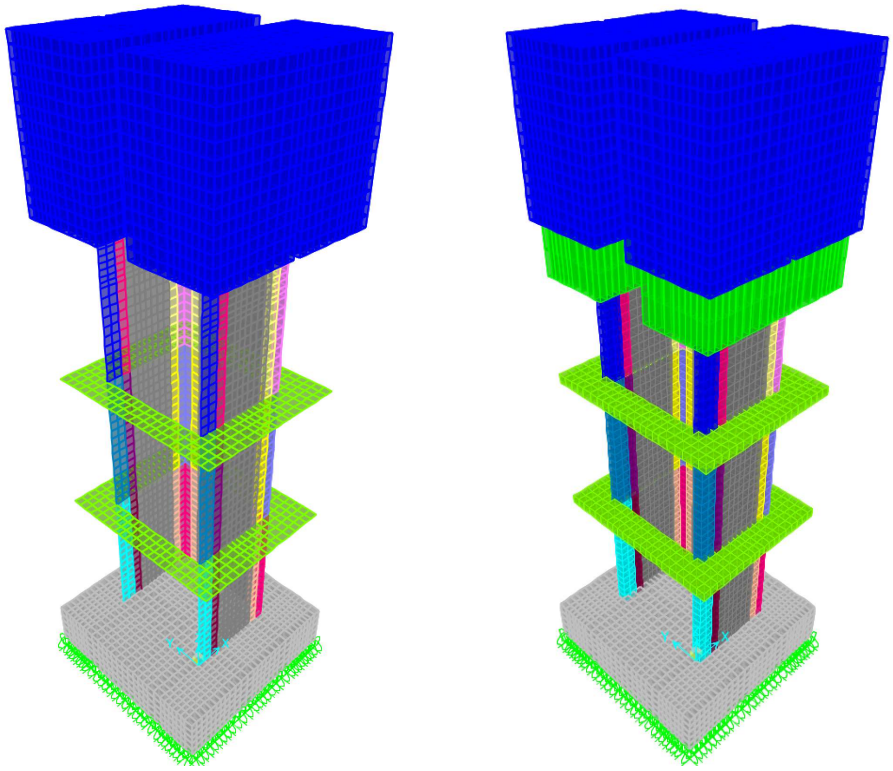

Figure 4-50 General 3D View and Mesh Discretization of the Specimen in SAP2000 (Left: Standard view, Right: Extrude view)

The wall section was modeled using nonlinear layered shell elements, consisting of a single homogeneous concrete layer assigned orthotropic material properties, along with four discrete reinforcement layers representing the longitudinal and transverse steel mats on each face of the wall cross-section. The single concrete layer has 5 integration points in the thickness direction.

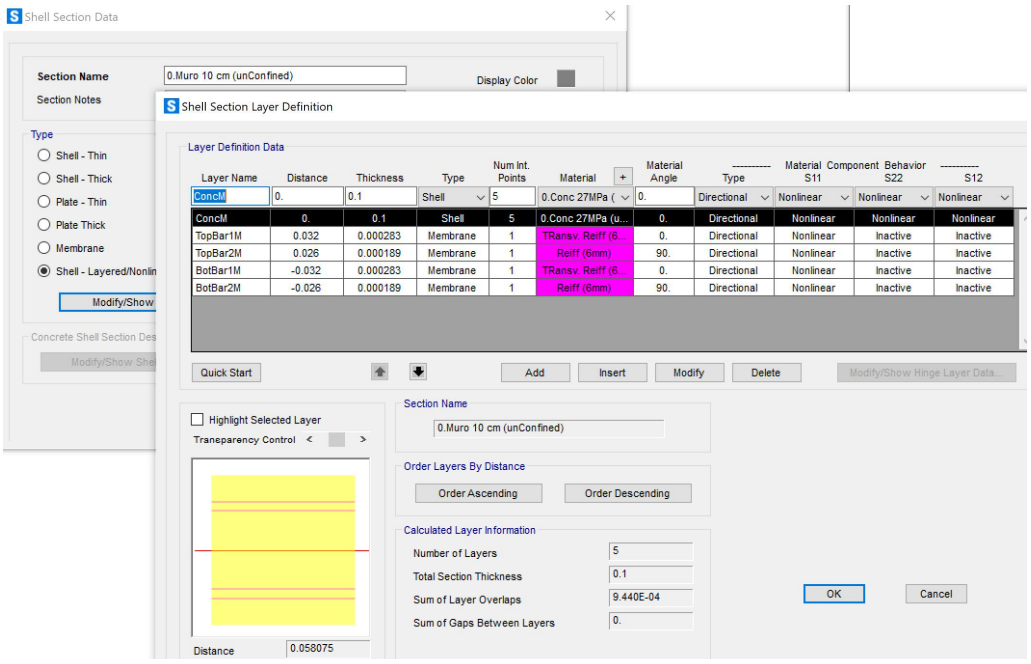

Figure 4-51 Shell layer Definition for unconfined wall section.

The layered shell formulation represents full shell behavior, combining both in-plane (membrane) actions and out-of-plane (plate bending) actions into a single formulation. However, even though the program assumes plane stress ($\sigma_{11}, \sigma_{22}, \tau_{12}$). It does not account for out-of-plane normal compressive stresses (σ_{22}) across the wall thickness. Therefore, the program is not likely to directly capture localized out-of-plane geometric instabilities, such as out-of-plane buckling or warping.

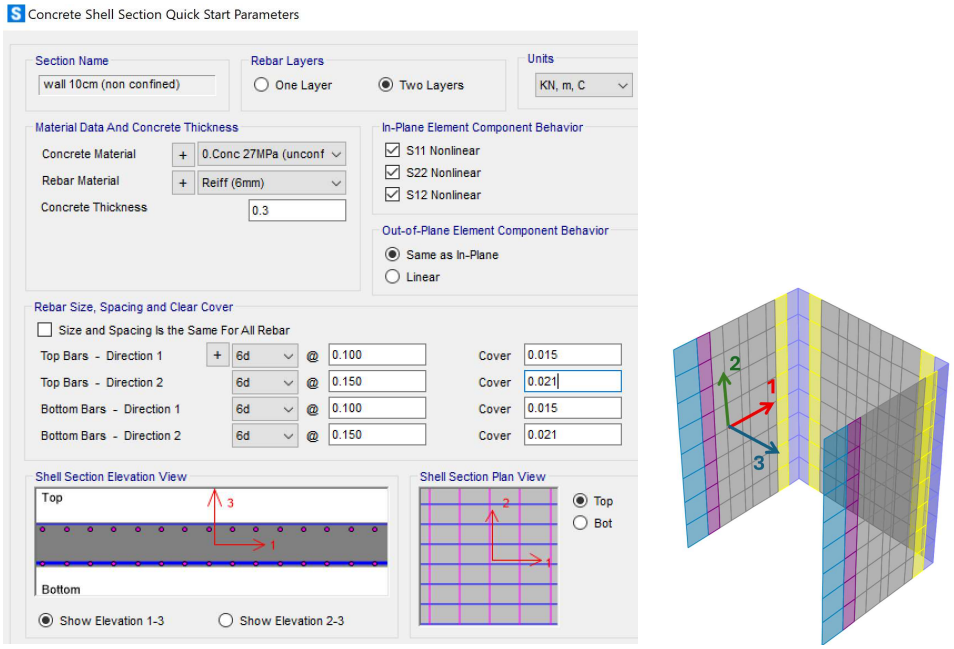

Figure 4-52 Shell layer Definition for unconfined wall section (Left: Quick Start Parameter, Right: Local axes on U-shaped wall)

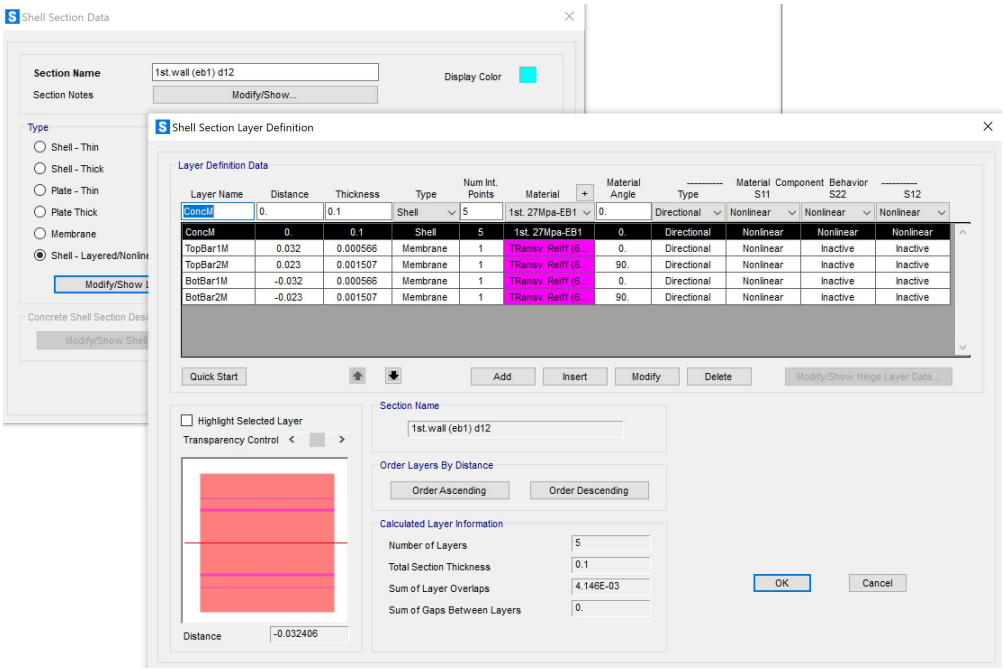

Figure 4-53 Shell layer Definition for confined boundary element EB1.

The collar was modeled using an Elastic Thin-Shell configuration to prevent concrete cracking within this element, thereby ensuring that non-linear material behavior and energy dissipation were concentrated strictly within the main U-shaped shear wall. The intermediate slabs were also modeled using this approach for consistency.

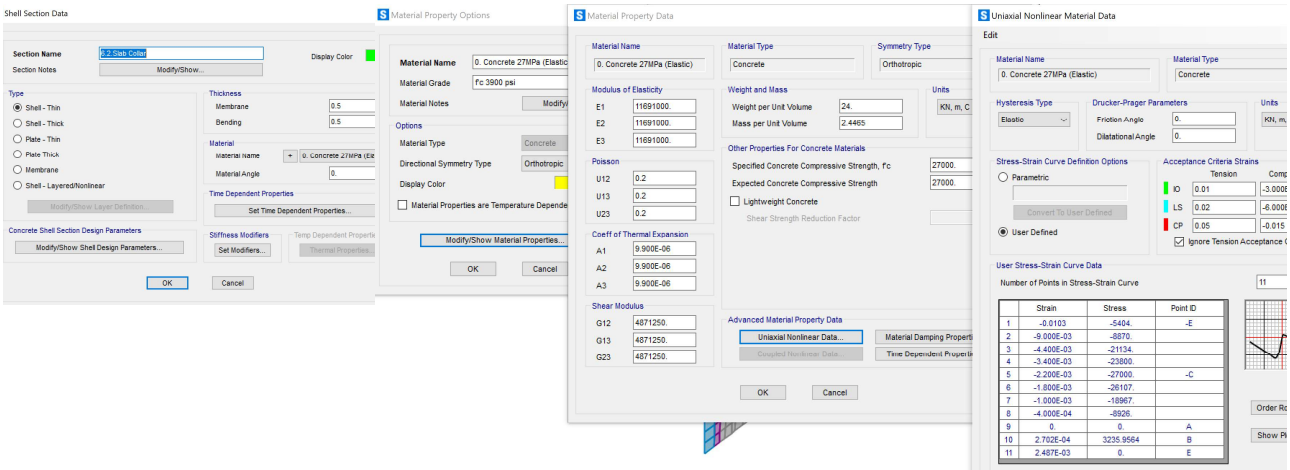

Figure 4-54 Shell Section and Material Definition for the Concrete Collar.

Above the collar element, the four loading tower blocks were modeled as solid elastic steel elements with an equivalent unit weight of 62.841 kN/m3. In contrast, the foundation block was modeled as solid elastic concrete. The foundation base was fully restrained at its bottom nodes. The calculated total vertical reaction

under self-weight and initial axial load was 372.6 kN in SAP2000, compared to 368 kN in ATENA and 361.9 kN (36.9 tonf) in the theoretical hand calculations (Table 4-3). This narrow range confirms an acceptable load estimate, accounting for minor connection hardware such as steel plates and bolts.

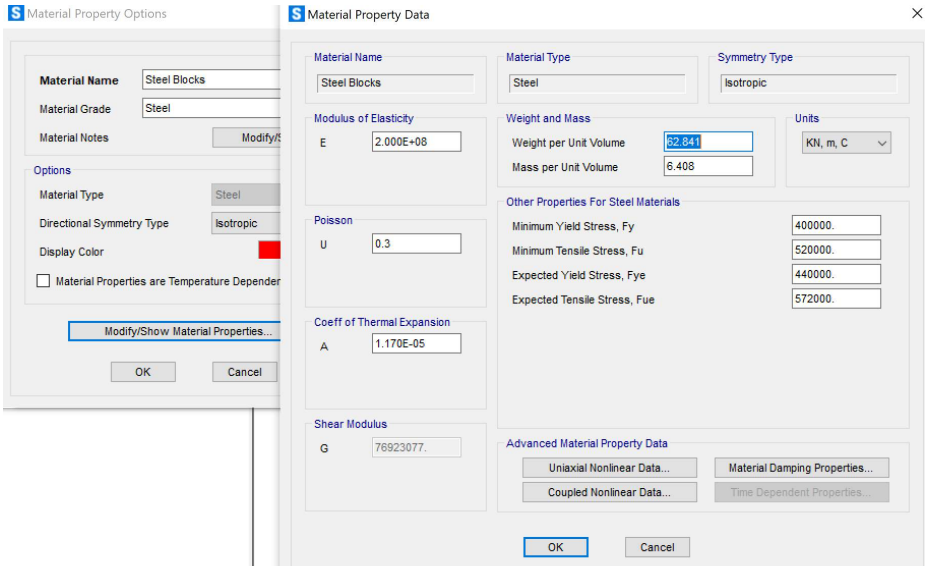

Figure 4-55 Solid Steel Blocks Material Definition.

The solid and shell elements were discretized with a characteristic mesh size of 0.10 m, matching the mesh resolution used in ATENA. Confinement effectiveness was accounted for by increasing both the peak compressive strength and ductility in the boundary elements, following the modified stress-strain relationship shown in Figure 4-39. The concrete material was defined as orthotropic non-linear with a maximum tensile strength of 3.2 MPa. Figure *4-57* to Figure *4-59* illustrate the concrete material properties assigned to the first-floor section, based on the material configuration defined in Figure 4-56.

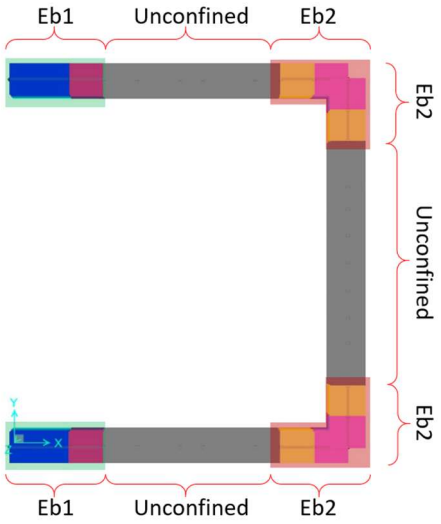

Figure 4-56 Material Discretization of Boundary Confinement Elements (Eb1, Eb2) and Unconfined Concrete for the U-Shaped Shear Wall Cross-Section.

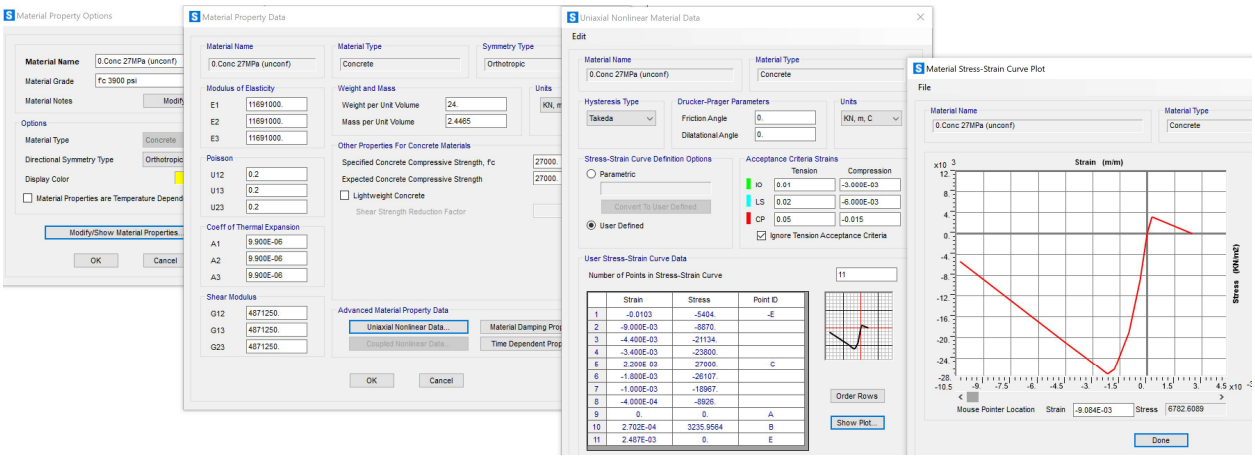

Figure 4-57 Material Definition for Unconfined Concrete

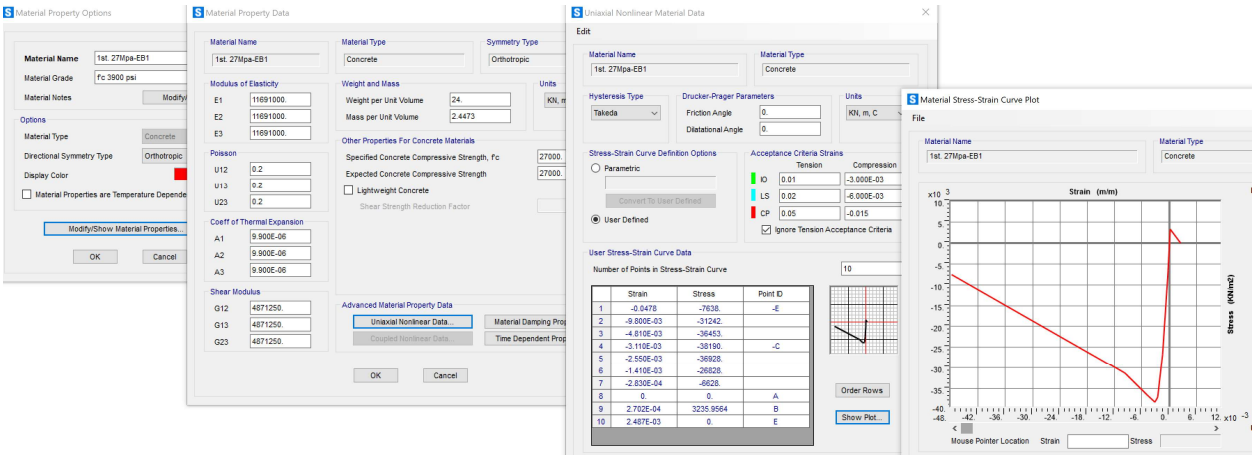

Figure 4-58 Material Definition for Confined Concrete Zone Eb1 (1st floor)

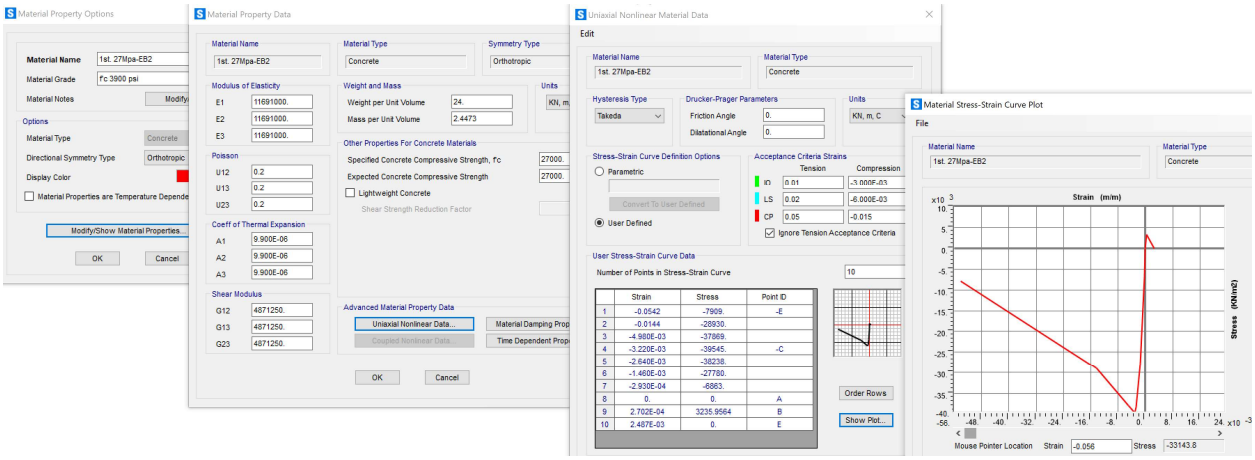

Figure 4-59 Material Definition for Confined Concrete Zone Eb2 (1st floor)

The reinforcement bars were modeled as non-linear materials using the stress-strain properties detailed in Section 4.2. Figure 4-60 illustrates the non-linear material definition for the 12mm diameter rebars, which was similarly applied to the 6mm and 8mm diameter reinforcement.

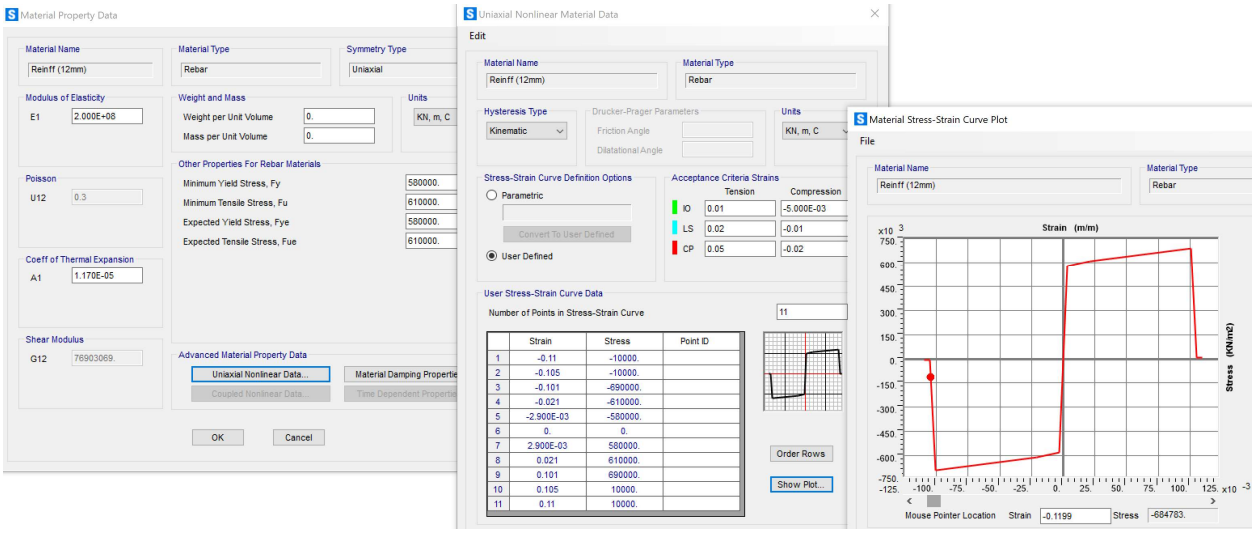

Figure 4-60 Material Definition for 12mm rebar

4.9.1 Loading Data

As previously stated, the first load case executed is the dead load case. This primary step is run nonlinearly from zero initial conditions to establish the structure's baseline stress state, incorporating geometric nonlinearity (P-Delta) to capture second-order load-deflection interactions.

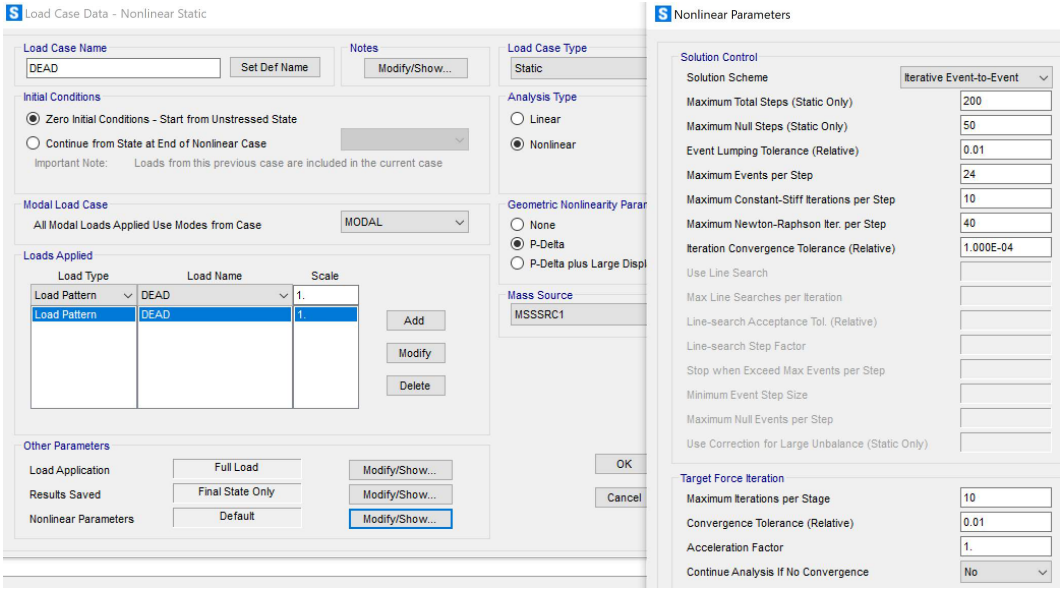

Figure 4-61 Concrete material definition - Sap2000

The dynamic seismic evaluation is conducted as a non-linear direct-integration time-history analysis, continuing directly from the end state of the nonlinear gravity load case (DEAD) to account for pre-stress

conditions. The seismic analysis is executed under a single continuous load case comprising GM1 through GM8 to capture the full effects of sequential ground motions. As illustrated in Figure 4-62, ground acceleration along the U1 and U2 axes is dynamically integrated over a duration of 247 seconds (49401-time steps at 0.005s increments) using the unconditionally stable Newmark average acceleration method (γ=0.5, β=0.2505). Energy dissipation is governed by a Rayleigh-proportional damping model anchored to 1% critical damping across key target response periods (T1=0.34s and T2=0.01s) within the structure's experimental fundamental natural period, T=0.33s. [34]

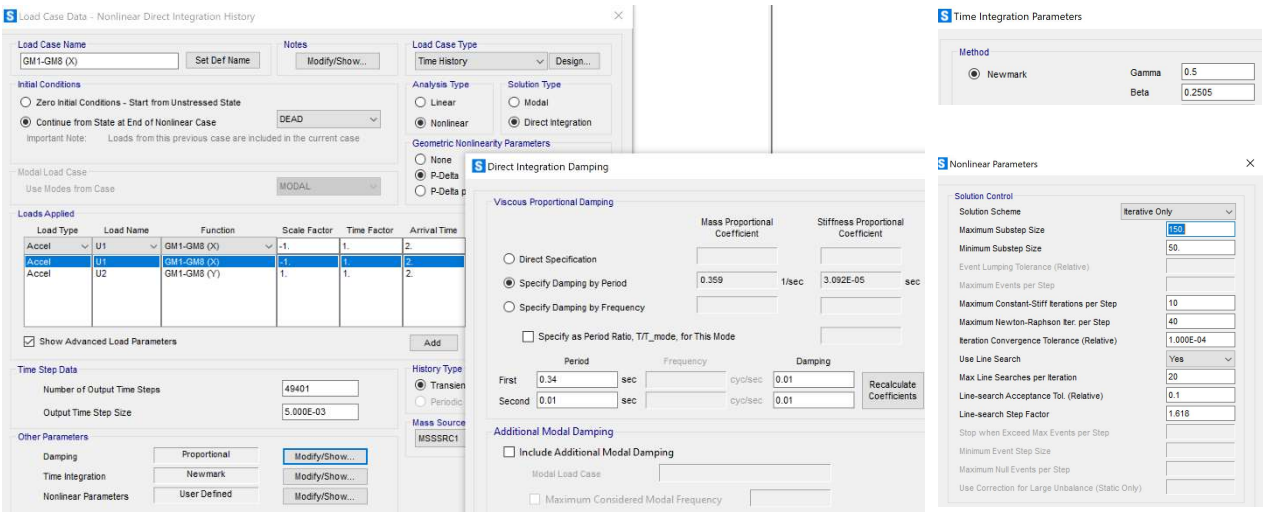

Figure 4-62 Dynamic Time History Load Case defined in Sap2000

4.9.2 Dynamic Performance

A modal analysis case was executed directly, using the mass source as the element's self-mass as defined in Figure 4-63, using the self-weight mass calculated from material densities assigned to the sections.

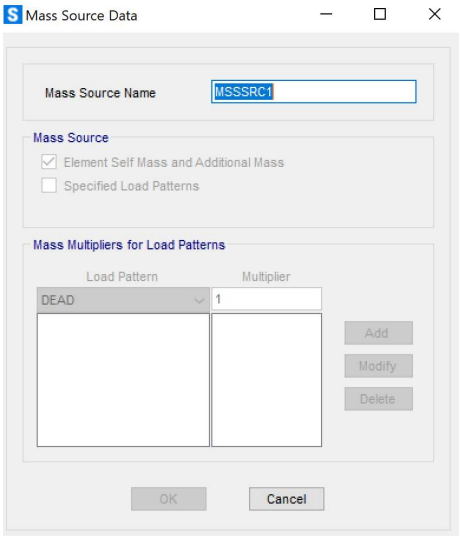

Figure 4-63 Mass Source Data

As shown in Figure 4-64, the first mode exhibits a coupled lateral-torsional shape with a fundamental period of 0.3189s. The second mode is purely translational along the axis of symmetry, with a period of 0.2755s. Finally, the third mode displays a pure torsional shape reflecting warping at the collar, with a period of 0.1234s.

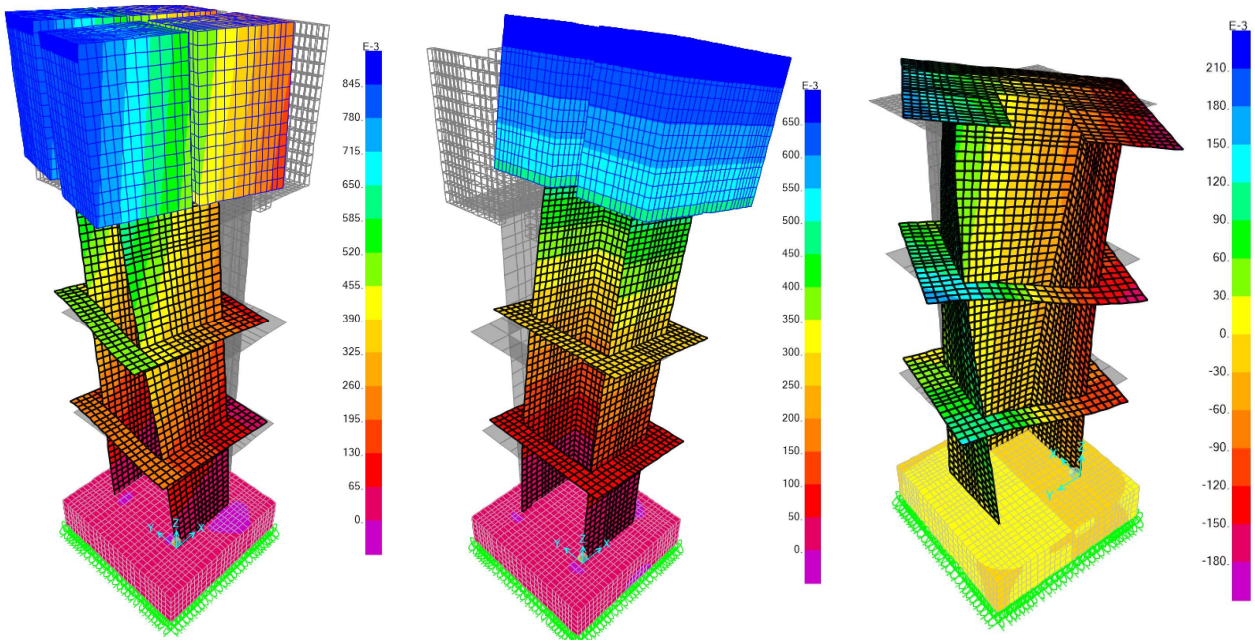

Mode 1
T=0.3198 s

Mode 2
T=0.2755 s

Mode 3
T=0.1234 s

Figure 4-64 Dynamic Mode Shapes and Natural Periods of the Structure; Mode 1: Lateral Displacement (Y-direction), Mode 2: Translational Displacement (X-direction), Mode 3: Pure Torsional/Warping Displacement (Z-direction), units in meters

The modal mass participation factors corresponding to these dynamic modes are summarized in Table 4-9. The designation 0.5E indicates that the concrete Young's modulus (E_c) was scaled by a factor of 0.5 (50%) to account for cracking and nonlinear degradation before dynamic response analysis. Mode 1 exhibits primary mass participation in the Y-direction (57.7%), acting transverse to the axis of symmetry and inducing torsional coupling due to section asymmetry. Mode 2 represents pure translation along the axis of symmetry (X = 77.9%), while Mode 3 is a higher-order torsional/transverse mode with dominant Y-direction participation (20.7%). The cumulative mass participation of Modes 1 and 3 accounts for 78.4% (57.7%+20.7%) of the total mass in the Y-direction, indicating that these two primary modes capture the predominant transverse dynamic response of the structure and govern its lateral-torsional behavior and upper-level torsional warping.

		Mode 1	**Mode 2**	**Mode 3**
0.5E$_c$	**Period (s)**	**0.3198**	**0.2755**	**0.1234**
	Mass Participation	X= 1.9785E-06 Y= 0.577 Rz= 0.2318	X= 0.779 Y= 1.648E-06 Rz= 2.639E-07	X= 2.266E-08 Y= 0.207 Rz= 0.5609

Table 4-9 Mass participation of each Mode

Figure 4-65 presents a comparative time-history evaluation of the specimen's dynamic response from ground motions GM1 through GM3, plotting experimental measurements alongside numerical predictions from ATENA (red) and SAP2000 (blue). Across both West-East (W-E) and North-South (N-S) displacement components, SAP2000 demonstrates strong in-phase agreement with the experimental record, similar to ATENA. However, SAP2000 consistently underestimates peak dynamic displacement demands due to higher numerical stiffness. Following the strong-motion phase of GM3, both numerical modeling methods capture a permanent residual displacement offset, though SAP2000 predicts a slightly larger residual offset (approximately 11 mm) than the experimental baseline.

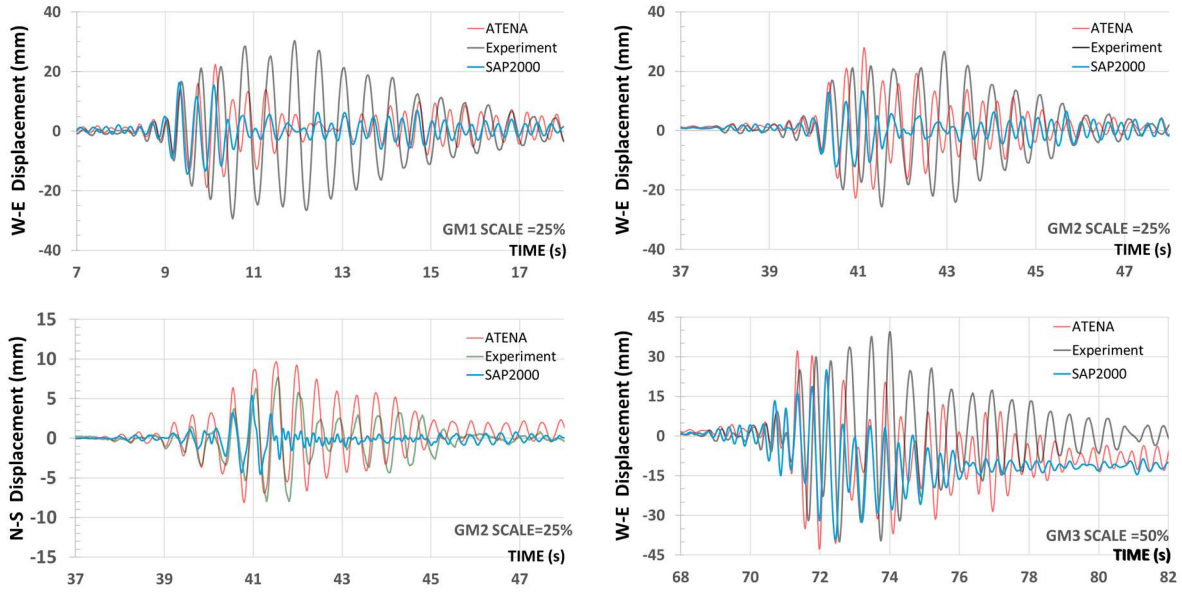

Figure 4-65 Comparison of experimental W-E and N-S displacement time-histories at the collar mid-height (black line in the W-E direction and Green line in the North-South direction), with ATENA finite element model predictions (red line) and SAP2000 model predictions (blue line) across ground motions GM1 to GM3

Additional parametric configurations evaluating variations in the concrete modulus of elasticity (E_c) are summarized in Table 4-10. The first row represents the baseline model ($0.5E_c$), discussed previously, which serves as the benchmark. In the second row, the 50% reduction factor was omitted, resulting in a stiffer structure that reduced the fundamental period (T_1) from 0.3198s to 0.3071s while increasing the Y-direction mass participation in Mode 1 to 59.2%. In the third row ($0.5E_c$*), the stiffness reduction factor was applied exclusively to the wall sections, leaving the rigid collar and intermediate slabs at full E_c. This configuration yielded results nearly identical to the full (E_c) model ($T_1 = 0.3073s$). The period calculations suggest that the top collar most strongly affects the period reduction. So, making the top collar stiffer apparently reduces warping and thereby affects the torsional mode; hence, the first and third mode periods, which have torsional components, are reduced more evidently than the second mode.

		Mode 1	Mode 2	Mode 3
$0.5E_c$	**Period (s)**	**0.3198**	**0.2755**	**0.1234**
	Mass Participation	X= 1.9785E-06 Y= 0.577 Rz= 0.2318	X= 0.779 Y= 1.648E-06 Rz= 2.769E-07	X= 2.266E-08 Y= 0.207 Rz= 0.5609
E_c	**Period (s)**	**0.3071**	**0.2754**	**0.1218**
	Mass Participation	X= 2.925E-06 Y= 0.592 Rz=0.2174	X= 0.779 Y= 2.414E-06 Rz= 4.449E-07	X= 1.843E-08 Y= 0.193 Rz= 0.5767
$0.5E_c$* (walls only)	**Period (s)**	**0.3073**	**0.2754**	**0.1218**
	Mass Participation	X= 2.907E-06 Y= 0.592 Rz= 0.2177	X= 0.779 Y= 2.399E-06 Rz= 4.419E-07	X= 1.844E-08 Y= 0.193 Rz= 0.5765
$0.5E_c$ (1*st* floor)**	**Period (s)**	**0.3072**	**0.2754**	**0.1218**
	Mass Participation	X= 2.925E-06 Y= 0.592	X= 0.779 Y= 2.414E-06	X= 1.843E-08 Y= 0.193

* Walls only

** 0.5E only on the first floor

Table 4-10 Parametric Study of Concrete Elastic Modulus Modifications

Plotting the mode shape profiles along the height for all four corner nodes (A, B, C, and D) of the U-shaped cross section clearly visualizes its deformation behavior (Figure 4-67 through Figure 4-69). These profiles illustrate the normalized displacement across each node.

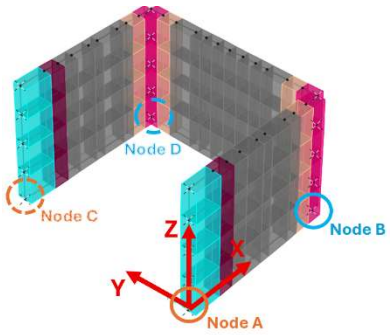

Figure 4-66 Nomenclature of the four corner nodes of the C-shaped section wall

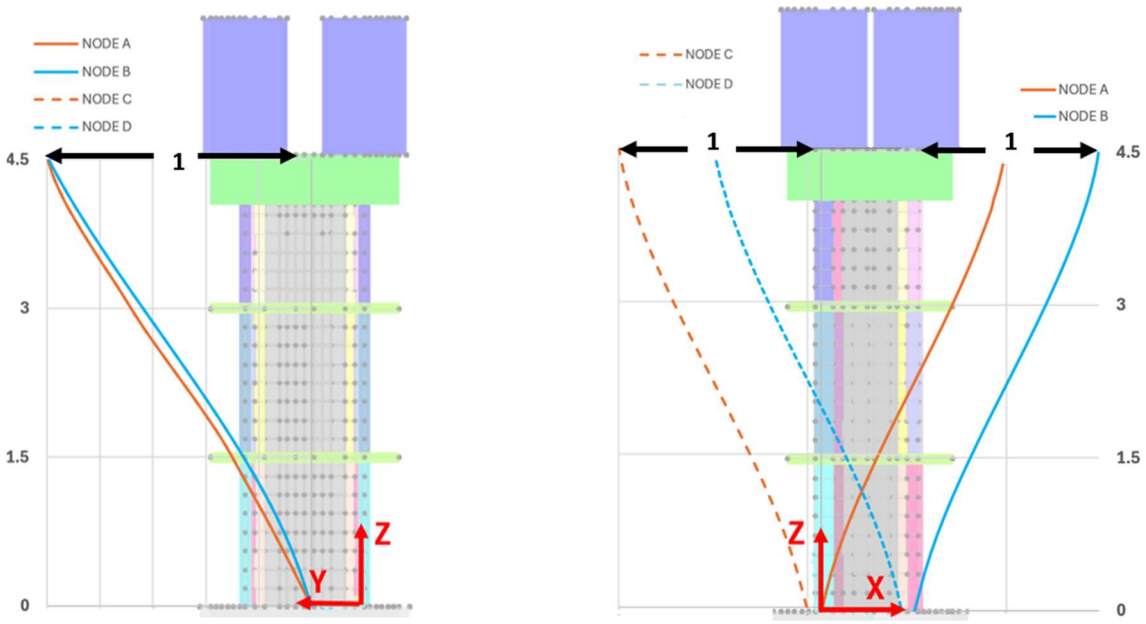

Figure 4-67 Deformation Shape Mode 1 (Left: Lateral deformation, Right: Transverse deformation)

In the first mode, Figure 4-67 shows all four tracking points deform uniformly in the same direction along the Y-axis. However, due to cross-sectional asymmetry, this lateral movement induces a torsional response: nodes on the right flange deflect in the positive X-direction, while those on the left flange deflect in the opposite direction.

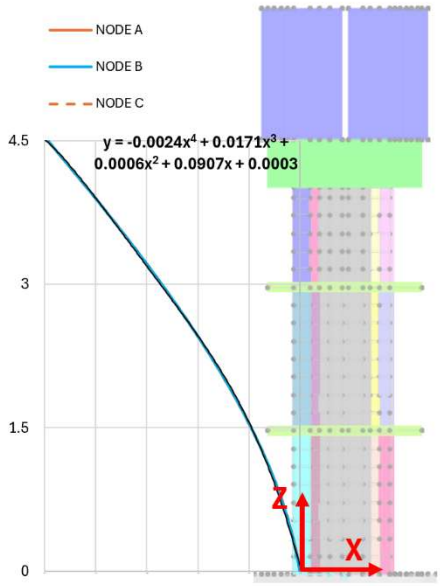

Figure 4-68 Deformation Shape Mode 2 - Transverse deformation

In the second mode, Figure 4-68 shows all four tracking points deform in the same direction along the axis of symmetry (negative X-axis).

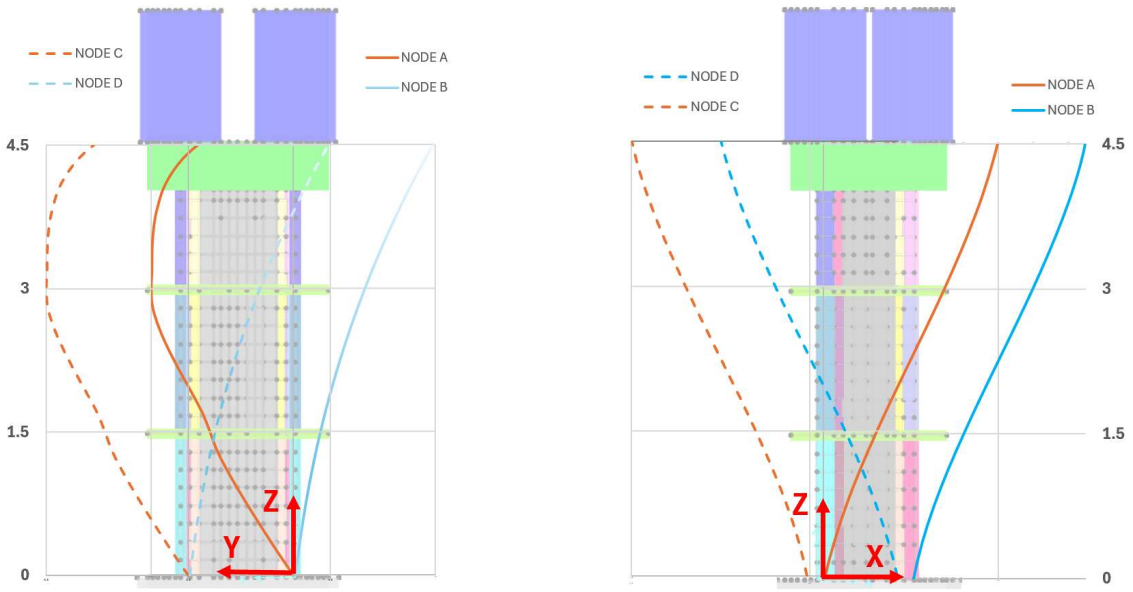

Figure 4-69 Deformation Shape Mode 3 (Left: Lateral deformation, Right: Transverse deformation)

In the third mode (Figure 4-69), a pure torsional response dominates the behavior. Along the Y-axis, the flange tips (Nodes A and C) displace in the positive direction, peaking near the second intermediate slab level, whereas the web-flange intersection nodes (Nodes B and D) deform linearly toward the negative Y-axis. In the X-direction, the nodes on the right flange deflect in the positive direction, while those on the left flange displace symmetrically in the opposite direction.

Considering the second mode of vibration, where the structure is displaced along the axis of symmetry, creating a flexural response with a period (T) of 0.2755s and a mass participation factor (α) of 0.779; the response spectrum can be used to determine the acceleration and subsequently calculate the maximum displacement.

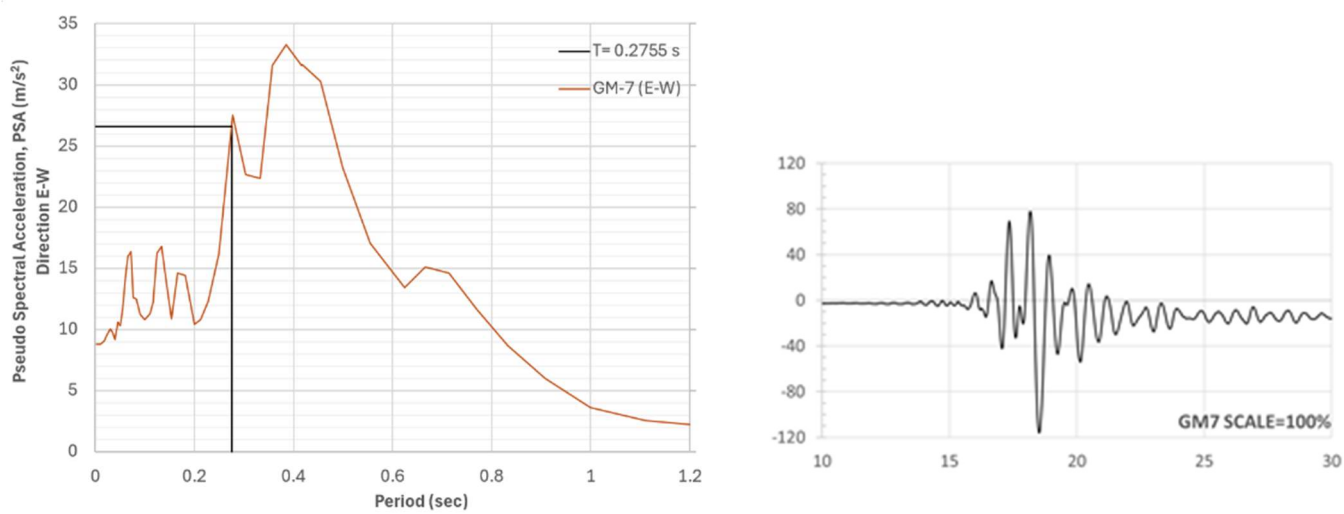

Figure 4-70 Pseudo-spectral acceleration of 3% damped from the 2016 Central Italy earthquake, from GM 7(Left), Experimental time-histories for GM 7 for W-E Displacement (Right).

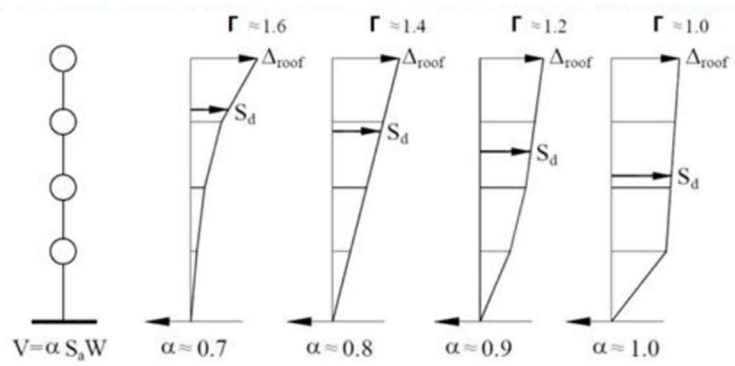

Figure 4-71 Modal participation factors and modal mass coefficients (ATC-40, 1996)

$$S_a = 26.6\ m/s^2$$

$$S_d = S_a\ (T/2\pi)^2$$

$$S_d = 26.6\ m/s^2 (0.2755\ s/2\pi)^2$$

$$S_d = 0.0511\ m = 51.14\ mm$$

$$\alpha = 0.779$$

$$\Gamma = 1.44$$

$$S_d = 1.44\ (51.14\ mm) = 73.64\ mm$$

Considering the second mode profile as an intermediate between a linear profile and a flexural cantilever shear wall (as shown in Figure 4-68), and given that SAP2000 provides an effective mass participation factor of $\alpha = 0.779$ interpolating the modal participation factor (Γ) gives us $\Gamma = 1.44$. To scale the displacement response from a single-degree-of-freedom (SDOF) system to a multi-degree-of-freedom (MDOF) system, the displacement obtained from the pseudo-spectral response is 51.14mm, multiplying it by Γ gives a displacement of 73.64mm at the collar. However, the maximum experimental displacement observed for GM7 is 116 mm (Figure 4-70). Therefore, an additional 42.4 mm must be considered to account for inelastic displacement and geometric nonlinearity.

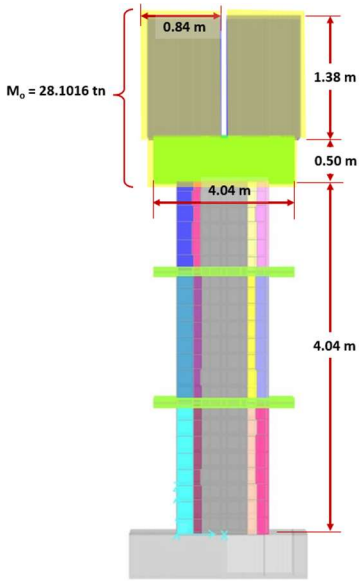

Figure 4-72 Lateral View of the U-shaped Wall

The distributed mass throughout the height of the wall is:

$$\overline{m} = (0.32\ m^2)\left(24\frac{kN}{m^3}\right) = 7.68\ kN/m$$

$$\overline{m} = 0.783\ tn/m$$

The total mass of the structure without considering the footing is:

$$M_{total} = 28.1016\ tn + (0.783\frac{tn}{m})(4.04\ m\ )$$

$$M_{total} = 31.264\ tn$$

Assuming Y(x) represents the transverse displacement along the wall height X, the mode shape is defined as (from Figure 4-68):

$$\Psi(x) = -0.0024\ x^4 + 0.0171\ x^3 + 0.0006\ x^2 + 0.0907\ x + 0.0003 \qquad \textit{Eq. 4-1}$$

The equivalent mass (m*) of the Equivalent Single-Degree-of-Freedom (ESDOF) system is given by:

$$m^* = \int_0^L m(x) \cdot [\Psi(x)]^2 \, dx + \sum_i M_i \cdot \left(\Psi_i(x)\right)^2 + \sum_i I_i \cdot (\Psi_i{}')^2 \qquad \textit{Eq. 4-2}$$

$$m(x) \int_0^{4.54} [\Psi(x)]^2 \, dx = m(x)(1.1775\, m) = (0.783\, tn/m)(1.1775\, m) = \mathbf{0.922\ tn}$$

$$\sum_i M_i \cdot \left(\Psi_i(x)\right)^2 = (28.1016\, tn)(1)^2 = \mathbf{28.1016\ tn}$$

$$\sum_i I_i \cdot (\Psi_i{}')^2 = \sum_i I_i \cdot (-0.0096\, x^3 + 0.0513\, x^2 + 0.0012\, x + 0.0907)^2$$

$$\Psi_i'(x = 4.54) = 0.255\, rad/m$$

For the polar moment of inertia of the 4-block system and the top collar, the geometry is simplified into an equivalent rectangular shape:

$$h = \frac{[(1{,}62)(0.5) = 2(1.38)(0.84)]}{1.62} = 1.9311m$$

With a polar moment of inertia (J_o) of:

$$J_o = M_o \cdot \frac{a^2 + b^2}{12} \qquad \textit{Eq. 4-3}$$

$$J_o = M_o \cdot \frac{1.62^2 + 1.9311^2}{12} = (28.1016tn)(0.53\, m^2) = 14.894\, tn \cdot m^2$$

$$\sum_i I_i \cdot (\Psi_i{}')^2 = (14.894\, tn \cdot m^2)\left(0.255 \frac{rad}{m}\right)^2 = \mathbf{0.9685tn}$$

Finally, the equivalent mass is computed as:

$$m^* = 0.922 + 28.1016 + 0.9685$$

$$\boldsymbol{m^* = 29.99\ tn}$$

The excitation factor ($\mathcal{L}^*$) is calculated as:

$$\mathcal{L}^* = \int_0^L m(x) \cdot \Psi(x)\, dx + \sum_i M_i \cdot \Psi_i(x) \qquad \textit{Eq. 4-4}$$

$$m(x) \int_0^{4.54} \Psi(x) = m(x)(1.845\, m) = (0.783\, tn/m)(1.845\, m) = \mathbf{1.44\ tn}$$

$$\mathcal{L}^* = 1.44tn + 28.1016\, tn$$

$$\boldsymbol{\mathcal{L}^* = 29.5416\ tn}$$

The mass participation factor (α^*) is

$$\alpha^* = \frac{(\mathcal{L}^*)^2}{(m^*)(M_{total})} \qquad \textit{Eq. 4-5}$$

$$\alpha^* = \frac{(29.5416)^2}{(29.99)(31.264)}$$

$$\boldsymbol{\alpha^* = 0.93}$$

The mode participation factor (Γ^*) is:

$$\Gamma^* = \frac{\mathcal{L}^*}{\mathrm{m}^*} \qquad \textit{Eq. 4-6}$$

$$\Gamma^* = \frac{29.5416}{29.99}$$

$$\boldsymbol{\Gamma^* = 0.985}$$

The structure stiffness is defined as:

$$k^* = \int_0^L EI(x) \cdot [\Psi\,''(x)]^2\ dx + \sum_i K_i \cdot \left(\Psi_i(x)\right)^2 \qquad \textit{Eq. 4-7}$$

$$k^* = \int_0^L EI(x) \cdot [\Psi\,''(x)]^2 = EI \cdot \int_0^L [-0.0288\,x^2 + 0.1026\,x + 0.0012\,]^2$$

$$k^* = \int_0^L EI(x) \cdot [\Psi\,''(x)]^2 = \left(0.5 \cdot 4500\sqrt{27} \cdot 1000\frac{kN}{m^2}\right)(0{,}0357m^4) \cdot 0.02103\frac{1}{m^3}$$

$$\boldsymbol{k^* = 8777.5\frac{kN}{m}}$$

The natural period (T) of the system is:

$$\mathrm{T} = 2\pi\sqrt{\frac{\mathrm{m}^*}{k^*}} = 2\pi\sqrt{\frac{29.99\ tn}{8777.5\frac{kN}{m}}} \qquad \textit{Eq. 4-8}$$

$$\boldsymbol{\mathrm{T} = 0.367\ s}$$

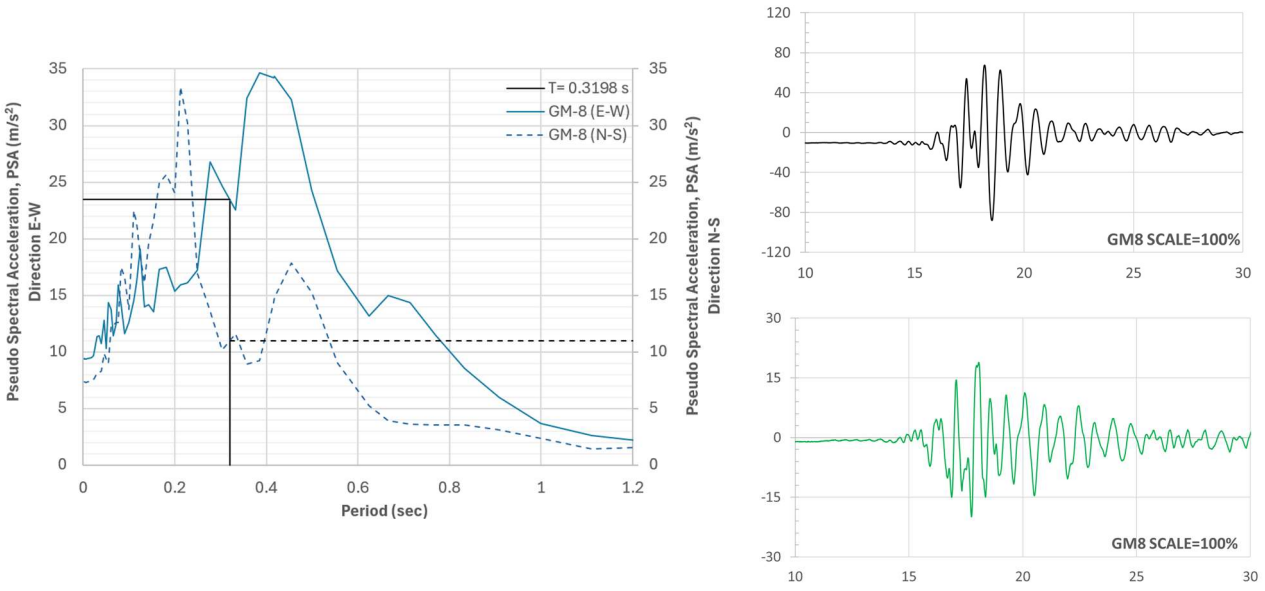

Figure 4-73 Pseudo-spectral acceleration of 3% damped from the 2016 Central Italy earthquake, from GM 8(Left), Experimental time-histories for GM 8 for W-E Displacement in mm (Top Right), Experimental time-histories for GM 8 for N-S Displacement in mm (Bottom Right).

Calculating the displacement based on the dynamic spectrum multiplied by the mode participation factor generates a total displacement of $50.373\,mm$. Compared with the experimental maximum displacement observed for GM7 (116 mm), the analytical ESDOF approach underestimates the actual structural response by a factor of 2.3. For GM8, the maximum experimental displacement is 88 mm in the East-West direction and 19.9 mm in the North-South direction (Figure 4-73). The spectrum depicts a displacement of 60.8mm in the East-West direction, and 28.44mm in the North-South direction.

For the fundamental mode, the SAP2000 linear mode profile (Figure 4-67) yields a mass participation factor of $\alpha = 0.577$ in the East-West direction. Figure 4-71 produces an equivalent mass participation factor of $\alpha = 0.8$ and a modal participation factor (Γ) of $\Gamma = 1.4$ for linear profiles. The resulting displacement calculated per ATC-40 guidelines is $85.12\,mm$, demonstrating strong agreement with the experimental data with an error margin of just 3.3%.

Chapter 5: Push-over Analysis & Parametric Investigation

Having successfully validated the analytical model against benchmark data, this chapter evaluates the performance of tall, U-shaped reinforced concrete shear walls through a comprehensive pushover analysis. The study addresses critical design gaps by investigating complex three-dimensional behaviors, such as torsion, out-of-plane buckling, and high axial loads, to ensure ductile performance and prevent premature failure.

Nonlinear pushover analysis provides a comprehensive view of the wall's post-peak behavior, capturing structural degradation up to ultimate failure and identifying residual strength. In this study, the pushover analysis was conducted using a displacement-control method. This entailed incrementally applying a displacement at a control node at mid-height of the collar along the axis of symmetry, displacing the wall parallel to its flanges while monitoring the corresponding lateral load required at each step.

Because the wall cross-section is asymmetric, the behavior was evaluated in three distinct directions. The first two loading scenarios are parallel to the flanges: one induces compression in the flanges, while the opposite direction induces tension. The final direction evaluated is perpendicular to the axis of symmetry. Because of the asymmetric geometry, this lateral loading induces torsional effects, which Section 5.2.4 analyzes in detail.

Initially, the study evaluates pushover behavior using the experimental setup described in Chapter 4.1. The objective is then to conduct a parametric sensitivity analysis with respect to five key parameters: the first concerns the Axial Load Ratio (Section 5.3.1), Longitudinal Reinforcement Ratio (Section 5.3.2), Transversal Reinforcement Ratio (Section 5.3.3), Torsion (Section 5.3.4) and the possible presence of lap splicing in longitudinal reinforcement (Section 5.3.5) Comparing these parameters captures the complex interaction between flexure, shear, and torsion inherent in U-shaped cross-sections.

5.1 Experimental Setup - ATENA

A nonlinear pushover analysis was conducted using the finite element software (ATENA) under the experimental boundary conditions to capture detailed structural behavior up to collapse. This analysis evaluates key performance parameters, including initial stiffness, ductility, ultimate strength, drift capacity, and governing failure modes, mapping the structure's performance levels as a function of lateral displacement.

Figure 5-1 illustrates the resulting load-displacement curves for lateral loading parallel to the wall flanges. Negative displacement corresponds to loading in the East direction, which places the wall flanges in compression; this direction is designated as FC (Flanges in Compression). Conversely, positive displacement places the web in compression and the flanges in tension, designated as FT (Flanges in Tension). Each direction

features two analytical curves: a solid line representing the material's nonlinear response alone, and a dotted line that incorporates geometric nonlinearity in the reinforcement to track true stress-strain behavior.

Due to this geometric nonlinearity, the model captures a more realistic, stable redistribution of internal stresses. Consequently, the abrupt capacity loss observed in the blue solid line at a drift ratio of 4.88% is delayed in the geometrically nonlinear model, which sustains loading up to a drift capacity of 6.4% (2.FT).

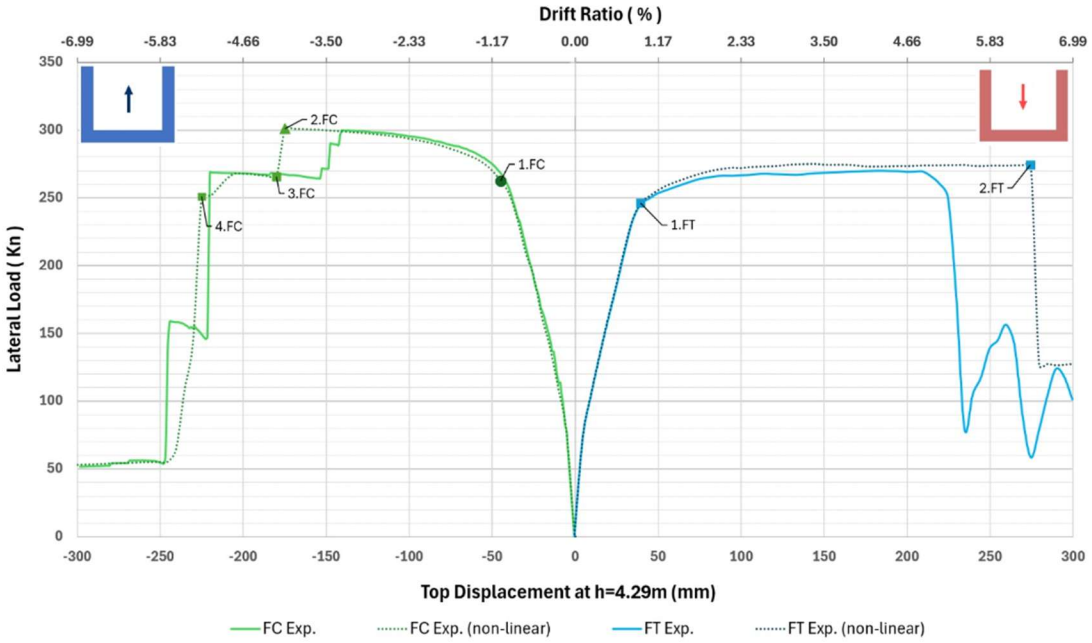

Figure 5-1 Pushover - Experiment Setup

The figure surprisingly shows symmetric elastic behavior up to a displacement of 40 mm (0.93% drift), after which asymmetric behavior becomes apparent. Because of this asymmetry, when the flanges are in compression, the maximum force capacity (300 kN) is reached sooner, at marker 2.FC (corresponding to a 4.1% drift). Beyond this, the curve descends sharply with some hardening along the way.

Conversely, when the loading direction places the flanges in tension (FT), the wall demonstrates a well-defined elastic-plastic yield plateau. In this orientation, the structure maintains its lateral load resistance while slowly climbing to a peak capacity of 275 kN, approximately 8% lower than the peak capacity observed in the FC direction. This plateau sustains its strength across a broad range of deformation demand, from 0.86% drift to a critical drift ratio of 6.4%, after which the strength plummets sharply to its residual value.

The reinforcement layout heavily governs this directional performance profile. The cross-section features concentrated boundary reinforcement consisting of 12mm bars at the flange tips and web-flange intersections, achieving a localized reinforcement ratio of approximately 2.6%. In contrast, the web has distributed reinforcement comprising 6 mm and 8mm bars.

This layout explains the progressive failure sequence: when the web is subjected to tension, the smaller 6 mm bars are expected to fracture first due to their limited cross-sectional area. The resulting incremental loss

of strength forces an internal stress redistribution to the boundary elements of 12mm bars at the corners. Furthermore, because the wall components have a low thickness-to-width ratio, out-of-plane displacements indicate that flange buckling is an active failure mode, though it is typically more prominent under high axial load ratios.

Figure 5-2 shows the lateral displacement profiles of the structure across key response stages. At the onset of yielding (marked by points 1.FT and 1.FC), the structure exhibits an approximately elastic, characteristic flexural deformation profile (indicated by the green lines). As demand increases into the inelastic range (points 2.FT, 3.FC, and 4.FC), the profiles transition to reflect a distinct nonlinear structural response.

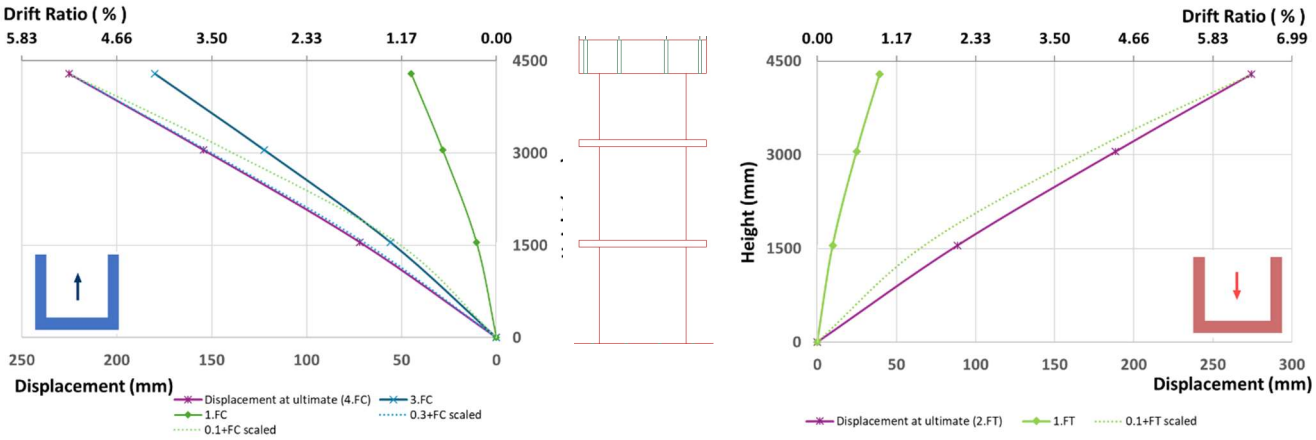

Figure 5-2 Lateral displacement profiles

A comparison between the scaled elastic mode shapes (dotted lines) and the ultimate nonlinear profiles reveals a notable shift in structural kinematics. Once significant material nonlinearity and localized damage initiate, the displacement profile deviates from its initial higher-order elastic curvature and progresses toward a more linear distribution. This shift suggests that plastic deformation is localizing (e.g., at the base plastic hinge), causing the upper portions of the wall to rotate and displace rigidly.

Loading East direction - Flanges in compression (FC)

To evaluate the localized structural response, detailed internal measurements were recorded across critical regions. These include longitudinal reinforcement strains, principal strains in concrete, crack widths, rebar slip, and out-of-plane displacements.

Reinforcement strains were monitored to track the material's inelastic performance, identifying the exact longitudinal progression of rebar yielding and eventual tensile fracture. Per the material properties detailed in Chapter 4.2, the ultimate fracture strain limit for the reinforcement is established as approximately 0.10. Concurrently, tracking the concrete principal compressive strains pinpoints the onset of crushing, which typically occurs at a limit of 0.0035 for unconfined concrete.

It is critical to highlight that because the flange tips and the web-to-flange corners of the U-shaped cross-section are heavily confined, this core confinement significantly enhances both the compressive strength and the ultimate strain capacity (ductility) of the concrete within these zones (see Chapter 4.6.11 Compression Curve (Confined Sections)).

To characterize the governing failure mechanisms, these localized strain profiles were analyzed at key behavioral markers, including sudden capacity drops and ultimate drift thresholds. For the loading direction inducing flexural flange compression (FC), the following markers were investigated:

- Marker 2.FC: Represents the initiation of primary failure, where the structure experiences an initial 12% loss in lateral load capacity.
- Marker 3.FC: Marks the termination of the sharp capacity drop and the onset of a temporary post-peak hardening plateau.
- Marker 4.FC: Identifies the ultimate drift capacity limit state, signifying the definitive structural failure of the wall.

Table 5-1 provides a detailed evaluation of localized internal stresses and strains, clarifying the structural mechanisms governing the response at each critical behavioral marker. Under the lateral pushover demand, the finite element model develops a maximum crack width of 18 mm (at Marker 4.FC) within the web elements near the foundation base. The overall cracks reveal distinct diagonal crack propagation. This behavior correlates closely with the maximum principal tensile strains, which map the formation of a diagonal compression strut extending from the flange base into the web. This strut forms at an angle of approximately 30° (as illustrated by the Maximum Principal Plastic Strain in Table 5-1) and extends to a height of 0.62 m in the structural web above the base. This can also be confirmed by the principal plastic strain (tension) distributions. Additionally, two distinct zones of concentrated flexural damage are observed along the height of the web's wall: one localized near the base at 0.15 m, and a secondary zone at 0.62m.

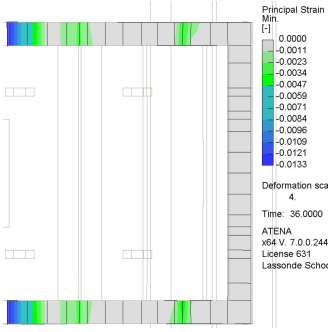

Figure 5-3 Principal Strain (compression) at 2.FC marker at a 0.5m height

Notably, by marker 2.FC, the principal compressive strains have already exceeded the unconfined concrete crushing limit (0.0035) shown in Figure 5-3 within the first story up to a height of 0.5m, indicating that the concrete cover has spalled.

Significant strain concentrations occur at the boundary elements within the flexural compression zones of the flanges. This concentration is particularly evident within the confined zones of the first two stories, highlighting severe damage localization in the plastic hinge region.

	2.FC	3.FC	4.FC
Crack width (m)	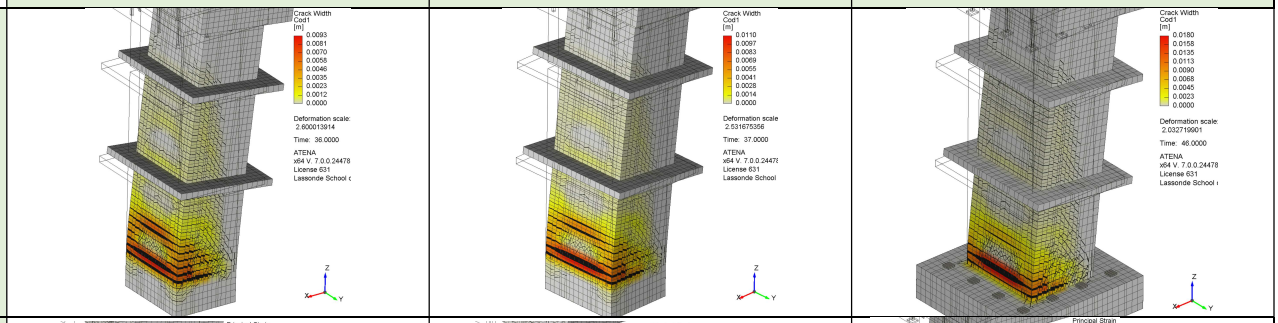		
Principal Strain (Max)	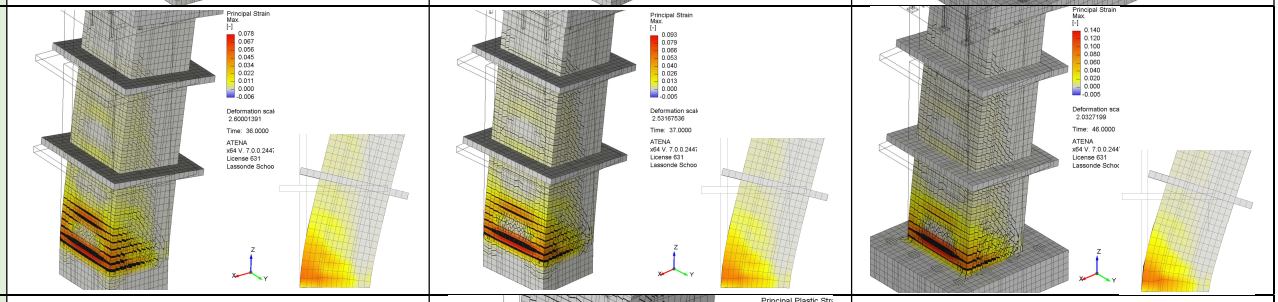		
Principal Plastic Strain (Max)	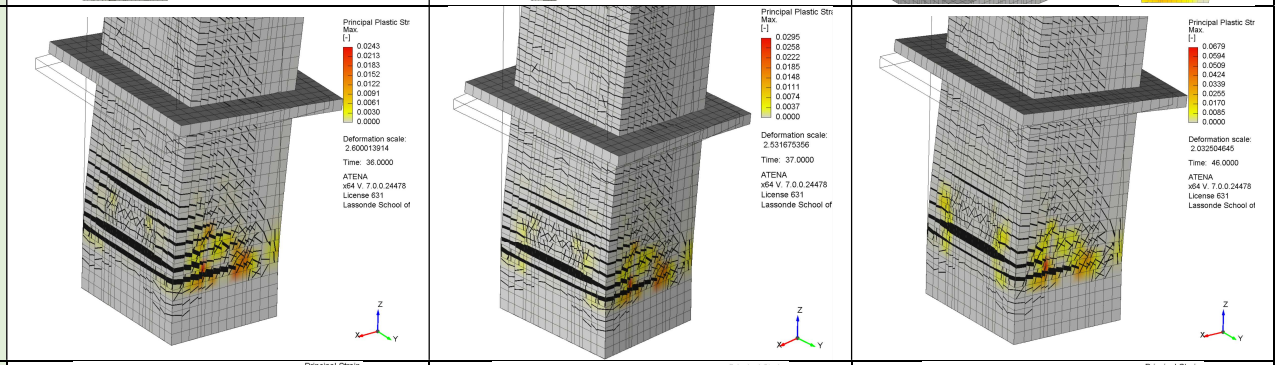		
Principal Strain (Min)	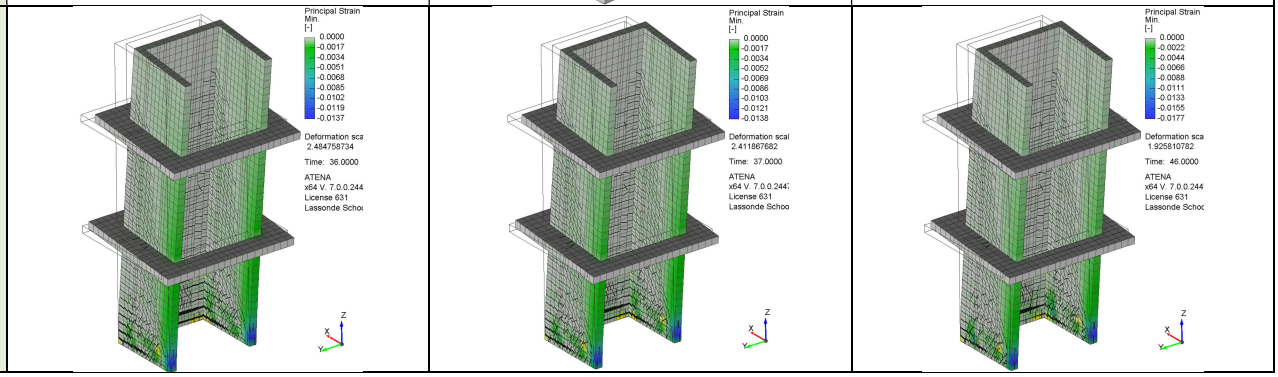		

Table 5-1 Numerical response parameters and damage indicators for the wall under Flanges in Compression (FC) loading

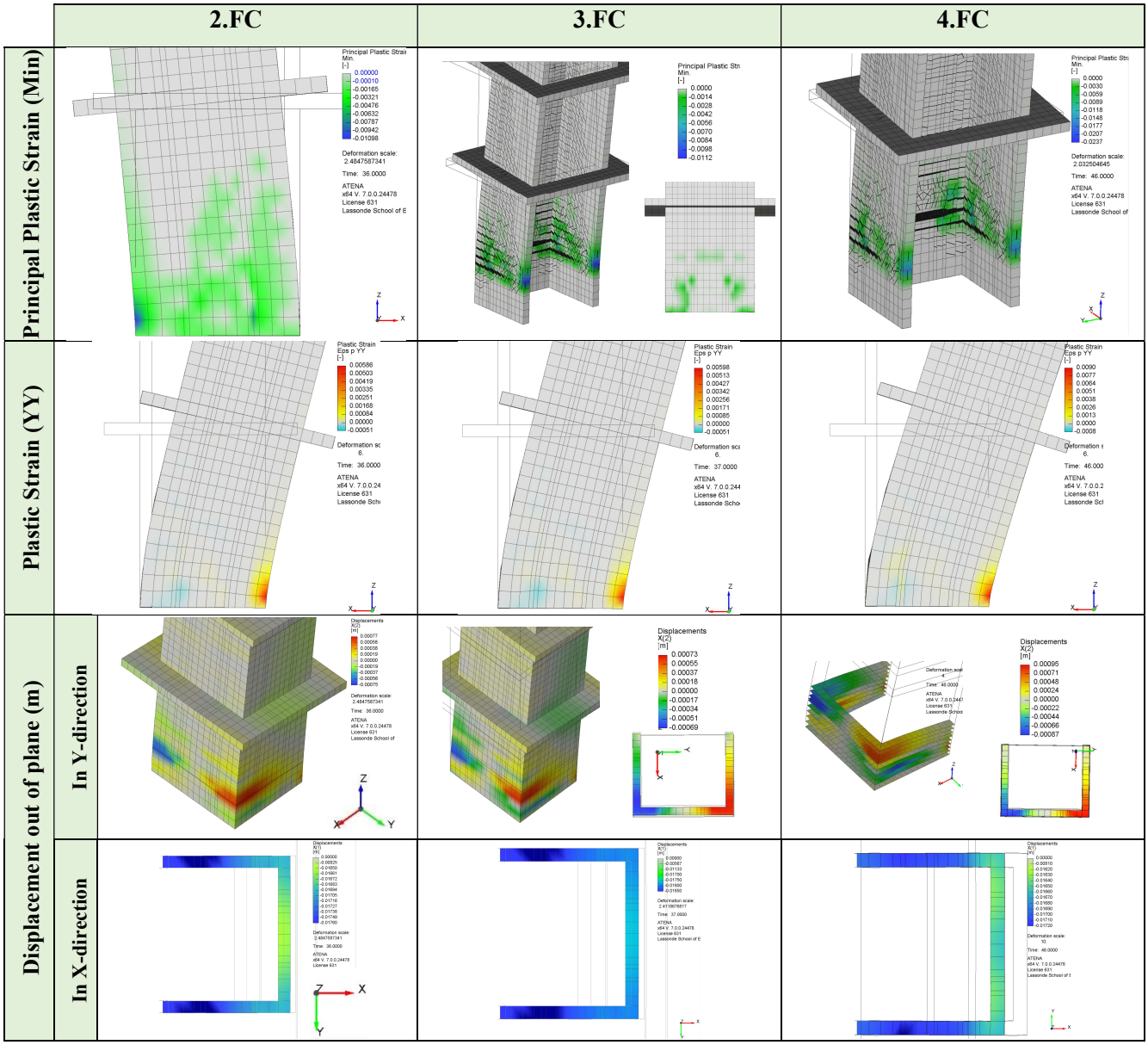

Table 5-1 Numerical response parameters and damage indicators for the wall under Flanges in Compression (FC) loading (Continued)

A critical failure mechanism frequently observed in this category of cross-sectional profiles is global or localized flange buckling. In this study, flange buckling susceptibility was evaluated by monitoring out-of-plane displacements; however, the numerical results show no evidence of physical out-of-plane flange buckling. Minor out-of-plane deformations (in the Y-direction) are isolated near the corner regions. Within the lowest 45mm of the wall height, these displacements initially project inward before shifting direction outward. Nevertheless, the magnitude of these localized out-of-plane movements remains below 1mm, so they are structurally negligible. Regarding the web, out-of-plane displacements (in the X-direction) exhibit a relatively uniform profile across the element, though the magnitudes are slightly elevated at the web-to-flange corners compared to the mid-width

of the web. Furthermore, the displacements recorded in the flanges are significantly greater than those in the web, demonstrating that the asymmetric cross-section undergoes non-uniform cross-section deformations without triggering physical web buckling. Web buckling may occur when the web is under severe flexural compression, corresponding to the loading direction that places the flanges in tension (FT).

The reinforcement strain distribution corroborates this progressive damage sequence, highlighting two distinct peaks along the web subjected to high tensile strain demands (as illustrated by the Strain in Figure 5-1).

- Marker 2.FC: Longitudinal reinforcement strains maintain a substantial capacity margin before reaching failure limits. This suggests that the abrupt drop in load-carrying capacity is triggered by crushing or spalling of the concrete cover at the flange tips, or by a shear-dominated failure.
- Marker 3.FC: The web reinforcement approaches its ultimate strain capacity, reaching a strain of 0.092 compared to the ultimate strain capacity of 0.095 for 6mm bars. Consequently, the flexural demands are transferred to the heavily detailed boundary reinforcement, forcing it to sustain the remaining plastic deformation demands up to marker 4.FC.
- Marker 4.FC: At this terminal stage, the strain capacity of the web reinforcement is already fractured. The boundary elements at the cross-section intersections are approaching their ultimate strain limits, triggering a sharp drop in the global load-displacement response to its residual capacity. Because the boundary zones carried the final resistance mechanisms, the definitive limit state occurs when the boundary reinforcement reaches its ultimate material strain capacity of 0.101 for 12mm bars.

	2.FC	3.FC	4.FC
Strain	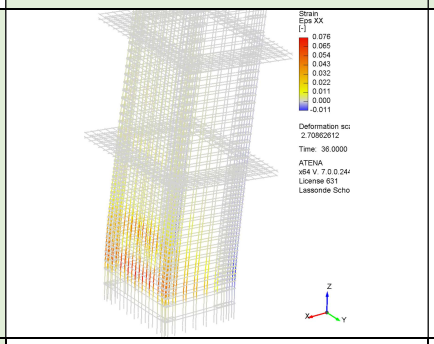	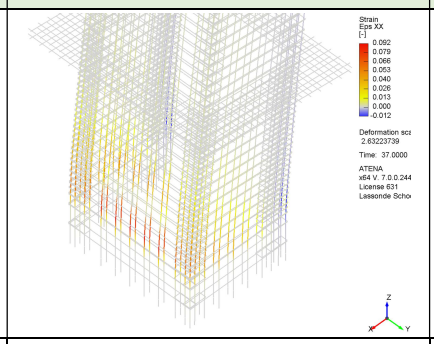	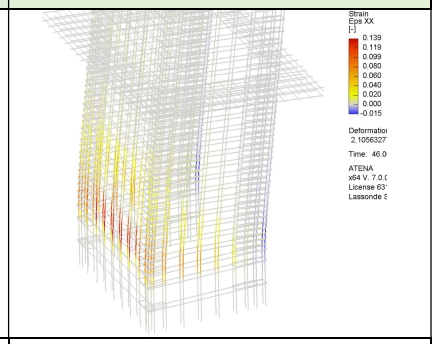
Strain (boundary Elem.)	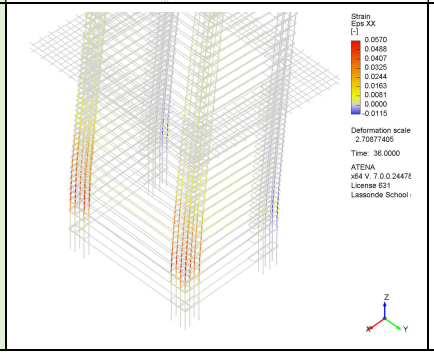	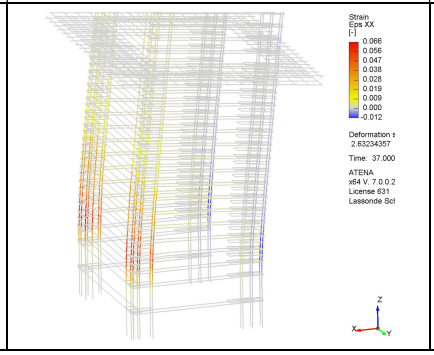	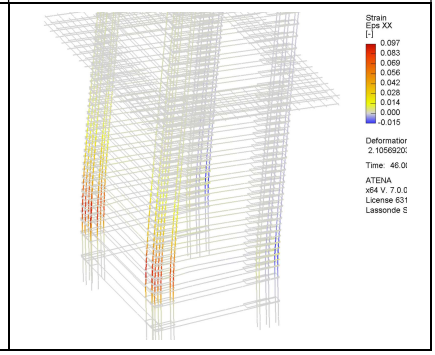

Table 5-2 Numerical response parameters and damage indicators for the walls reinforcement under Flanges in Compression (FC) loading

	2.FC	3.FC	4.FC
Plastic Strain	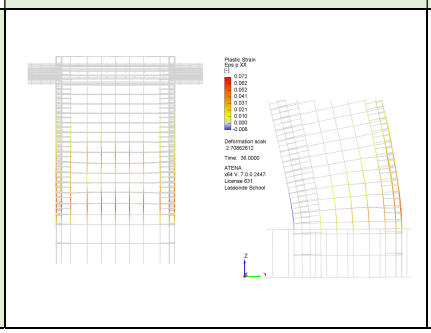	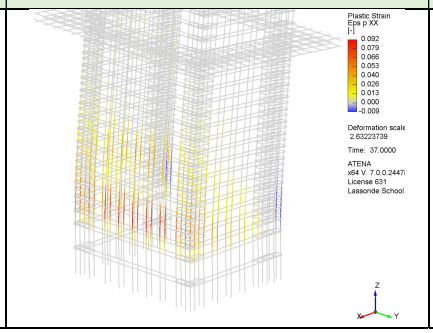	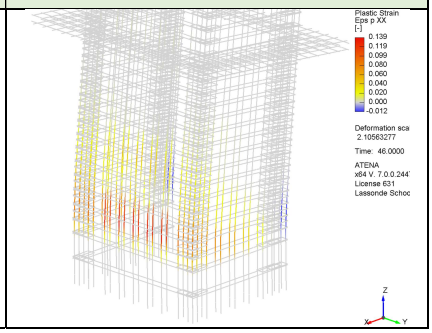

Table 5-2 Numerical response parameters and damage indicators for the walls reinforcement under Flanges in Compression (FC) loading (Continued)

Another key parameter and damage indicator is the slip of the reinforcement relative to the concrete, at the base of the wall, where tension is generated in the web. As shown in Figure 5-4, a maximum slip of 0.3 mm is observed at Marker 4.FC. Because this value remains well within the bond capacity (see Figure 4-25), there is no evidence of significant bond slippage or failure.

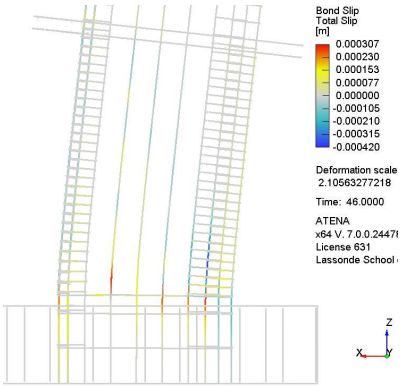

Figure 5-4 Bond Slip under Flanges in Compression (FC)

Based on the localized material states analyzed at key milestones along the experimental load-displacement curve, the primary mechanism driving the first sudden capacity drop (between markers 2.FC and 3.FC) is shear-dominated failure. The internal stress fields confirm the development of a diagonal concrete compression strut, which initiates at the base of the flange tips and propagates diagonally into the web at approximately 30°.

At marker 2.FC, localized damage occurred, characterized by premature loss of concrete cover at the flange tips. This spalling causes a localized loss of boundary-element confinement within the first story, extending up to an elevation of 0.5m above the foundation base.

In this loading direction, the structure achieves an ultimate drift capacity of 5.24%. However, the wall experiences primary shear failure at a drift ratio of 4.1%. Consequently, the structure's definitive failure mechanism is classified as a combined shear-flexure failure.

Loading in the West direction - Flanges in Tension (FT)

Due to its asymmetric cross-sectional geometry, a comprehensive evaluation requires analyzing the pushover response in the opposite loading direction. In this reverse orientation, the structure exhibits a well-defined yield plateau with a more ductile response, free of sudden strength degradation. This behavior aligns with expectations, indicating a stable, flexure-governed failure mode that avoids brittle shear mechanisms.

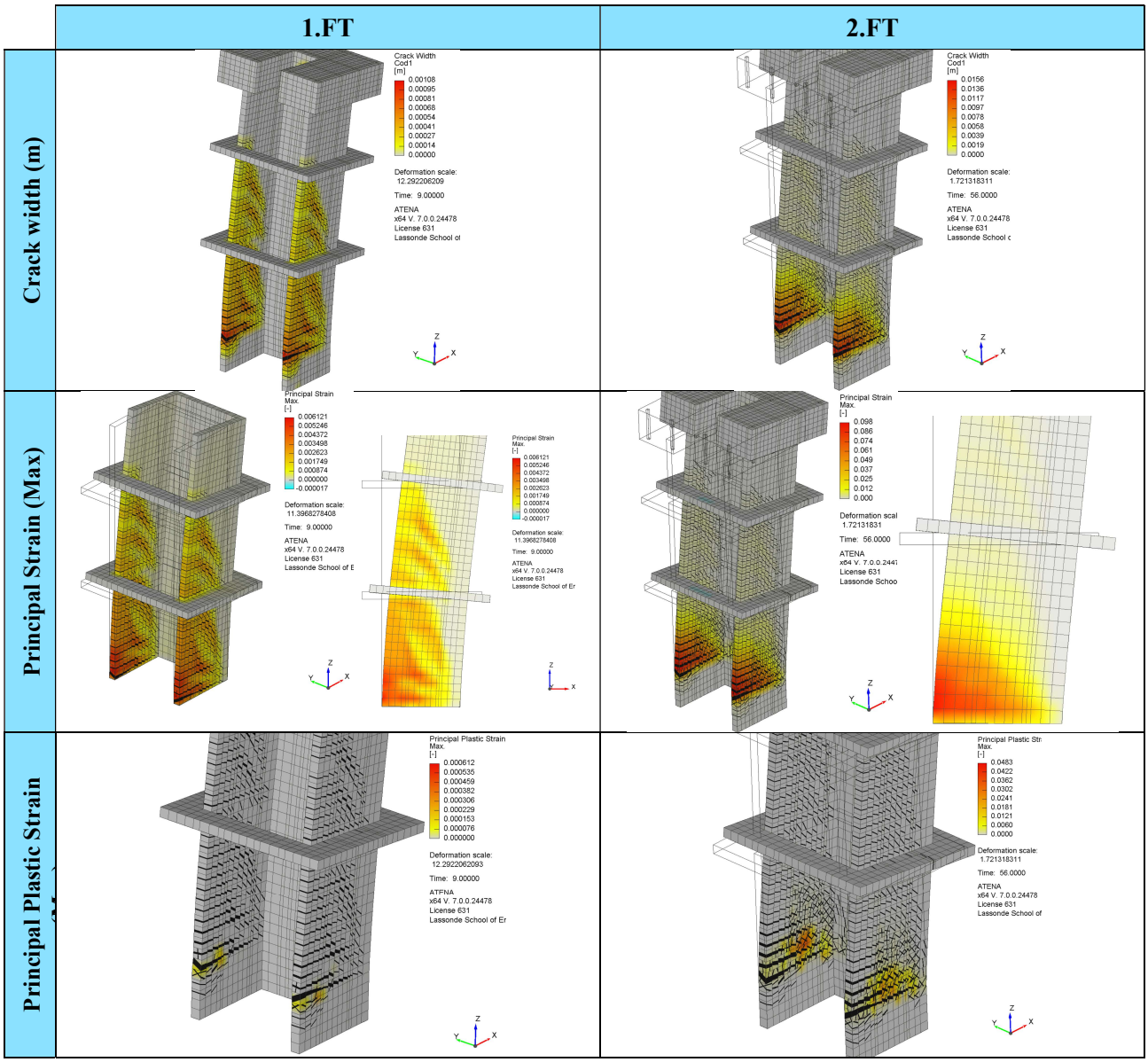

Table 5-3 Numerical response parameters and damage indicators for the wall under Flange in Tension (FT) loading

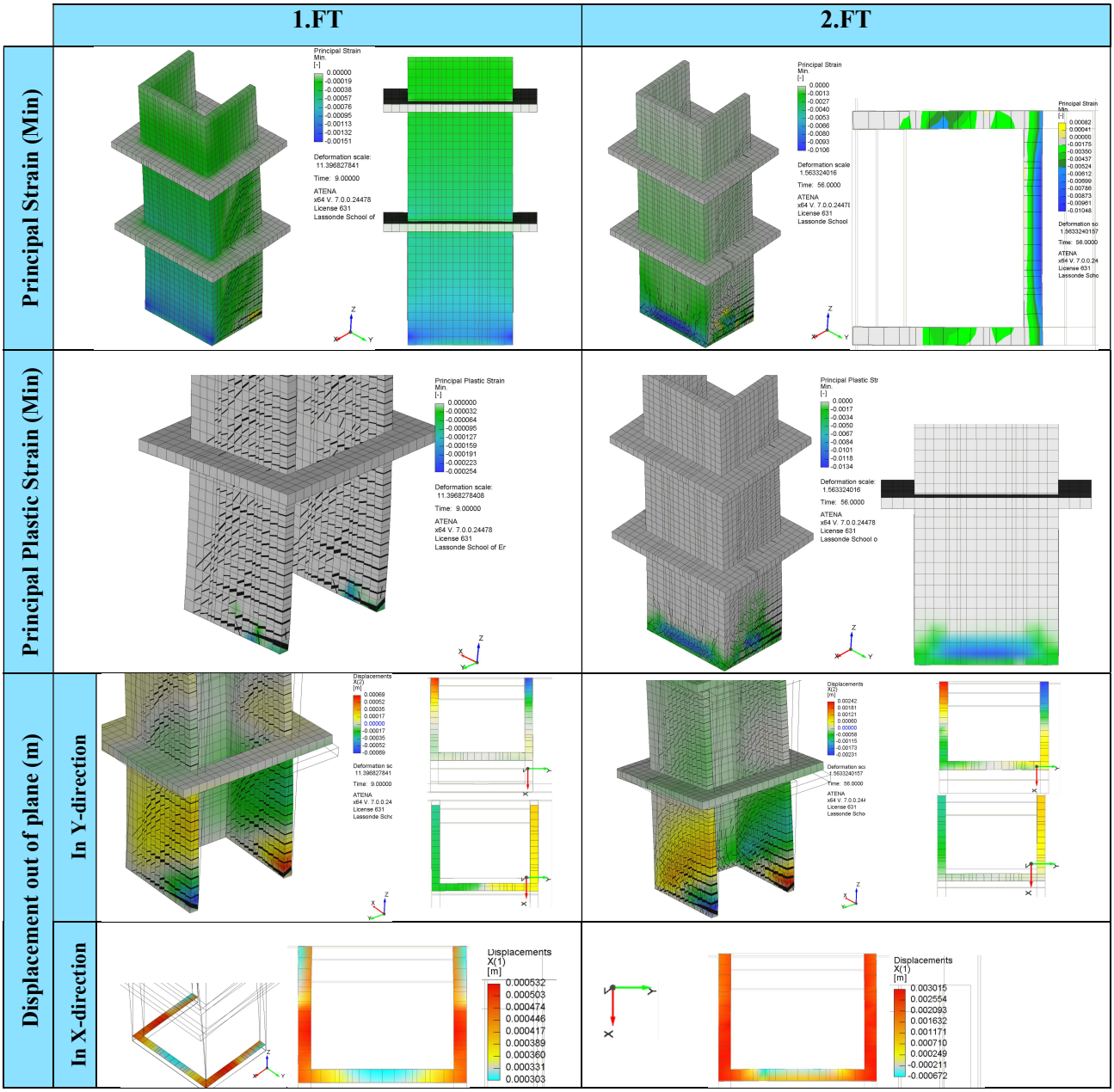

Table 5-3 Numerical response parameters and damage indicators for the wall under Flange in Tension (FT) loading (Continued)

In this loading direction, the progressive development of the failure mechanism is clearly apparent. At marker 1.FT (Figure 5-1), diagonal strain fields develop across the first two stories, and the longitudinal reinforcement within the boundary elements has yielded. Concurrently, compressive strains concentrate at the web-to-flange intersections. This compressive field remains predominantly within the elastic range, exhibiting negligible plastic strain and a principal concrete compressive strain of 0.0015, approximately half of the unconfined strain capacity, confirming that the concrete cover remains undamaged at this stage.

Spalling of the concrete cover initiates midway between markers 1.FT and 2.FT at a lateral displacement of approximately 130 mm (3% drift). This contrasts with the reverse loading direction (FC), where cover spalling occurred before the onset of yielding. Ultimately, a flexural failure mechanism governs at marker 2.FT is characterized by the formation of a fully developed plastic hinge. At this terminal stage, extensive concrete crushing occurs across the web, with local compressive strains reaching 0.010, well beyond the unconfined crushing threshold. Furthermore, over half of the web thickness exhibits severe strain demands exceeding 0.035.

At this ultimate limit state, the tensile strains in the boundary-element reinforcement approach the material's ultimate capacity, triggering the structure's definitive failure. Additionally, due to the high tensile strain demands imposed on the flange reinforcement, the potential for bond-slip failure was explicitly evaluated. However, the numerical results indicate that bond-slips do not govern the limit state, with the peak slip demand reaching only 44% of the ultimate bond capacity.

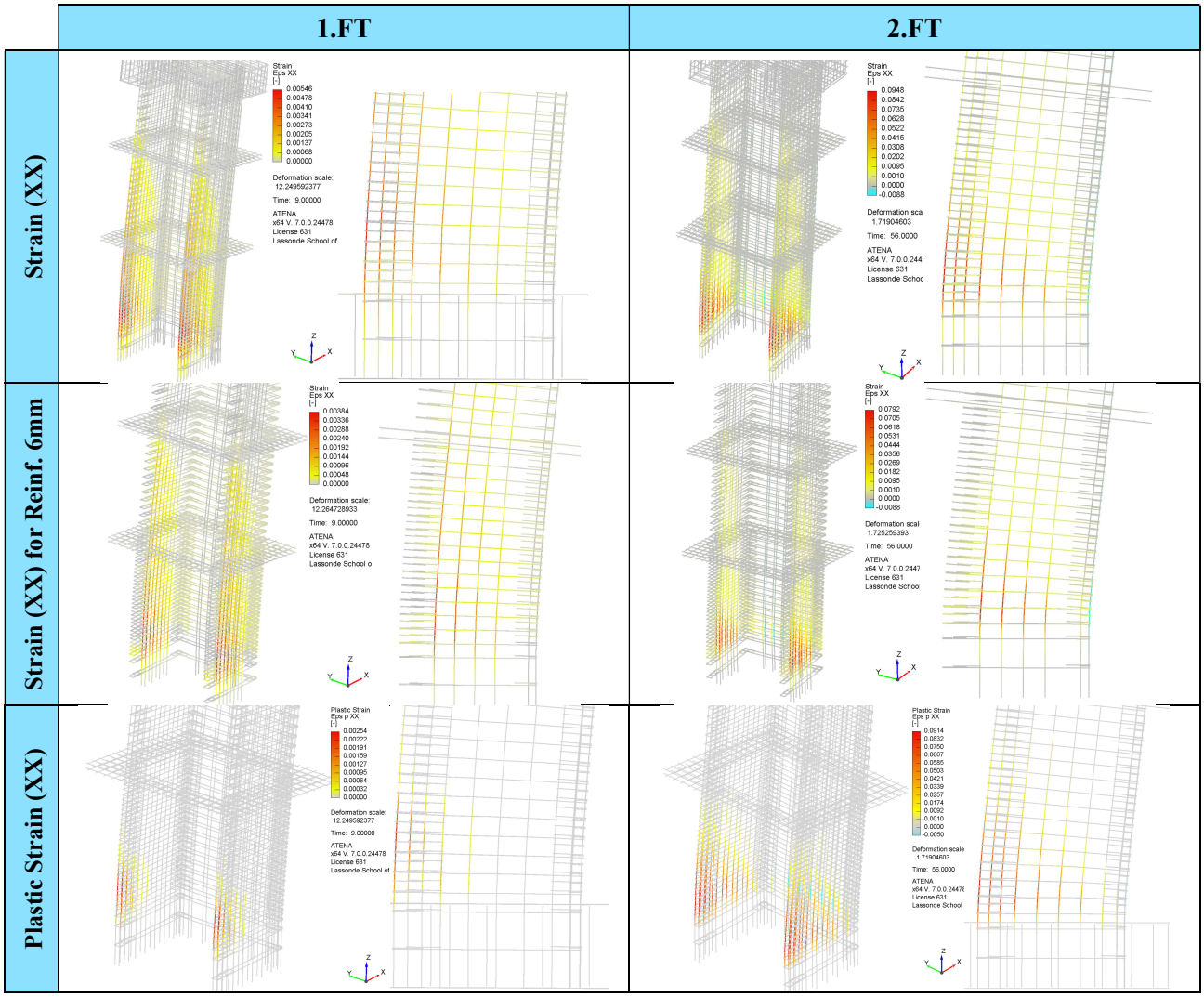

Table 5-4 Numerical response parameters and damage indicators for the walls reinforcement under Flanges in Tension (FT) loading

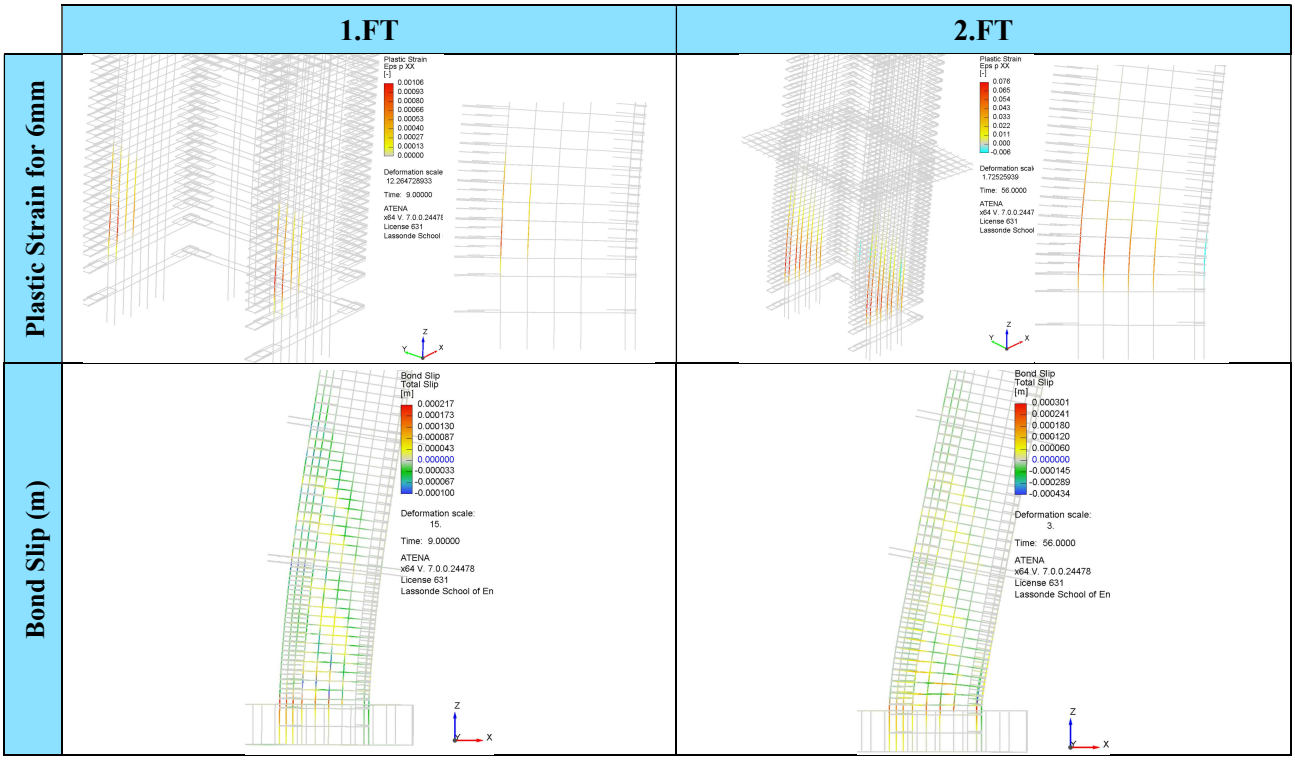

Table 5-4 Numerical response parameters and damage indicators for the walls reinforcement under Flanges in Tension (FT) loading. (Continued)

In this loading direction, the shear wall exhibits a highly ductile failure mechanism coupled with an enhanced ultimate drift capacity. The ultimate limit state is governed by pure flexural failure, characterized by the progressive tensile fracture of the concentrated boundary reinforcement within the flanges and extensive compressive crushing of the web concrete; see progressive principal strain in Figure 5-5.

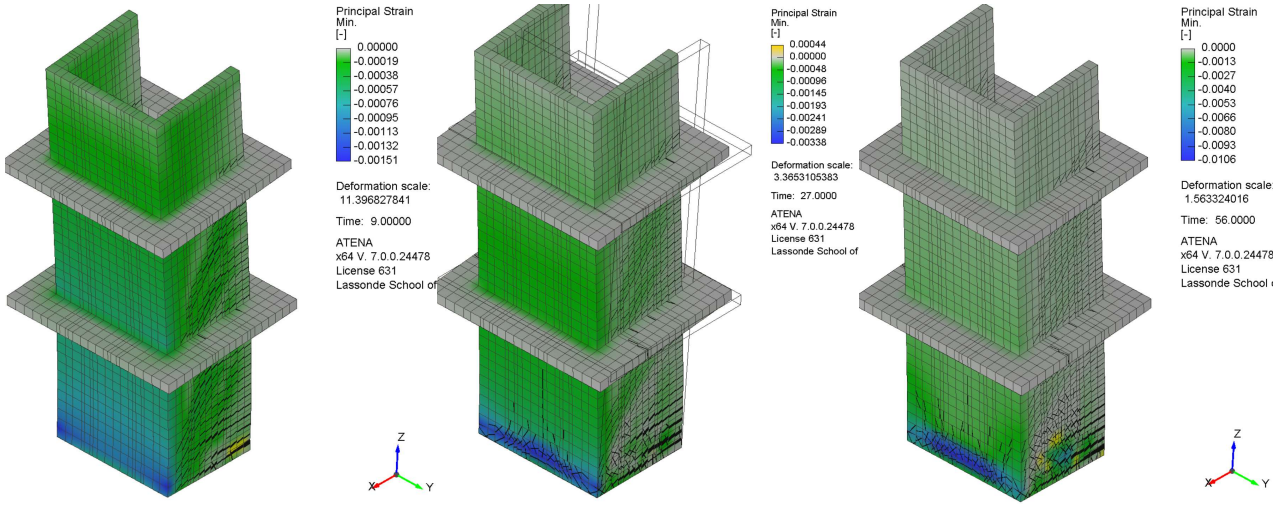

Figure 5-5 Principal Strain (web in compression)

Having characterized the structural response in both directions parallel to the axis of symmetry, the analysis proceeds to evaluate the structural behavior under loading transverse to the axis of symmetry. Due to

the asymmetric geometric profile of the U-shaped cross-section in this orthogonal direction, the lateral demand inherently induces a significant torsional response.

Subsequently, a parametric study was conducted to investigate the influence of the axial load ratio, longitudinal reinforcement ratio, and transverse reinforcement ratio on the wall's overall behavior. This analysis primarily aims to evaluate how variations in these key design parameters affect the wall's lateral strength, ductility, and ultimate failure mode.

To evaluate the maximum lateral force of the experimental U-shaped shear wall, the response is compared with the pushover curve derived using the analytical formulation presented in Chapter 3. Considering the moment-shear interaction relationship (Figure 5-6), the corresponding moment and shear capacities are calculated using Eq. 3-21 and Eq. 3-22, as shown below:

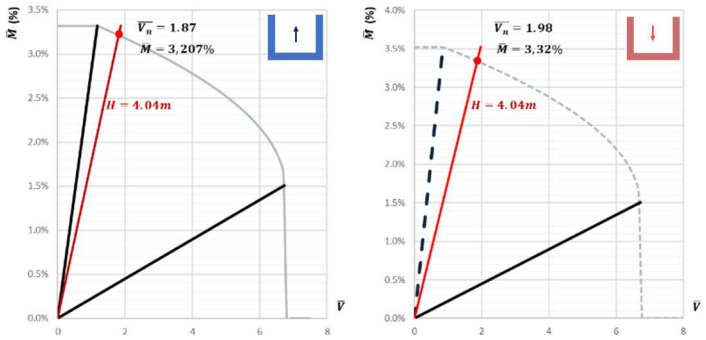

Figure 5-6 Moment-Shear interaction curves

$$M = \bar{M}\,(\alpha_1\, f_c'\, l_w\, l_f^2)$$

$$M = \bar{M}\ (0.81 \cdot 27 \cdot 1.3 \cdot 1.05^2) \cdot 1000$$

$$\boldsymbol{M = 1005.2\ kN \cdot m\ \uparrow;\ 1040.6\ kN \cdot m\ \downarrow}$$

$$V = \bar{V}\,(0.083\,\sqrt{f_c'}\,A_g)$$

$$V = \bar{V}\,(0.083\ \cdot\sqrt{27}\ \cdot 0.32) \cdot 1000$$

$$\boldsymbol{V = 258.1\ kN\uparrow; 273.2\ kN}$$

Comparing the analytical predictions of lateral force of 273.2 kN derived from the moment-shear interaction against the numerical results of pushover capacity of 270 kN, in the direction where the flanges are in tension, reveals a 1% error. Conversely, for the opposite loading direction, the analytical formulation conservatively underestimates the peak lateral capacity by 15%.

5.2 Experimental Setup - Response 2000

Another approach is conducting a pushover analysis using RESPONSE2000, a specialized 1D member analysis integrating sectional behaviors across the full length of the element to capture global shear-flexure interaction, load distribution, and non-linear deflections, to compare it against ATENA and establish whether this simpler practical tool can be used to estimate the response of these complex U-shaped members

Member Response uses a non-linear sectional integration approach. At each slice, Response-2000 runs a layer-by-layer sectional analysis under the specific combined N-M-V demands. It iteratively solves for strain profiles, principal compressive stresses in concrete, principal tensile stresses, diagonal crack angles, and steel reinforcement stresses.

Assuming the reinforced wall acts as a cantilever element with a fixed base, the pushover analysis applies a constant gravitational force alongside a point load that induces a constant shear force and a linear bending moment diagram. Throughout the step-by-step incremental member response up to failure, the lateral load magnitude increases while maintaining a consistent internal force distribution along the member length. Additionally, a constant axial load was applied to simulate the mass of the four blocks positioned on top of the collar.

As established in Chapter 3, T-shaped sections were evaluated as equivalent to U-shaped cross-sections when analyzed for bending about the axis of symmetry, see Figure 5-7. This geometry was adopted because Response-2000 does not directly support open U-shaped cross-sections. To maintain equivalent longitudinal reinforcement, the flange rebar was modeled using two steel branches with twice as many bars, preserving the total steel area of the four-branch experimental setup.

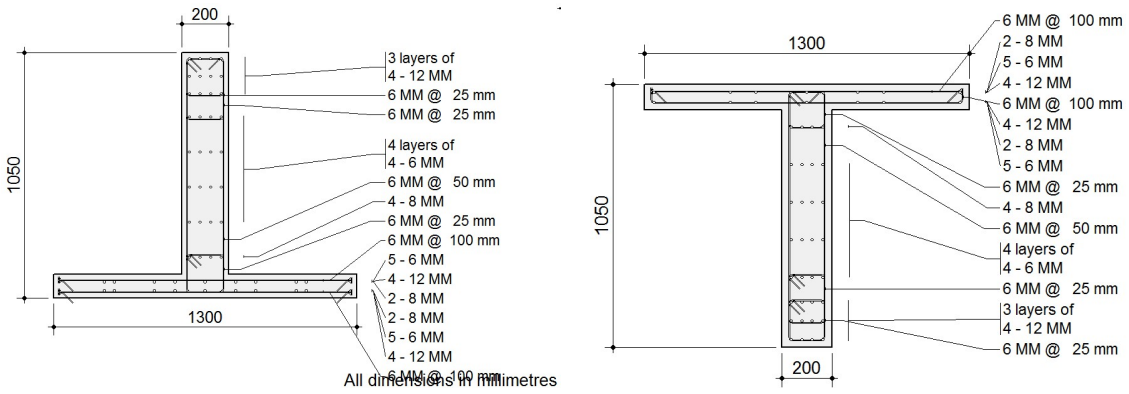

Geometric Properties	Gross Conc.	Trans (n=8.29)
Area (mm^2) x 10^3	320.0	344.8
Inertia (mm^4) x 10^6	35672.7	40441.6
y_t (mm)	688	679
y_b (mm)	362	371
S_t (mm^3) x 10^3	51828.7	59603.9
S_b (mm^3) x 10^3	98620.1	108861.9

Geometric Properties	Gross Conc.	Trans (n=8.29)
Area (mm^2) x 10^3	320.0	343.4
Inertia (mm^4) x 10^6	35672.7	40144.0
y_t (mm)	362	371
y_b (mm)	688	679
S_t (mm^3) x 10^3	98620.1	108078.2
S_b (mm^3) x 10^3	51828.7	59160.2

Figure 5-7 T-Cross-sectional details and geometric properties of the experiment on Response 2000.

Figure 5-8 illustrates the ATENA pushover analysis (dotted lines), which was conducted by applying displacement control at the mid-height of the collar, parallel to the plane of symmetry. Conversely, Response-2000 (solid lines) uses a force-controlled, full-member analysis under a constant axial gravity load combined with a point load, imposing a constant shear force of increasing magnitude that produces a linear bending moment distribution along the height.

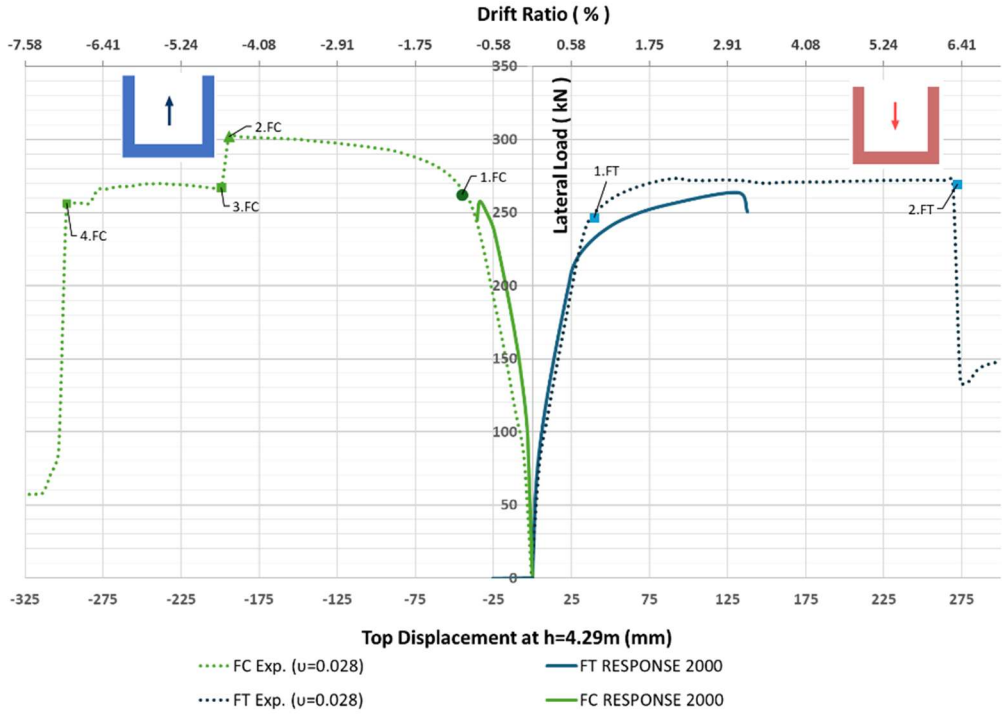

Figure 5-8 Pushover - Parametric study of Axial Load Ratio (ν)

While Response-2000 reliably predicts the initial stiffness, yield point, and early force-displacement response of the section, non-linear finite element modeling in ATENA is necessary to accurately capture post-yield drift capacity, localized failure mechanisms, and complex crack patterns.

As shown in the load-displacement response, Response-2000 captures initial yield effectively; however, under flange-compression loading (FC), it underpredicts the ultimate displacement before numerical termination. Conversely, under flange-tension loading (FT), Response-2000 tracks the experimental yield envelope closely up to moderate drifts and predicts higher overall drift capacity than in the reverse direction. Nevertheless, capturing severe strength degradation, concrete crushing, and out-of-plane buckling at large drifts ultimately requires detailed 3D finite element analysis in ATENA.

Figure 5-8 illustrates the crack patterns and crack width contours (in mm) calculated by Response-2000 along the member length for both loading directions. Under flange-tension/web-compression loading (red), the limited concrete tension area in the web results in severe crack localization near the base, with maximum crack

widths reaching 4.42 mm and cracking extending significantly higher up the wall height. Conversely, under flange-compression/web-tension loading (blue), the larger compression zone provided by the web restricts crack growth, yielding a maximum base crack width of only 0.62mm. This demonstrates Response2000's ability to reflect directional crack-width asymmetry and crack-height distribution.

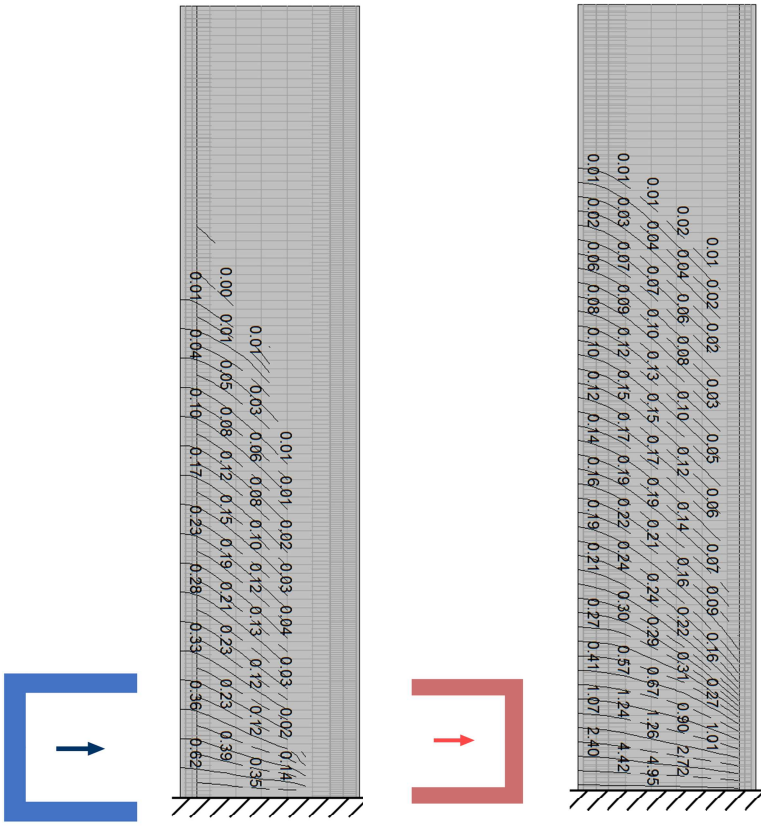

Figure 5-9 Crack patterns and crack width contours (mm) in Response2000.

Figure 5-10 compares the longitudinal member-response profiles generated by Response-2000 for both loading directions. While the linear moment diagrams reflect standard cantilever behavior up to the base (approximately 1105 to 1130 kN), the resulting deformation demand varies significantly with loading orientation. Under web-compression loading (right), the curvature demand localizes intensely at the base, reaching a maximum curvature of -52.0 mrad/m, compared to only -8.0 mrad/m in the reverse direction. Additionally, the shear strain distribution highlights a peak shear deformation of 1.90mm/m near the lower critical zone (base), capturing the coupled flexural-shear interaction.

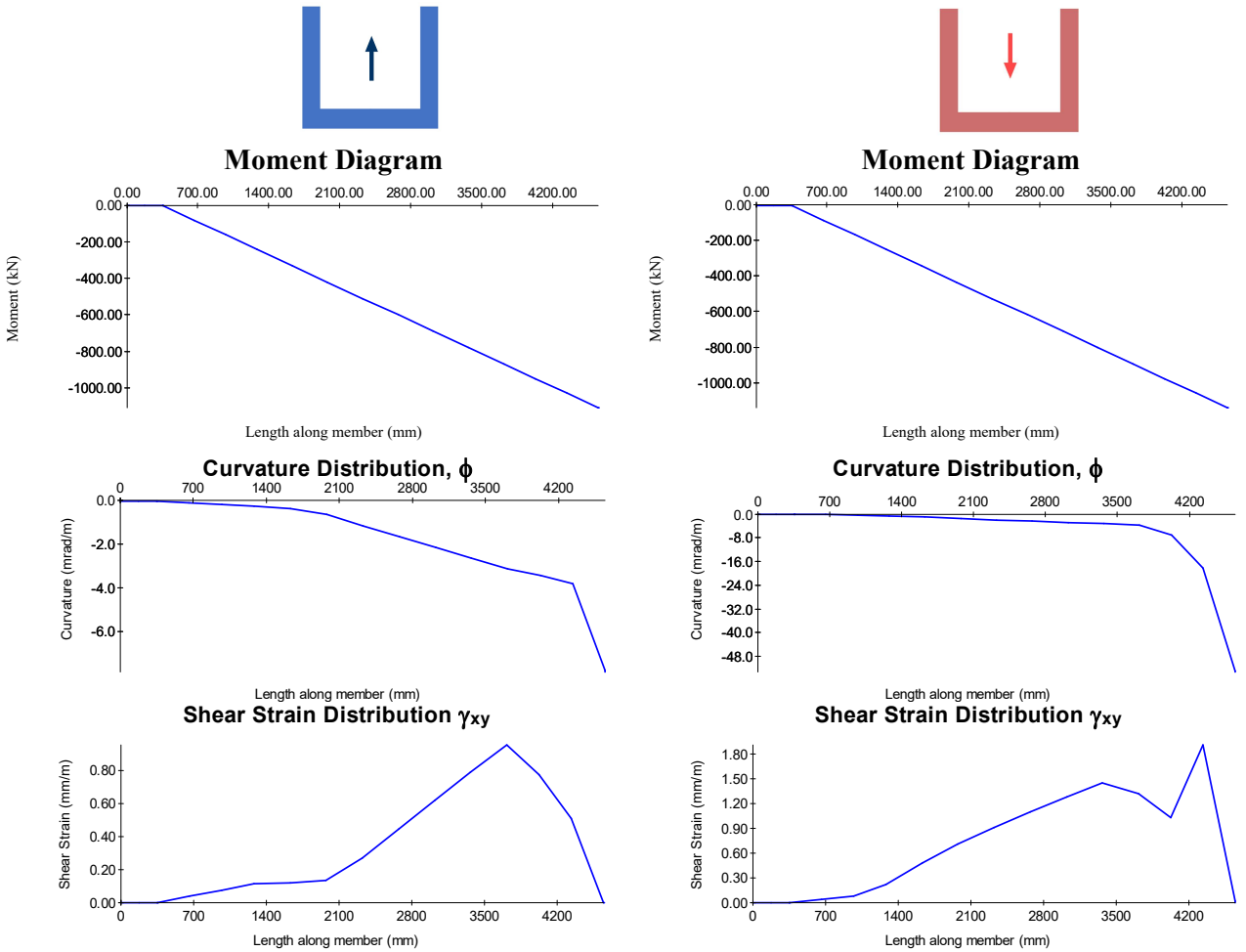

Figure 5-10 Response-2000, member response profiles showing bending moment, curvature distribution, and shear strain distribution at final force control stage.

Overall, Response-2000 demonstrates strong potential as a practical, preliminary tool for analyzing complex U-shaped reinforced concrete shear walls via equivalent T-section modeling. Although 3D finite element analysis in ATENA remains indispensable for modeling large-drift post-yield softening, out-of-plane effects, and ultimate failure mechanisms, Response-2000 successfully captures the initial force-displacement envelope, yield points, and directional crack/curvature asymmetry with minimal computational cost.

5.3 Parametric Study

To comprehensively evaluate the seismic performance of U-shaped reinforced concrete shear walls under multi-directional loading, this study presents a parametric sensitivity analysis focusing on five primary parameters: the axial load ratio (Section 5.2.1), longitudinal reinforcement ratio (Section 5.2.2), transverse reinforcement ratio (Section 5.2.3), torsional demand (Section 5.2.4), and the potential presence of lap splicing in the longitudinal reinforcement (Section 5.2.5). Evaluating and comparing these parameters collectively captures the complex interactions among flexure, shear, and torsion inherent in U-shaped cross-sections.

Because U-shaped cross-sections do not behave like simple planar elements, their lateral response is highly coupled. The analytical framework must transition beyond basic sectional flexure to isolate and evaluate how shear, torsion, and axial demands interact at the local material level. Specifically, this study aims to account for tension shift, asymmetric torsional demand, and global out-of-plane instability to systematically map how variations of the five primary parameters mentioned above govern the wall's ultimate capacity, ductility, and failure modes:

Tension shift effect: a structural phenomenon where the demand on longitudinal reinforcement increases because the steel must resist not only the bending moment but also the horizontal component of the diagonal concrete compression struts. This is the most direct way shear reduces flexural capacity. To maintain equilibrium in a diagonal compression field, the longitudinal reinforcement must sustain higher stress levels. This effect will be evaluated through the following parameters:

- Axial load ratio (ν): High axial loads will be analyzed for their ability to "close" diagonal cracks, increasing the concrete's contribution to shear resistance and potentially reducing the additional demand on the tension steel.
- Transverse Reinforcement (ρ_t): Increasing the transverse steel ratio is expected to change the crack angle; a higher ρ_t reduces the tension shift effect compared to a wall with minimal transverse steel.

Torsion Sensitivity and Asymmetric Demand in U-Shaped walls: Unlike rectangular walls, U-shaped walls exhibit a significant offset between the shear center and the centroid. This eccentricity (e) induces twisting moments under lateral loading, reducing overall flexural efficiency. Torsion introduces additional shear stresses that superimpose on the direct lateral shear, causing one flange to experience amplified tension and shear, while the opposing flange experiences a reduction.

These effects are systematically explored through the following parameters:

- Reinforcement Ratios in Boundary Elements ($\rho_{v,eb}$,$\rho_{t,eb1}$): Higher longitudinal reinforcement ($\rho_{v,eb}$) increases the section's warping stiffness. Simultaneously, the increased demand for confinement due to torsion is addressed by varying $\rho_{t,eb}$ which prevents the "outer" corners from degrading under high shear-torsion interaction.
- Axial loads ratio (ν): Torsional effects and warping become much more critical when the wall has a high axial load ratio, as it often leads to out-of-plane buckling.

Stability and Out-of-Plane Buckling: This phase investigates the susceptibility of slender, U-shaped walls to global instability, where concentrated compressive strains in the boundary elements trigger out-of-plane deformation and buckling. The transition from ductile flexure to a stability-governed failure is evaluated using the following parameters:

- Axial load ratio (ν): High axial loads increase the compressive demand on the wall's "thin" sections, accelerating concrete softening and increasing the risk of web buckling. High axial load ratios typically reduce displacement capacity and can trigger brittle, sudden concrete crushing immediately after cover spalling, severely limiting overall ductility.
- Transverse Reinforcement Spacing (S_t): Decreasing the vertical spacing of stirrups/hoops within the boundary elements provides lateral restraint to the longitudinal bars. This is a critical check to ensure that longitudinal reinforcement buckling does not occur before the section reaches its intended ultimate deformation capacity.

To provide a comprehensive overview of the variables considered in this research, Table 5-5 summarizes the parametric matrix developed for the U-shaped wall study. The values shown in red represent the primary parameters systematically altered to assess their influence on the global and local structural response. The second line shows the baseline values from the benchmark experimental data (highlighted with a blue background).

The study parameters fall into two domains: loading conditions (orange) and reinforcement detailing (pink). The matrix is organized around three of the five previously discussed key parameters: the axial load ratio, longitudinal reinforcement ratio, and transverse reinforcement ratio, with each column representing a unique analyzed wall case. The complex interaction between these variables ultimately governs the failure mechanism, determining whether the wall exhibits a highly ductile flexural response or a brittle, stability-governed failure.

		Axial Load Ratio $v = P / F'_c A_g$	Vertical Reinforcement Ratio (eb_1) ρ_{eb1}	Vertical Reinforcement Ratio (eb_2) ρ_{eb2}	Transversal Reinforcement Spacing (web and flange) S_w, S_f *(mm)*	Transversal Reinforcement Ratio (web and flange) $\rho_{t,w}$	Transversal Reinforcement Spacing (Bondary elements) S_w, S_f *(mm)*	Transversal Reinforcement Ratio (Bondary elements) $\rho_{t,eb}$
Experiment Values		0.028	2.59%	2.76%	100	0.56%	(50, 100, 200)	(1.12%, 0.56%, 0.28%)
Axial Load Ratio	v = 0.05	**0.050**	2.59%	2.76%	100	0.56%	(50, 100, 200)	(1.12%, 0.56%, 0.28%)
	v = 0.1	**0.100**	2.59%	2.76%	100	0.56%	(50, 100, 200)	(1.12%, 0.56%, 0.28%)
	v = 0.2	**0.200**	2.59%	2.76%	100	0.56%	(50, 100, 200)	(1.12%, 0.56%, 0.28%)
Vertical Reinforcement Ratio (eb)	2.59 %	0.0350	2.59%	2.76%	100	0.56%	(50, 100, 200)	(1.12%, 0.56%, 0.28%)
	4.11 %	0.0810	**4.11%**	**4.21%**	100	0.56%	(50, 100, 200)	(1.12%, 0.56%, 0.28%)
	6.05 %	0.1042	**6.05%**	2.76%	100	0.56%	(50, 100, 200)	(1.12%, 0.56%, 0.28%)
	2.59 %	0.1042	2.59%	**6.08%**	100	0.56%	(50, 100, 200)	(1.12%, 0.56%, 0.28%)
	6.05 %	0.1505	**6.05%**	**6.08%**	100	0.28%	(50, 100, 200)	(1.12%, 0.56%, 0.28%)
Transversal Reinforcement Spacing (web and flange) S_w, S_f	100 mm	0.0350	2.59%	2.76%	100	0.56%	(50, 100, 200)	(1.12%, 0.56%, 0.28%)
	50 mm	0.1505	2.59%	2.76%	**50**	0.37%	**25**	(1.12%, 0.56%, 0.28%)
	200 mm	0.2083	2.59%	2.76%	**200**	0.28%	(50, 100, 200)	(1.12%, 0.56%, 0.28%)
Transversal Reinforcement Ratio (Bondary elements)		0.0350	2.59%	2.76%	100	0.56%	(50, 100, 200)	(1.12%, 0.56%, 0.28%)
	1 %	0.1505	2.59%	2.76%	100	1.00%	**NONE**	1.00%
	1.13 %	0.2083	2.59%	2.76%	100	2.26%	**200**	1.13%

Table 5-5 Parametric matrix used for the U-shaped wall study.

5.3.1 Axial Load Ratio

One of the key parametric studies conducted in the context of the thesis focuses on the axial load ratio (ν) because axial dead loads directly affect both flexural and shear capacity, primarily by restricting the propagation and width of cracks generated by lateral loading. However, higher axial load ratios introduce a brittle failure mode: out-of-plane buckling of the thin structural elements. In tall, non-planar shear walls, a prominent failure mechanism emerges as buckling of the flanges, driven by the low thickness-to-width ratio of the cross-section components. Consequently, a sensitivity analysis is conducted under lateral loading parallel to the axis of symmetry, comparing the benchmark experimental model (ν=0.028) with scenarios at higher axial load levels (ν=0.10 and ν=0.20).

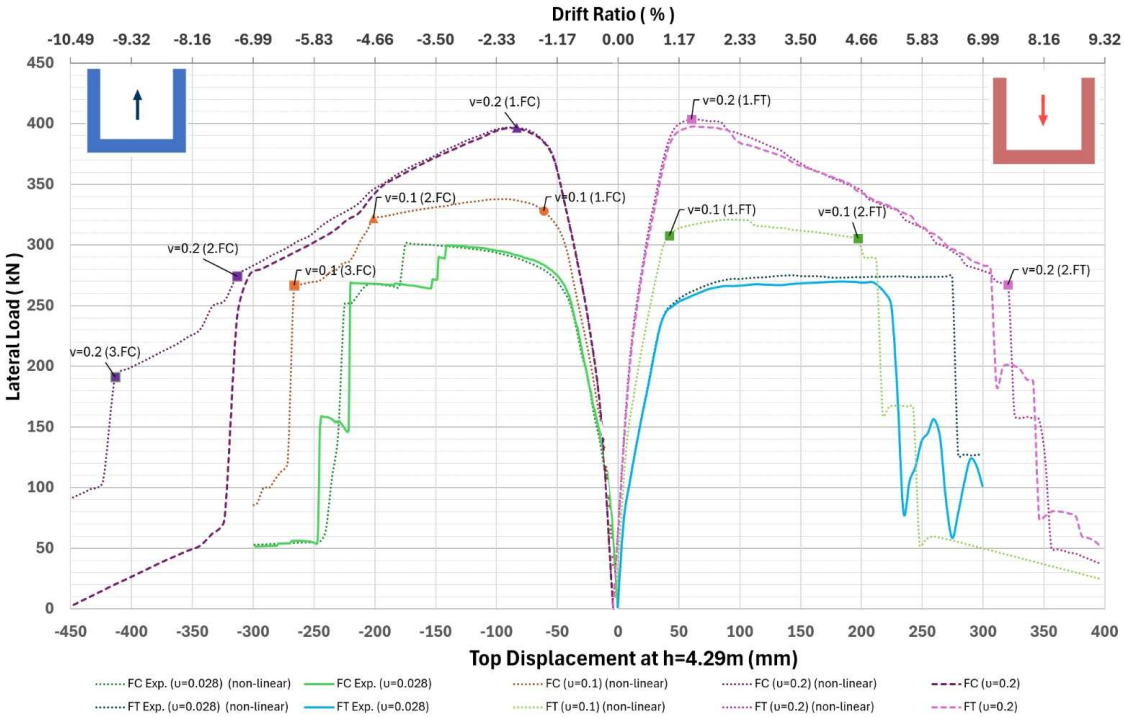

Figure 5-11 Pushover - Parametric study of Axial Load Ratio (ν)

Figure 5-11 illustrates the comparative lateral load-displacement and drift ratio responses of the U-shaped shear wall under varying axial load ratios for both the Flanges in Compression (FC) and Flanges in Tension (FT) loading directions. As expected and consistent with the principles reviewed in Chapter 3, the wall with the higher axial load shows a significant increase in peak lateral load strength. For instance, in the FC direction, the peak lateral load strength increases by approximately 100 kN from the benchmark experimental model (ν=0.028) to the model with a high axial load ratio (ν=0.20). However, alongside this strength increase, the wall exhibits a less ductile response, with a much more abrupt and premature drop in strength after its peak. This brittle behavior is typically associated with shear failure mechanisms or out-of-plane buckling of the structural elements.

The comparison also confirms that incorporating geometric nonlinearity (represented by the dashed lines) in the reinforcement is essential for accurately capturing the post-peak softening and residual strength stages. Furthermore, under high axial forces (ν=0.20), the lateral load-drift responses become notably symmetrical between both loading directions. In both the FC and FT directions, a peak strength of approximately 400kN is reached at a drift ratio of roughly 1.2 to 1.8%. After the peak, strength decreases linearly from 400 kN to 275 kN at a drift ratio of approximately 7.3%, beyond which the curves begin to diverge.

To identify failure mechanisms not visible in the global load-displacement curves, a localized behavioral analysis evaluates strain distributions, cracking patterns, and bond-slip behavior. This evaluation focuses closely on the stability of the wall elements, particularly during the Flanges in Compression (FC) loading phase within the plastic hinge region. This zone is highly susceptible to out-of-plane buckling because of the combination of elevated compressive stresses and the wall's small cross-section thickness.

	v=0.2 (1.FC)	v=0.2 (2.FC)	v=0.2 (3.FC)
Crack width (m)	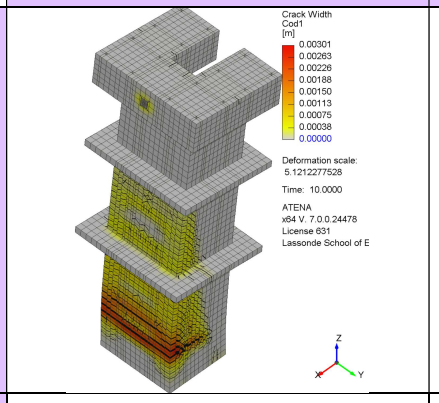	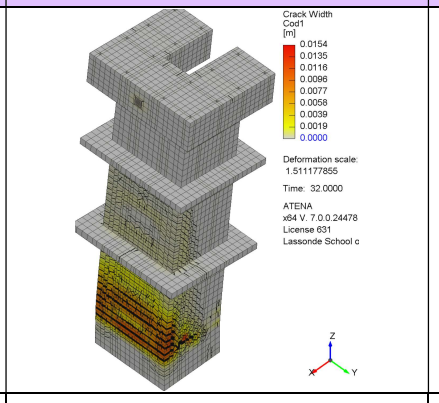	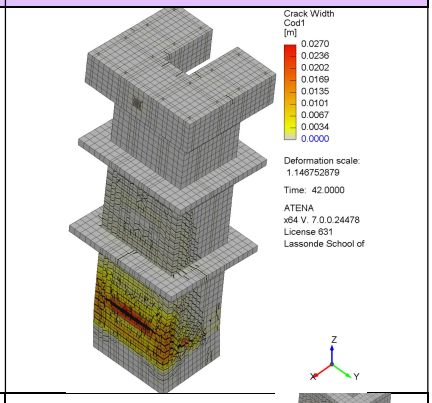
Principal Strain (Max)	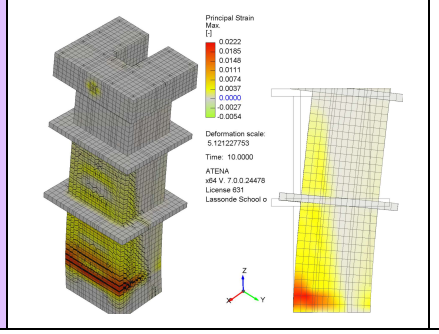	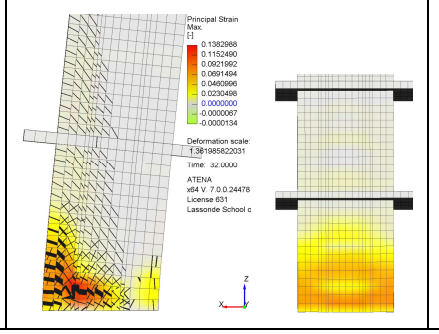	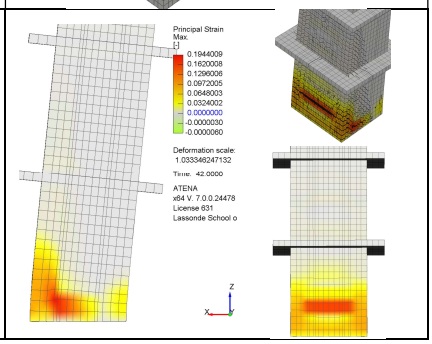

Table 5-6 Numerical response parameters and damage indicators for the walls under axial load ratio (ν=0.20) under Flanges in Compression (FC) loading

	v=0.2 (1.FC)	v=0.2 (2.FC)	v=0.2 (3.FC)
Principal Plastic Strain (Max)	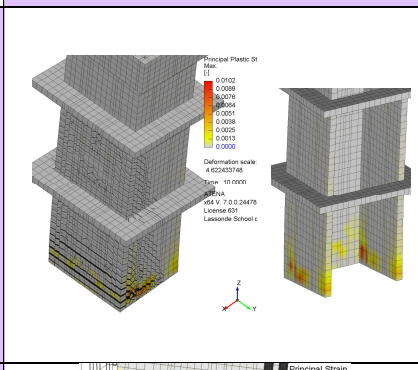	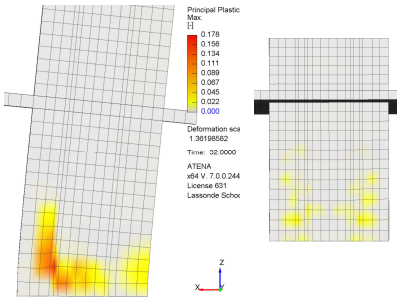	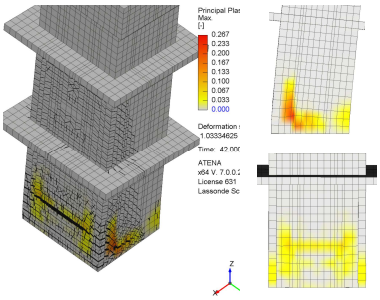
Principal Strain (Min)	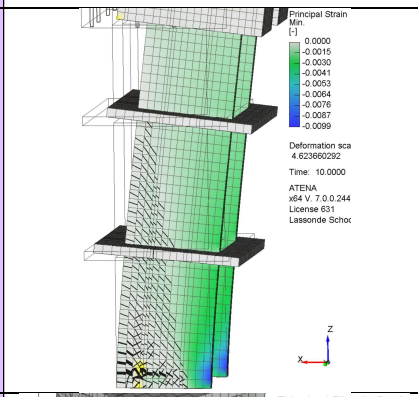	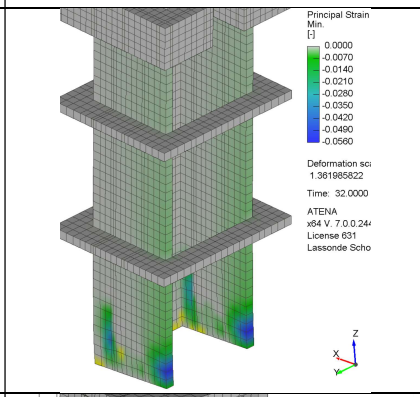	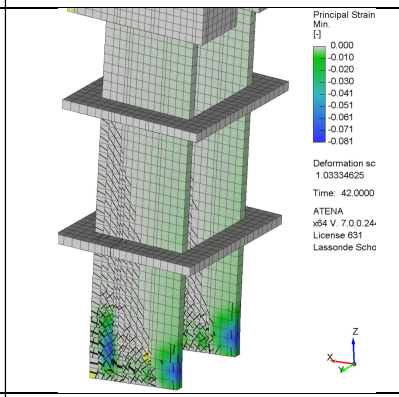
Principal Plastic Strain (Min)	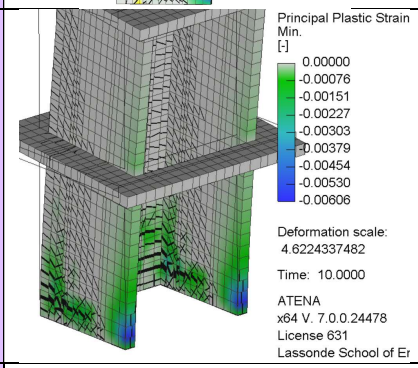	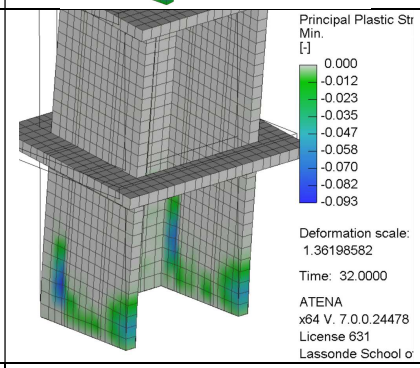	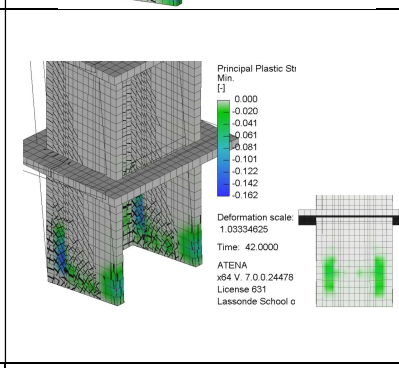
Out of plane displacement (Y-Direction)	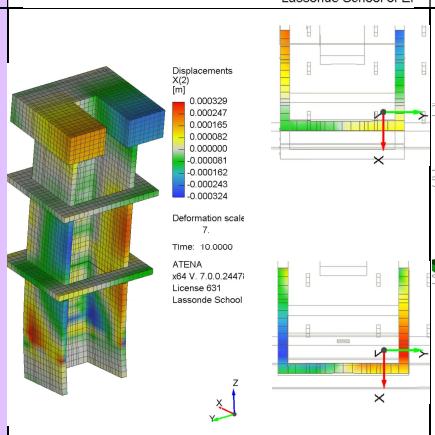	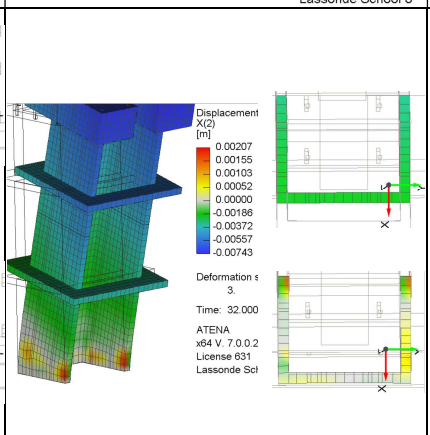	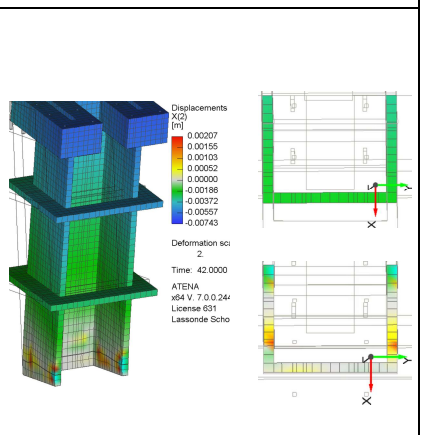

Table 5-6 Numerical response parameters and damage indicators for the walls under axial load ratio (v=0.20) for the Flanges in Compression (FC) loading (Continued)

Images from Table 5-6 indicate a flexural-shear type of failure. The strain and crack patterns show a critical stage in marker 1.FC from Figure 5-11. The finite element results from ATENA indicate severe damage localization at the base of the wall; wide horizontal flexural cracks develop extensively along the outer face of the wall's web, reaching a maximum calculated crack width of approximately 3.00 mm and propagating toward the flanges. This concentration of horizontal cracking at the lower base highlights the formation of a primary plastic hinge zone. The strain at the flange tips near the base shows high compressive strains, with a maximum compressive strain of approximately 0.0099, which significantly exceeds the typical unconfined concrete crushing strain limit (generally taken as -0.003 to -0.0035). This high strain demand is concentrated in the localized plastic hinge region at the foundation interface, confirming severe concrete crushing and cover spalling in these heavily demanded zones, while the upper stories remain relatively undamaged.

At marker 1.FC, out-of-plane displacements develop in the Y-direction, revealing a clear out-of-plane pattern developing along the cross-section profile, particularly within the first and second stories of the U-shaped wall. Near the base and close to the web-flange intersection, the flanges tend to deform outward. Conversely, at higher elevations above mid-height, the flange tips exhibit inward displacement. Nonetheless, the maximum out-of-plane displacements reach only approximately 0.3mm, indicating that these localized movements are not substantial enough to trigger a major global stability failure at this loading stage. Furthermore, these specific out-of-plane patterns are suppressed in later loading stages, where dominant flexural-shear failure mechanisms take over.

At marker 3.FC, just before the structure plummets in terms of lateral capacity, Table 5-5 records a maximum horizontal crack width of 2.7 cm in the web at an elevation of 0.45m from its base, approximately 1/3 of the first-floor clear height, outlining a diagonal compressive strut that extends from the base of the flanges into the web. This compression strut develops at an inclination angle of approximately 30˚, closely matching both the observed cracking patterns and the localized failure mechanism documented in the experimental benchmark pushover analysis.

Finally, regarding the reinforcement response, the numerical model indicates that at Marker 1.FC, the steel reinforcement reaches a strain of 0.02, representing approximately 20% of its ultimate strain capacity. The first drastic drop in lateral load strength is observed at Marker 2.FC, where the 6mm reinforcement exceeds its ultimate strain capacity and fractures. Consequently, the remaining boundary elements and flanges must withstand the redistributed flexural demands. Beyond this point, geometric nonlinearity becomes highly evident. If the reinforcement is modeled considering material nonlinearity only (represented by the dotted lines in Figure 5-11), the post-peak capacity degrades more gradually because the longitudinal reinforcement continues to sustain the structural demands. Conversely, when geometric nonlinearity is considered linear, the structural response plummets much more rapidly toward its residual lateral load capacity.

	v=0.2 (1.FC)	v=0.2 (2.FC)	v=0.2 (3.FC)
Strain (XX)	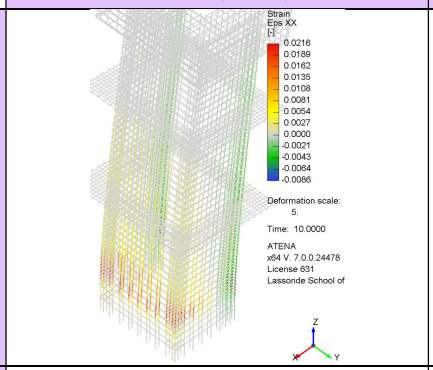	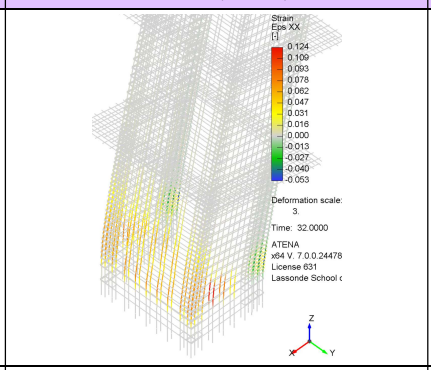	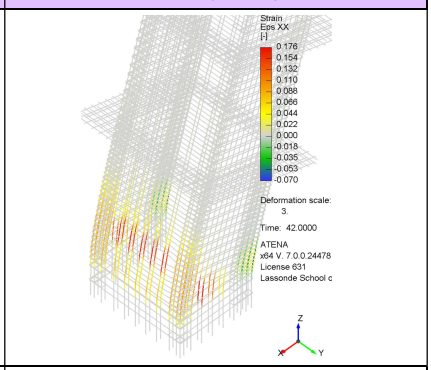
Strain (XX) of boundary Elem	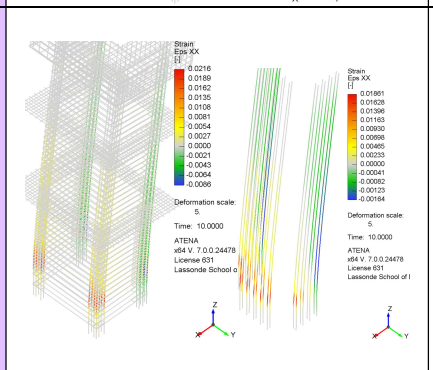	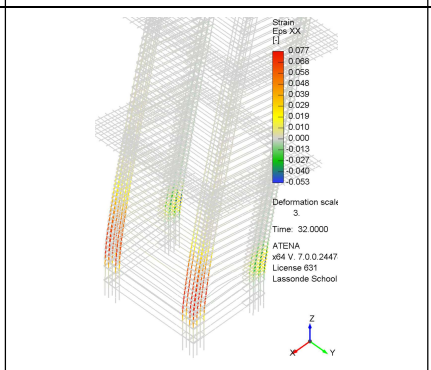	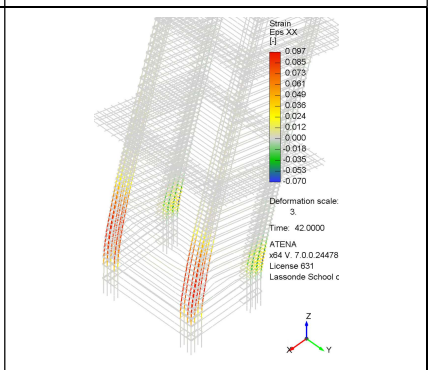
Plastic Strain (XX)	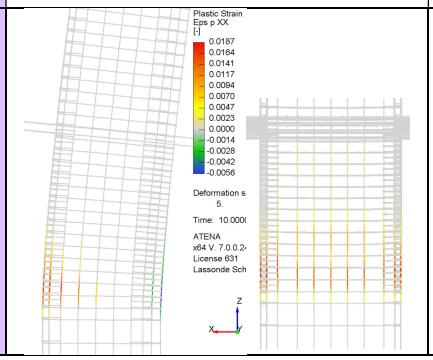	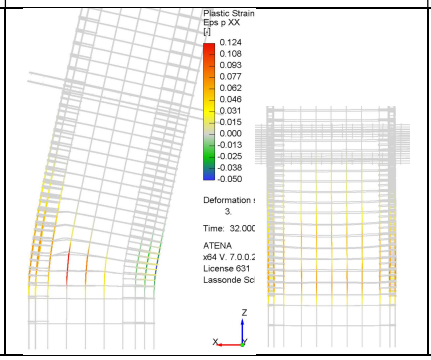	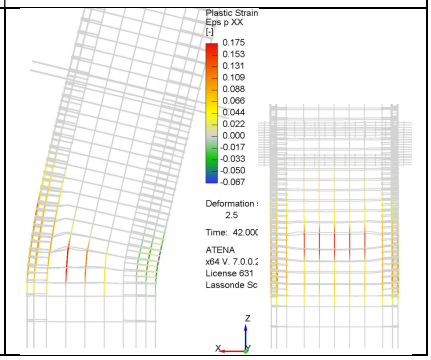

Table 5-7 Numerical response parameters and damage indicators for the wall's reinforcement under axial load ratio (ν=0.20) under Flanges in Compression (FC) loading.

When evaluating the bond-slip behavior of the reinforcement at the base of the wall (Figure 5-12), an increase in slip of 0.16mm is observed relative to the benchmark pushover analysis. Although this represents a significant increase in slip demand, the absolute value remains well within the structural bond capacity (see Figure 4.26). Consequently, there is no evidence of significant bond slippage or anchorage failure along the development length.

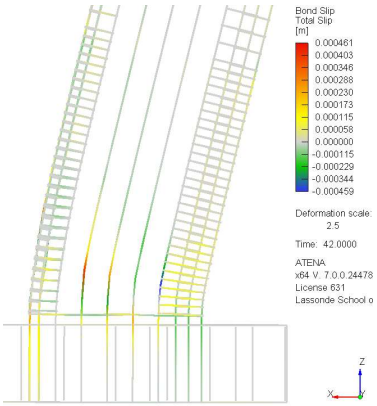

Figure 5-12 Bond Slip reinforcement under Flanges in Compression (FC)

Evaluating the wall in the other direction, clear evidence of shear-flexural failure is also observed. In Table 5-8, wide vertical and inclined flexural-shear crack widths are evident propagating along the tensile zones. The maximum principal tensile strains and corresponding principal plastic strains localize primarily in the lower-story boundary regions. At marker 1.FT, there is significant extensive concrete cracking and progressive yielding of the embedded reinforcement core. Conversely, the minimum principal strains and minimum plastic strains remain concentrated within the heavily compressed web elements, indicating that the cross-section is approaching its concrete crushing threshold but has not yet experienced catastrophic spalling.

At marker 2.FT, the horizontal and diagonal crack widths expand significantly, resulting in severe macro-cracking fields near the foundation interface. This damage localization correlates with an extreme concentration of maximum principal plastic strains, signaling severe degradation of the concrete matrix. Minimum principal strain distributions indicate widespread concrete crushing at the base.

Concurrently, minor out-of-plane displacements develop across the cross-sectional profile. These localized out-of-plane patterns reveal a mild secondary deformation mode within the first and second stories, though they remain well within stable geometric bounds at this peak limit.

	v=0.2 (1.FT)	v=0.2 (2.FT)
Crack width (m)	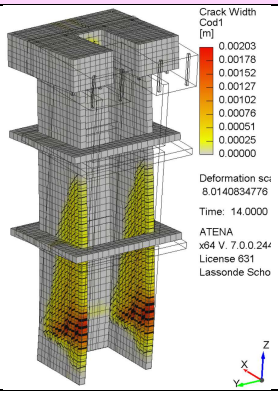	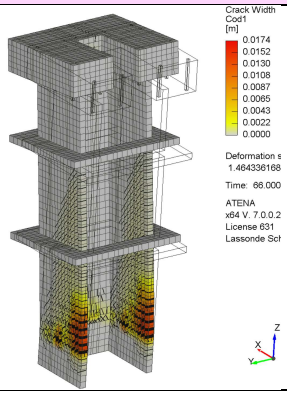

Table 5-8 Numerical response parameters and damage indicators for the walls under axial load ratio (v=0.20) under Flanges in Tension (FT) loading

	v=0.2 (1.FT)	v=0.2 (2.FT)
Principal Strain (Max)	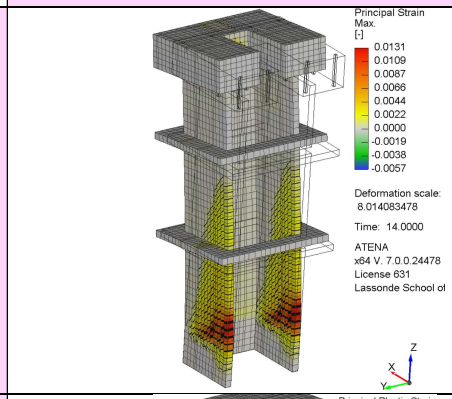	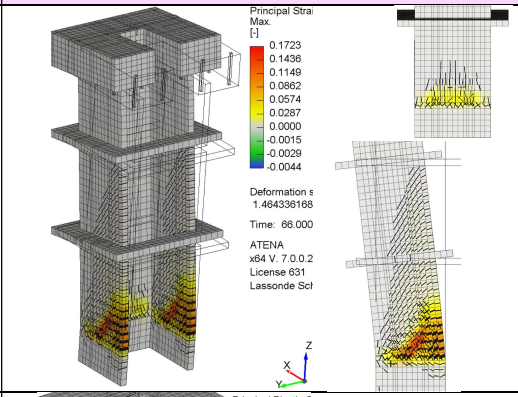
Principal Plastic Strain (Max)	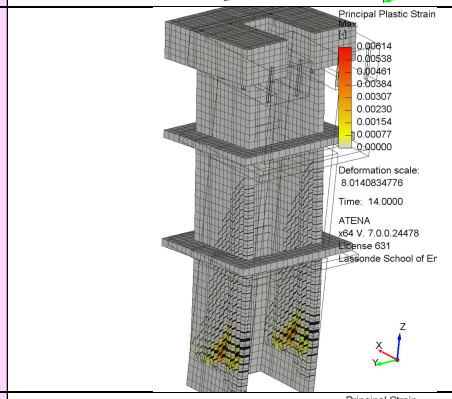	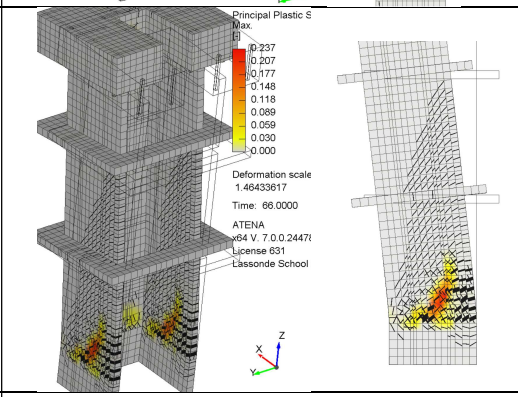
Principal Strain (Min)	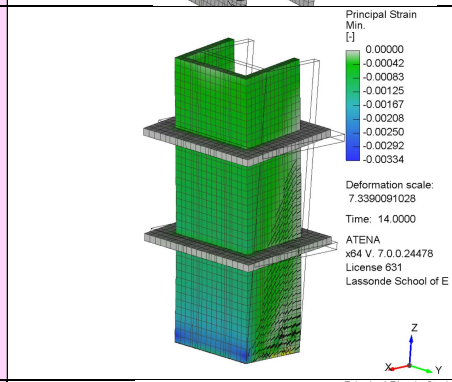	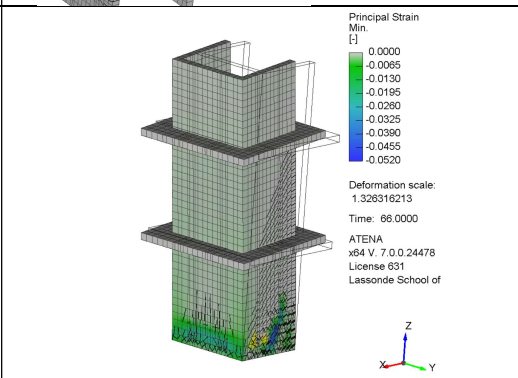
Principal Plastic Strain (Min)	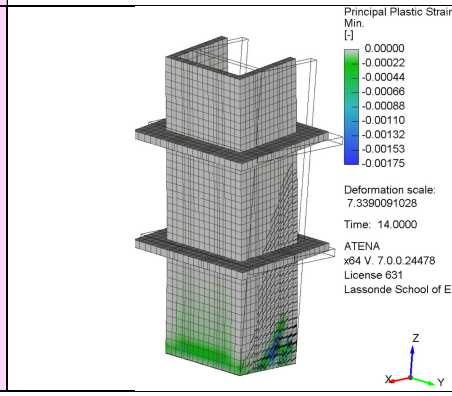	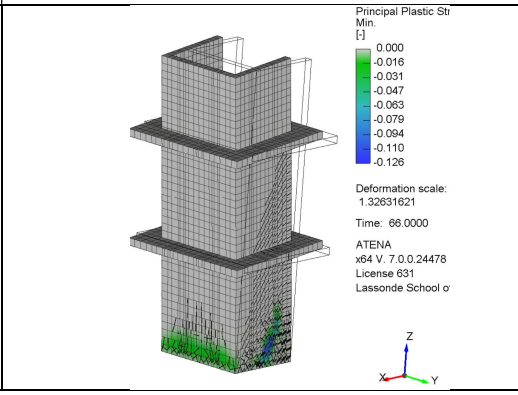

Table 5-8 Numerical response parameters and damage indicators for the walls under axial load ratio (v=0.20) under Flanges in Tension (FT) loading (Continued)

	v=0.2 (1.FT)	v=0.2 (2.FT)
Displacement out of plane	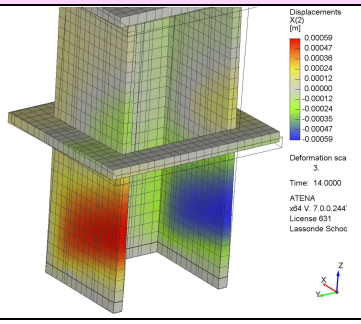	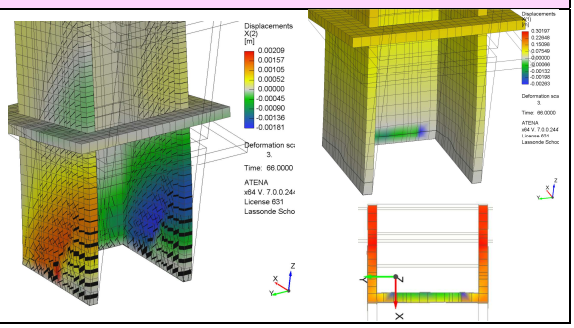

Table 5-8 Numerical response parameters and damage indicators for the walls under axial load ratio (v=0.20) under Flanges in Tension (FT) loading (Continued)

The evaluation of the reinforcement parameters (Table 5-9) shows that both normal and plastic strains have increased rapidly. Specifically, within the boundary elements, the longitudinal bars experience significant tensile demands, providing the primary mechanism that keeps the structural flexural demands stable. At marker 2.FT, the explanation for the sharp drop in lateral load resistance becomes evident. The normal and plastic tensile strains within the boundary elements exceed their ultimate uniform elongation limits, leading to sequential reinforcement fracture. This loss of rebar continuity drastically impairs the remaining cross-sectional moment capacity, causing a rapid decline in residual lateral load capacity.

	v=0.2 (1.FT)	v=0.2 (2.FT)
Strain (XX)	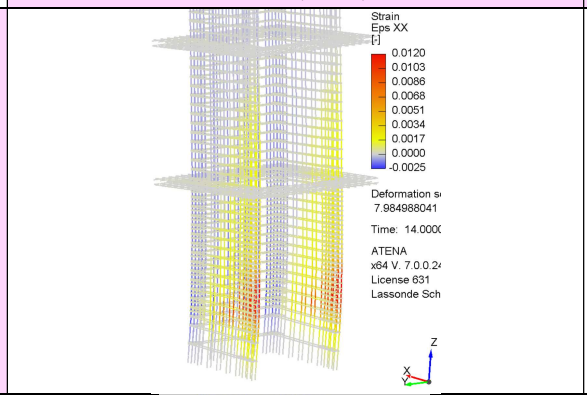	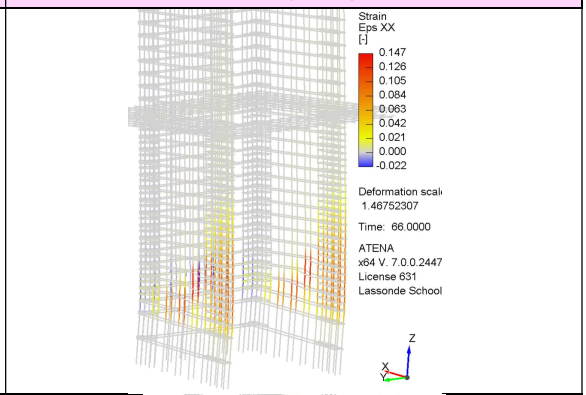
Strain (XX) of boundary Elem	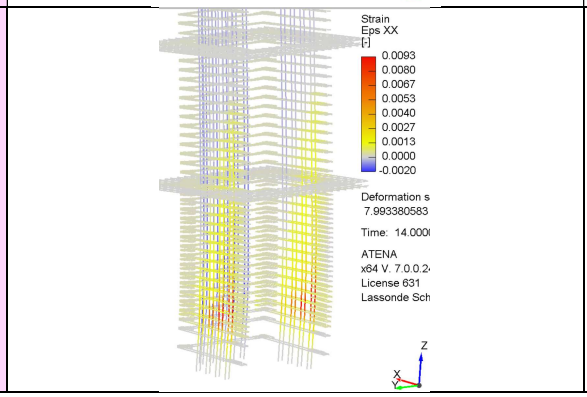	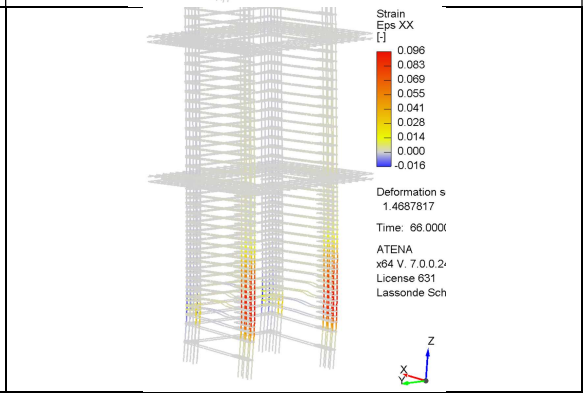

Table 5-9 Numerical response parameters and damage indicators for the wall's reinforcement under axial load ratio (v=0.20) under Flanges in Tension (FT) loading

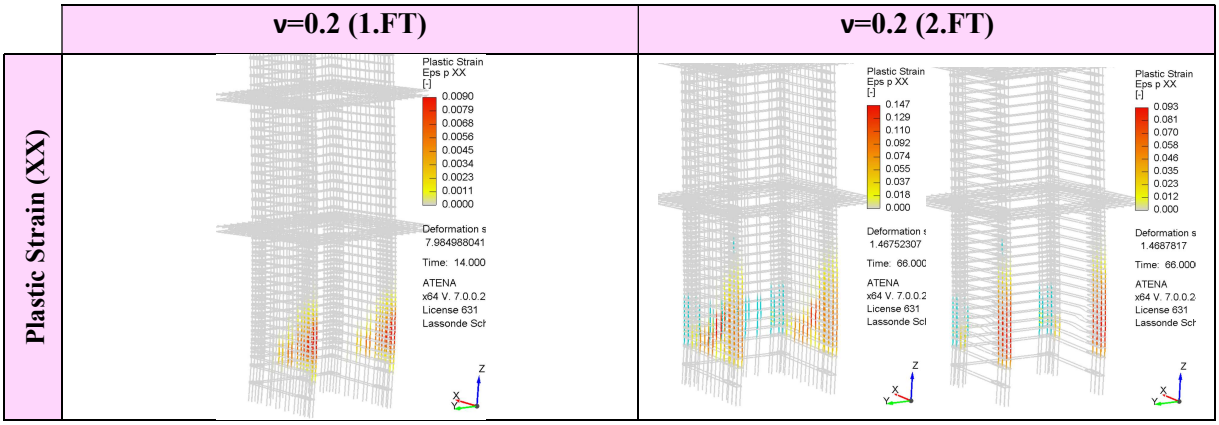

Table 5-9 Numerical response parameters and damage indicators for the wall's reinforcement under axial load ratio (ν=0.20) under Flanges in Tension (FT) loading (Continued).

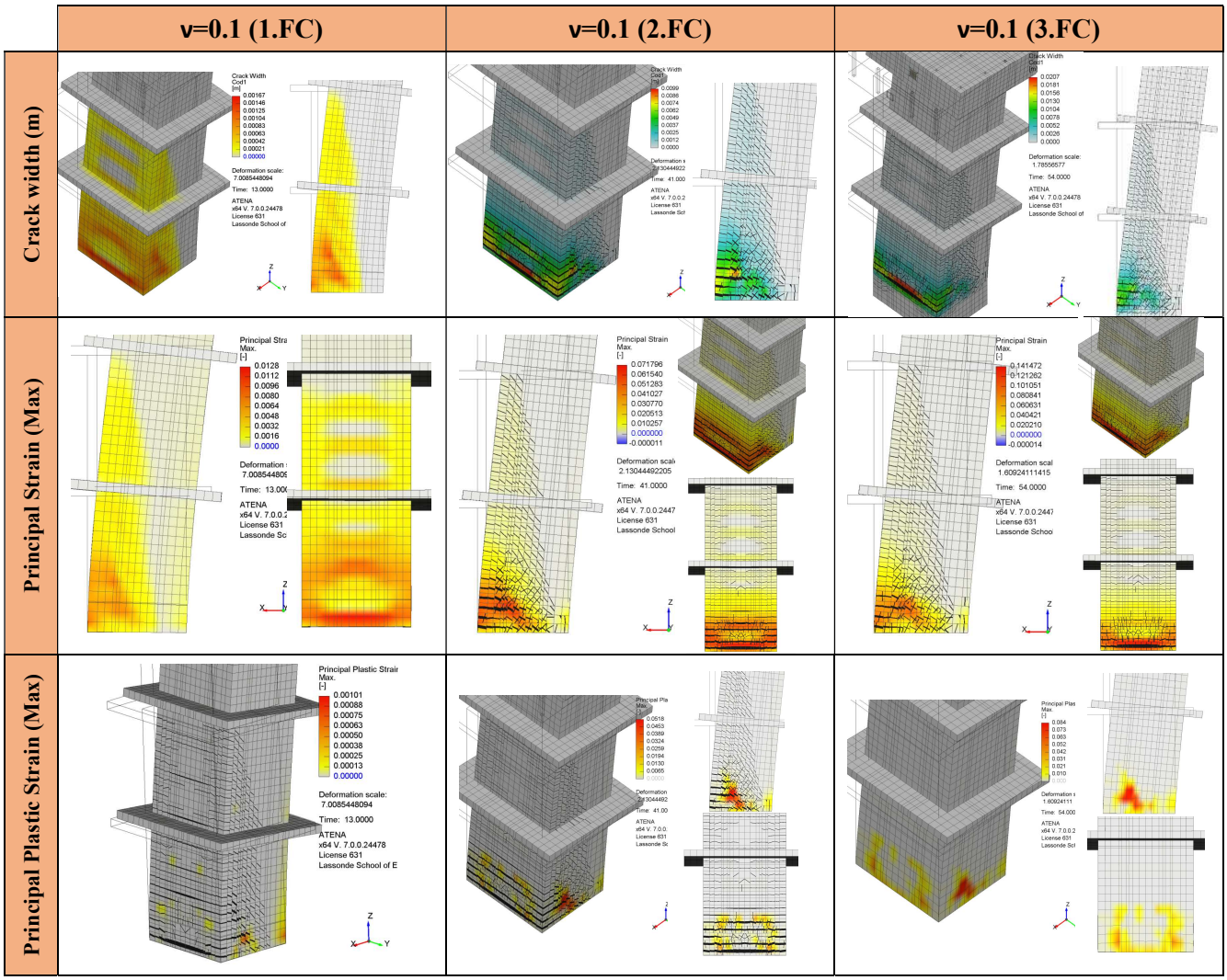

Table 5-10 Numerical response parameters and damage indicators for the wall under Axial load ratio (ν=0.10) under Flanges in Compression (FC) loading

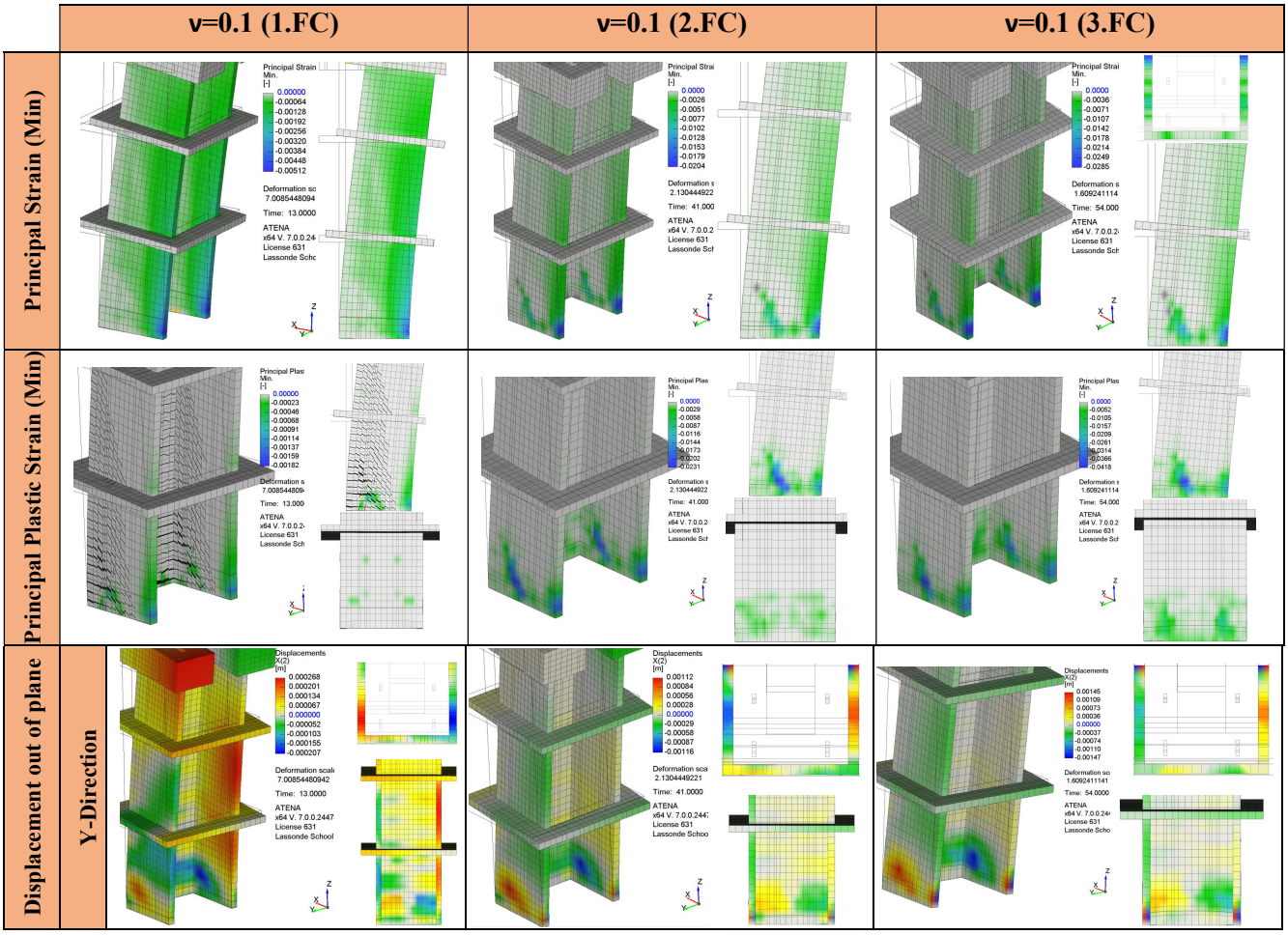

Table 5-10 Numerical response parameters and damage indicators for the wall under Axial load ratio (ν=0.10) under Flanges in Compression (FC) loading (Continued).

Behavior under Flanges in Compression (FC) Loading (ν=0.10) Evaluation at Marker 1.FC (Peak Capacity Window) indicates a gradual evolution of horizontal and flexural-shear crack widths. Maximum principal tensile strains and their corresponding plastic offsets localize at the base of the tensile zones (the flange tips) as they experience clear flexural elongation. Minimum plastic compressive strains begin to concentrate near the web-flange intersections, which are subjected to heavy compressive stresses under this loading orientation.

At Marker 2.FC and 3.FC captures a pronounced horizontal crack-width localization in the web at approximately one-third of the first-story height. This damage forms a clear diagonal concrete compressive strut that propagates from the base of the flanges into the web zone. At Marker 2.FC Minimum principal strains and minimum plastic strains expand deeply into the web, signifying the onset of significant concrete crushing and cover spalling at the base. Finally, when reaching 3.FC strains peak drastically at the base of the web, confirming total concrete crushing and structural degradation within the localized plastic hinge.

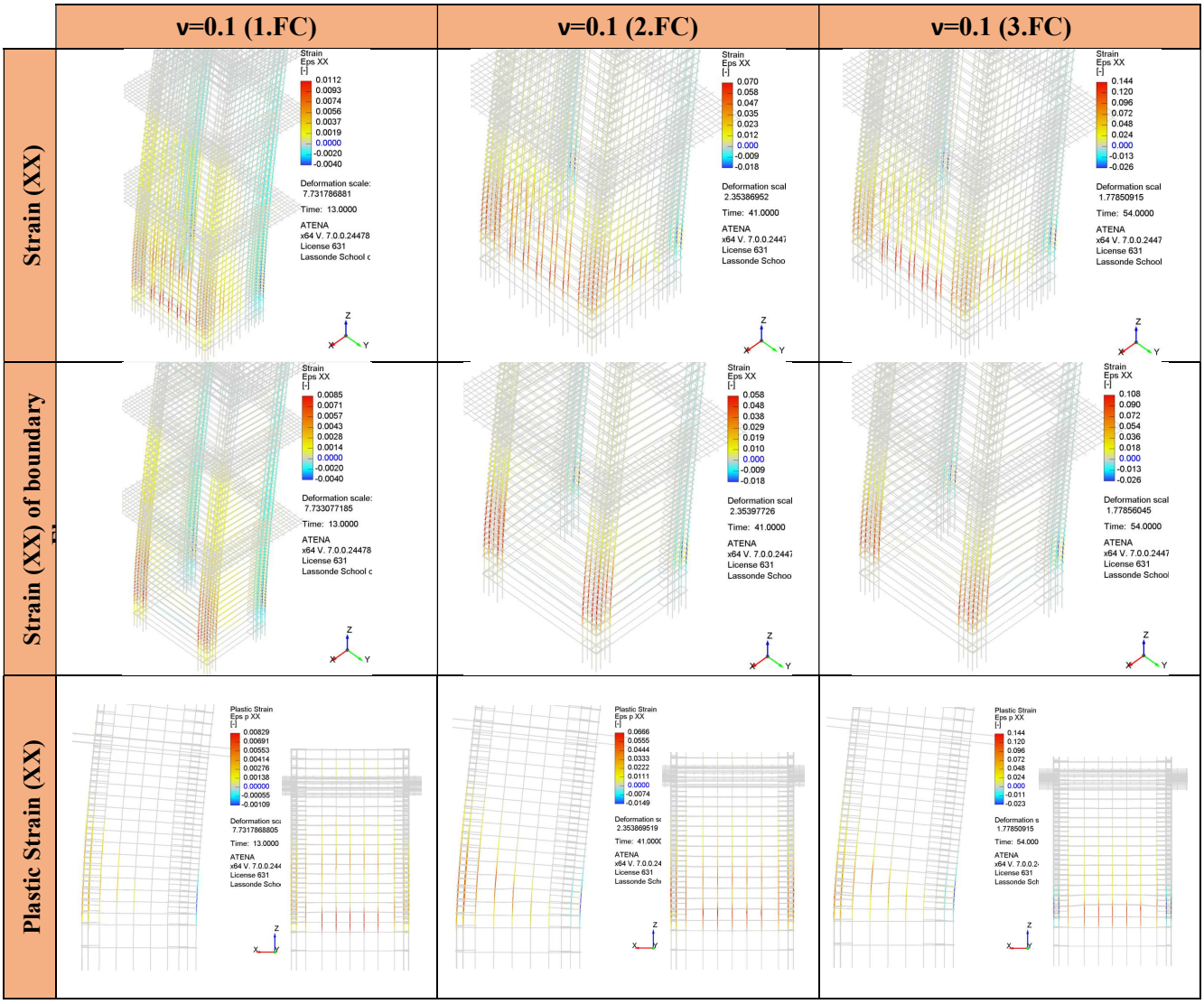

Table 5-11 Numerical response parameters and damage indicators for the wall's reinforcement under axial load ratio (ν=0.10) under Flanges in Compression (FC) loading

According to Table 5-11 (Marker 1.FC), the normal steel strains and accumulated plastic strains remain well within stable bounds. The boundary element longitudinal bars carry the primary flexural tension, ensuring stable load propagation across the cross-section. However, when the structure reaches marker 2.FC, there is a sudden drop in lateral capacity load directly caused by a sudden strain surge where the internal 6mm reinforcement layers reach their ultimate limits and fail. This shifts the remaining flexural demands onto the boundary element longitudinal reinforcement. Finally, at marker 3.FC strains within the boundary element bars reach critical levels. Past this threshold, the flexural capacity plummets instantaneously.

Under reverse FT loading, the wall shows a highly ductile response, reaching an early plastic plateau. Because the flanges are subjected to tension under this loading direction, wide horizontal flexural crack widths form extensively at the base of both flanges, causing a rapid expansion of maximum principal tensile strains and

plastic tensile offsets. As illustrated in Table 5-12 (marker 2.FT), maximum principal plastic strains and crack fields expand significantly along the full length of the tensile flanges. Minimum principal plastic strains at the base of the web also begin to increase, indicating gradual compression softening of the concrete core.

	ν=0.1 (1.FT)	**ν=0.1 (2.FT)**
Crack width (m)	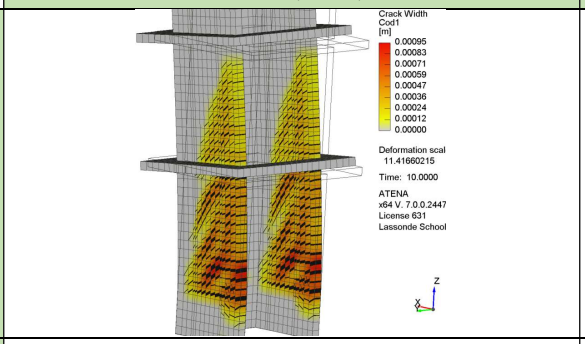	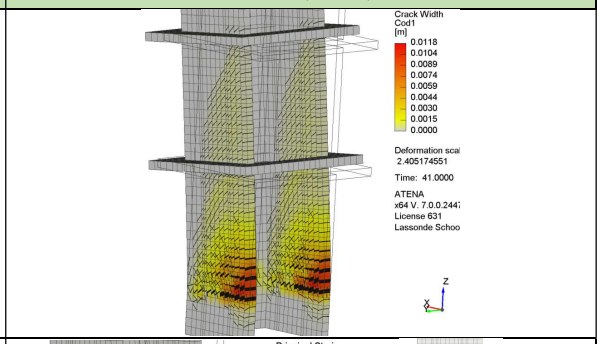
Principal Strain (Max)	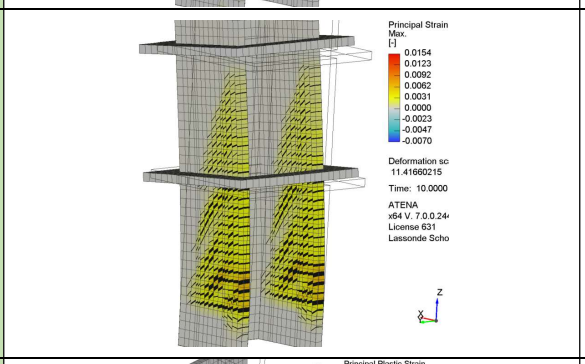	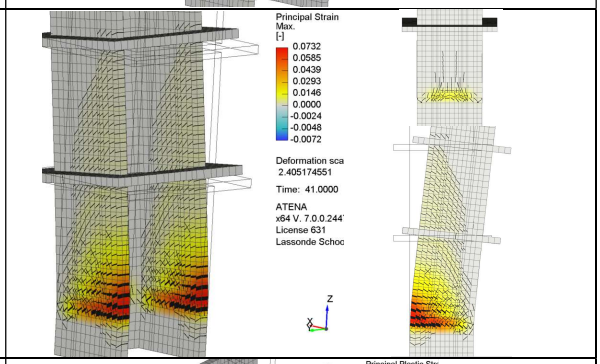
Principal Plastic Strain (Max)	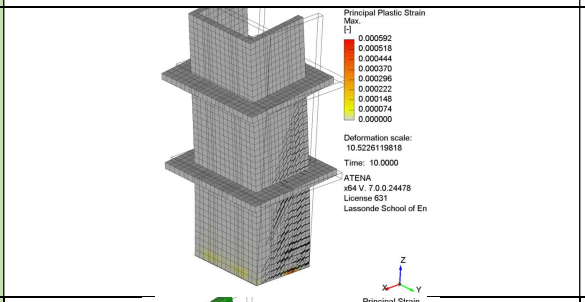	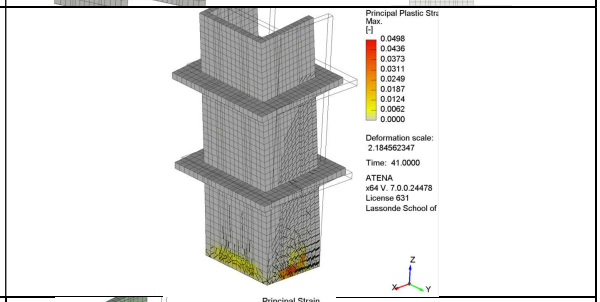
Principal Strain (Min)	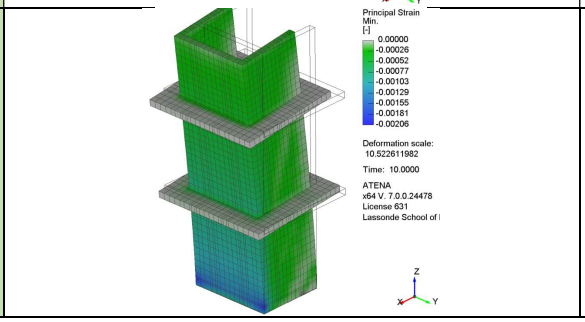	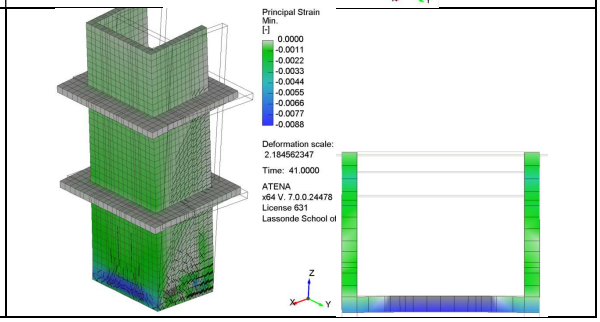

Table 5-12 Numerical response parameters and damage indicators for the wall under Axial load ratio (ν=0.10) under Flanges in Tension (FT) loading

	v=0.1 (1.FT)	v=0.1 (2.FT)
Principal Plastic Strain (Min)	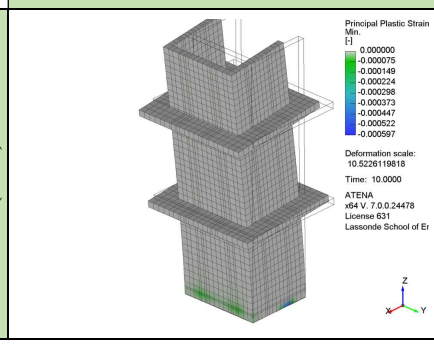	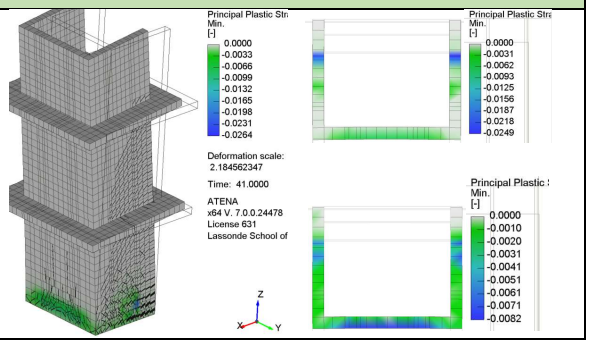

Table 5-12 Numerical response parameters and damage indicators for the wall under Axial load ratio (ν=0.10) under Flanges in Tension (FT) loading (Continued)

Table 5-13 reveals a uniform and substantial increase in normal strains and plastic strains across the flange and boundary longitudinal steel, confirming widespread yielding that supports the ductile plastic plateau observed in the global response. At marker 2.FT, the boundary element longitudinal reinforcement accumulates severe normal and plastic tensile strains. This extensive plastic deformation allows the wall to maintain high energy dissipation capacity over large cyclic drift demands before individual bar fractures initiate the final softening branch.

	v=0.1 (1.FT)	v=0.1 (2.FT)
Strain (XX)	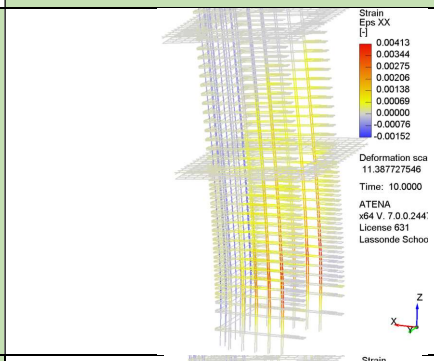	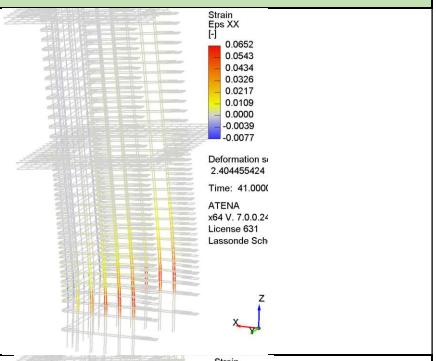
Strain (XX) of boundary Elem	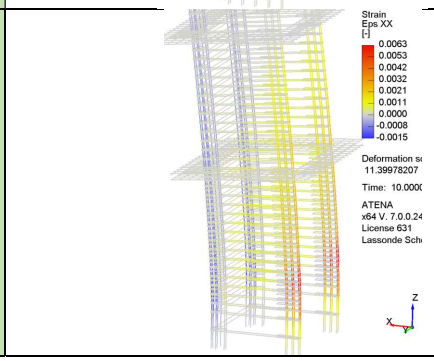	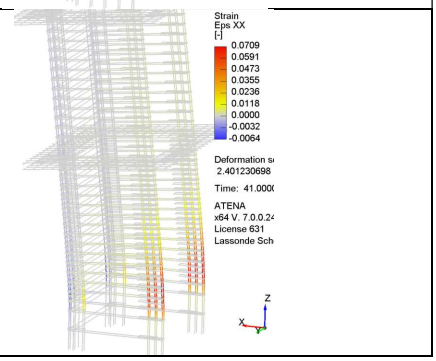

Table 5-13 Numerical response parameters and damage indicators for the wall's reinforcement under axial load ratio (ν=0.10) under Flanges in Compression (FC) loading.

	v=0.1 (1.FT)	v=0.1 (2.FT)
Plastic Strain (XX)	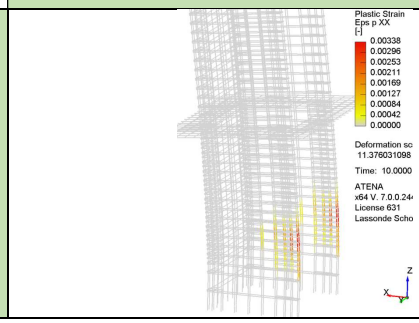	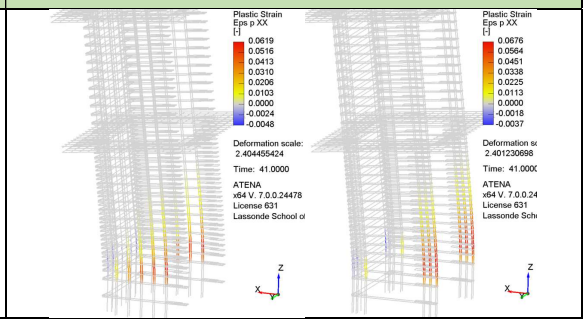

Table 5-13 Numerical response parameters and damage indicators for the wall's reinforcement under axial load ratio (v=0.10) under Flanges in Compression (FC) loading (Continued)

Figure 5-13 illustrates the normal strain distribution at an advanced loading stage past marker 2.FT, immediately prior to the severe degradation of lateral load capacity. The maximum longitudinal steel strain reaches a peak value of approximately 0.089 within the boundary element bars, indicating extensive plastic yielding and suggesting that the boundary reinforcement is approaching its ultimate uniform elongation or fracture limit. The subsequent failure of these primary tensile bars triggers a brittle structural response, indicating that the remaining reinforcement within the flanges lacks the residual capacity to withstand further cyclic demands.

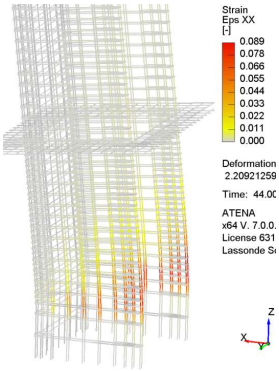

Figure 5-13 Strain of Reinforcement under axial load ratio (v=0.10)

5.3.2 Longitudinal Reinforcement (Boundary Element)

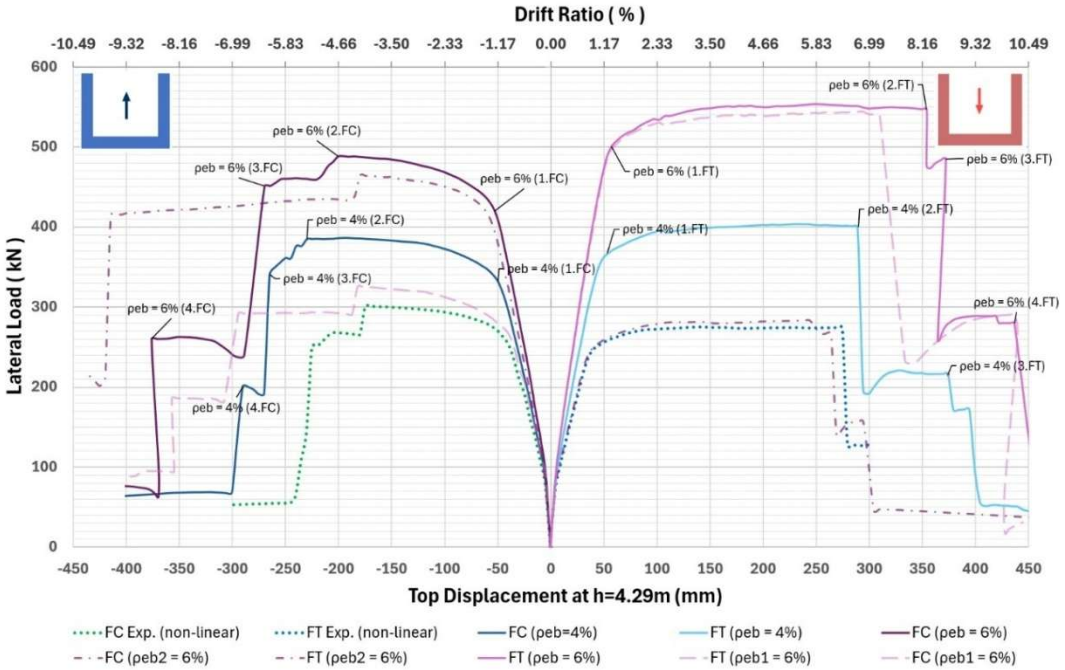

Figure 5-14 Pushover - Parametric study of Boundary Element Reinforcement Ratio

To evaluate the impact of confinement and longitudinal reinforcement areas within the boundary zones, this section compares walls with boundary element reinforcement ratios of 4% and 6%. The pushover analysis curves are plotted in Figure 5-14, while localized damage states at critical performance markers are captured via finite element field outputs.

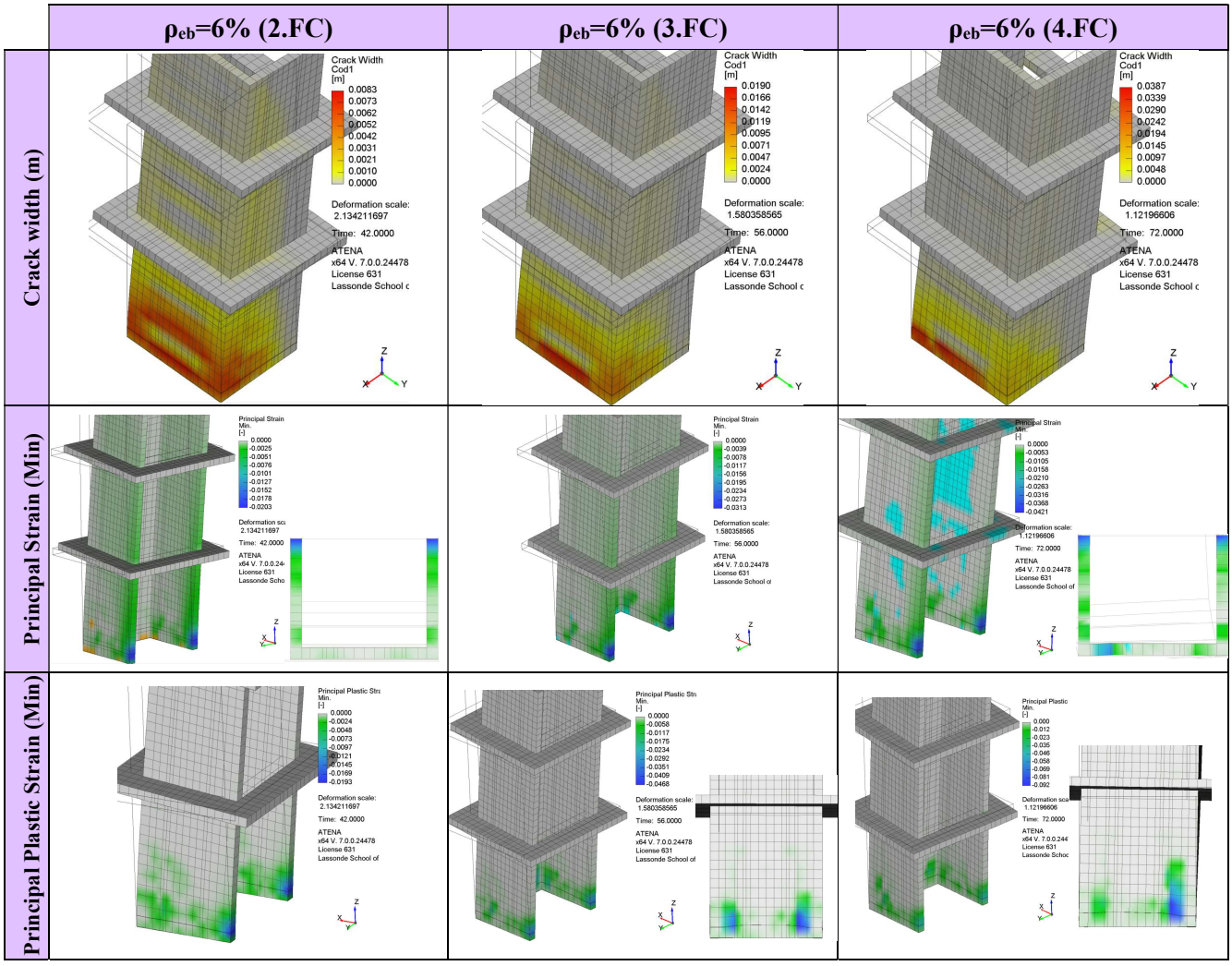

Table 5-14 Numerical response parameters and damage indicators for the walls with boundary reinforcement ratios (ρ_{eb} =6%) for the flanges in Compression (FC) loading

	ρ_{eb}=6% (2.FC)	ρ_{eb}=6% (3.FC)	ρ_{eb}=6% (4.FC)
Strain (XX)	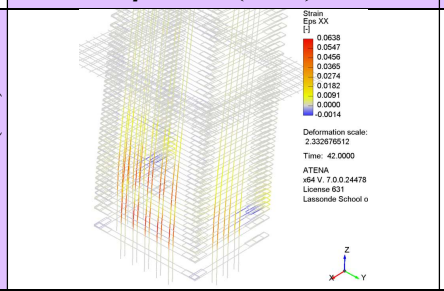	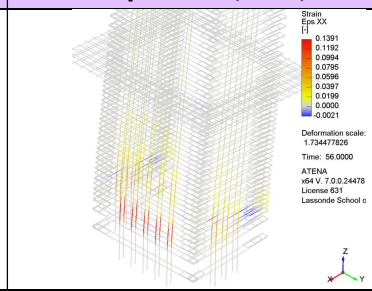	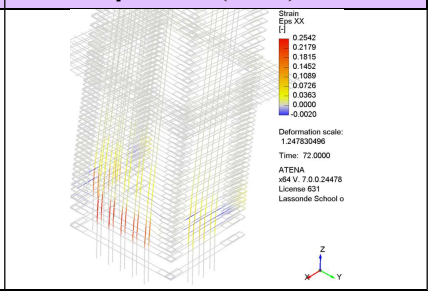
Strain (XX) of boundary	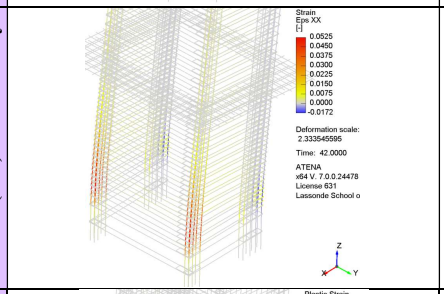	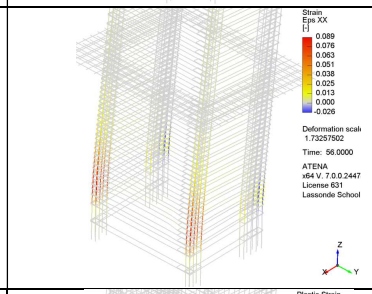	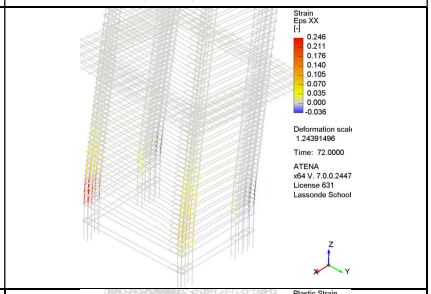
Plastic Strain (XX)	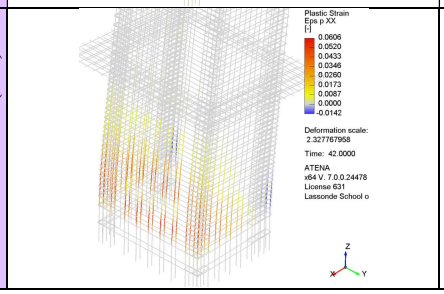	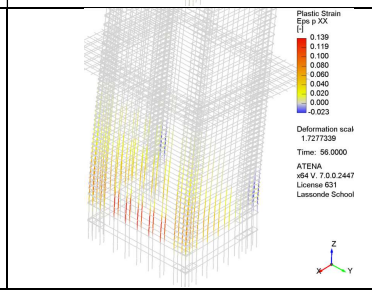	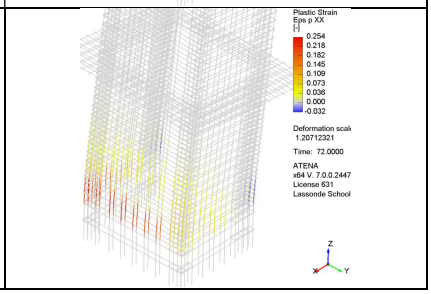

Table 5-15 Numerical response parameters and damage indicators for the wall's reinforcement with boundary reinforcement ratios (ρ_{eb} =6%) for the Flanges in Compression (FC) loading

For the wall with an elevated boundary reinforcement ratio ($\rho_{eb} = 6\%$) under Flanges in Compression (FC) loading, the progressive failure mechanism is characterized by a sequential interaction between material degradation and structural softening across the post-peak markers (Table 5-15). At Marker 2.FC, which corresponds to the peak lateral load plateau of approximately 490kN, the concrete matrix suffers initial damage localized at the base, manifested by expanding horizontal crack widths and an accumulation of minimum principal compressive strains at the extreme compressed boundary zones. As displacement demands intensify toward Marker 3.FC, a sudden reduction in lateral resistance occurs; this drop is physically governed by severe concrete crushing and cover spalling at the foundation interface, quantified by a dramatic spike in the minimum principal plastic strains coupled with the sudden yielding and subsequent failure of the internal 6mm horizontal web reinforcement. Finally, at Marker 4.FC, the structure settles into its residual capacity stage. Here, although the concrete crushing zone extends deeper into the web and the out-of-plane geometric instabilities in the lower stories become more pronounced, the high-density longitudinal reinforcement in the boundary elements prevents catastrophic unzipping fracture. Instead, these robust boundary bars maintain high plastic tensile strains,

stabilizing the remaining cross-section and allowing the heavily degraded wall to retain a controlled, transitional residual strength rather than undergoing instantaneous global collapse.

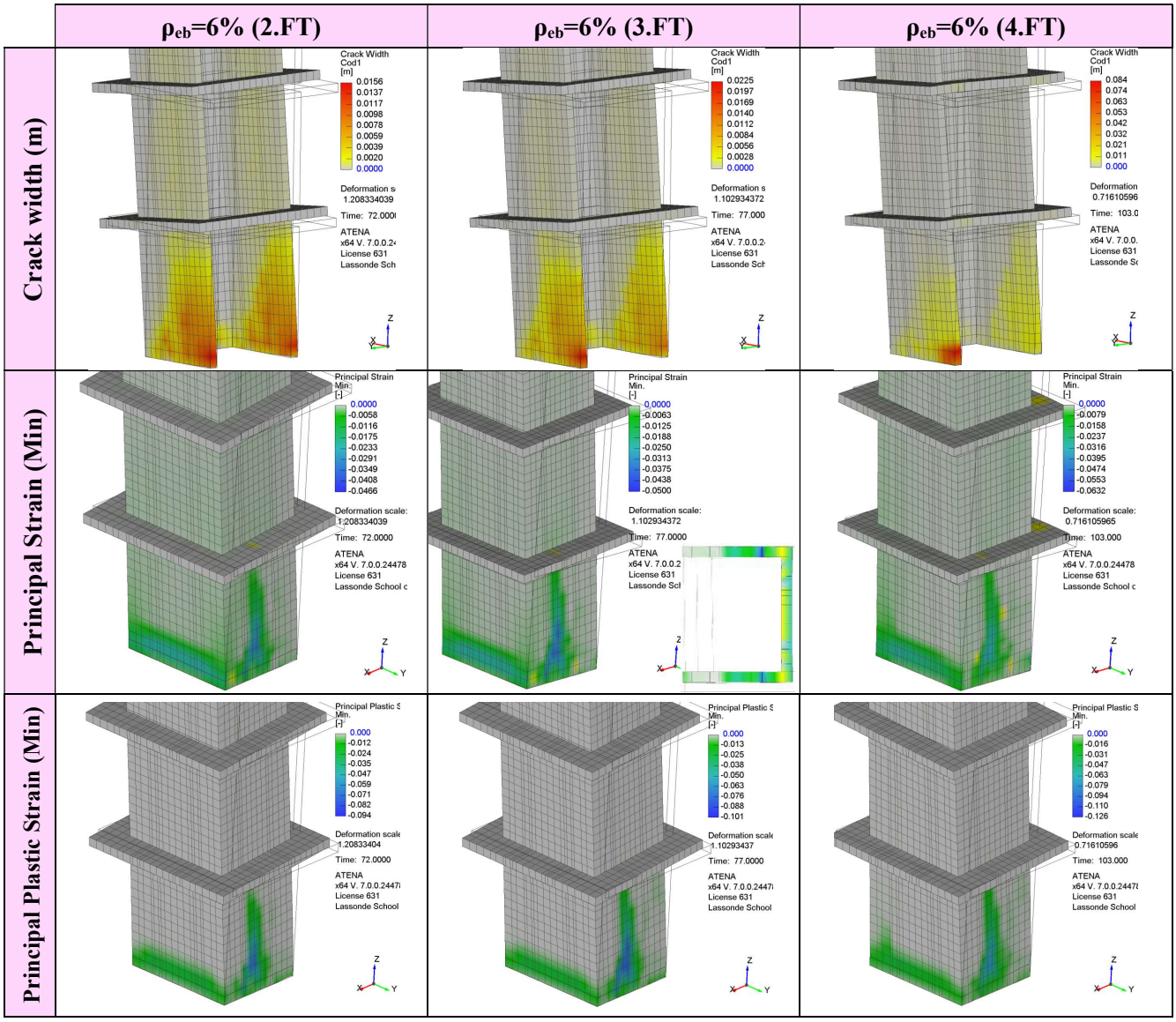

Table 5-16 Numerical response parameters and damage indicators for the walls with boundary reinforcement ratios (ρ_{eb} =6%) for the Flanges in Tension (FT) loading

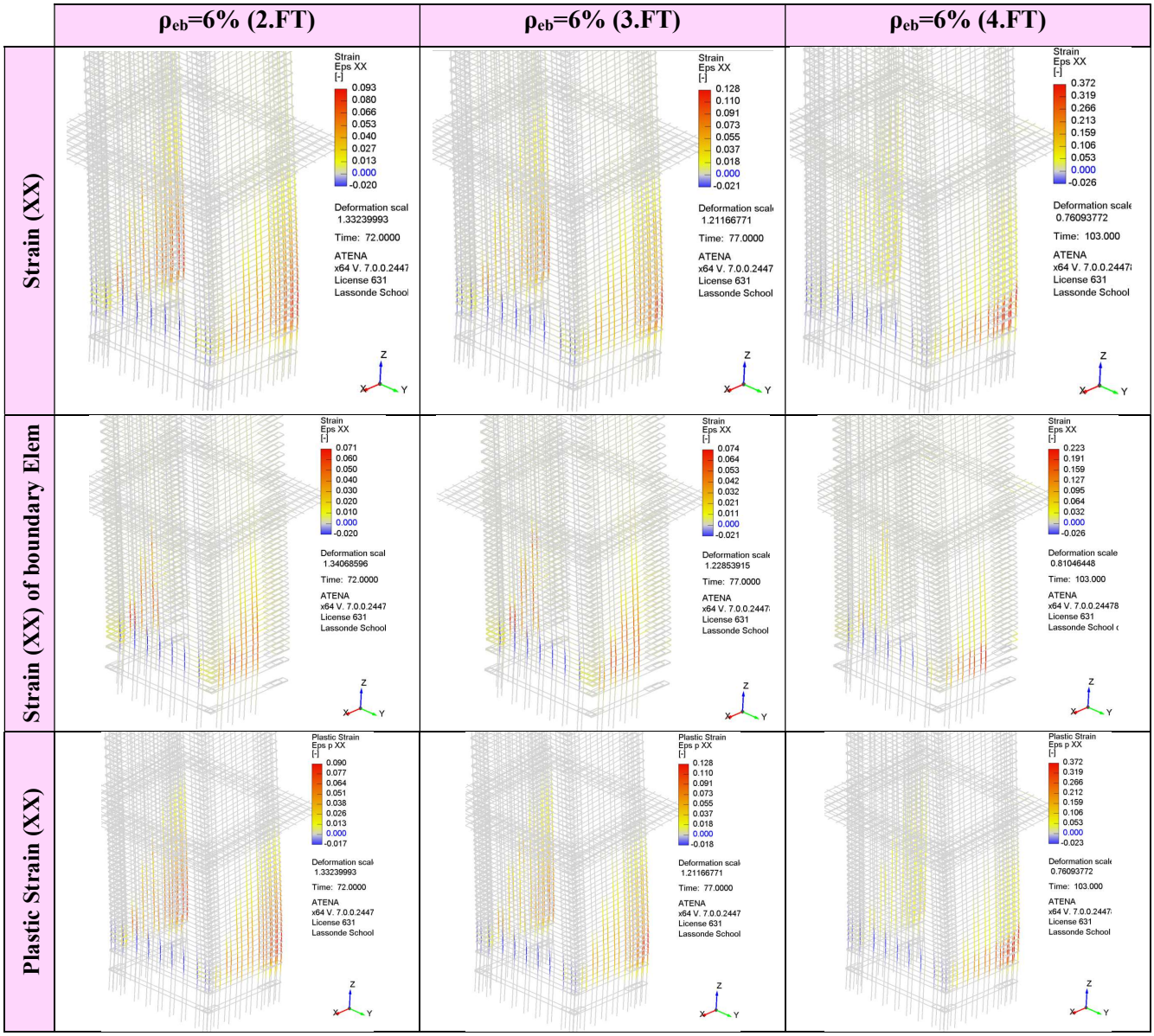

Table 5-17 Numerical response parameters and damage indicators for the wall's reinforcement with boundary reinforcement ratios (ρ_{eb} =6%) for the Flanges in Tension (FT) loading

Conversely, when evaluating the structural response in the reverse direction for the Flanges in Tension (FT) loading, the wall with an elevated boundary reinforcement ratio ($\rho_{eb} = 6\%$) demonstrates highly ductile behavior followed by a distinct post-peak failure mechanism across the advanced thresholds (Table 5-17). At Marker 2.FT, the structure maintains an elongated plastic plateau peaking near its maximum overstrength capacity of approximately 550 kN, where severe horizontal flexural crack widths accumulate uniformly across the tensile flanges, driving extensive yielding in the longitudinal reinforcement core. As displacement demands progress to Marker 3.FT, the first major drop in lateral load resistance occurs; this drop is physically triggered as the normal strains within the boundary element longitudinal steel surpass their uniform elongation capacity

and initiate sequential bar fracture, rapidly transferring the immense tensile demands onto the remaining intact rebar within the flanges. Finally, by Marker 4.FT, the system settles into its residual capacity stage. In this terminal phase, while minimum principal strains and minimum plastic compressive strains widen across the web to capture a late-stage localized concrete crushing zone at the base, the global failure mode is predominantly controlled by the exhaustion of the remaining tensile steel. The widespread distribution of high plastic strains throughout the robust boundary configuration prevents an instantaneous collapse, resulting in a controlled, transitional reduction in flexural capacity toward its residual lateral load plateau.

	ρ_{eb}=4% (2.FC)	ρ_{eb}=4% (3.FC)	ρ_{eb}=4% (4.FC)
Crack width (m)	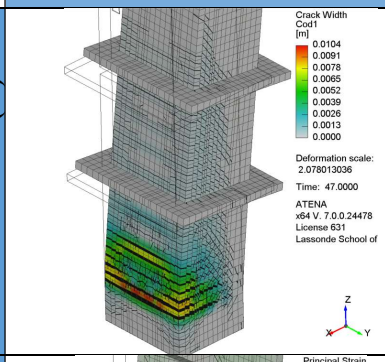	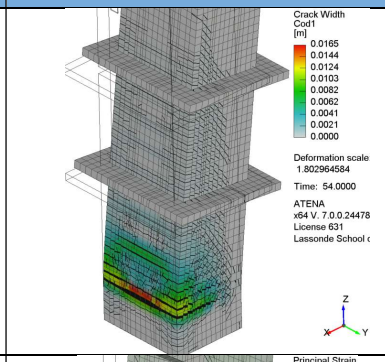	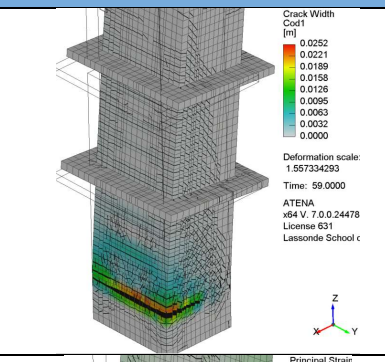
Principal Strain (Min)	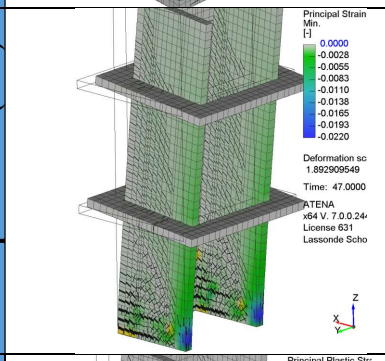	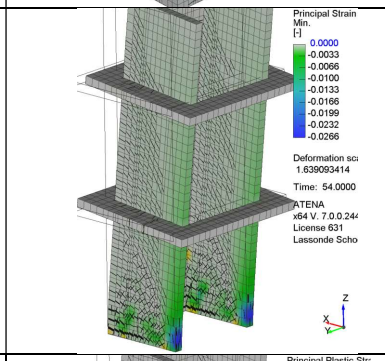	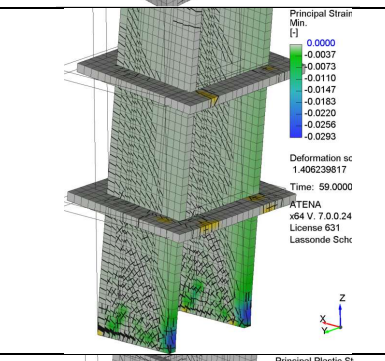
Principal Plastic Strain (Min)	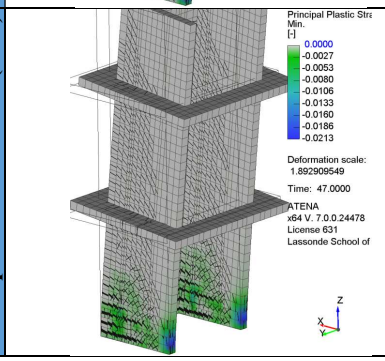	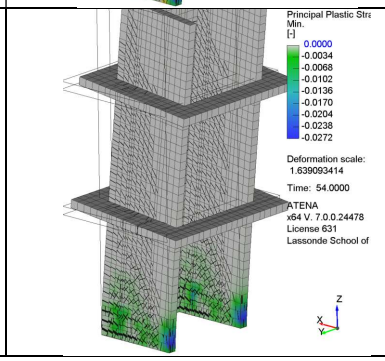	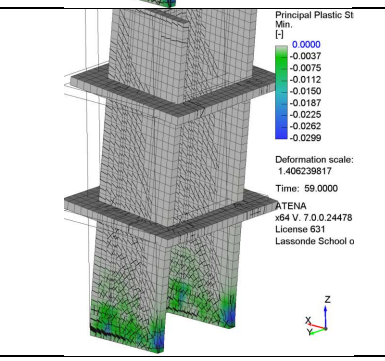

Table 5-18 Numerical response parameters and damage indicators for the walls with boundary reinforcement ratios (ρ_{eb} =6%) for the Flanges in Compression (FC) loading

	ρ_{eb}=4% (2.FC)	ρ_{eb}=4% (3.FC)	ρ_{eb}=4% (4.FC)
Displacement out of plane Y-direction	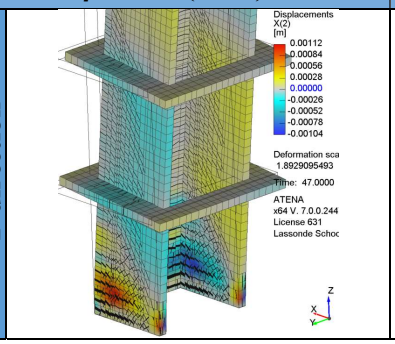	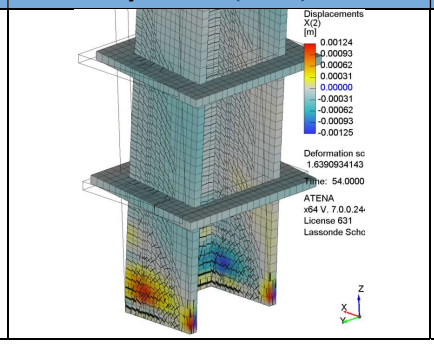	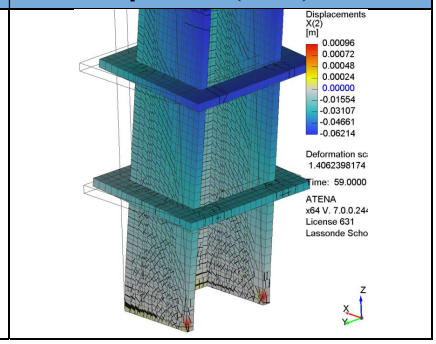

Table 5-18 Numerical response parameters and damage indicators for the walls with boundary reinforcement ratios (ρ_{eb} =6%) for the Flanges in Compression (FC) loading (Continued)

	ρ_{eb}=4% (2.FC)	ρ_{eb}=4% (3.FC)	ρ_{eb}=4% (4.FC)
Strain (XX)	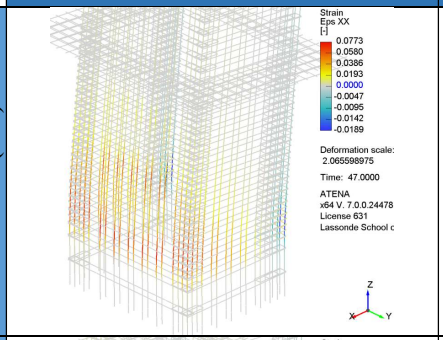	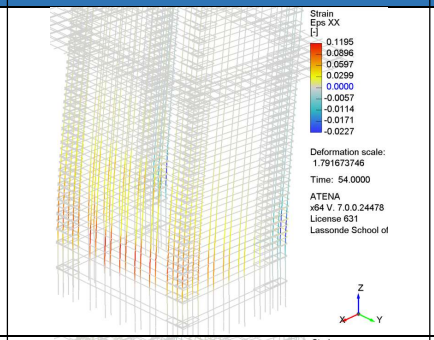	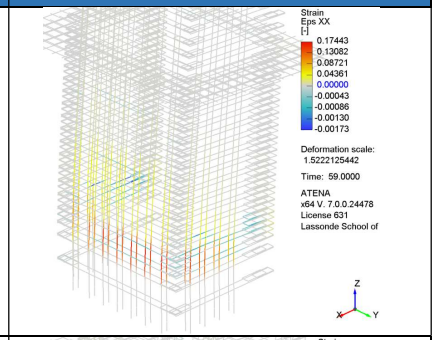
Strain (XX) of boundary	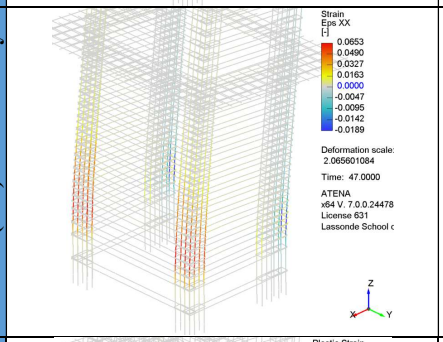	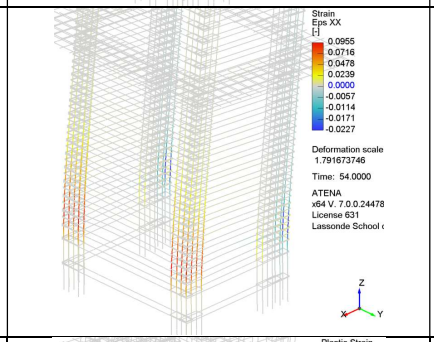	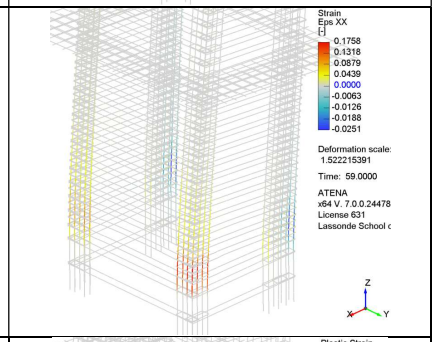
Plastic Strain (XX)	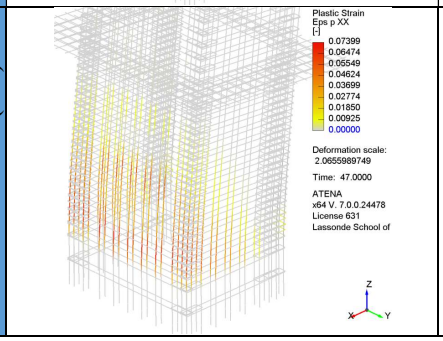	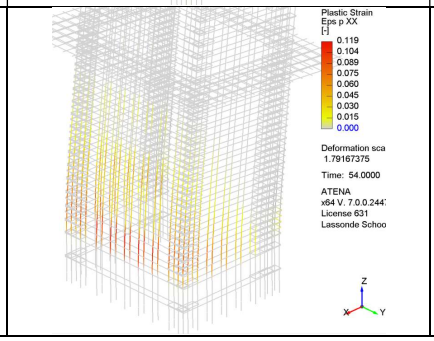	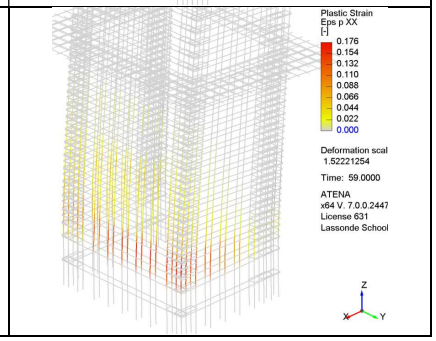

Table 5-19 Numerical response parameters and damage indicators for the wall's reinforcement with boundary reinforcement ratios (ρ_{eb} =4%) for the Flanges in Compression (FC) loading

For the Flanges in Compression (FC) loading, the wall with a lower boundary reinforcement ratio ($\rho_{eb} = 4\%$) exhibits a more rapid and severe degradation sequence across its post-peak markers than its ($\rho_{eb} = 6\%$) counterpart. At Marker 2.FC, where the wall reaches a plateau of approximately 385 kN lateral load, the lower reinforcement density leads to earlier concentration of concrete macro-cracking and minimum principal compressive strains at the base of the wall profile. As displacement demands advance toward Marker 3.FC, the lateral capacity plummets sharply to approximately 200 kN. This severe drop is driven by extensive concrete crushing, indicated by a significant increase in minimum principal plastic strains at the web-flange junctions, acting concurrently with a sharp surge in out-of-plane displacements in the Y-direction across the lower two stories. Unlike the heavily reinforced $\rho_{eb} = 6\%$ wall, which provides robust lateral boundary stability, the $\rho_{eb} = 4\%$ wall undergoes localized out-of-plane buckling deformations that introduce cross-sectional eccentricities and accelerate material destabilization. By the time the structure settles into its residual stage at Marker 4.FC, normal and plastic strains within the boundary elements have become excessively localized.

Because fewer boundary bars are available to redistribute the secondary flexural demands, the longitudinal rebar experiences progressive damage, forcing the structure into a significantly lower residual capacity plateau of roughly 70, which contrasts sharply with the stable, elevated residual plateau of 260 kN sustained by the $\rho_{eb} = 6\%$ reinforcement assembly.

	ρ_{eb}=4% (2.FT)	ρ_{eb}=4% (3.FT)
Crack width (m)	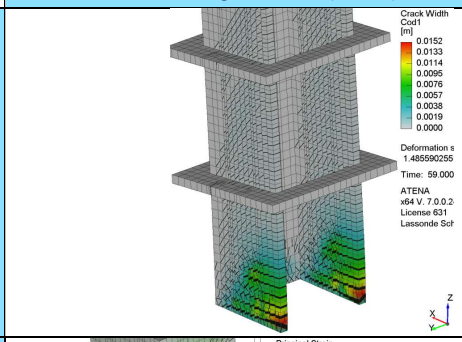	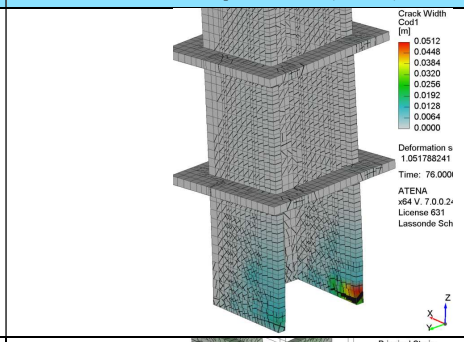
Principal Strain (Min)	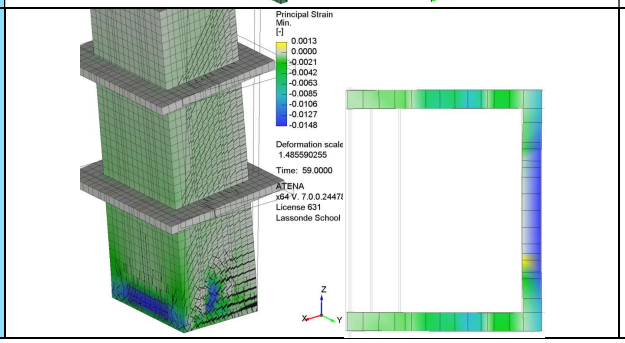	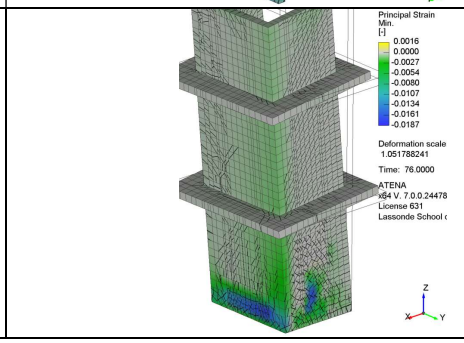

Table 5-20 Numerical response parameters and damage indicators for the walls with boundary reinforcement ratios (ρ_{eb} =4%) for the Flanges in Tension (FT) loading

	ρ_{eb}=4% (2.FT)	ρ_{eb}=4% (3.FT)
Principal Plastic Strain (Min)	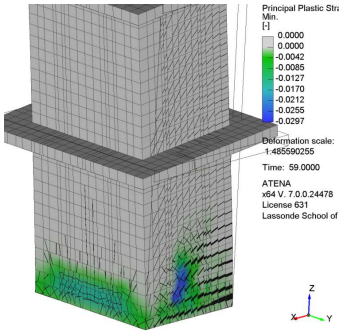	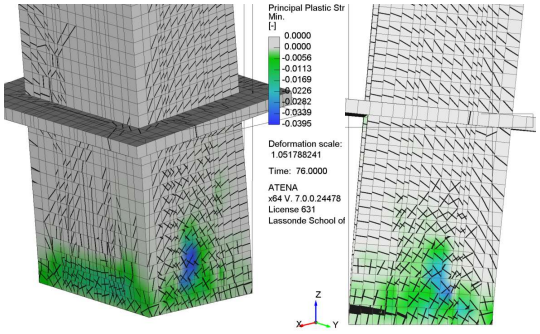
Displacement out of plane (Y-direction)	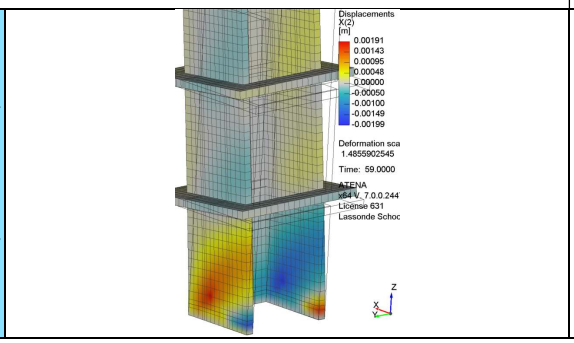	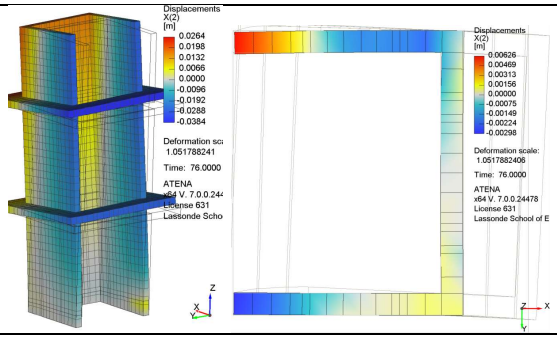

Table 5-20 Numerical response parameters and damage indicators for the walls with boundary reinforcement ratios (ρ_{eb} =4%) for the Flanges in Tension (FT) loading (Continued)

A matching vulnerability to premature damage localization is observed for the reverse Flanges in Tension (FT) loading direction for the $\rho_{eb} = 4\%$ configuration. At Marker 2.FT, the wall reaches a strength plateau near 400 kN, accompanied by widespread horizontal flexural cracking and high normal strains distributed across the tensile flange zones. However, the plastic plateau is significantly shorter than the highly ductile envelope sustained by the $\rho_{eb} = 6\%$ wall.

	ρ_{eb}=4% (2.FT)	ρ_{eb}=4% (3.FT)
Strain	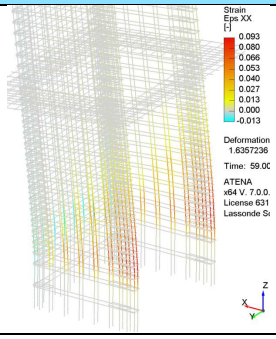	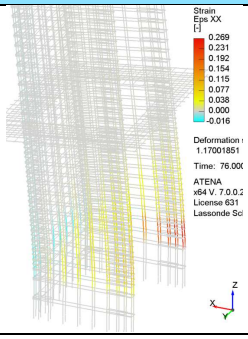

Table 5-21 Numerical response parameters and damage indicators for the walls with boundary reinforcement ratios (ρ_{eb} =4%) for the Flanges in Tension (FT) loading.

	ρ_{eb}=4% (2.FT)	ρ_{eb}=4% (3.FT)
Strain (XX) of 6mm Reinf.	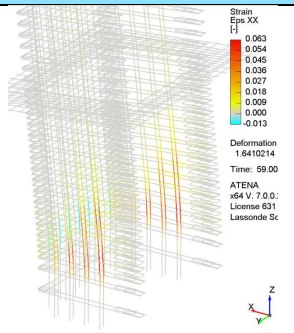	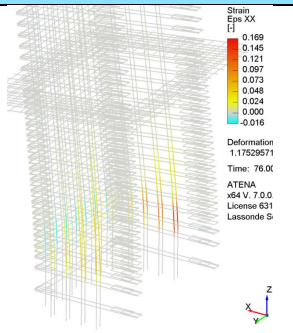
Plastic Strain	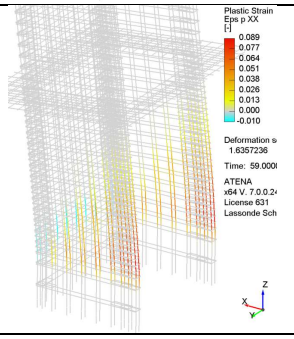	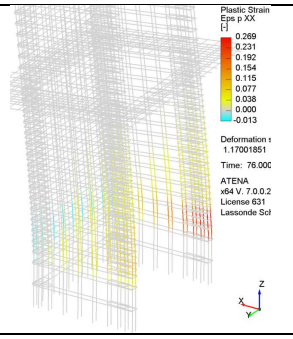

Table 5-22 Numerical response parameters and damage indicators for the walls with boundary reinforcement ratios (ρ_{eb} =4%) for the Flanges in Tension (FT) loading

At Marker 3.FT, the wall undergoes an immediate, severe capacity drop down to a residual load of approximately 220 kN. This brittle drop is governed by the rapid exhaustion of the boundary reinforcement's uniform elongation capacity; the lower volume of boundary steel causes the normal and plastic tensile strains to spike abruptly, triggering sequential bar fractures. This localized rebar failure immediately transfers the high tensile demands to the secondary 6 mm reinforcement distributed within the flanges. Because these smaller diameter bars lack the cross-sectional area to carry the redistributed demands, they yield and fail almost simultaneously. This progressive reinforcement exhaustion triggers late-stage concrete crushing at the base of the web, verified by localized minimum principal plastic strain fields, and induces substantial out-of-plane flange deformation that compromises cross-sectional symmetry and drives the structural response directly into its lower residual strength limit.

5.3.3 Transverse Reinforcement

To isolate the effects of concrete confinement and anti-buckling lateral support within the critical plastic hinge zone, a parametric study focused on transverse reinforcement spacing. Figure 5-15 illustrates the comparative global lateral load-displacement responses for the U-shaped shear walls configured with varying stirrup and tie spacings. Varying the transverse reinforcement directly alters the compressive state of the concrete core and modifies the unsupported length of the vertical boundary bars. With larger stirrup spacing, the boundary elements become more vulnerable to inelastic longitudinal reinforcement buckling under high compressive stresses.

To prevent nonlinear longitudinal reinforcement buckling in confined zones, Section 21.3.2.6.3 of CSA A23.3:24 specifies that the ratio of the transverse reinforcement spacing to the longitudinal bar diameter must satisfy the limit $S/D_b < 5$, when the specified yield strength of the steel exceeds 400 MPa, where D_b represents the diameter of the smallest longitudinal bar in the confinement zone. Because the experimental boundary element configuration utilizes an 8mm diameter longitudinal bar (the smallest bar size within the confinement zone), the code-prescribed maximum spacing limit is 40mm. Furthermore, excessive spacing of transverse reinforcement in the webs and flanges can lead to premature shear failure, significantly reducing the overall lateral load strength.

The numerical curves plotted in Figure 5-15 capture variations in peak lateral load strength, post-peak elongation, and final softening behavior, establishing a clear correlation between tight confinement spacing and enhanced structural ductility. The benchmark curve from the experimental configurations shown in dotted lines is compared with the parametric models.

The solid orange lines represent a configuration where the reinforcement spacing has been reduced by half, resulting in a tight 25 mm spacing for the boundary element ties and a 50mm spacing for the remaining transverse reinforcement. This modification effectively doubles the amount of transverse steel in the first story. Because the flanges are more heavily reinforced, their susceptibility to buckling under compression is reduced, mobilizing a higher compressive capacity. Consequently, this setup slightly increases both ductility and peak strength. However, in the reverse loading direction, lateral strength remains unchanged, while ultimate ductility decreases slightly due to an unclear localized mechanism.

To analyze the specific impact of transverse reinforcement on shear resistance, a model in which the flange and web stirrup spacing was doubled from 100mm to 200mm was evaluated, as represented by the solid green line in Figure 5-10. When the flange is in compression, this wider spacing exhibits negligible deviation from the benchmark response. Conversely, when loaded in the reverse direction, placing the web in compression, clear evidence of reduced structural ductility is observed. This behavior shows that the wall's ultimate failure is

not governed by shear, because reducing shear reinforcement does not significantly alter the global response; thus, the structural boundary conditions maintain a predominantly flexure-dominated limit state.

To further evaluate the localized importance of dense boundary ties, a parametric variant isolated the boundary zones by widening their tie spacing to 200mm while keeping the remaining web and flange transverse reinforcement at 100mm (solid blue line). This configuration shows a pronounced reduction in both absolute lateral strength and plastic ductility capacity. Finally, when the wall is analyzed without the proper prescriptive transverse reinforcement configuration (solid pink line), a severe, uniform degradation in both strength and deformation capacity is observed.

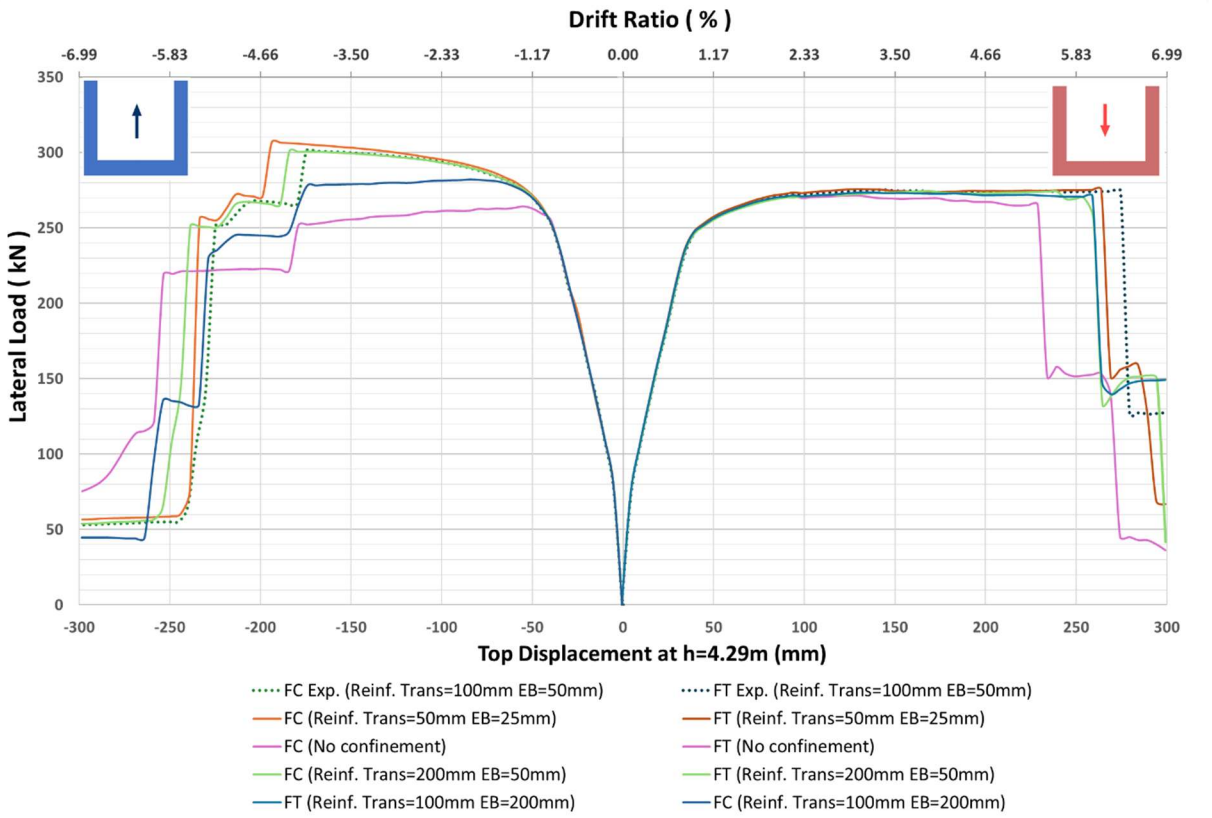

Figure 5-15 Pushover - Parametric study of Transverse Reinforcement spacing

As illustrated by the parametric responses in Figure 5-15, variations in transverse reinforcement and confinement spacing show low sensitivity with respect to global structural behavior. Although peak lateral load capacity and ultimate plastic ductility show minor deviations, the overall force-displacement envelope remains largely uniform across the analyzed configurations. The structure maintains a highly consistent damage progression, scaling similarly under increasing demand and initiating structural softening at similar drift ratios. This indicates that within the evaluated geometric bounds, tightening the transverse reinforcement provides diminishing returns in global strength and deformation capacity, as the failure mechanism remains governed by the primary cross-sectional dimensions and longitudinal reinforcement layouts.

In concrete shear walls subjected to high seismic demands, increasing the transverse reinforcement spacing, particularly within the boundary elements (e.g., the S=200mm case indicated by the blue line in Figure 5-15), makes the longitudinal flange reinforcement more susceptible to compressive buckling than in the benchmark experiment. While Figure 5-15 shows a slight reduction in lateral strength under high flange compression, this specific model configuration does not explicitly capture physical bar buckling. However, this phenomenon can be captured under cyclic loading conditions, where the longitudinal bars in the boundary elements experience alternating high tensile strains (which open cracks) and extreme compressive strains. When the surrounding cover concrete cracks or spalls under tension, these vertical bars lose their continuous lateral support. Consequently, upon load reversal, the combination of lost concrete confinement and excessively wide transverse tie spacing (relative to the longitudinal bar diameter) causes the vertical bars to undergo inelastic buckling under compression. This mechanism triggers an immediate drop in the wall's lateral capacity, a nonlinear phenomenon evaluated in detail within Chapter 6:, Hysteretic Response.

5.3.4 Torsion

Non-planar shear walls, such as U-shaped configurations, are highly susceptible to torsional warping and twist when subjected to eccentric lateral forces or when the center of mass deviates from the center of rigidity. For pushover analysis perpendicular to the axis of symmetry, selecting an appropriate control node for displacement control is challenging because of the geometric complexity. To address this, a hybrid approach was adopted. First, a force-controlled analysis was performed by applying a lateral load pattern proportional to the wall's self-weight, with the gravitational field applied in the direction of study (perpendicular to the axis of symmetry), up to peak lateral capacity. Because force control cannot capture the descending post-peak branch, the analysis was paused at peak capacity and shifted to displacement control on the verge of failure. Using the deformed profile from the final force step as the initial state, the collar was incrementally displaced along the same trajectory, enabling the model to capture the post-peak softening branch smoothly.

Using the baseline pushover curve presented in Figure 5-16 (blue dotted line), which plots the lateral load against the mid-height collar displacement and corresponding drift ratio, the markers in each curve represent the transition between the force-controlled method and the displacement-controlled method. A series of parametric analyses was conducted. These analyses investigate the wall's torsional response under different loading assumptions, varying tributary areas per floor, and applying different axial load levels to the U-shaped wall. The baseline axial load was established by assuming a scaled tributary area of 10m x 10m per floor, factoring in both dead and live loads acting on the slab.

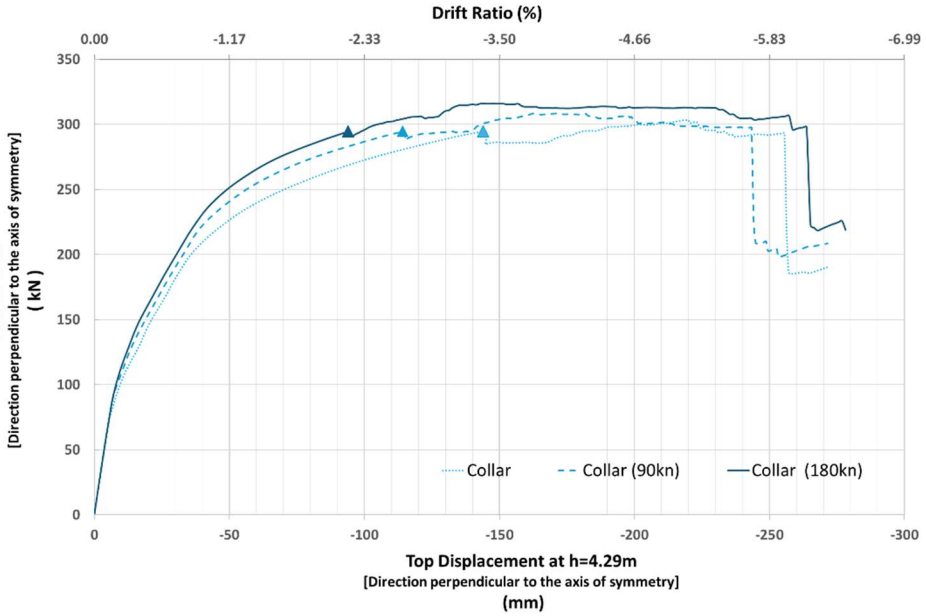

Figure 5-16 Pushover - Parametric study of Torsion with Tributary Load in the Collar

As illustrated in Figure 5-16, the structure exhibits a remarkably high ultimate drift capacity of 5.8%. Interestingly, when the model is subjected to a substantial axial load of 180 kN, it shows an apparent increase in ductility. Conversely, a minor increase in axial load from the baseline to 90kN results in a paradoxical reduction in ductility. This highly sensitive, non-monotonic trend suggests that a standard monotonic pushover analysis may lack the consistency needed to accurately capture complex, interactive failure mechanisms, such as second-order geometric effects combined with cyclic material degradation. Consequently, pushover metrics alone cannot validate this high drift capacity; it must be rigorously evaluated under cyclic demands using a full hysteretic analysis framework.

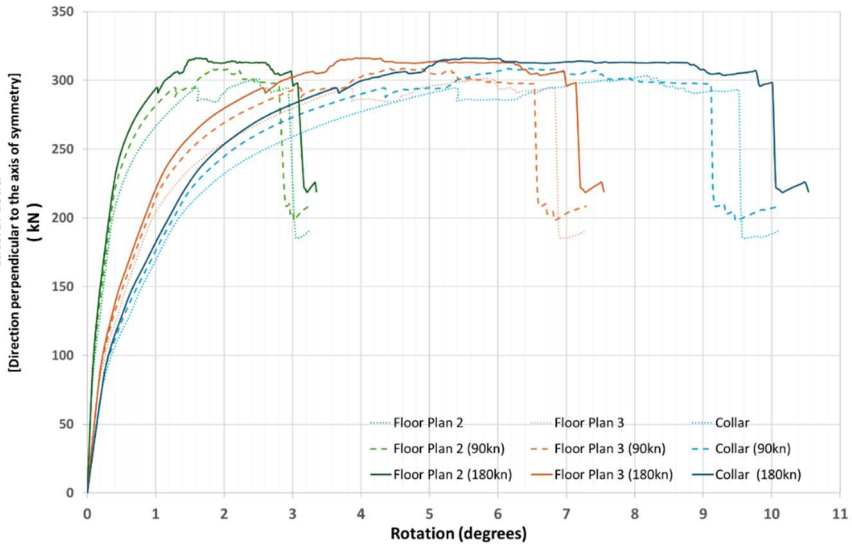

Figure 5-17 Pushover - Lateral load-rotation response perpendicular to the axis of the three-floor level of loading

The collar arrangement allows the wall to twist continuously up to an ultimate rotation exceeding 9.5° before a brittle drop occurs. This prolonged plateau indicates more uniform shear and warping stress redistribution throughout the thin-walled components than under localized floor-plan constraints.

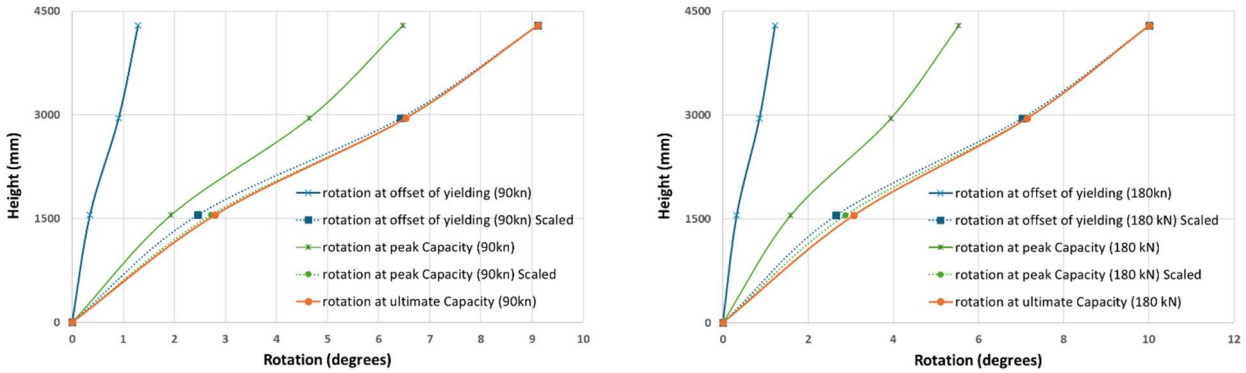

Figure 5-18 Lateral Rotation profiles (a) for an axial load of 90 kN and (b) for an axial load of 180 kN

Figure 5-18 shows that the elastic response (blue line) can be scaled to obtain the ultimate rotation profile. The close agreement between the solid and dotted lines shows that, in the first slab at a height of 1500, it introduces only minor changes to the overall rotation profile, though it slightly reduces the peak twist demands near mid-height.

5.3.5 Lap Splice (l_d)

A critical failure occurs in the lap splice region when it occurs at the wall base, usually near the start-up of the wall, mostly due to construction facilities. This parametric study analyzes several cases. Since the American code (ACI318) recommends avoiding lap splices in the boundary element on the first floor, our first parameter generates lap splices in the flanges and web region, avoiding the confinement regions. A second study ignores this recommendation and adds lap splices to all reinforcement at the start of the wall, where a plastic hinge is likely to form. The lap splice length is the development length calculated from equation 5-1:

$$l_d = \left(0.9 \frac{f_y}{\sqrt{f_c'}} \frac{k_d \; k_l \, k_c \, k_s \, k_g}{\left(\frac{d_{cs} + K_{tr}}{d_b} \right)} \right) d_b \qquad \textit{Eq. 5-1}$$

The parameters used in the equation are shown in Table 5-23. For reinforcement diameters of 6mm and 8mm, calculations showed development lengths below the minimum threshold specified by design standards; consequently, a minimum length of 300mm was modeled. Conversely, for the confined longitudinal bars, lap splice lengths of the calculated 555mm as well as an increased length of 730mm were evaluated to investigate the influence of lap splice length within this critical region.

d_b	*mm*	6	8	12
F'c	*Mpa*	27	27	27
F_y	*Mpa*	550	538	580
K_d		1	1	1
K_l		1	1	1
K_c		1	1	1
K_s		0.8	0.8	0.8
K_g		1.17	1.16	1.20
d_{cs}	*mm*	18	19	21
n		11	11	11
s	*mm*	50	50	50
A_{tr}	mm^2	56.55	56.55	56.5
K_{tr}		4.11	4.11	4.11
$\left(\frac{d_{cs}+K_{tr}}{d_b}\right)$		2.50	2.50	2.09
# d_b		***35.70***	***34.52***	***46.3***
Calculated l_d	*mm*	214	276	555
Code Min. l_d	*mm*	**300**	**300**	**555**

Table 5-23 Lap splice Calculations

Figure 5-19 compares the pushover curve of the experimental benchmark (green dotted line) with a parametric study evaluating the effects of lap splicing. The orange solid line represents a configuration with lap splices restricted to the 6 mm bars in the web and in the flanges, but located outside the boundary elements. This configuration adheres to the ACI 318 recommendation to avoid placing lap splices in critical plastic hinge zones, such as the first-floor boundary elements. As shown in the graph, this splice detail has a negligible impact on the overall lateral load capacity. However, it appears to slightly enhance ductility when the flanges are in compression. Conversely, when the loading direction places the flanges in tension, ductility is reduced. This premature loss of ductility may result from bond failure or slip in the tension-loaded lap splices of the flange boundary elements.

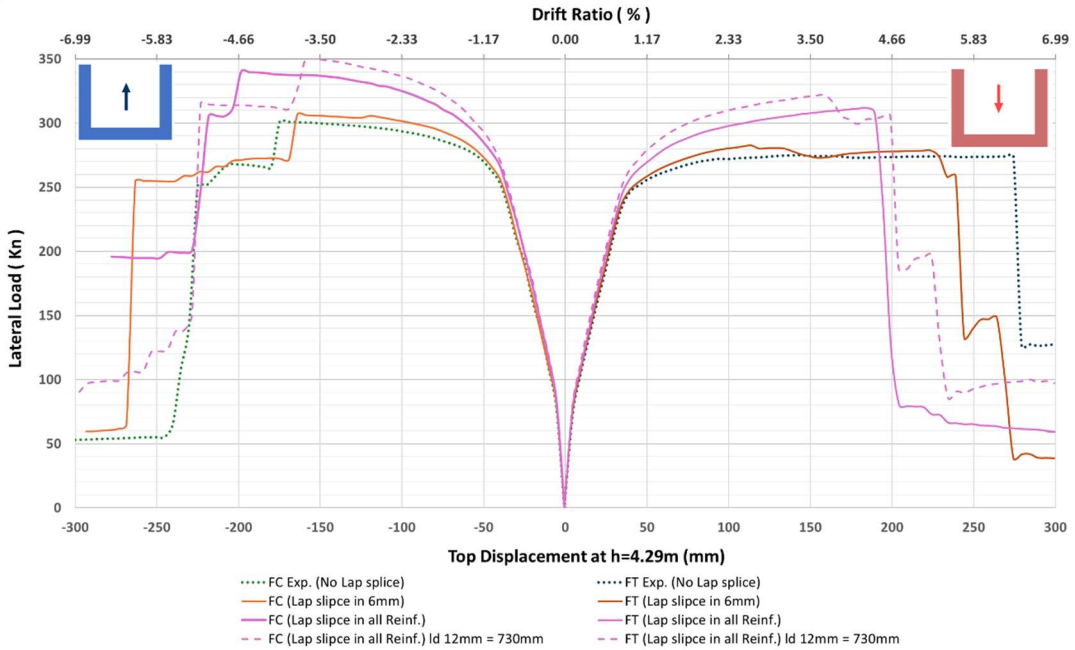

Figure 5-19 Pushover - Parametric study of Lap splice in plastic Hinge region

Chapter 6: Hysteretic Response

Reviewing the non-linear pushover analysis indicates that monotonic loading alone cannot fully capture alternative cyclic failure mechanisms, such as longitudinal buckling, stiffness degradation, and low-cycle fatigue. Consequently, this section analyzes the response under load reversal to understand the hysteretic behavior. Figure 6-1 illustrates the structural response when subjected to fully reversed cyclic displacements in the direction parallel to the axis of symmetry corresponding to top drift ratios of 0.93% (40mm), 1.86% (80mm), and 3.26% (140mm).

As shown in Figure 6-1a, the initial loading protocol displaces the wall, causing the flanges to compress (placing the web in tension) until the target drift ratio is reached, then reverses the load fully in the opposite direction. Conversely, Figure 6-1b shows the inverse loading sequence, where the structure is initially displaced so the flanges undergo primary tension.

Throughout Figure 6-1, solid lines denote the first complete cycle experienced by the structure at a given amplitude, whereas the dashed and dotted trajectories represent subsequent consecutive loops. Additionally, the line colors explicitly indicate the instantaneous loading direction: blue curves track the path when the wall flanges are in compression (move in that direction). In contrast, maroon curves represent the loading phase in the opposite direction.

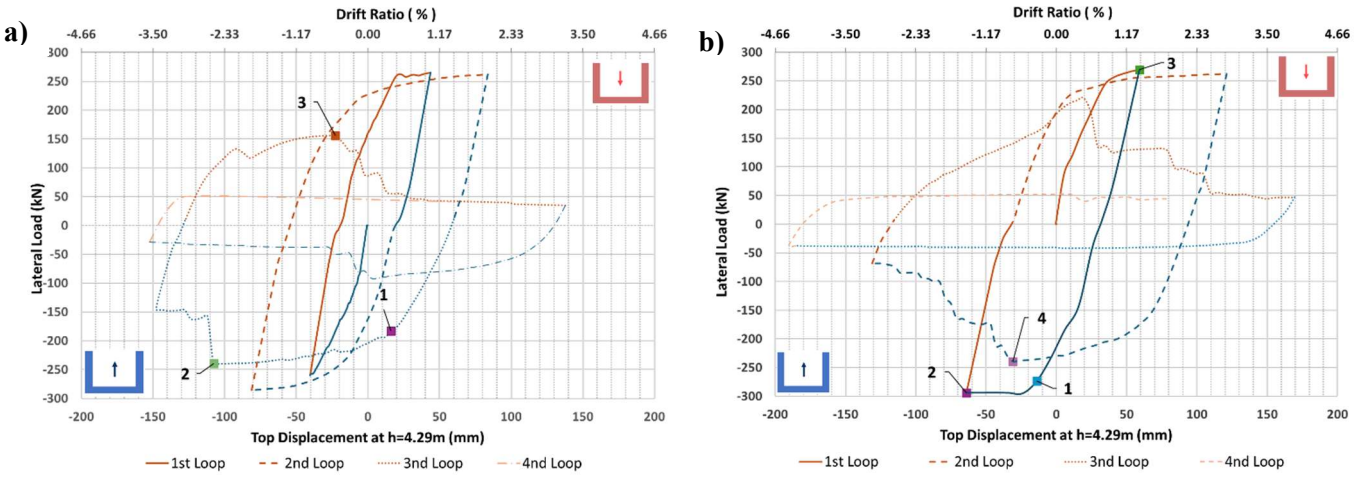

Figure 6-1 Lateral Load vs. Top Displacement / Drift Ratio curves for U-shaped reinforced concrete shear wall under cyclic loading, a) Hysteresis flanges in compression first b) Hysteresis flanges in Tension first.

As shown in Figure 6-1a, when the wall is initially loaded to a 1.02% drift ratio (subjecting the flanges to compression first) and subsequently unloaded to a zero-lateral-load state, it retains a prominent drift ratio of 0.45%. (This represents half of the peak demand imposed during that cycle). And, upon completing the full reverse-loading cycle, the structure closes the loop with a residual drift ratio of 0.45%.

The global response exhibits greater ductility when the flanges are in compression, and the web is in tension. This behavior can be attributed to loading asymmetry; when the load path reverses and places the web in compression, the high tensile strain demand imposed on the vertical boundary reinforcement at the extreme tips of the flanges can trigger premature rebar fracture or localized buckling. Losing these critical boundary elements induces a sudden, brittle failure mechanism, manifesting as a sharp drop in lateral load capacity with minimal evidence of post-peak ductility.

In the hysteresis curve in Figure 6-1a, after the second loop, when the flanges are placed under compression, the structure exhibits a sustained strain-hardening response past initial yielding (0.64% drift) up to Marker 2 at -2.80% drift. This represents a prolonged yield plateau spanning a plastic drift increment, during which the wall maintains a high lateral load resistance of 240 kN prior to ultimate strength degradation.

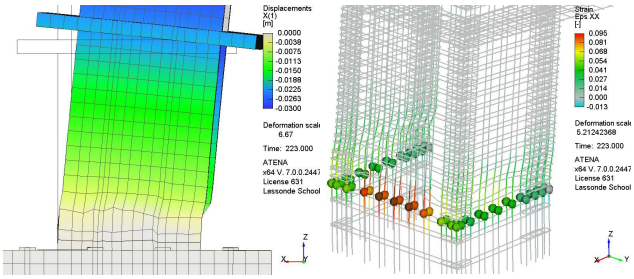

Figure 6-2 Plastic Hinge displacement and reinforcement strain

Plastic hinge formation begins at the base of the wall at Marker 1 (Figure 6-1a), marked by the rupture of three 6 mm web bars seen in Figure 6-2. As lateral displacement increases, the web reinforcement fails sequentially until it reaches Marker 2, where it fails completely.

After Marker 2, the first escalated reduction is held at a drift of 2.8%, 1.2% lower drift as compared with the push-over curve shown in Figure 5-1, attributed to reinforcement fracture of the reinforcement at the web.

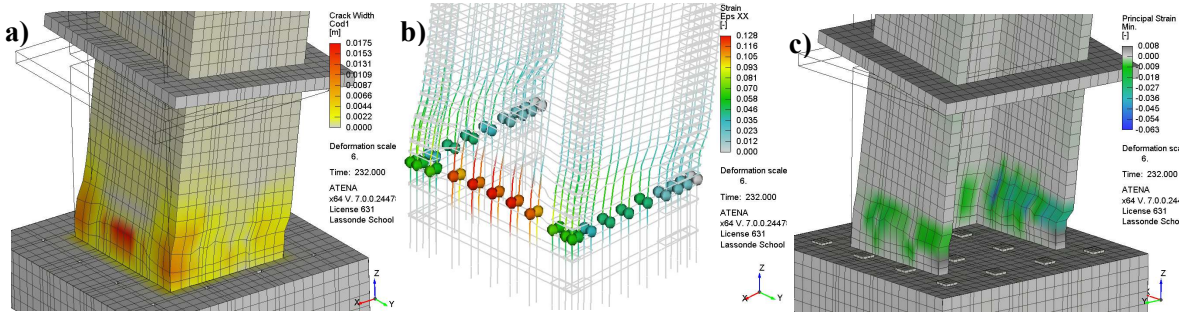

Figure 6-3 Marker 2 wall behavior a) Crack width b) Reinforcement strain c) Concrete principal strain

Upon reverse loading, the structure reaches a lateral load of approximately 150 kN at Marker 3, where nonlinear buckling deformations evidently develop within the web of the plastic hinge zone (as shown in Figure 6-3a). Beyond Marker 3, the structure's lateral load capacity degrades significantly; after dropping to a residual lateral capacity of 50 kN, it cannot recover strength or ductility. At this stage, the structure is considered to have failed.

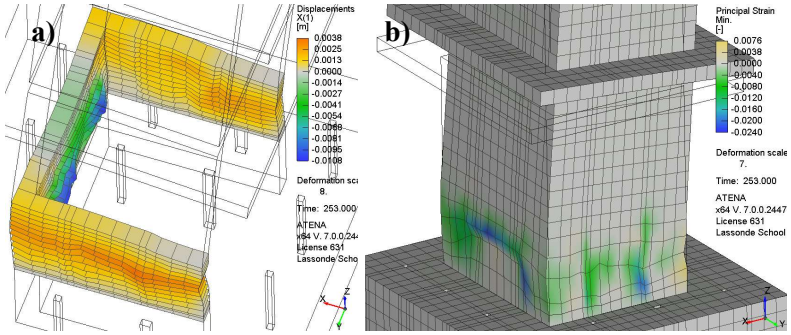

Figure 6-4 Marker 3 wall behavior a) non-linear displacement (x-axis) b) Concrete principal strain

In Figure 6-1b), four specific points marked along the hysteresis curve highlight key behavioral stages, indicating where key mechanisms and failures occurred. During initial loading, the flanges are subjected to tension, inducing microcracking. Upon unloading, the response closely mirrors the initial loading path, with near-parallel loading and unloading curves reflecting predominantly elastic behavior. This continues until a negative lateral load of -120kN near zero drift, where yielding initiates and continues up to a peak load of -287kN at 1.12% drift. The subsequent unloading stage initially follows a near-vertical path, exhibiting a substantial reduction in lateral force and minimal change in displacement. As the load approaches zero, the curve exhibits a pinching effect, forming an S-shape with reduced stiffness near zero force due to crack closure and transitions in aggregate interlock. Upon reaching zero lateral force, the structure exhibits permanent plastic deformation, resulting in a residual drift of 0.66%.

At Marker 1, the vertical reinforcement has yielded and entered the strain-hardening regime, reaching approximately one-quarter of its ultimate strain capacity across both the flanges and the web (Figure 6-1a). At the base, localized primary horizontal crack widths reach up to 3.9 mm, characteristic of a flexural-dominated failure mechanism. Concurrently, smaller diagonal cracks extend into higher elevations toward the web-flange regions, indicating early flexure-shear interaction.

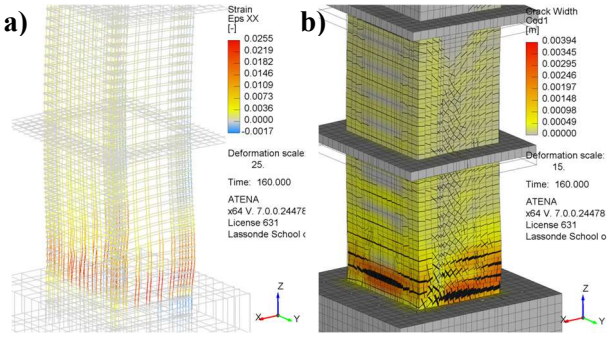

Figure 6-5 Marker 1 wall behavior, a) Reinforcement strain b) Crack width

In Marker 2, the flanges experience compression. At a drift of 2.2%, the maximum horizontal crack width reached 12.7 mm in the web, as shown in Figure 6-6a, while the 6mm diameter bars on the web are on the borderline of failure with a strain of 0.085. At this point, a horizontal section of the concrete has been crushed,

causing localized deformation; a nonlinear hinge has formed at the base of the wall, as corroborated by the plastic strains in Figure 6-6a and Figure 6-6b.

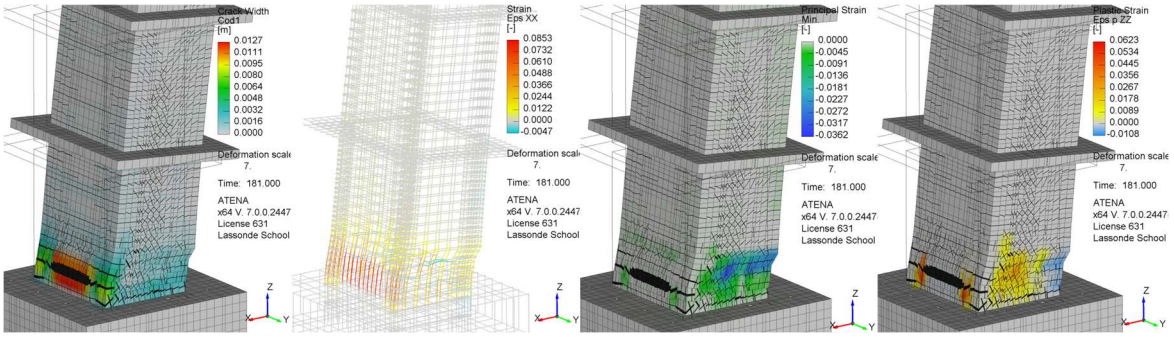

Figure 6-6 Marker 2 wall behavior: a) Crack width; b) Reinforcement strain; c) Concrete principal strain; d) Plastic strain in the Z direction.

In Marker 3, the flanges experience tension. At a drift of 1.63%, the wall flanges displays extensive flexural-shear crack opening of 9.2 mm along the lower portion of the wall, as shown in Figure 6-7a, while the 12mm diameter bars have an abrupt increase in strain form 0.065 to 0.087 shown in Figure 6-7b and Figure 6-7c, this change coincides with a step reduceduction on the wall strength following marker 3 illustrated in Figure 6-1b. Beyond marker 3, there is a scaled degradation of the wall strength that can be attributed to the sequential failure of the longitudinal reinforcement at the tip of the flanges, culminating in a reversal load at 2.9% drift, where the reinforcement in the boundary element at the tip has fractured. At marker 3, the web experiences compression, with compressive concrete plastic strains reaching -0.0175 near the corner of the web-flange intersection (Figure 6-7d), signaling concrete crushing and non-linear softening under extreme compression.

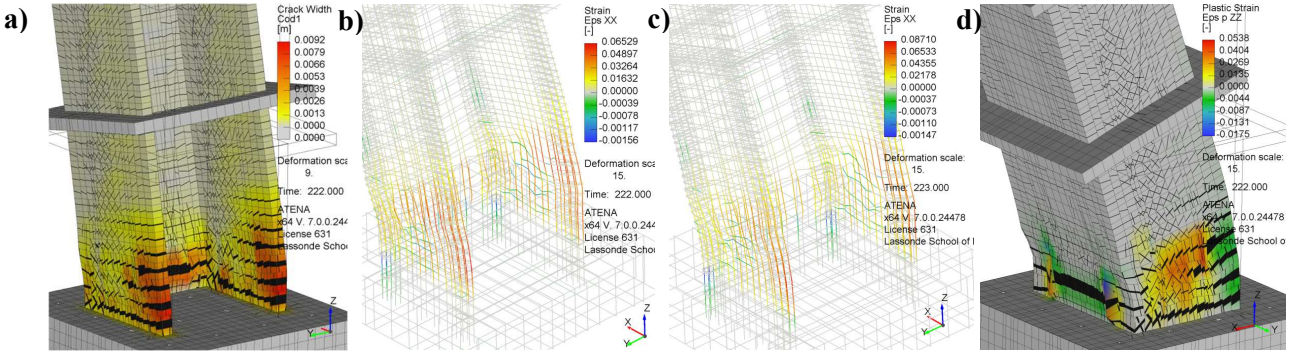

Figure 6-7 Marker 3 walls behavior a) Crack width b) Reinforcement strain c) Reinforcement strain for next step d) Concrete plastic stain

In marker 3, there is evidence of out-of-plane web buckling illustrated in Figure 6-8, sharp localized peaks displacing inward in a negative direction of -7mm, while the rest of the structure displaces in the opposite direction. This is corroborated by the high plastic compressive strain (Figure 6-7d) in the web, showing concrete yielding under extreme vertical flexural demand.



Figure 6-8 Marker 3 wall behavior, out-of-plane displacement (x-axis)

In Marker 4, the web experiences tension at a drift of 1.31%, before the structure loses lateral strength in a scaled manner. Figure 6-9 shows the wall behavior at Marker 4; at this point, the web reinforcement is near fracture with a stain of 0.093. The concrete compressive principal strain is also concentrated at -0.0335 at the end of plastic hinge formation. Although one side of the flange experiences a lower strain of -0.02, the flange with higher in-plane deformations than the other exhibits torsional effects in the deformed cross section shown in Figure 6-10.

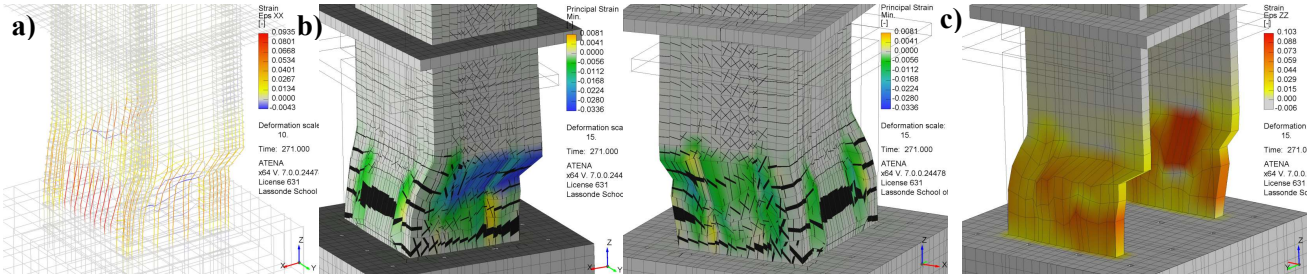

Figure 6-9 Marker 4 walls behavior a) Reinforcement train b) Concrete principal strain c) Concrete plastic stain

Figure 6-10 illustrates the FE cross-sectional deformation profiles, where Figure (a) displays out-of-plane displacements in the Y-direction and Figure (b) in the X-direction. The U-shaped wall exhibits significant cross-sectional warping and local out-of-plane web buckling. Under the applied loading demand, the thin web region undergoes pronounced out-of-plane flexural distortion, while the free flange legs exhibit asymmetric transverse displacements. The fixed base prevents torsional warping of the wall, which manifests as out-of-plane web buckling and asymmetric transverse displacement of the flange tips. This torsional distortion accelerates local instability and non-uniform compression failure in the concrete within the plastic hinge zone.

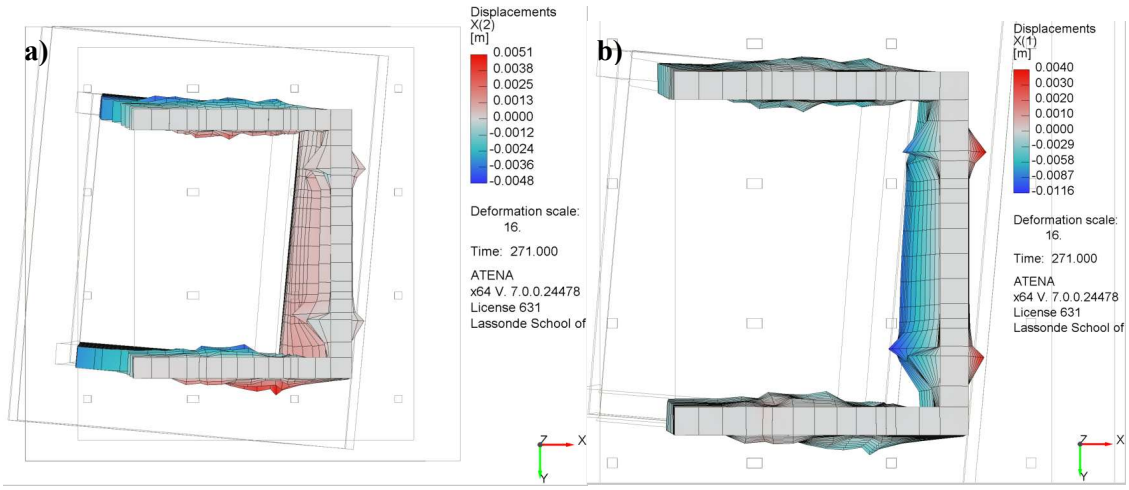

Figure 6-10 Marker 4 walls behavior a) out of plane displacement (y-axis) b) out of plane displacement (x-axis)

Chapter 7: Conclusions

7.1 General Conclusions

This research program presented a comprehensive finite-element investigation of the structural performance, damage evolution, and parametric sensitivity of non-planar, thin-walled U-shaped reinforced concrete shear walls. By tracking global load-displacement indicators alongside localized material behavior, such as macro-crack widths, concrete plastic compressive strains, and internal reinforcement demands, the primary failure mechanisms were systematically isolated. The major findings and conclusions derived from this study are summarized below:

Dynamic validation of the finite element model in ATENA against the experimental test results demonstrates good agreement during the initial data in the ground motion phases (GM1 and GM2). Experimentally, the shear wall exhibits a distinct structural beating effect; however, while the ATENA model replicates the overall response up to a certain point, it fails to capture this beating phenomenon. The analytical and experimental responses maintain synchronized periods during the early stages of the time history, but their phase alignment diverges after peak displacements: the test specimen exhibits period elongation that the numerical model cannot capture. The ATENA model also consistently overestimated the measured rotational response.

An auxiliary analysis conducted in SAP2000, using non-linear material parameters equivalent to those defined in ATENA, identified a coupled torsional-lateral mode as the first fundamental mode, with a period of T=0.32s (assuming a linear mode profile). Following ATC-40 guidelines, an equivalent mass participation factor of $\alpha = 0.8$ and a modal participation factor of $\Gamma = 1.4$ yield a calculated maximum displacement of 85.12 mm. This shows strong agreement with the peak experimental displacement of 88mm in time history GM8, representing an error of only 3.3% for the fundamental mode. However, this simplified modal parameter contrasts with the actual SAP2000 output mass participation factor of α=0.577. Furthermore, the non-linear time-history analysis in SAP2000 underestimated displacements and failed to replicate the full experimental response.

A parametric study in SAP2000, varying the concrete modulus of elasticity (E_c) for both the wall and the top collar, showed that collar stiffness significantly influences the model's fundamental period. Increasing collar stiffness mitigates cross-sectional warping effects, suppressing torsional modal contributions and thereby reducing the fundamental period for modes with torsional components

The global lateral load capacity and corresponding ductility profiles of U-shaped shear walls are highly sensitive to the orientation of the horizontal demands. In the push-over curves, when the lateral load causes the flanges to be in tension, the wall exhibits an elongated, highly ductile plateau supported by uniform tensile

yielding throughout the flange longitudinal steel grid. The structural wall response is also highly sensitive to its axial load ratio. The analytical numerical predictions derived from the moment-shear interaction reveal strong alignment when the loading places the flanges in tension (1% error). Conversely, for the opposite loading direction, the analytical formulation conservatively underestimates the peak lateral capacity.

The pushover curve demonstrates that increasing the axial load ratio directly enhances both flexural and shear capacity by suppressing flexural cracking. However, as illustrated in Figure 5-11, a higher axial load ratio promotes a more brittle failure mode; upon reaching peak capacity, the structure exhibits linear strength degradation.

Increasing the longitudinal reinforcement ratio in the boundary element from 2.6% to 4% significantly increased initial stiffness and produced substantial flexural overstrength, increasing lateral load capacity by up to 28% under certain loading profiles. More critically, the higher reinforcement density fundamentally altered the drift limit capacity: while the wall's drift capacity increased by 0.9% when the flanges were subjected to compression, the increase was less pronounced in the opposite loading direction, rising by only 0.36%.

Parametric variations in transverse stirrup and tie spacing during pushover modeling showed unexpectedly low sensitivity to the global force-displacement relationships, with peak capacities and degradation trajectories remaining nearly identical. This highlights a limitation of the current finite element formulation. Consequently, the higher sensitivity associated with tie confinement must be cross-validated against cyclic experimental data to examine nonlinear failure modes not captured by monotonic analysis.

Based on the high concentration of strains observed in the pushover curves at both the flange tips and the web-to-flange junctions, there is a critical need for localized transverse reinforcement within these regions. Under severe lateral loading, these critical cross-sectional locations experience the largest compressive strains, directly triggering cover concrete spalling. This localized degradation significantly increases the demand for effective transverse confinement. Providing well-anchored confinement ties at these high-strain zones not only enhances concrete compressive strength and ultimate strain capacity (ductility), but also fundamentally improves the overall structural response of the shear wall. Furthermore, under reversed cyclic loading, this closely spaced transverse reinforcement provides essential lateral restraint to prevent premature out-of-plane buckling of the longitudinal reinforcement after cover spalling occurs.

Monotonic pushover analyses cannot fully capture complex cyclic damage mechanisms such as bar buckling, stiffness degradation, and low-cycle fatigue. For instance, when a cross-section is subjected to tension, flexural cracking initiates. Upon load reversal, as the same section transitions into compression, the complex sequence of crack closure and aggregate interlock can trigger out-of-plane buckling before the cracks fully re-engage. Furthermore, comparing the calculated maximum lateral force of 258.1 kN (derived using the formulation in Chapter 3 against the predicted peak pushover capacity of 275 kN, which represents the minimum

directional capacity for the governing critical case, reveals a 6% discrepancy. This demonstrates that the analytical formulation provides a close yet conservative estimate of the experimental capacity.

The wall's response under asymmetric, torsional demands depends heavily on the kinematic constraints imposed by adjacent floor slabs. Rigid, isolated constraint configurations (such as Floor Plan 2) induce high initial torsional stiffness at the expense of deformation capacity, triggering premature, brittle structural softening. Furthermore, while increasing gravity loads slightly increased torsional capacity by delaying concrete flexural-shear cracking, they did not extend ductility; all axial load variants under pure torsional warping experienced sharp, simultaneous capacity drops within a narrow displacement window.

Vertical profile tracking confirms that structural twist increases progressively with wall height. Prior to macro-cracking, the torsional deformation remained strictly linear. At ultimate limit states, however, non-planar cross-sectional warping induced an exponential increase in rotation demands in the upper stories, peaking near 10 degrees. Modest axial load variations altered these global rotation profiles only marginally, confirming that the localized warping distribution is fundamentally dictated by the thin-walled, open geometry of the U-shaped cross-section.

The hysteretic curve demonstrates that the wall dissipates more energy when the flanges are in compression (negative displacement), as shown by fuller, less-pinched loops that enclose a larger area than the more severely pinched response under flange tension.

7.2 Recommendations for Future Research

Although this study provides critical insights into the seismic behavior and non-linear response of U-shaped reinforced concrete structural walls, several complex phenomena remain open to further investigation. To advance the understanding of non-planar wall systems and to bridge remaining knowledge gaps in multi-directional seismic performance and complex cross-sectional interactions, the following topics are recommended for future research:

- Implementation of Advanced Cyclic Hysteresis Frameworks: Because monotonic pushover analyses exhibit sensitive or inconsistent ductility assessments under coupled axial-torsional demands, full cyclic hysteretic simulations are required to rigorously evaluate progressive material degradation under alternating load reversals.
- Refine cyclic hysteresis formulations to account for strength degradation, stiffness decay, and the localized breakdown of concrete-rebar bond-slip, particularly around lap splice zones located within or near plastic hinge regions.
- Refining cyclic constitutive hysteresis relationships under coupled torsional and lateral loading to capture stiffness degradation, strength deterioration, and residual capacity in open-section structural walls.
- Examine the impact of rigid and flexible floor slabs interacting with U-shaped core walls. Floor diaphragms impose out-of-plane constraints and alter torsional stiffness, which affects how warping stresses transfer to the foundation.
- Investigate the impact of height variations and key section dimensions, specifically flange length, web length, and overall height-to-width aspect ratios, to assess how cross-sectional geometry influences flexural-shear interaction, warping torsion distribution, and localized plasticity spread in non-planar structural walls.
- Investigate the dynamic response under elevated axial load ratios ($v > 0.10$-0.20) to observe whether higher gravity demands accelerate brittle concrete crushing in boundary elements or intensify out-of-plane web/flange buckling.
- Formulate simplified, computationally lean macro-modeling guidelines in SAP2000 that incorporate effective shear stiffness decay factors post-yielding, ensuring practicing engineers do not overestimate initial stiffness or flexural capacity.
- Investigate non-planar configurations featuring architectural voids and geometric openings (such as MEP penetrations in the web or flanges).

Bibliography

[1] A. K. H. Kwan *Shear lag in shear/core walls* (1996). J. Struct. Eng. 122(9): 1097-1104 https://doi.org/10.1061/(ASCE)0733-9445(1996)122:9(1097)

[2] Aaleti, S., B. L. Brueggen, B. Johnson, C. E. French, and S. Sritharan (2013). *Cyclic response of reinforced concrete walls with different anchorage details: Experimental investigation*. J. Struct. Eng. 139 (7): 1181–1191. https://doi.org/10.1061/(ASCE)ST.1943-541X.0000732

[3] Abdullah SA, Wallace JW (2021) *Drift Capacity at Axial Failure of RC Structural Walls and Wall Piers*. J. Struct. Eng. 147(6): 04021062 https://doi.org/10.1061/(ASCE)ST.1943-541X.0003009

[4] Abdullah S.A (2019). *Reinforced Concrete Structural Walls: Test Database and Modeling Parameters*. University of California, Los Angeles, California, USA

[5] Abdullah SA, Wallace JW (2019). *Drift capacity of reinforced concrete structural walls with special boundary elements*. ACI Structural Journal. https://doi.org/10.14359/51710864

[6] Abdullah SA, Wallace JW (2018*) UCLA-RC walls database for reinforced concrete structural walls.* Procs. of 11th National Conference in Earthquake Engineering, Los Angeles, California, USA

[7] Ahmed KA, Lowes LN, Lehman DE (2023) *Investigation of the behavior of slender reinforced concrete walls with complex configurations using nonlinear finite element analysis.* Resilient Cities and Structures 2(1):120–142. https://doi.org/10.1016/j.rcns.2023.02.010

[8] Almeida, J.P.;Prodan, O.; Rosso, A.; Beyer, K. (2016) *Tests on Thin Reinforced Concrete Walls Subjected to In-Plane and Out-of-Plane Cyclic Loading*, Earthquake Spectra, Vol. 33, No. 1, pp. 323-345. https://doi.org/10.1193/101915eqs154dp

[9] Almeida, J.P.; Tarquini, D.; Beyer, K. (2016) *Modelling Approaches for Inelastic Behaviour of RC Walls: Multi-level Assessment and Dependability of Results*. Arch. Comput. Methods Eng. 23,69–100. https://doi.org/10.1007/s11831-014-9131-y

[10] Arabzadeh, H.; Galal, K.(2018) *Seismic-Response Analysis of RC C-Shaped Core Walls Subjected to Combined Flexure, Shear, and Torsion.* J. Struct. Eng. 144(10): 04018165. https://doi.org/10.1061/(ASCE)ST.1943-541X.0002181

[11] Arteta C, Segura C, Piedrahita J (2025) *Boundary Element Detailing Provisions for Special Walls*. ACI 318 Subcommittee H: Spring 2025, Committee. Toronto, Ontario, Canada. April 1, 2025

[12] Arteta, C. A., Piedrahita, J., & Segura Jr, C. L. (2025). *Autoregularized Model of Compressive Behavior of Structural Wall Boundary Elements*. ACI Structural Journal, 122(2), 87-100. https://doi.org/10.14359/51743302

[13] Behrouzi AA, Mock AW, Lehman DE, Lowes LN, Kuchma DA (2020) *Impact of bi-directional loading on the seismic performance of C-shaped piers of core walls*. Eng Struct 225:111289 https://doi.org/10.1016/j.engstruct.2020.111289

[14] Beyer K, Dazio A, Priestley MJN (2008) *Quasi-Static Cyclic Tests of Two U-Shaped Reinforced Concrete Walls*. J Earthquake Eng. 12(7):1023–53. https://doi.org/10.1080/13632460802003272

[15] Beyer K, Dazio A, Priestley MJN (2008) *Inelastic wide-column models for U-shaped reinforced concrete walls*. J Earthq Eng 12(S1):1–33 https://doi.org/10.1080/13632460801922571

[16] Beyer K, Dazio A, Priestley MJN (2007) *Seismic design of torsionally eccentric buildings with U-shaped RC walls* (PhD) Pavia, Italy. Research Report, ROSE School, (ROSE-2008/0X).

[17] Blandon C, Arteta C, Bonett R, Carrillo J, Beyer K, Almeida J (2024) *Experimental and numerical evaluation of a U-shaped thin lightly reinforced concrete wall tested undercyclic loading*. Bulletin of Earthquake Engineering. https://doi.org/10.1007/s10518-024-01994-x

[18] Cardenas, A., and Magura, D. (1972). *Strength of High-Rise Shear Walls-Rectangular Cross Section*. ACI Special Publication, SP 36-7, pp. 119-150.

[19] Constantin R (2016) *Seismic behavior and analysis of U-shaped RC walls*. École polytechnique fédérale de Lausanne, Lausanne, Switzerland.

[20] Constantin R, Beyer K (2016) *Behavior of U-shaped RC walls under quasi-static cyclic diagonal loading*, in Engineering Structures, vol. 106, num. 1, p. 36-52. https://doi.org/10.1016/j.engstruct.2015.10.018

[21] Constantin R, Beyer K (2014) *Non-Rectangular Rc Walls: A Review on Experimental Investigations*. 2nd European Conference on Earthquake Engineering and Seismology, Istanbul, Turkey.

[22] Constantin R, Beyer K (2014) *Quasi-static cyclic tests on U-shaped reinforced concrete walls subjected to diagonal loading*. 2nd European Conference on Earthquake Engineering and Seismology, Istanbul, Turkey.

[23] Constantin R, Beyer K (2012) *Modelling of reinforced concrete core walls under bi-directional loading.* 15th World Conference on Earthquake Engineering, Lisbon, Portugal.

[24] Dameh, F. (2021). *Seismic Performance of Reinforced Concrete Nonconforming Columns*. York University, Master's thesis.

[25] Dezhdar E., Kolozvari K. (2025). *Case study of influence of vertical ground shaking on lateral and vertical response of a concrete shear wall building*. Proceedings of 2025 Los Angeles Tall Buildings Structural Design Council Annual Conference; https://www.latallbuildings.org/past-conference-proceedings.

[26] Dlubal Software. (n.d.). 2.4.3 Tension Stiffening. RF-CONCRETE Members Online Manual. Retrieved June 21, 2026, from https://www.dlubal.com/en/downloads-and-information/documents/online-manuals/rf-concrete-members/004579

[27] Farrokhi R, Epackachi S, Sadeghian V (2025). *Effectiveness of Various Types of Macro-Modeling Methods for Reinforced Concrete Shear Walls*. ACI Structural Journal. https://doi.org/10.14359/51746675

[28] Feng DC, Ren XD, Li J (2018) *Cyclic behavior modeling of reinforced concrete shear walls based on softened damage-plasticity model*. Eng Struct 166:363–375. https://doi.org/10.1016/j.engstruct.2018.03.085

[29] Ghosh S.K., Taylor A.W. (2021) *Changes in ACI 318 Code Provisions for Earthquake-Resistant Structures, Part 2*. ACI Structural Journal. https://doi.org/10.14359/51732696

[30] Hasan M.,Qasem M., Muhamad R., *Finite element modeling of precast reinforced concrete wall with dual boundary elements under lateral load, Materials Today*. https://doi.org/10.1016/j.matpr.2023.03.688

[31] Hognestad, E. (1951). *A study of Combined Bending and Axial Load in Reinforced Concrete Members*. University of Illinois Engineering Exp. Sta. Bull. no.399.

[32] Hoult R (2021) *Torsional capacity of reinforced concrete U-shaped walls*. Structures 31: 190–204. https://doi.org/10.1016/j.istruc.2021.01.104

[33] Hoult R (2019) *Shear lag effects in Reinforced concrete C-shaped walls*. J Struct Eng 145(3):04018270. https://doi.org/10.1061/(ASCE)ST.1943-541X.0002272

[34] Hoult R, Correia AA, Bertholet A, Candeias PX, Cumunel G, Doneux C, Garnier D, Han Y, Isakovic T, Janevski A, Lo Feudo S, Orgnoni A, Payen B, Palermo D, Pinho R, Ribeiro F,De Almeida JP (2025) *Shake-table tests on two 40-ton reinforced concrete U-shaped walls with uniaxial and bidirectional-torsional response*. https://doi.org/10.1177/87552930251378247

[35] Hoult R, Almeida JP, Correia AA (2024) *Overview and blind prediction from shake table tests of a large-scale RC U-shaped core wall*. Procs. of 18th World Conference on Earthquake Engineering, Milan, Italy

[36] Hoult R, Almeida JP (2024) *Torque Capacity of U- and H-Shaped Reinforced Concrte Walls Usimg Warping-Equivalent Bending Moment*. ACI Structural Journal. https://doi.org/10.14359/51740574

[37] Hoult R, Almeida JP (2024b) *Flexure-torsion response of compressed open reinforced-concrete cores: experimental strain gradients, numerical methods, and interaction diagrams.* J Struct Eng 150(9):04024111. https://doi.org/10.1061/JSENDH.STENG-13147

[38] Hoult R, Almeida JP (2024b) *Modified compression field theory and disturbed stress field model on the simulation of the global and local behaviour of non-planar reinforced concrete walls under cyclic and dynamic loading*. Bull. of Earth. Eng. https://doi.org/10.1007/s10518-024-01982-1

[39] Hoult R, Almeida JP (2023) *ERIES - ALL4wALL 2023 Blind Prediction Competition: Shake-table Response of 40-ton RC U-shaped Wall*. Université catholique de Louvain (UCLouvain) https://www.uclouvain.be/en/research-institutes/immc/given-information-0

[40] Hoult R, Doneux C, De Almeida JP (2023b) *Tests on reinforced concrete U-shaped walls subjected to torsion and flexure. Earthquake Spectra* 39(4): 2685–2710. https://doi.org/10.1177/87552930231195315

[41] Hoult R, Correia AA, Almeida JP (2023b) *Beam-truss models to simulate the axial-flexural-torsional performance of RC U-shaped wall buildings*. CivilEng 4(1):292–310. https://doi.org/10.3390/civileng4010017

[42] Hoult R, Doneux C, Almeida JP (2022) *Blind prediction results of two RC U-shaped walls subjected to flexure and torsion.* In Proceedings of the Australian Earthquake Engineering (AEES) Conference, Mt Macedon, Victoria, Australia.

[43] Hoult R, Doneux C, Almeida JP (2022) *A blind prediction of the seismic and torsional performance of RC U-shaped core walls*. In Proceedings of the 3rd European Conference on Earthquake Engineering and Seismology, Bucharest, Romania.

[44] Hoult R, Beyer K (2021) *RC U-shaped walls subjected to in-plane, diagonal, and torsional loading: new experimental findings*. Eng Struct 233:111873. https://doi.org/10.1016/j.engstruct.2021.111873

[45] Ile N, Reynouard JM (2005) *Behaviour of U-shaped walls subjected to Uniaxial and Biaxial cyclic lateral loading*. J Earthquake Eng 09(01):67–94. https://doi.org/10.1080/13632460509350534

[46] Kazaz, İ., Bilge, İ. H., & Gürbüz, M. (2024). *Near-fault ground motion characteristics and its effects on a collapsed reinforced concrete structure in Hatay during the February 6, 2023 Mw7.8 Kahramanmaraş earthquake*. Engineering Structures, 298. https://doi.org/10.1016/j.engstruct.2023.117067

[47] Khaloo A.; Tabiee M.; Abdoos H. (2022) *A Numerical Laboratory for Simulation of Flanged Reinforced Concrete Shear Walls. Numerical Methods in Civil Engineering* 6(3) 92-102

[48] Kolozvari K, Kalbasi K, Orakcal K, Wallace J (2021a) *Three-dimensional model for nonlinear analysis of slender flanged reinforced concrete walls*. Eng Struct. https://doi.org/10.1016/j.engstruct.2021.112105

[49] Li W, Li QN (2012) *Seismic performance of L-shaped RC shear wall subjected to cyclic loading*. Struct Des Tall Spec Build 21(12):855–866. https://doi.org/10.1002/tal.645

[50] Lowes LN, Lehman DE, Whitman Z,.(2019) *Investigation of failure mechanisms and development of design recommendations for flexural reinforced concrete walls.* Eng Struct 186:323–335. https://doi.org/10.1016/j.engstruct.2019.01.122

[51] Lowes LN, Lehman DE, Birely AC, Kuchma DA, Marley KP, Hart CR. (2012) *Earthquake response of slender planar concrete walls with modern detailing*. Eng Struct 43:31–47. https://doi.org/10.1016/j.engstruct.2012.04.040

[52] Lu X, Xie L, Guan H, Huang Y, Lu X (2015) *A shear wall element for nonlinear seismic analysis of super-tall buildings with OpenSees*. Finite Elements in Analysis and Design 98:14–25. https://doi.org/10.1016/j.finel.2015.01.006

[53] Lu Y, Panagiotou M (2014) *Three-dimensional Cyclic beam-truss model for nonplanar reinforced concrete walls*. J Struct Eng 140(3):04013071. https://doi.org/10.1061/(ASCE)ST.1943-541X.000085

[54] Mavros M, Murcia J, Panagiotou M, Koutromanos I,. (2025) *Flexural and torsional response analysis of U-shaped RC walls using the BTM method: insights from a blind-prediction competition and post-test analyses*. Bulletin of Earthquake Engineering. https://doi.org/10.1007/s10518-025-02096-y

[55] Mergos PE, Beyer K (2013) *Modelling shear–flexure interaction in equivalent frame models of slender RC walls. Tall and Special Buildings* https://doi.org/10.1002/tal.1114

[56] Park, R., Priestley, M.J.N. and Gill, W.D. (1982). *Ductility of Square-Confined Concrete Columns*. https://doi.org/10.1061/JSDEAG.0005933

[57] Paulay T, Priestley MJN (1992) *Seismic design of reinforced concrete and masonry buildings*. John Wiley & Sons, Inc. https://doi.org/10.1002/9780470172841

[58] Priestley, M. J. N. and Park, R. (1987) *Strength and ductility of concrete bridge columns under seismic loading*. ACI Structural Journal, Vol. 84, No. 1, pp. 61–76. https://doi.org/10.14359/2800

[59] Pugh JS, Lowes LN, Lehman DE. *Nonlinear line-element modeling of flexural reinforced concrete walls*. Eng Struct 2015;104:174–92. https://doi.org/10.1016/j.engstruct.2015.08.037

[60] Rojas-León, M., Wallace, J. W., Abdullah, S. A., & Kolozvari, K. (2024). *New Equations to Estimate Reinforced Concrete Wall Shear Strength Derived from Machine Learning and Statistical Methods*. ACI Structural Journal, 121(1), 89–104. https://doi.org/10.14359/51739187

[61] Sun, B.; Gu, Q.; Zhang, P.; Li, Y.; and Ou, J.,(2019) *Efficient Simulation of RC Shear Walls in High-Rise Buildings Using a Practical Multi-Cross-Line-Model*. Journal of Earthquake Engineering, pp. 1732-1761. https://doi.org/10.1080/13632469.2019.1597785

[62] Sittipunt, C., and S. L. Wood. (1993) *Finite element analysis of reinforced concrete shear walls*. Technical report, University of Illinois at Urbana-Champaign. http://hdl.handle.net/2142/14203.

[63] Tura C, Orakcal K, Gullu MF, Ilki A (2025) *A new layered shell model for reinforced concrete walls I: model description and dynamic response simulations*. Bulletin of Earthquake Engineering. https://doi.org/10.1007/s10518-025-02148-3

[64] Tura C, Orakcal K, Gullu MF, Ilki A (2025) *A new layered shell model for reinforced concrete walls II: experimental validation against quasi-static tests*. Bulletin of Earthquake Engineering. https://doi.org/10.1007/s10518-025-02165-2

[65] Vecchio F, Collins M (1986) *The Modified Compression-Field Theory for Reinforced Concrete Elements Subjected to Shear*. ACI Struct J 83(2):219. https://doi.org/10.14359/10416

CODES

I. ACI 318 -19 (American Concrete Institute). “Building Code Requirements for Structural Concrete and Commentary”, Farmington Hills, MI.

II. ACI 318 -14 (American Concrete Institute). “Building Code Requirements for Structural Concrete and Commentary”, Farmington Hills, MI.

III. ACI Committee 374A, 2025, “Design of Reinforced Concrete Structures for Functional Recovery” American Concrete Institute, Farmington Hills.

IV. ASCE-41-17. (American Society of Civil Engineers). “Seismic Evaluation and Retrofit of Existing Buildings”. ASCE Standard. Reston, VA:. (ASCE/SEI Standard 41-17).

V. CSA A.23.3-24. (Canadian Standards Association). “Design of Concrete Structures”, Mississauga, Ontario, Canada. (CAN/CSA Standard No. A23.3-24).

VI. CSA A.23.3-14. (Canadian Standards Association). “Design of Concrete Structures”, Mississauga, Ontario, Canada. (CAN/CSA Standard No. A23.3-14).

VII. FEMA 273. (1997). NEHRP Guidelines for the Seismic Rehabilitation of Buildings. Report No. FEMA-273, Federal Emergency Management Agency, Washington D.C.

VIII. FEMA 356. (2000). “Pre-standard and Commentary for the Seismic Rehabilitation of Buildings”

IX. Model Code (2020). final draft, fib – Bulletin 65. Vol. 1. www.fib-international.org.

X. Model Code (2010). final draft, fib – Bulletin 65. Vol. 1. www.fib-international.org.

XI. Model Code (1990). final draft, fib – Bulletin 65. Vol. 1. www.fib-international.org.

XII. National Research Council Canada, "National Building Code of Canada 2020," Ottawa, ON, Canada, 2020. https://doi.org/10.4224/26fz-gg26

Appendix A

Rectangular Cross-Section with Uniformly Distributed Reinforcement

As stated, Cárdenas and Magura Illustrated in Figure A-1 the cross-section of a rectangular shear wall subjected to combined flexure and axial loading. In this analytical model, the total area of vertical reinforcement (A_s) is idealized as a continuous, uniform line of steel extending along the entire length (l_w) of the wall. Figure A-1 b depicts the assumed strain distribution at the ultimate limit state. This linear distribution assumes tension-controlled failure, occurring at an axial load level below the balanced failure condition. Under these circumstances, the extreme compression fiber reaches the conventional crushing strain of 0.003 while the tension reinforcement has already yielded.

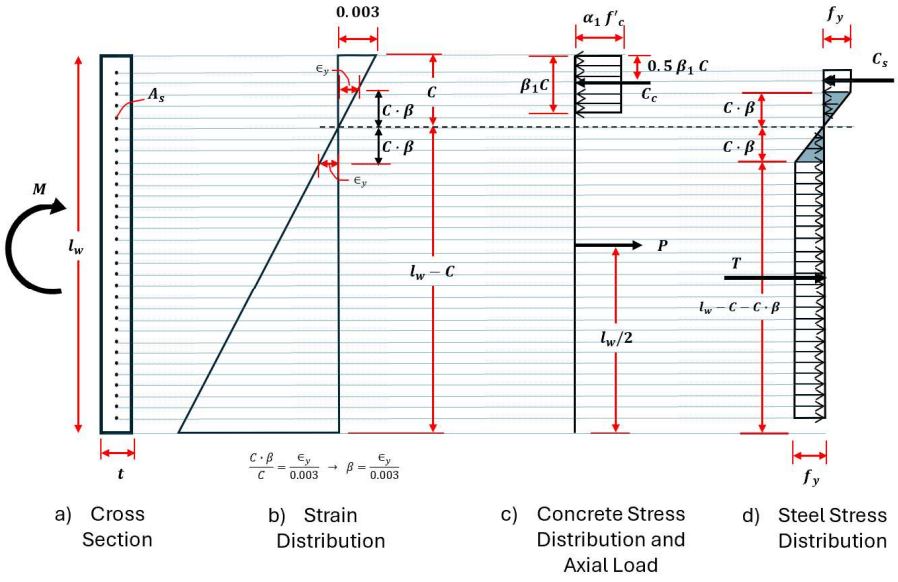

Figure A-1 Rectangular cross-section under the state of equilibrium (Uniformly distributed reinforcement).

Based on the equilibrium of internal and external forces shown in the stress diagram, the relationship between the axial load and the internal stress resultants can be established as follows:

$$T + P = C_c + C_s$$

$$\frac{[l_w - C - C\,\beta)]}{l_w} A_s\, f_y + P = \alpha_1\, f_c'\, \beta_1\, t\, C + \frac{(C - C\,\beta)}{l_w}\, A_s\, f_y$$

Where $\frac{A_s}{l_w} = \rho_v\, t$

$$[l_w - C\,(1+\beta)]\,\rho_v\, t\, f_y + P = \alpha_1\, f_c'\, \beta_1 t\, C + C\,(1-\beta)\,\rho_v\, t\, f_y$$

$$C = \frac{A_s\, f_y + P}{\alpha_1\, f_c'\, \beta_1\, t + \frac{2\, A_s\, f_y}{l_w}}$$

$$\frac{C}{l_w} = \frac{A_s f_y + P}{\alpha_1 f_c' \beta_1 t l_w + 2 A_s f_y}$$

$$\frac{C}{l_w} = \frac{\frac{A_s f_y}{f_c' l_w t} + \frac{P}{f_c' l_w t}}{\alpha_1 \beta_1 + 2 \frac{A_s f_y}{f_c' l_w t}}$$

Where $\boldsymbol{\omega}$ represents the reinforcement index and $\boldsymbol{\alpha}$ represents the axial load index

$$\omega = \frac{A_s f_y}{f_c' l_w t} \qquad \alpha = \frac{P}{f_c' l_w t}$$

$$\boldsymbol{\frac{C}{l_w} = \frac{\omega + \alpha}{\alpha_1 \beta_1 + 2 \omega}} \qquad \textbf{\textit{Eq. A-1}}$$

Taking the moment about the geometric center ($l_w/2$) of the wall accounts for the concrete compression force (Cc), the resultant of the distributed tensile steel stress (T), and the concentrated compression steel force (C_s). Summing up these components, the nominal moment capacity is expressed as:

$$M = C_c \left(\frac{l_w}{2} - 0.5\beta_1 C\right) + T\left(\frac{l_w}{2} - \frac{l_w - C - C\,\beta}{2}\right) + C_t\left(\frac{l_w}{2} - \frac{(C - C\,\beta)}{2}\right)$$

$$M = (\alpha_1 f_c' \beta_1 C\, t)\left(\frac{l_w}{2} - 0.5\beta_1 C\right) + \left(A_s f_y \frac{[l_w - C - C\,\beta)]}{l_w}\right)\left(\frac{l_w}{2} - \frac{l_w - C - C\,\beta}{2}\right) + \left(A_s f_y \frac{(C - C\,\beta)}{l_w}\right)\left(\frac{l_w}{2} - \frac{C(1-\beta)}{2}\right)$$

$$M = (\alpha_1 f_c' \beta_1 C\, t)\left(\frac{l_w}{2} - 0.5\beta_1 C\right) + \left(A_s f_y \frac{[l_w - C(1 + \beta)]}{l_w}\right)\left(\frac{C(1+\beta)}{2}\right) + \left(A_s f_y \frac{C\,(1-\beta)}{l_w}\right)\left(\frac{l_w - C(1-\beta)}{2}\right)$$

$$M = (\alpha_1 f_c' \beta_1 C\, t)\left(\frac{l_w}{2} - 0.5\beta_1 C\right) + (\omega\, f'_c\, t\, [l_w - C(1 + \beta)])\left(\frac{C(1+\beta)}{2}\right) + (\omega\, f'_c\, t\, [C\,(1-\beta)])\left(\frac{l_w - C(1-\beta)}{2}\right)$$

$$M = (\alpha_1 f_c' \beta_1 C\, t)\left(\frac{l_w}{2} - 0.5\beta_1 C\right) + \omega\, f'_c\, t\left[\left(\frac{C(1+\beta)[l_w - C(1 + \beta)]}{2}\right) + \left(\frac{C(1-\beta)[l_w - C(1 - \beta)]}{2}\right)\right]$$

$$M = (\alpha_1 f_c' \beta_1 C\, t)\left(\frac{l_w}{2} - 0.5\beta_1 C\right) + \frac{A_s f_y}{f'c\, l_w\, t} f'_c\, t\, [C\, l_w - C^2(1 + \beta^2)]$$

$$\boldsymbol{M = (0.5\,\alpha_1 f_c' \beta_1 C\, t)(l_w - \beta_1 C) + \rho_v f_y t\, [C\, l_w - C^2(1 + \beta^2)]} \qquad \textbf{\textit{Eq. A-2}}$$

However, Cárdenas and Magura simplify the nominal moment strength (M_n) as the sum of these forces multiplied by their distance from the wall's plastic neutral axis (the centerline):

$$M_u = C_c\,(arm_c) + \int (Steel\ Forces \cdot arms)$$

For a wall with uniformly distributed reinforcement, Cárdenas and Magura performed the integration of all those individual bar forces across the "line of steel." This resulted in the following relationship:

$$M_u = A_s f_y l_w \left[\left(1 + \frac{N_u}{A_s f_y}\right)\left(\frac{1}{2} - \frac{\beta_1 c}{2\, l_w}\right) - \frac{c^2}{l_w^2}\left(1 + \frac{\beta^2}{3} - \beta_1\right)\right]$$

Eliminating the minor terms $\left(\frac{c^2}{l_w^2},\ \beta_1\right)$ for practical calculation, while maintaining a high degree of precision, the equation reduces to:

$$M_u = 0.5\, A_s f_y l_w \left[\left(1 + \frac{N_u}{A_s f_y}\right)\left(1 - \frac{c}{l_w}\right)\right] \qquad \textit{Eq. A-3}$$

An alternative expression is derived by neglecting the contribution of compression reinforcement, assuming that vertical bars may buckle before reaching their yield capacity. This follows directly from the lack of confinement reinforcement typical in standard wall sections, particularly thin shear walls lacking specialized boundary elements. Consequently, the concrete is assumed to resist the internal compressive resultant alone. By equating the internal forces to solve for the neutral axis depth c, the following expression is obtained:

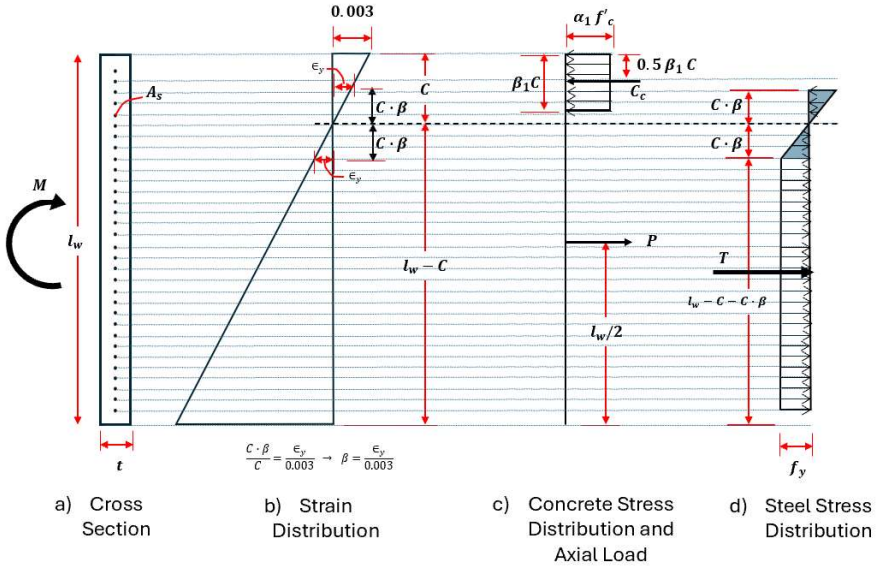

Figure A-2 Rectangular cross-section under the state of equilibrium (without considering reinforcement in compression).

$$T + P = C_c$$

$$A_s \frac{[l_w - C - C\,\beta)]}{l_w} f_y + P = \alpha_1 f'_c \beta_1 t\, C$$

$$C = \frac{l_w (A_s f_y + P)}{\alpha_1 f'_c \beta_1 t\, l_w + A_s f_y (1 + \beta)}$$

$$\frac{C}{l_w} = \frac{A_s f_y + P}{\alpha_1 f'_c \beta_1 t\, l_w + A_s f_y (1 + \beta)}$$

$$\frac{C}{l_w} = \frac{\frac{A_s f_y}{f'_c l_w t} + \frac{P}{f'_c l_w t}}{\alpha_1 \beta_1 + (1 + \beta)\frac{A_s f_y}{f'_c l_w t}}$$

$$\frac{\boldsymbol{C}}{\boldsymbol{l_w}} = \frac{\boldsymbol{\omega + \alpha}}{\boldsymbol{\alpha_1 \beta_1 + (1 + \beta)\,\omega}} \qquad \textit{Eq. A-4}$$

Where $\boldsymbol{\omega}$ represents the reinforcement index and $\boldsymbol{\alpha}$ represents the axial load index.

This expression simplifies to Equation 1 when $\beta = 1$. Furthermore, the condition when $\beta = 0$ implies that the reinforcement yields immediately upon any deformation. In this case, the triangular transition zones (labeled

C β) disappear, and the steel stress distribution effectively becomes a uniform rectangular block of magnitude f_y across the entire tension zone. This results in a smaller denominator, leading to a larger neutral axis depth ratio (c/l_w) relative to the case where β=1.

The nominal moment capacity is expressed as

$$M = C_c \left(\frac{l_w}{2} - 0.5\beta_1 C\right) + T\left(\frac{l_w}{2} - \frac{l_w - C - C\,\beta}{2}\right)$$

$$M = (\alpha_1\, f_c'\, \beta_1 C\, t)\left(\frac{l_w}{2} - 0.5\beta_1 C\right) + \left(A_s\, f_y \frac{[l_w - C - C\,\beta)]}{l_w}\right)\left(\frac{l_w}{2} - \frac{l_w - C - C\,\beta}{2}\right)$$

$$M = (\alpha_1\, f_c'\, \beta_1 C\, t)\left(\frac{l_w}{2} - 0.5\beta_1 C\right) + \left(A_s\, f_y \frac{[l_w - C(1+\beta)]}{l_w}\right)\left(\frac{C(1+\beta)}{2}\right)$$

$$M = (\alpha_1\, f_c'\, \beta_1 C\, t)\left(\frac{l_w}{2} - 0.5\beta_1 C\right) + \frac{A_s\, f_y}{2l_w}[l_w - C(1+\beta)]\cdot[C(1+\beta)]$$

$$\boldsymbol{M = (\alpha_1\, f_c'\, \beta_1 C\, t)\left(\frac{l_w}{2} - 0.5\beta_1 C\right) + \frac{\rho_v\, t\, f_y}{2}[l_w - C(1+\beta)]\cdot[C(1+\beta)]} \qquad \textbf{Eq. A-5}$$

Finally, Dr. Pantazopoulou developed a refined analytical expression. This model assumes that only 70% of the reinforcement in the tension zone reaches yielding, while the internal compressive resistance is provided exclusively by the concrete stress block, as illustrated below:

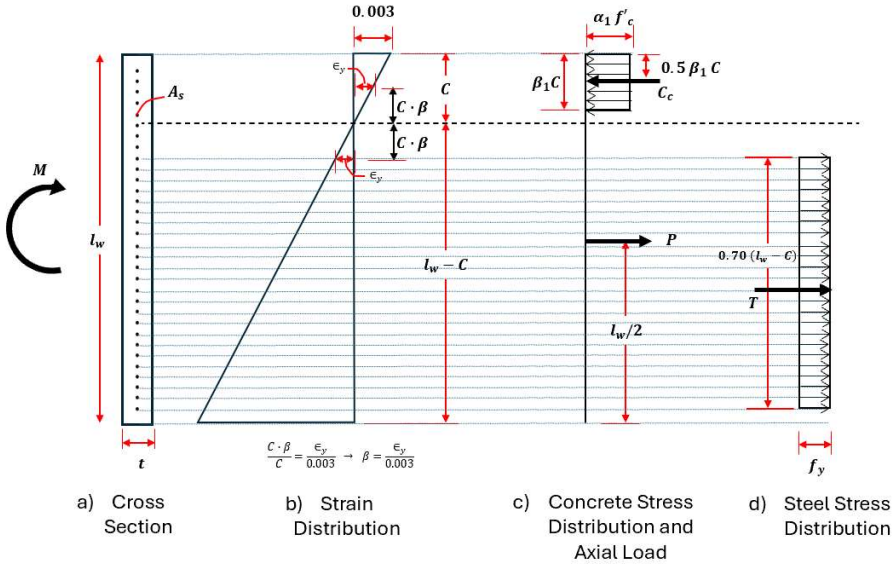

Figure A-3 Rectangular cross-section under the state of equilibrium (considering 70% reinforcement in Tension).

$$T + P = C_c$$

$$\rho_v = A_s/A_g$$

$$0.7\,\rho_v\, A_g\left[\frac{l_w - C}{l_w}\right] f_y + P = \alpha_1\, f_c'\, \beta_1 C\, t$$

$$0.7\,\rho_v\,A_g\left[1-\frac{C}{l_w}\right]f_y + P = \alpha_1\,f_c'\,\beta_1 C\,t$$

$$C = \frac{\left(0.7\,\rho_v\,A_g\,f_y + P\right)l_w}{\alpha_1\,f_c'\,\beta_1\;t\,l_w + 0.7\,\rho_v\,A_g\,f_y}$$

$$\boldsymbol{\frac{C}{l_w} = \frac{0.7\,\rho_v\,A_g\,f_y + P}{\alpha_1\,f_c'\,\beta_1\;t\,l_w + 0.7\,\rho_v\,A_g\,f_y}} \qquad \textit{Eq. A-6}$$

The nominal moment capacity is expressed as

$$M = C_c\left(\frac{l_w}{2} - 0.5\beta_1 C\right) + T\left(\frac{l_w}{2} - \frac{0.7\,(l_w - C)}{2}\right)$$

$$M = (\alpha_1\,f'c\,\beta_1 C\,t)\left(\frac{l_w}{2} - 0.5\beta_1 C\right) + \left(0.7\,\rho_v\,A_g\left[\frac{l_w - C}{l_w}\right]f_y\right)\left(\frac{l_w}{2} - \frac{0.7\,(l_w - C)}{2}\right)$$

$$M = (\alpha_1\,f'c\,\beta_1 C\,t\,l_w)\left(0.5 - \frac{\beta_1 C}{2\,l_w}\right) + 0.7\,\rho_v\,A_g\,f_y\left[1-\frac{C}{l_w}\right](0.15\,l_w + 0.35\,C)$$

$$\boldsymbol{M = (\alpha_1\,f'c\,\beta_1 C\,t\,l_w)\left(0.5 - \frac{\beta_1 C}{2\,l_w}\right) + 0.7\,\rho_v\,A_g\,f_y\left[1-\frac{C}{l_w}\right](0.15\,l_w + 0.35\,C)} \qquad \textit{Eq. A-7}$$

Five separate cases were analyzed featuring a shear wall with reinforcement distributed uniformly along its length. These analytical results are compared with outputs from Response-2000, which accounts for "tension stiffening" and bond-slip effects (see Appendix). This comparison aims to accurately capture the wall's ultimate strength while accounting for non-linear behavior, thereby validating the derived equations against Response-2000 as a benchmark.

The comparison reveals that the maximum compressive strain often fails to reach the theoretical limit of 0.003. This discrepancy is attributed to bond stress in the tension-zone reinforcement exceeding its capacity before full concrete crushing occurs.

Examples 1, 4, and 5 maintain identical geometry while varying the reinforcement ratios. Examples 2 and 3 follow a similar pattern, sharing consistent geometry with varying reinforcement.

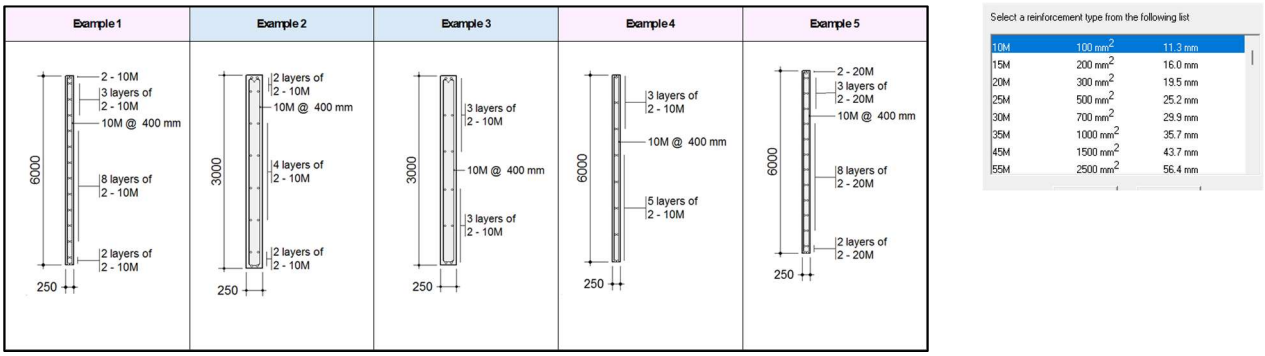

Figure A-4 Five Rectangular cross-section used in example on Response 2000.

The study evaluates the neutral axis depth (C) and nominal moment capacity (M) for each wall specimen using four analytical approaches and one computational benchmark. The organization of the comparative data is as follows:

I. Equations A-1 and A-2: While the neutral axis depth (c) is determined using the Cárdenas and Magura formula, the moment capacity is calculated via Equation A-2. Calculated about the geometric center ($l_w/2$) of the wall, accounting for the concrete compression force (C_c), the resultant of the distributed tensile steel (T), and the concentrated compression steel force (C_s).

II. Equations A-1 and A-3: This approach also uses the Cárdenas and Magura equation to calculate the compression depth (c) and the simplified moment capacity as equation A-3. This method integrates the individual forces of each reinforcing bar across the "line of steel," a procedure commonly adopted in modern design codes.

III. Equations A-4 and A.5: This approach simplifies the section analysis by neglecting the contribution of reinforcement in the compression zone (notice that in this case $\beta=0$)

IV. Equations A-6 and A-7: This model introduces a conservative assumption that only 70% of the reinforcement within the tension zone reaches its full yield strength.

V. Response 2000 (flexural): To establish a reference point for wall strength, results were obtained from Response-2000 software (Depicted in red)

VI. Response 2000 + Shear: For a comprehensive view of nonlinear behavior, additional software runs were performed to account for shear-flexure interaction at specific shear spans (L= 2 m and L= 4.02 m)

		F_y	F'_c	L_t	L_w	t	A_s	P	α_1	β_1	β	ρ_v	C / L	C	Error	M	Error
		Mpa	Mpa	mm	mm	mm	mm^2	N						mm		kN*m	
Example 1	EQ1.1 & EQ 1.2	400	30	6000	6000	250	2800	4041000	0.81	0.90	**1.00**	0.187%	0.149	893	*10%*	13255	*11%*
	EQ1.1 & EQ 1.3										-		**0.149**	**893**	***10%***	**13678**	*8%*
	EQ2.1 & EQ 2.2										**0.00**		0.154	923	*7%*	13342	*10%*
	EQ3.1 & EQ3.2										-		0.145	872	*12%*	13103	*12%*
	Resp. 2000 (flexural)												**0.165**	**990**		**14868**	
	Resp. 2000 + Shear (L= 2 m)												0.735	4412	*78%*	5669	*62%*
	Resp. 2000 + Shear (L= 4.02 m)												0.633	3800	*74%*	8867	*40%*
Example 2	EQ1.1 & EQ 1.2	400	30	3000	3000	250	1600	4041000	0.81	0.90	**1.00**	0.213%	0.268	803	2%	5188	*11%*
	EQ1.1 & EQ 1.3										-		**0.268**	**803**	2%	**5399**	*7%*
	EQ2.1 & EQ 2.2										**0.00**		0.278	833	2%	5268	*9%*
	EQ3.1 & EQ3.2										-		0.269	808	1%	5212	*10%*
	Resp. 2000 (flexural)												**0.272**	**815**		**5820**	
	Resp. 2000 + Shear (L= 2 m)												0.709	2127	*62%*	3178	*45%*
	Resp. 2000 + Shear (L= 4.02 m)												0.338	1014	*20%*	4607	*21%*
Example 3	EQ1.1 & EQ 1.2	400	30	3000	3000	250	1200	4041000	0.81	0.90	**1.00**	0.160%	0.263	790	3%	5073	*9%*
	EQ1.1 & EQ 1.3										-		**0.263**	**790**	3%	**5186**	*7%*
	EQ2.1 & EQ 2.2										**0.00**		0.271	813	0%	5132	*8%*
	EQ3.1 & EQ3.2										-		0.265	794	3%	5089	*9%*
	Resp. 2000 (flexural)												**0.272**	**817**		**5593**	
	Resp. 2000 + Shear (L= 2 m)												0.709	2127	*62%*	3112	*44%*
	Resp. 2000 + Shear (L= 4.02 m)												0.358	1075	*24%*	4422	*21%*
Example 4	EQ1.1 & EQ 1.2	400	30	6000	6000	250	1600	4041000	0.81	0.90	**1.00**	0.107%	0.139	833	*25%*	12215	*5%*
	EQ1.1 & EQ 1.3										-		**0.139**	**833**	***25%***	**12359**	***4%***
	EQ2.1 & EQ 2.2										**0.00**		0.142	850	*23%*	12259	*5%*
	EQ3.1 & EQ3.2										-		0.137	819	*26%*	12119	*6%*
	Resp. 2000 (flexural)												**0.185**	**1109**		**12923**	
	Resp. 2000 + Shear (L= 2 m)												0.703	4216	*74%*	5516	*57%*
	Resp. 2000 + Shear (L= 4.02 m)												0.623	3738	*70%*	8427	*35%*
Example 5	EQ1.1 & EQ 1.2	400	30	6000	6000	250	8400	4041000	0.81	0.90	**1.00**	0.560%	0.189	1135	4%	17649	*14%*
	EQ1.1 & EQ 1.3										-		**0.189**	**1135**	4%	**19911**	*3%*
	EQ2.1 & EQ 2.2										**0.00**		0.207	1241	5%	18047	*12%*
	EQ3.1 & EQ3.2										-		0.184	1103	*7%*	17408	*15%*
	Resp. 2000 (flexural)												**0.197**	**1184**		**20583**	
	Resp. 2000 + Shear (L= 2 m)												0.735	4412	*73%*	6084	*70%*
	Resp. 2000 + Shear (L= 4.02 m)												0.127	764	*55%*	10214	*50%*

Figure A-5 Rectangular wall (uniform reinforcement distribution) neutral axis depth and flexural calculations.

Under pure flexural conditions, Equations A-1 to A-7 show a strong correlation with the Response-2000 (Flexural) benchmarks. However, Example 4 exhibits a significantly higher error rate when calculating the neutral axis depth (c). Despite this discrepancy in the compression zone, the predicted nominal moment strength remains highly consistent with the software results. It is important to note that the vertical reinforcement ratio (ρ_v) for this specific specimen is 0.107%, which falls below the minimum longitudinal reinforcement requirements specified by ACI 318 and CSA A23.3. This under-reinforced condition likely contributes to the observed sensitivity in the analytical prediction of the neutral axis.

Additionally, all analytical approaches yielded results that are conservative relative to the Response-2000 benchmark. Among the methods evaluated, Equations A-1 and A-3 produced the most precise results, using the Cárdenas and Magura derivation and reflecting the methodology used in current design codes. Equations A-4 and A-5 followed closely. These findings validate these governing equilibrium equations as a baseline, allowing the analysis to proceed toward deriving similar expressions for sections with concentrated boundary elements.

Rectangular Cross-Section with Concentrated Boundary Reinforcement

By concentrating longitudinal reinforcement in boundary elements at the wall ends, the internal moment arm increases significantly. This configuration yields a higher flexural strength capacity than walls with

uniformly distributed reinforcement. Following the design principles established in Chapter 3.1, a series of equations were developed and analyzed to determine the ultimate moment capacity (M_u) for this specific reinforcement layout.

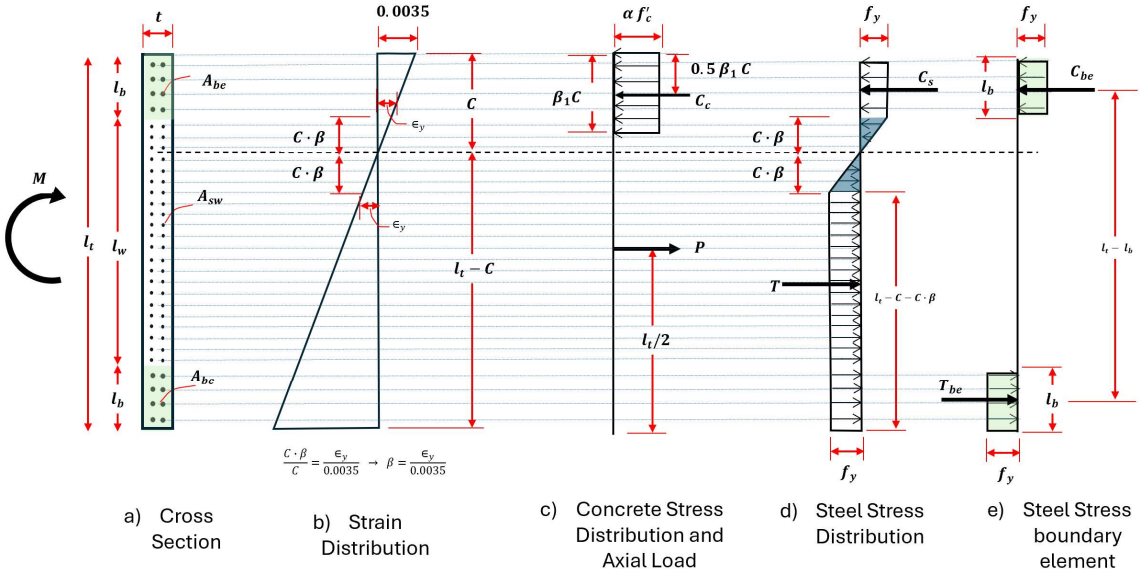

Figure A-6 Rectangular cross-section under the state of equilibrium (Concentrated Boundary Reinforcement).

Because the longitudinal reinforcement is concentrated at the wall ends, the total steel is categorized into two distinct components: the distributed web reinforcement (A_s), as shown in Diagram (d), and the concentrated boundary element steel (A_{be}), shown in Diagram (e). The boundary reinforcement (A_{be}) provides a significantly larger tensile force resultant (T_{be}) acting over an increased moment arm (l_t - l_b), thereby enhancing the wall's overall flexural capacity.

Based on the equilibrium of internal and external forces shown in the stress diagram, the relationship between the axial load and the internal stress resultants can be established as follows:

$$T_{be} + T + P = C_c + C_s + C_{be}$$

$$A_{be} f_{ybe} + \frac{[l_t - C - C\,\beta)]}{l_w} A_{sw}\, f_y + P = (\alpha\, f'_c\, \beta_1\, C\, t) + \frac{(C - C\,\beta)}{l_w} A_{sw}\, f_y + A_{be} f_{ybe}$$

Due to the symmetry of the boundary reinforcement, the compressive and tensile forces generated by the boundary elements (T_{be} and C_{be}) cancel each other out in the net axial force equilibrium.

$$\frac{[l_t - C - C\,\beta)]}{l_w} A_{sw}\, f_y + P = \alpha_1\, f'_c\, \beta_1\, t\, C + \frac{(C - C\,\beta)}{l_w} A_{sw}\, f_y$$

$$C = \frac{\frac{l_t}{l_w} A_{sw}\, f_y + P}{\alpha_1\, f'_c\, \beta_1\, t + \frac{2\, A_{sw}\, f_y}{l_w}}$$

$$C = \frac{l_t\, A_{sw}\, f_y + P\, l_w}{\alpha_1\, f_c'\, \beta_1\, t\, l_w + 2\, A_{sw}\, f_y}$$

$$C = \frac{\left(\ A_{sw}\, f_y + P\, l_w / \ l_t\right) l_t}{\alpha_1\, f_c'\, \beta_1\, t\, l_w + 2\, A_{sw}\, f_y}$$

$$\frac{C}{l_t} = \frac{\left(\frac{A_{sw}\, f_y}{f_c'\, l_w\, t} + \frac{P}{f_c'\, l_w\, t} \cdot \frac{l_w}{l_t}\right)}{\alpha_1\, \beta_1 + 2\, \frac{A_{sw}\, f_y}{f_c'\, l_w\, t}}$$

$$\boldsymbol{\frac{C}{l_t} = \frac{\left(\frac{A_{sw}\, f_y}{f_c'\, l_w\, t} + \frac{P}{f_c'\, l_w\, t} \cdot \frac{l_w}{l_t}\right)}{\alpha_1\, \beta_1 + 2\, \frac{A_{sw}\, f_y}{f_c'\, l_w\, t}}} \qquad \textbf{\textit{Eq.A-8}}$$

Following the same principles used for uniformly distributed reinforcement, assume the web reinforcement ratio spans the entire length of the wall (l_t). However, in the boundary zones, the concentrated reinforcement (A_{be}) is notably higher than the distributed steel. To account for this overlap and simplify the calculation of the wall's mechanical properties, the mechanical reinforcement index ω is actualized and expressed as:

The reinforcement factor $\boldsymbol{\omega}$ requires adjustment to account for the concentration of steel in the boundary elements, which deviates from a uniform distribution.

$$\omega' = \frac{\left(A_s + 2A_s \frac{l_b}{l_w}\right) f_y}{f_c'\, l_w\, t} \qquad \alpha = \frac{P}{f_c'\, l_w\, t}$$

$$\boldsymbol{\frac{C}{l_t} = \frac{\omega + \alpha\, \frac{l_w}{l_t}}{\alpha_1\, \beta_1 + 2\, \omega}} \qquad \textbf{\textit{Eq. A-9}}$$

By taking the moment about the geometric center ($l_w/2$) of the wall, which accounts for the concrete compression force (Cc), the resultant of the distributed tensile steel stress (T), and the force couples from the concentrated boundary reinforcement (T_{be} and C_{be}). By multiplying each force by its respective lever arm, the ultimate flexural strength capacity M is derived as:

$$M = C_c \left(\frac{l_t}{2} - 0.5\beta_1 C\right) + T\left(\frac{l_t}{2} - \frac{l_t - C - C\,\beta}{2}\right) + T_{be}(l_t - l_b)$$

$$M = (\alpha_1\, f_c'\, \beta_1 C\, t)\left(\frac{l_t}{2} - 0.5\beta_1 C\right) + \left(A_{sf}\, f_y \frac{[l_t - C - C\,\beta)]}{l_w}\right)\left(\frac{l_t}{2} - \frac{l_t - C - C\,\beta}{2}\right) + A_{be} f_{y,be}(l_t - l_b)$$

$$M = (\alpha_1\, f_c'\, \beta_1 C\, t)\left(\frac{l_t}{2} - 0.5\beta_1 C\right) + \left(A_{sf}\, f_y \frac{[l_t - C(1+\beta)]}{l_w}\right)\left(\frac{C(1+\beta)}{2}\right) + A_{be} f_{y,be}(l_t - l_b)$$

$$\boldsymbol{M = (\alpha_1\, f_c'\, \beta_1 C\, t)\left(\frac{l_w}{2} - 0.5\beta_1 C\right) + \frac{A_{sf}\, f_y\, C}{2\, l_w}\,[l_t - C(1+\beta)](1+\beta) + A_{be} f_{y,be}(l_t - l_b)} \qquad \textbf{\textit{Eq. A-10}}$$

An alternative expression is derived by neglecting the contribution of the concentrated compression steel boundary force (C_{be}) and assuming the concrete carries the compressive strength, provided the compression reinforcement is not required to reach its full yield strength for equilibrium.

By equating the internal forces to solve for the neutral axis depth c, the expression is obtained:

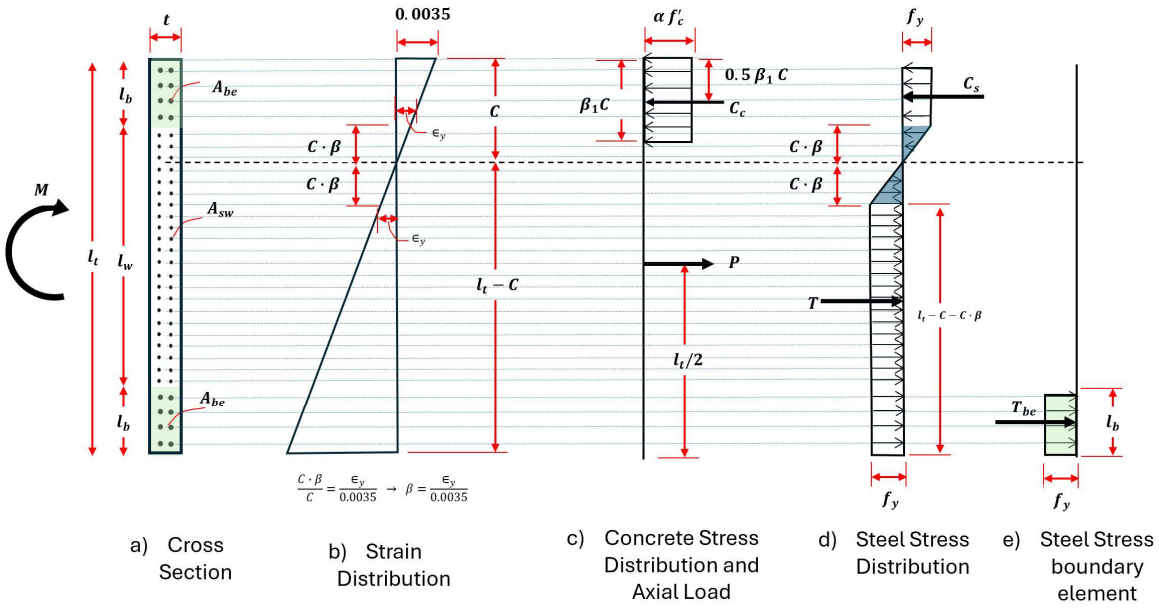

Figure A-7 Rectangular cross-section under the state of equilibrium (Concentrated Boundary Reinforcement in Tension only)

$$T_{be} + T + P = C_c + C_s$$

$$A_{be} f_{ybe} + \frac{[l_t - C - C\,\beta)]}{l_t} A_{sf}\, f_y + P = (\alpha\, f'_c\, \beta_1\, C\, t) + \frac{(C - C\,\beta)}{l_w} A_s\, f_y$$

$$C = \frac{l_w\,(A_{be} f_{ybe} + P) + l_t A_{sf}\, f_y}{l_w\,\alpha\, f'_c\, \beta_1\, t\, + 2\, A_{sf}\, f_y}$$

$$\frac{C}{l_t} = \frac{\frac{l_w}{l_t}\left(\frac{A_{be} f_{ybe}}{f'_c\, l_w\, t} + \frac{P}{f'_c\, l_w\, t}\right) + \frac{A_{sf}\, f_y}{f'_c\, l_w\, t}}{l_w\,\alpha\, f'_c\, \beta_1\, t\, + \frac{2\, A_{sf}\, f_y}{f'_c\, l_w\, t}}$$

$$\omega = \frac{\left(A_s + 2A_s \frac{l_b}{l_w}\right) f_y}{f'_c\, l_w\, t} \qquad \omega_{be} = \frac{A_{be}\, f_{ybe}}{f'_c\, l_w\, t} \qquad \alpha = \frac{P}{f'_c\, l_w\, t}$$

$$\boldsymbol{\frac{C}{l_t} = \frac{\frac{l_w}{l_t}(\omega_{be} + \alpha) + \omega}{\alpha_1\, \beta_1 + 2\, \omega}} \qquad \textbf{Eq. A-11}$$

Equation 4.1 provides the most accurate approximation of the ultimate moment capacity (M) for wall sections featuring concentrated reinforcement at their ends. It accounts for the simultaneous contributions of distributed web reinforcement across the entire wall length and the increased strength of the boundary elements. By integrating these two reinforcement types, the expression serves as the primary analytical tool for determining the flexural strength of walls with high-performance boundary reinforcement.

Finally, a refined analytical expression for walls with boundary elements was developed in collaboration with Dr. Pantazopoulou. This model assumes that the total tensile resistance comprises the concentrated boundary force (T_{be}) and a reduced contribution from the web reinforcement, where only 70% of the distributed steel in the tension zone is considered to reach yielding. Concurrently, the internal compressive resistance is assumed to come exclusively from the concrete stress block, neglecting the contribution of compression reinforcement to ensure a conservative, simplified equilibrium. This mechanical behavior is illustrated in the stress and strain profiles below:

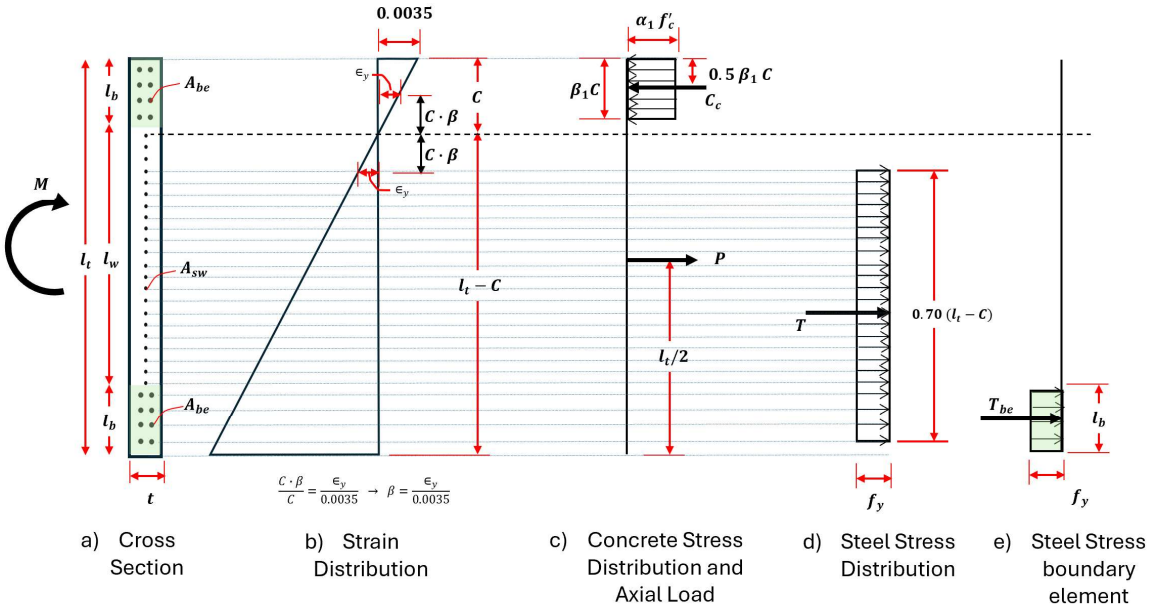

Figure A-8 Rectangular cross-section under the state of equilibrium considering 70% reinforcement in Tension (Concentrated Boundary Reinforcement in Tension only).

$$T + P + T_b = C_c$$

$$\rho_{vw} = A_s / t\, l_w$$

$$0.7\,\rho_{vw}\,(t\,l_w)\left[\frac{l_t - C}{l_t}\right] f_y + P + A_{sb}\,f_y = \alpha_1\,f'c\,\beta_1 C\,t$$

$$0.7\,\rho_{vw}\,(t\,l_w)\left[1 - \frac{C}{l_t}\right] f_y + P + A_{sb}\,f_y = \alpha_1\,f'c\,\beta_1 C\,t$$

$$C = \frac{0.7\,\rho_{vw}\,(t\,l_w)\,f_y + P + A_{sb}\,f_y}{\alpha\,f'c\,\beta_1\;t + \dfrac{0.7\,\rho_{vw}\,(t\,l_w)\,f_y}{l_t}}$$

$$C = \frac{\left(0.7\,\rho_{vw}\,(t\,l_w)\,f_y + P + A_{sb}\,f_y\right) l_t}{\alpha\,f'c\,\beta_1\;t\,l_t + 0.7\,\rho_{vw}\,(t\,l_w)\,f_y}$$

$$\boldsymbol{\frac{C}{l_t} = \frac{0.7\,\rho_{vw}\,(t\,l_w)\,f_y + P + A_{sb}\,f_y}{\alpha\,f'c\,\beta_1\;t\,l_t + 0.7\,\rho_{vw}\,(t\,l_w)\,f_y}} \qquad \textbf{Eq. A-12}$$

The nominal moment capacity (M) is derived by summing the moments of the internal force resultants about the geometric center of the wall. This expression integrates the concentrated forces from the boundary elements (T_{be} and C_{be}), the reduced contribution of the distributed web reinforcement, and the concrete compressive resultant (C_c).

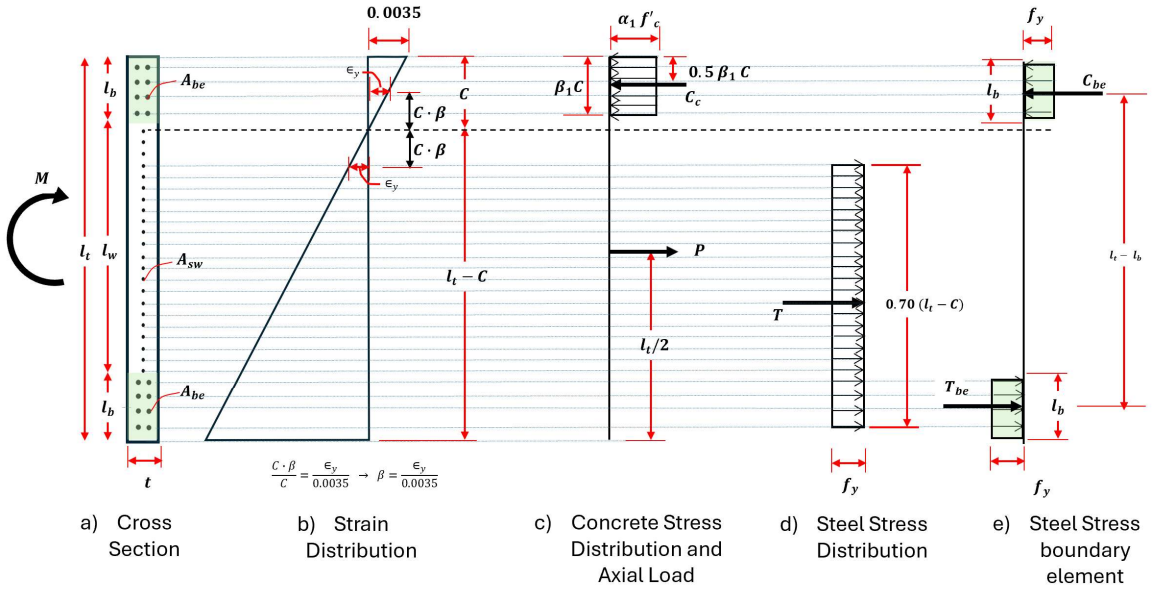

Figure A-9 Rectangular cross-section under the state of equilibrium considering 70% reinforcement in Tension (Concentrated Reinforcement Boundaries).

The nominal moment capacity is expressed as:

$$M = C_c\left(\frac{l_t}{2} - 0.5\beta_1 C\right) + T\left(\frac{l_t}{2} - \left(\frac{0.7\,(l_t - C)}{2} + l_b\right)\right) + T_b\left(\frac{l_t}{2} - \frac{l_b}{2}\right)$$

$$M = (\alpha_1\, f'c\, \beta_1 C\, t)\ \left(\frac{l_t}{2} - 0.5\beta_1 C\right) + \left(0.7\,\rho_v\, A_g\, f_y\left[\frac{l_t - C}{l_t}\right]\right)\left(\frac{l_t}{2} - \left(\frac{0.7\,(l_t - C)}{2} + l_b\right)\right) + A_{sb}\, f_y\left(\frac{l_t}{2} - \frac{l_b}{2}\right)$$

$$\boldsymbol{M = (0.5\,\alpha_1\, f'c\, \beta_1 C\, t\, l_t)\left(1 - \frac{\beta_1 C}{l_t}\right) + 0.7\,\rho_v\, A_g\, f_y\left[1 - \frac{C}{l_t}\right](0.15\, l_t + 0.35\, C - l_b) + 0.5\, A_{sb}\, f_y(l_t - l_b)} \qquad \textit{Eq. A-13}$$

Four additional cases were analyzed featuring a shear wall with boundary reinforcement. These analytical results are compared with outputs from Response-2000 (see Appendix). The objective of this comparison is to accurately capture the ultimate strength of the wall while validating the derived equations against Response-2000 as a recognized benchmark for sectional analysis.

Examples 6 and 9 maintain identical cross-sectional geometry while varying the reinforcement ratios to isolate the impact of steel density on capacity. Similarly, Examples 7 and 8 utilize consistent geometric parameters with varying reinforcement configurations. This approach allows for a direct evaluation of how reinforcement ratios influence the flexural performance of walls with boundary elements.

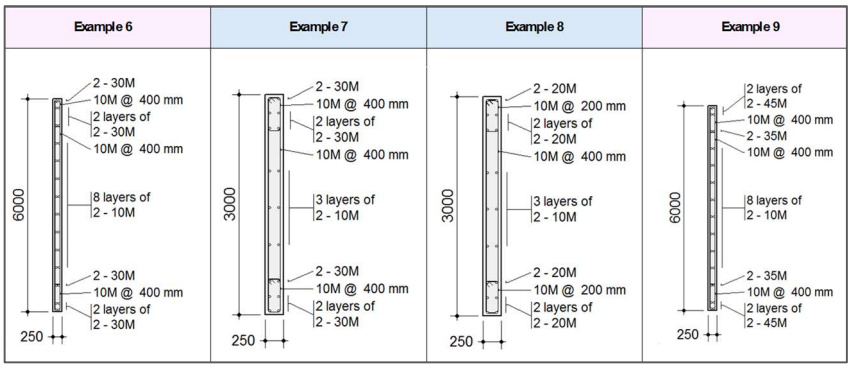

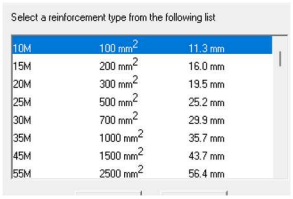

Figure A-10 Four rectangular cross-sections with boundary reinforcement (Ex6 to Ex9) on Response 2000.

The study evaluates the neutral axis depth (C) and nominal moment capacity (M) for each wall specimen using three analytical approaches and one computational benchmark. The organization of the comparative data is as follows:

I. Equations A-9 and A-10: are derived using the fundamental principles established in the Cárdenas and Magura formulations. The primary distinction in this approach lies in the explicit separation of the boundary elements from the web reinforcement, allowing their unique contribution to be integrated directly into the flexural strength formulation.

II. Equation A-11: This approach simplifies the section analysis by neglecting the contribution of the concentrated compression steel boundary force (Cbe)

III. Equation A-12 and A-13: This model introduces a conservative assumption that only 70% of the uniformly distributed reinforcement within the tension zone reaches its full yield strength.

IV. Response 2000 (flexural): To establish a reference point for wall strength, results were obtained from Response-2000 software (Depicted in red)

V. Response 2000 + Shear: For a comprehensive view of nonlinear behavior, additional software runs were performed to account for shear-flexure interaction at specific shear spans (L= 2 m and L= 4.02 m)

		F_y	F'_c	L_t	L_w	L_b	t	A_s	A_{sb}	P	ω	α	α_1	β_1	β	ρ_v	C / L	C	Error	M	Error
		Mpa	Mpa	mm	mm	mm	mm	mm^2	mm^2	N								mm		kN*m	
Example 6	EQ4.1 & EQ 4.2	400	30	6000	4400	800	250	1600	4200	4041000	0.026	0.1225	0.81	0.90	**1.00**	0.667%	0.150	902	*13%*	21940	*6%*
	EQ5 & EQ 4.2																0.161	968	*7%*	22734	*2%*
	EQ6 & EQ 6.1																0.188	1126	*-8%*	20680	*11%*
	Resp. 2000 (flexural)																**0.174**	**1042**		**23252**	
	Resp. 2000 + Shear (L= 2 m)																0.323	1938	*46%*	6387	*73%*
	Resp. 2000 + Shear (L= 4.02 m)																0.340	2038	*96%*	10749	*54%*
Example 7	EQ4.1 & EQ 4.2	400	30	3000	1900	550	250	600	4200	4041000	0.027	0.2836	0.81	0.90	**1.00**	1.200%	0.267	800	*8%*	9192	*3%*
	EQ5 & EQ 4.2																0.289	866	**0%**	9460	*0%*
	EQ6 & EQ 6.1																0.360	1079	*-24%*	8435	*11%*
	Resp. 2000 (flexural)																**0.289**	**868**		**9503**	
	Resp. 2000 + Shear (L= 2 m)																0.513	1539	*44%*	3564	*62%*
	Resp. 2000 + Shear (L= 4.02 m)																0.388	1165	*34%*	6167	*35%*
Example 8	EQ4.1 & EQ 4.2	400	30	3000	1900	550	250	600	1800	4041000	0.027	0.2836	0.81	0.90	**1.00**	0.560%	0.267	800	*5%*	6840	*5%*
	EQ5 & EQ 4.2																0.246	738	*12%*	6570	*8%*
	EQ6 & EQ 6.1																0.301	903	*-7%*	6406	*11%*
	Resp. 2000 (flexural)																**0.281**	**842**		**7179**	
	Resp. 2000 + Shear (L= 2 m)																0.530	1591	*47%*	3416	*52%*
	Resp. 2000 + Shear (L= 4.02 m)																0.309	927	*10%*	5232	*27%*
Example 9	EQ4.1 & EQ 4.2	400	30	6000	4400	800	250	1600	8000	4041000	0.026	0.1225	0.81	0.90	**1.00**	1.173%	0.150	902	*19%*	29844	*7%*
	EQ5 & EQ 4.2																0.195	1171	**-5%**	32926	*-3%*
	EQ6 & EQ 6.1																0.234	1404	*-26%*	28541	*11%*
	Resp. 2000 (flexural)																**0.186**	**1115**		**32096**	
	Resp. 2000 + Shear (L= 2 m)																0.305	1832	*39%*	6798	*79%*
	Resp. 2000 + Shear (L= 4.02 m)																0.274	1642	*47%*	12707	*60%*

Figure A-11 Rectangular wall (boundary elements) neutral axis depth and flexural calculations.

Under pure flexural conditions, the analytical approaches represented by Equations A-9 through A-13demonstrate a strong correlation with the Response-2000 benchmarks. Specifically, Equations A-11 and A-10 yielded the most precise results when compared to the computational data. However, in Example 9, the formulation produced an over-strength result, predicting a capacity higher than the benchmark. From a structural safety perspective, this discrepancy must be carefully addressed, as design methodologies should prioritize conservatism to mitigate the risk of failure.

Equations 4.1 and 4.2 were also highly accurate. These findings validate these governing equilibrium equations as a robust baseline for sectional analysis. With this validation complete, the analysis can proceed to derive strength expressions for U-shaped cross-sections featuring concentrated boundary elements in their corners.

Appendix B

Confinement Effectiveness

Confinement models are applied to the distinct boundary element zones of the U-shaped wall. Since the stirrup spacing varies by floor (50 mm, 100 mm, and 200 mm), the confinement effectiveness changes accordingly.

Confined EB1 (1st Floor)

b	100	mm
h	300	mm
cover	15	mm
d_b	Φ6	mm
b_c	70	mm
h_c	270	mm
s_h	50	mm
Σb_i^2	47500	mm
k_e	0.3390	
A_{sw}(mm²)	28.27	mm²
ρ_w	0.02035	
$\rho_{w,eff}$	0.006897	
f'c	27	Mpa
fy	550	Mpa

$k_e = \left(1-\frac{\sum b_i^2}{2b_c}\right)\left(1-\frac{s_h}{2h_c}\right)\left(1-\frac{\sum_{nw} b_i^2}{6b_c h_c}\right)$

Effect of the heights arrangement — Effect of cross sectional pattern

0.643 0.907 0.581

$\rho_w = \frac{A_{sw}\cdot(2b_c+2h_c)}{b_c\cdot h_c\cdot s}$ $\rho_w = \frac{A_{sw}\cdot 4\cdot b_c}{b_c^2\cdot s}$

$\rho_{w,eff} = k_e\rho_w$

Long.		
R_{eff}. b	2	Φ12
R_{eff}. h	4	Φ12

b_i	50	mm	2
h_{i1}	75	mm	4
h_{i2}	100	mm	2

Transvers.		
R_{eff}. b	2	Φ6
R_{eff}. h	4	Φ6

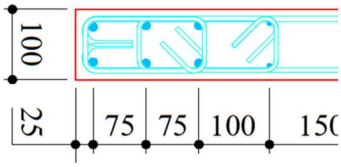

Richart et al.

$$f_{cc}^{'} = f_c^{'} + 4.1\sigma_{lat} \approx f_c^{'}(1+2k_e\rho_w\frac{f_{yw}}{f_c^{'}});$$
$$\varepsilon_{cc,u} = \varepsilon_{co}(1+5(\frac{f_{cc}^{'}}{f_c^{'}}-1)) = \varepsilon_{co}(1+10k_e\rho_w\frac{f_{yw}}{f_c^{'}}) = \varepsilon_{co}(1+20k_e\rho_w\frac{f_{yw}}{f_c^{'}})$$

$\sigma_{lat\ h}$	4.147			
$\sigma_{lat\ b}$	6.220			
$f'_{cc\ h}$	**31.15**	Mpa	≈	34.587
$f'_{cc\ b}$	**33.22**	Mpa		

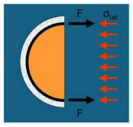

σ_{lat} = 2F/D for spiral confinement. The highest value of σ_{lat} occurs at the onset of stirrup yielding :
F = $f_{yw}A_{sw}$/s (kN per leg per 1 m length)
σ_{lat} = 2$f_{yw}A_{sw}$/D·s (internal pressure)

f'_{cc}	**31.15**	Mpa		
ε_{co}	**0.0022**		$\varepsilon_o = 2f_c/E_o \approx 0.0022$ for common strength concrete	
$\varepsilon_{cc,u}$	0.0038895		≈ 0.00529	≈ 0.00838

CEB-FIP

$$f_{cc} = f_c(1+2.5k_e\omega_w) \quad (k_e\omega_w \le 0.1);$$
$$f_{cc} = f_c(1.125+1.25k_e\omega_w) \quad (k_e\omega_w \ge 0.1)$$
$$\varepsilon_{cc,o} = \varepsilon_{co}\left(\frac{f_{cc}}{f_c}\right)^2; \qquad \varepsilon_{cc,85} = \varepsilon_{c,85} + 0.1k_e\omega_w$$

k_e	0.3390	and the mechanic	
ω_w	0.4144	$\omega_w = \rho_w\frac{f_{yw}}{f_c} \Rightarrow$	
$k_e\,\omega_w$	0.1405	>	0.1
f'_{cc}	**35.12**	Mpa	
$\varepsilon_{cc,u}$	0.003722		
$\varepsilon_{c,85}$	**0.0035**	*(UNCONFINED)*	
$\varepsilon_{cc,85}$	0.017549		

Park, Priestley

$$f_{cc}^{'} = f_c^{'} + \rho_w f_{wy} = Kf_c^{'}; \quad K = 1+\rho_w\frac{f_{wy}}{f_c^{'}}; \quad f_{cc,res} \doteq 20-30\%f_{cc}$$
$$Z = \frac{0.5}{\varepsilon_{cc,50}-\varepsilon_{cc,o}}; \quad \varepsilon_{cc,50} = \frac{3+0.29f_c^{'}}{145f_c^{'}-1000} + 0.75\rho_w\left(\frac{b_c}{s}\right)^{1/2};$$

f'_{cc}	**38.19**	Mpa
K	1.414	
$\varepsilon_{cc,50}$	0.021770	
	0.039174	
Z	25.55	

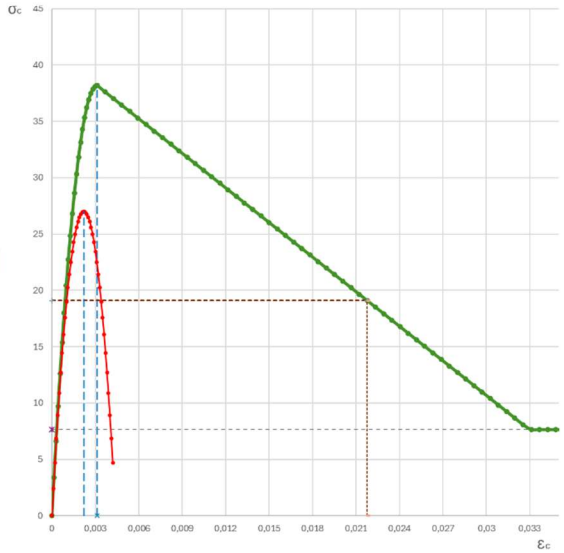

Confined EB1 (2nd Floor)

b	100	mm
h	300	mm
cover	15	mm
d_b	Φ6	mm
b_c	70	mm
h_c	270	mm
s_h	100	mm
Σb_i^2	47500	mm
k_e	0.1353	
A_{sw}(mm²)	28.27	mm²
ρ_w	0.01017	
$\rho_{w,eff}$	0.001376	
f'c	27	Mpa
fy	550	Mpa

$$k_e = \left(1-\frac{s_h}{2b_c}\right)\left(1-\frac{s_h}{2h_c}\right)\left(1-\frac{\sum b_i^2}{6b_c h_c}\right)$$

(Effect of the heightwise arrangement; Effect of cross sectional pattern)

0.286 0.815 0.581

$$\rho_w = \frac{A_{sw} * (2b_c + 2h_c)}{b_c\, h_c * s}$$

$$\rho_{w,eff} = k_e \rho_w$$

Long.		
R_{eff}· b	2	Φ12
R_{eff}· h	4	Φ12

b_i	50	mm	2
h_i	75	mm	4
	100		2

$$\rho_w = \frac{A_{sw} \cdot 4 \cdot b_c}{b_c^2 \cdot s}$$

Transvers.		
R_{eff}· b	2	Φ6
R_{eff}· h	4	Φ6

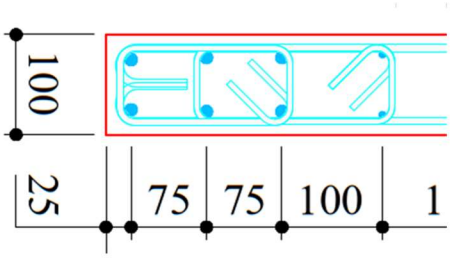

Richart et al.

$$f'_{cc} = f'_c + 4.1\sigma_{lat} \approx f'_c(1 + 2k_e\rho_w \frac{f_{yw}}{f'_c});$$

$$\varepsilon_{cc,u} = \varepsilon_{co}(1 + 5(\frac{f'_{cc}}{f'_c} - 1)) = \varepsilon_{co}(1 + 10k_e\rho_w \frac{f_{yw}}{f'_c}) = \varepsilon_{co}(1 + 20k_e\rho_w \frac{f_{yw}}{f'_c})$$

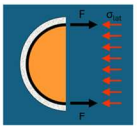

$\sigma_{lat} = 2F/D$ for spiral confinement. The highest value of σ_{lat} occurs at the onset of stirrup yielding :

$F = f_{yw}A_{sw}/s$ (kN per leg per 1 m length)

$\sigma_{lat} = 2f_{yw}A_{sw}/D{\cdot}s$ (internal pressure)

$\sigma_{lat\,h}$	2.073			
$\sigma_{lat\,b}$	3.110			
$f'_{cc\,h}$	29.07	Mpa		
$f'_{cc\,b}$	30.11	Mpa	≈	28.514

f'_{cc}	29.07	Mpa		
ε_{co}	0.0022		$\varepsilon_o = 2f'_c/E_o \approx 0.0022$ for common strength concrete	
$\varepsilon_{cc,u}$	0.0030447		≈ 0.00282	≈ 0.00343

CEB-FIP

$$f_{cc} = f_c(1 + 2.5k_e\omega_w) \quad (k_e\omega_w \le 0.1);$$
$$f_{cc} = f_c(1.125 + 1.25k_e\omega_w) \quad (k_e\omega_w \ge 0.1)$$

$$\varepsilon_{cc,o} = \varepsilon_{co}\left(\frac{f_{cc}}{f_c}\right)^2; \qquad \varepsilon_{cc,85} = \varepsilon_{c,85} + 0.1k_e\omega_w$$

k_e	0.1353	and the mechanic	$\omega_w = \rho_w \frac{f_{yw}}{f'_c} \Rightarrow$
ω_w	0.2072		
$k_e\,\omega_w$	0.0280	<	0.1
f'_{cc}	28.89	Mpa	
$\varepsilon_{cc,u}$	0.002519		
$\varepsilon_{c,85}$	0.0035	*(UNCONFINED)*	
$\varepsilon_{cc,85}$	0.006304		

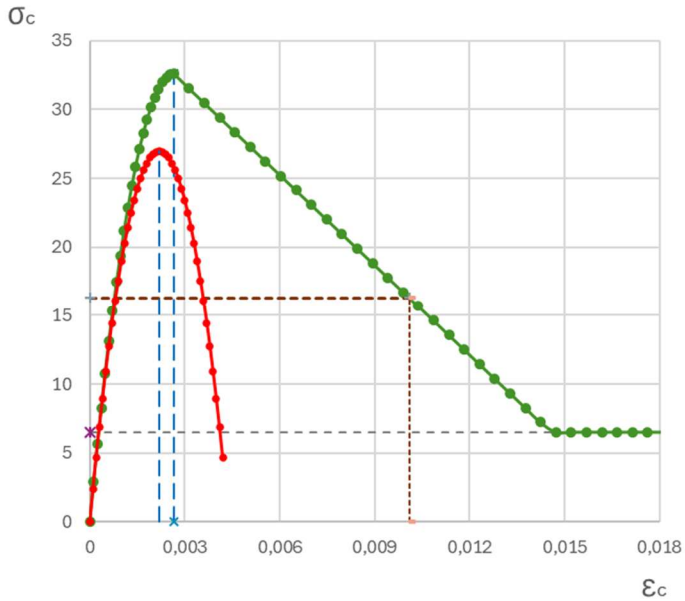

Park, Priestley

$$f'_{cc} = f'_c + \rho_w f_{wy} = Kf'_c; \quad K = 1 + \rho_w \frac{f_{wy}}{f'_c}; \quad f_{cc,res} \doteq 20 - 30\% f_{cc}$$

$$Z = \frac{0.5}{\varepsilon_{cc,50} - \varepsilon_{cc,o}}; \quad \varepsilon_{cc,50} = \frac{3 + 0.29f'_c}{145f'_c - 1000} + 0.75\rho_w\left(\frac{b_c}{s}\right)^{1/2};$$

f'_{cc}	32.60	Mpa
K	1.207	
$\varepsilon_{cc,50}$	0.010099	
	0.016252	
Z	63.30	

Confined EB1 (3nd Floor)

b	100	mm
h	300	mm
cover	15	mm
d_b	Φ6	mm
b_c	70	mm
h_c	270	mm
s_h	200	mm
Σb_i^2	47500	mm
k_e	-0.1568	
A_{sw} (mm²)	28.27	mm²
ρ_w	0.00509	
$\rho_{w,eff}$	-0.000798	
f'c	27	Mpa
fy	550	Mpa

$$k_e = \left(1-\frac{s_h}{2b_c}\right)\left(1-\frac{s_h}{2h_c}\right)\left(1-\frac{\sum b_i^2}{6b_c h_c}\right)$$

Effect of the heightwise arrangement — Effect of cross sectional pattern

-0.429 0.630 0.581

$$\rho_w = \frac{A_{sw} * (2b_c + 2h_c)}{b_c\, h_c * s}$$

$$\rho_{w,eff} = k_e \rho_w$$

$$\rho_w = \frac{A_{sw} \cdot 4 \cdot b_c}{b_c^2 \cdot s}$$

Long.

$R_{eff.}$ b	2	Φ12
$R_{eff.}$ h	4	Φ12

b_i	50	mm	2
h_i	75	mm	4
	100		2

Transvers.

$R_{eff.}$ b	2	Φ6
$R_{eff.}$ h	4	Φ6

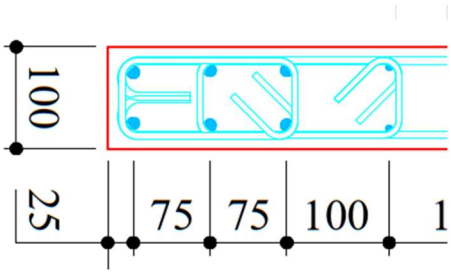

Richart et al.

$$f_{cc}^{'} = f_c^{'} + 4.1\sigma_{lat} \approx f_c^{'}(1 + 2k_e\rho_w \frac{f_{yw}}{f_c^{'}});$$

$$\varepsilon_{cc,u} = \varepsilon_{co}(1 + 5(\frac{f_{cc}^{'}}{f_c^{'}} - 1)) = \varepsilon_{co}(1 + 10k_e\rho_w \frac{f_{yw}}{f_c^{'}}) = \varepsilon_{co}(1 + 20k_e\rho_w \frac{f_{yw}}{f_c^{'}})$$

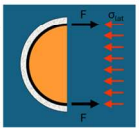

$\sigma_{lat} = 2F/D$ for spiral confinement. The highest value of σ_{lat} occurs at the onset of stirrup yielding :

F = $f_{yw}A_{sw}$/s (kN per leg per 1 m length)

$\sigma_{lat} = 2f_{yw}A_{sw}/D{\cdot}s$ (internal pressure)

$\sigma_{lat\ h}$	1.037			
$\sigma_{lat\ b}$	1.555			
$f'_{cc\ h}$	28.04	Mpa	≈	26.123
$f'_{cc\ b}$	28.56	Mpa		

f'_{cc}	28.04	Mpa	
ε_{co}	0.0022		$\varepsilon_o = 2f_c/E_o \approx 0.0022$ for common strength concrete
$\varepsilon_{cc,\ u}$	0.0026224	≈ 0.00184	≈ 0.00149

CEB-FIP

$$f_{cc} = f_c(1 + 2.5k_e\omega_w) \quad (k_e\omega_w \le 0.1);$$
$$f_{cc} = f_c(1.125 + 1.25k_e\omega_w) \quad (k_e\omega_w \ge 0.1)$$
$$\varepsilon_{cc,o} = \varepsilon_{co}\left(\frac{f_{cc}}{f_c}\right)^2; \qquad \varepsilon_{cc,85} = \varepsilon_{c,85} + 0.1k_e\omega_w$$

k_e	-0.1568	and the mechanic	
ω_w	0.1036	$\omega_w = \rho_w \frac{f_{yw}}{f_c} \Rightarrow$	
$k_e\,\omega_w$	-0.0162	<	0.1
f'_{cc}	25.90	Mpa	
$\varepsilon_{cc,\ u}$	0.002025		
$\varepsilon_{c,\ 85}$	0.0035	*(UNCONFINED)*	
$\varepsilon_{cc,\ 85}$	0.001875		

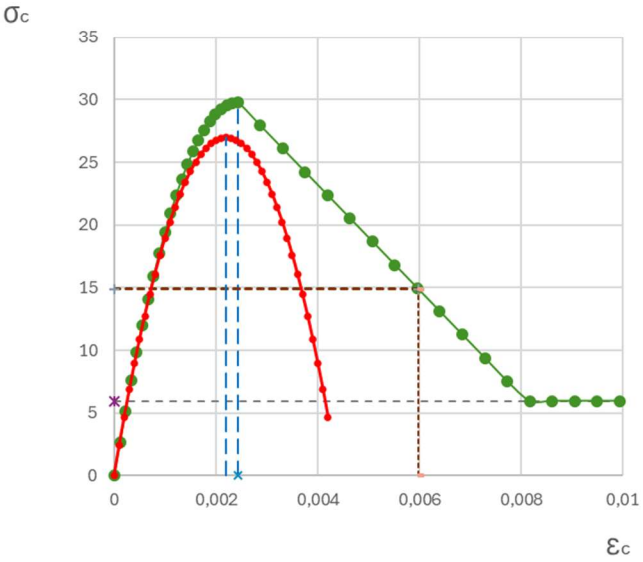

Park, Priestley

$$f_{cc}^{'} = f_c^{'} + \rho_w f_{wy} = Kf_c^{'}; \quad K = 1 + \rho_w \frac{f_{wy}}{f_c^{'}}; \quad f_{cc,res} \doteq 20 - 30\% f_{cc}$$
$$Z = \frac{0.5}{\varepsilon_{cc,50} - \varepsilon_{cc,o}}; \quad \varepsilon_{cc,50} = \frac{3 + 0.29f_c^{'}}{145f_c^{'} - 1000} + 0.75\rho_w\left(\frac{b_c}{s}\right)^{1/2};$$

f'_{cc}	29.80	Mpa
K	1.104	
$\varepsilon_{cc,\ 50}$	0.005972	
	0.008148	
Z	132.55	

Confined EB2 (1st Floor)

b	100	mm
h	200	mm
cover	15	mm
d_b	Φ6	mm
b_c	70	mm
h_c	170	mm
s_h	50	mm
Σb_i^2	30000	mm
k_e	0.3179	
A_{sw}(mm²)	28.27	mm²
ρ_w	0.02281	
$\rho_{w,eff}$	0.007252	
f'c	27	Mpa
fy	550	Mpa

$$k_e = \left(1-\frac{s_h}{2b_c}\right)\left(1-\frac{s_h}{2h_c}\right)\left(1-\frac{\sum b_i^2}{6b_c h_c}\right)$$

(Effect of the heighwise arrangement; Effect of cross sectional pattern)

0.643 0.853 0.580

$$\rho_w = \frac{A_{sw} * (2b_c + 2h_c)}{b_c h_c * s}$$

$$\rho_{w,eff} = k_e \rho_w$$

Long.		
R_{eff}. b	2	Φ 12
R_{eff}. h	3	Φ 12

b_i	50	mm	2
h_i	50	mm	2
	100		2

$$\rho_w = \frac{A_{sw} \cdot 4 \cdot b_c}{b_c^2 \cdot s}$$

Transvers.		
R_{eff}. b	2	Φ 6
R_{eff}. h	2	Φ 6

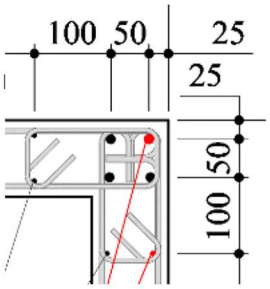

Richart et al.

$$f'_{cc} = f'_c + 4.1\sigma_{lat} \approx f'_c(1 + 2k_e\rho_w \frac{f_{yw}}{f'_c});$$

$$\varepsilon_{cc,u} = \varepsilon_{co}(1 + 5(\frac{f'_{cc}}{f'_c} - 1)) = \varepsilon_{co}(1 + 10k_e\rho_w \frac{f_{yw}}{f'_c}) = \varepsilon_{co}(1 + 20k_e\rho_w \frac{f_{yw}}{f'_c})$$

$\sigma_{lat\ h}$	3.110			
$\sigma_{lat\ b}$	6.220			
$f'_{cc\ h}$	**30.11**	Mpa	≈	34.977
$f'_{cc\ b}$	**33.22**	Mpa		

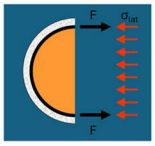

$\sigma_{lat} = 2F/D$ for spiral confinement. The highest value of σ_{lat} occurs at the onset of stirrup yielding :

$F = f_{yw}A_{sw}/s$ (kN per leg per 1 m length)

$\sigma_{lat} = 2f_{yw}A_{sw}/D{\cdot}s$ (internal pressure)

f'_{cc}	**30.11**	Mpa	
ε_{co}	**0.0022**		$\varepsilon_o = 2f_c/E_o \approx 0.0022$ for common strength concrete
$\varepsilon_{cc,\ u}$	0.0034671	≈ 0.00545	≈ 0.00870

CEB-FIP

$$f_{cc} = f_c(1 + 2.5k_e\omega_w) \quad (k_e\omega_w \le 0.1);$$
$$f_{cc} = f_c(1.125 + 1.25k_e\omega_w) \quad (k_e\omega_w \ge 0.1)$$
$$\varepsilon_{cc,o} = \varepsilon_{co}\left(\frac{f_{cc}}{f_c}\right)^2; \qquad \varepsilon_{cc,85} = \varepsilon_{c,85} + 0.1k_e\omega_w$$

k_e	0.3179	and the mechanic	
ω_w	0.4646	$\omega_w = \rho_w \frac{f_{yw}}{f_c} \Rightarrow$	
$k_e\ \omega_w$	0.1477	>	0.1
f'_{cc}	**35.36**	Mpa	
$\varepsilon_{cc,\ u}$	0.003773		
$\varepsilon_{c,\ 85}$	**0.0035**	*(UNCONFINED)*	
$\varepsilon_{cc,\ 85}$	0.018272		

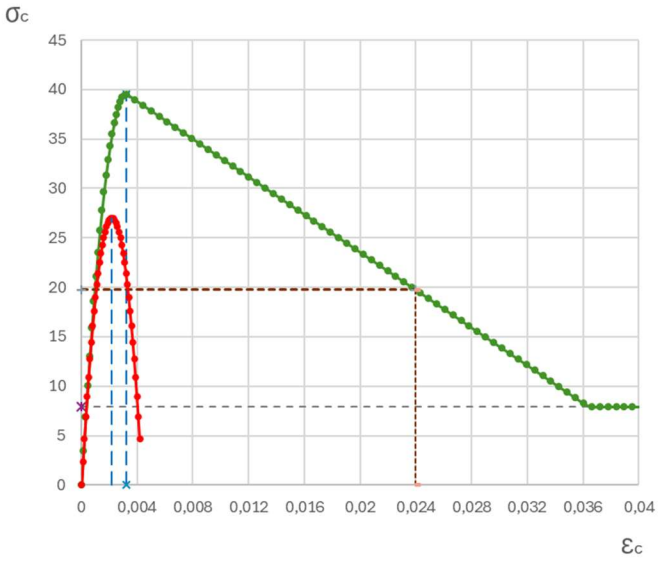

Park, Priestley

$$f'_{cc} = f'_c + \rho_w f_{wy} = Kf'_c; \quad K = 1 + \rho_w \frac{f_{wy}}{f'_c}; \quad f_{cc,res} \doteq 20 - 30\% f_{cc}$$
$$Z = \frac{0.5}{\varepsilon_{cc,50} - \varepsilon_{cc,o}}; \quad \varepsilon_{cc,50} = \frac{3 + 0.29f'_c}{145f'_c - 1000} + 0.75\rho_w\left(\frac{b_c}{s}\right)^{1/2};$$

f'_{cc}	**39.55**	Mpa
K	1.465	
$\varepsilon_{cc,\ 50}$	0.023957	
	0.035259	
Z	22.98	

Confined EB2 (2nd Floor)

b	100	mm
h	200	mm
cover	15	mm
d_b	Φ6	mm
b_c	70	mm
h_c	170	mm
s_h	100	mm
Σb_i^2	30000	mm
k_e	0.1169	
A_{sw} (mm²)	28.27	mm²
ρ_w	0.01140	
$\rho_{w,eff}$	0.001334	
f'c	27	Mpa
fy	550	Mpa

$$k_e = \left(1-\frac{s_h}{2b_c}\right)\left(1-\frac{s_h}{2h_c}\right)\left(1-\frac{\sum b_i^2}{6b_c h_c}\right)$$

(Effect of the heightwise arrangement; Effect of cross sectional pattern)

0.286 0.706 0.580

$$\rho_w = \frac{A_{sw} * (2b_c + 2h_c)}{b_c\, h_c * s}$$

$$\rho_{w,eff} = k_e \rho_w$$

Long.

$R_{eff.}$ b	2	Φ12
$R_{eff.}$ h	3	Φ12

b_i	50	mm	2
h_i	50	mm	2
	100		2

$$\rho_w = \frac{A_{sw} \cdot 4 \cdot b_c}{b_c^2 \cdot s}$$

Transvers.

$R_{eff.}$ b	2	Φ6
$R_{eff.}$ h	2	Φ6

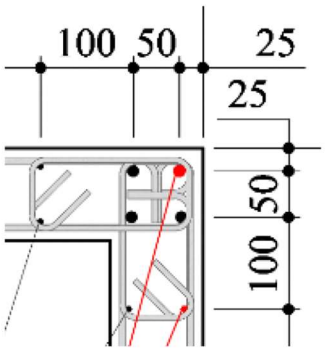

Richart et al.

$$f_{cc}^{'} = f_c^{'} + 4.1\sigma_{lat} \approx f_c^{'}(1 + 2k_e\rho_w \frac{f_{yw}}{f_c^{'}});$$

$$\varepsilon_{cc,u} = \varepsilon_{co}(1 + 5(\frac{f_{cc}^{'}}{f_c^{'}} - 1)) = \varepsilon_{co}(1 + 10k_e\rho_w \frac{f_{yw}}{f_c^{'}}) = \varepsilon_{co}(1 + 20k_e\rho_w \frac{f_{yw}}{f_c^{'}})$$

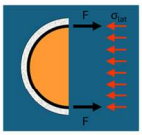

σ_{lat} = **2F/D** for spiral confinement. The highest value of σ_{lat} occurs at the onset of stirrup yielding :

F = $f_{yw}A_{sw}$/s (kN per leg per 1 m length)

σ_{lat} = $2f_{yw}A_{sw}$/D·s (internal pressure)

$\sigma_{lat\,h}$	1.555			
$\sigma_{lat\,b}$	3.110			
$f'_{cc\,h}$	28.56	Mpa	≈	28.467
$f'_{cc\,b}$	30.11	Mpa		

f'_{cc}	28.56	Mpa
ε_{co}	0.0022	$\varepsilon_o = 2f_c/E_o \approx 0.0022$ for common strength concrete
$\varepsilon_{cc,u}$	0.0028336	≈ 0.00280 ≈ 0.00340

CEB-FIP

$$f_{cc} = f_c(1 + 2.5k_e\omega_w) \quad (k_e\omega_w \le 0.1);$$
$$f_{cc} = f_c(1.125 + 1.25k_e\omega_w) \quad (k_e\omega_w \ge 0.1)$$
$$\varepsilon_{cc,o} = \varepsilon_{co}\left(\frac{f_{cc}}{f_c}\right)^2; \qquad \varepsilon_{cc,85} = \varepsilon_{c,85} + 0.1k_e\omega_w$$

k_e	0.1169	and the mechanic $\omega_w = \rho_w \frac{f_{yw}}{f_c} \Rightarrow$		
ω_w	0.2323			
$k_e\,\omega_w$	0.0272	<	0.1	
f'_{cc}	28.83	Mpa		
$\varepsilon_{cc,u}$	0.002509			
$\varepsilon_{c,85}$	0.0035	*(UNCONFINED)*		
$\varepsilon_{cc,85}$	0.006217			

Park, Priestley

$$f_{cc}^{'} = f_c^{'} + \rho_w f_{wy} = Kf_c^{'}; \quad K = 1 + \rho_w \frac{f_{wy}}{f_c^{'}}; \quad f_{cc,res} \doteq 20 - 30\% f_{cc}$$
$$Z = \frac{0.5}{\varepsilon_{cc,50} - \varepsilon_{cc,o}}; \quad \varepsilon_{cc,50} = \frac{3 + 0.29f_c^{'}}{145f_c^{'} - 1000} + 0.75\rho_w\left(\frac{b_c}{s}\right)^{1/2};$$

f'_{cc}	33.27	Mpa
K	1.232	
$\varepsilon_{cc,50}$	0.010872	
	0.014868	
Z	57.66	

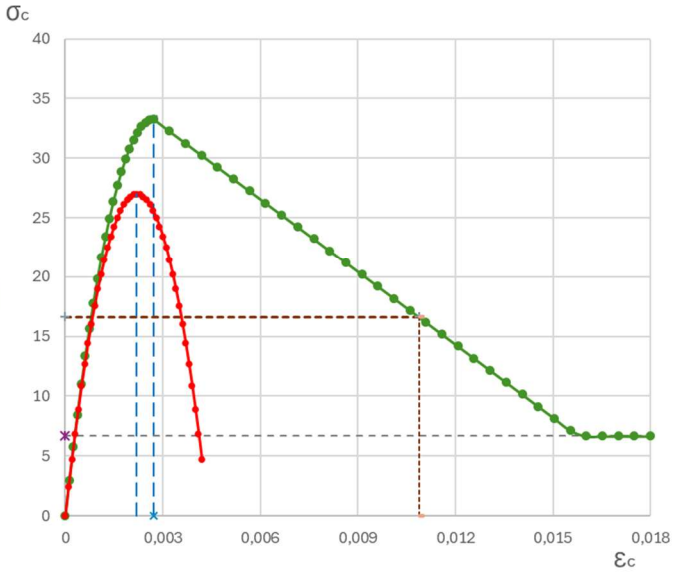

Confined EB2 (3nd Floor)

b	100	mm
h	200	mm
cover	15	mm
d_b	Φ6	mm
b_c	70	mm
h_c	170	mm
s_h	200	mm
Σb_i^2	30000	mm
k_e	-0.1023	
A_{sw} (mm²)	28.27	mm²
ρ_w	0.00570	
$\rho_{w,eff}$	-0.000583	
f'c	27	Mpa
fy	550	Mpa

$$k_e = \left(1-\frac{s_h}{2b_c}\right)\left(1-\frac{s_h}{2h_c}\right)\left(1-\frac{\sum b_i^2}{6b_c h_c}\right)$$

(Effect of the heightwise arrangement; Effect of cross sectional pattern)

-0.429 0.412 0.580

$$\rho_w = \frac{A_{sw} * (2b_c + 2h_c)}{b_c\, h_c * s}$$

$$\rho_{w,eff} = k_e \rho_w$$

Long.		
$R_{eff.}$ b	2	Φ12
$R_{eff.}$ h	3	Φ12

b_i	50	mm	2
h_i	50	mm	2
	100		2

$$\rho_w = \frac{A_{sw} \cdot 4 \cdot b_c}{b_c^2 \cdot s}$$

Transvers.		
$R_{eff.}$ b	2	Φ6
$R_{eff.}$ h	2	Φ6

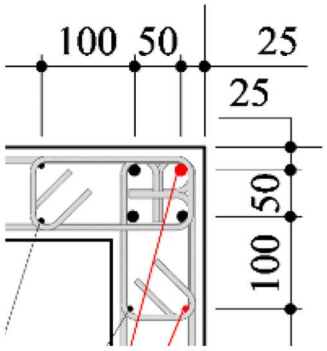

Richart et al.

$$f'_{cc} = f'_c + 4.1\sigma_{lat} \approx f'_c(1 + 2k_e\rho_w \frac{f_{yw}}{f'_c});$$

$$\varepsilon_{cc,lt} = \varepsilon_{co}(1 + 5(\frac{f'_{cc}}{f'_c} - 1)) = \varepsilon_{co}(1 + 10k_e\rho_w \frac{f_{yw}}{f'_c}) = \varepsilon_{co}(1 + 20k_e\rho_w \frac{f_{yw}}{f'_c})$$

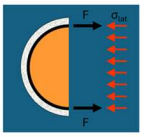

σ_{lat} = 2F/D for spiral confinement. The highest value of σ_{lat} occurs at the onset of stirrup yielding :

F = $f_{yw}A_{sw}$/s (kN per leg per 1 m length)

σ_{lat} = $2f_{yw}A_{sw}$/D·s (internal pressure)

$\sigma_{lat\ h}$	0.778			
$\sigma_{lat\ b}$	1.555			
$f'_{cc\ h}$	27.78	Mpa		
$f'_{cc\ b}$	28.56	Mpa	≈	26.358

f'_{cc}	27.78	Mpa		
ε_{co}	0.0022		$\varepsilon_o = 2f'_c/E_o \approx 0.0022$ for common strength concrete	
$\varepsilon_{cc,u}$	0.0025168		≈ 0.00194	≈ 0.00168

CEB-FIP

$$f_{cc} = f_c(1 + 2.5k_e\omega_w) \quad (k_e\omega_w \le 0.1);$$
$$f_{cc} = f_c(1.125 + 1.25k_e\omega_w) \quad (k_e\omega_w \ge 0.1)$$
$$\varepsilon_{cc,o} = \varepsilon_{co}\left(\frac{f_{cc}}{f_c}\right)^2; \qquad \varepsilon_{cc,85} = \varepsilon_{c,85} + 0.1k_e\omega_w$$

k_e	-0.1023	and the mechanic $\omega_w = \rho_w \frac{f_{yw}}{f_c} \Rightarrow$		
ω_w	0.1162			
$k_e\,\omega_w$	-0.0119	<	0.1	
f'_{cc}	26.20	Mpa		
$\varepsilon_{cc,u}$	0.002071			
$\varepsilon_{c,85}$	0.0035	*(UNCONFINED)*		
$\varepsilon_{cc,85}$	0.002311			

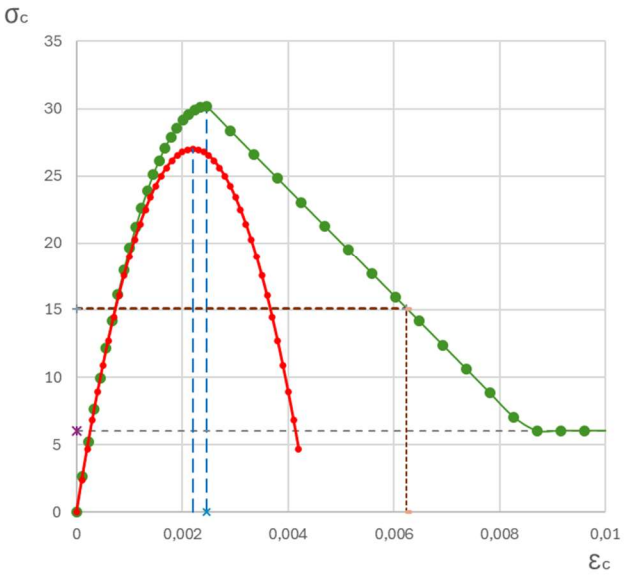

Park, Priestley

$$f'_{cc} = f'_c + \rho_w f_{wy} = Kf'_c; \quad K = 1 + \rho_w \frac{f_{wy}}{f'_c}; \quad f_{cc,res} \doteq 20 - 30\% f_{cc}$$
$$Z = \frac{0.5}{\varepsilon_{cc,50} - \varepsilon_{cc,o}}; \quad \varepsilon_{cc,50} = \frac{3 + 0.29f'_c}{145f'_c - 1000} + 0.75\rho_w\left(\frac{b_c}{s}\right)^{1/2};$$

f'_{cc}	30.14	Mpa
K	1.116	
$\varepsilon_{cc,50}$	0.006245	
	0.007658	
Z	123.60	

Appendix C

Theoretical Flexural Response (without Shear)

Example 6

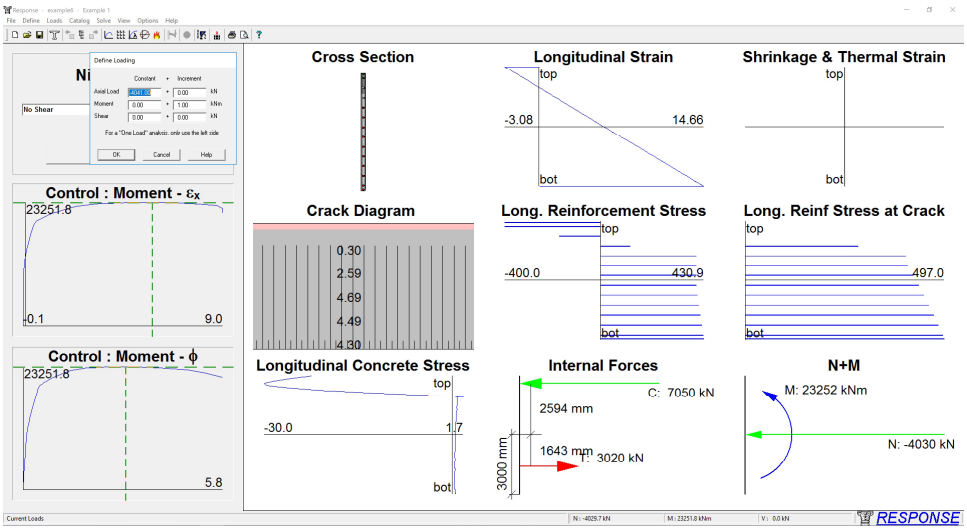

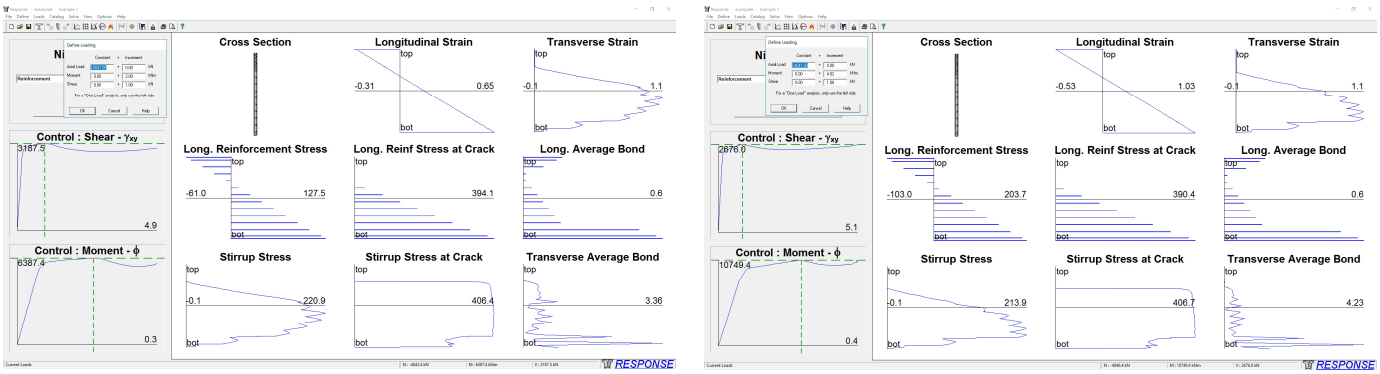

Figure A-12 Response 2000 - Rectangular wall (boundary elements) Example 6.

Example 7

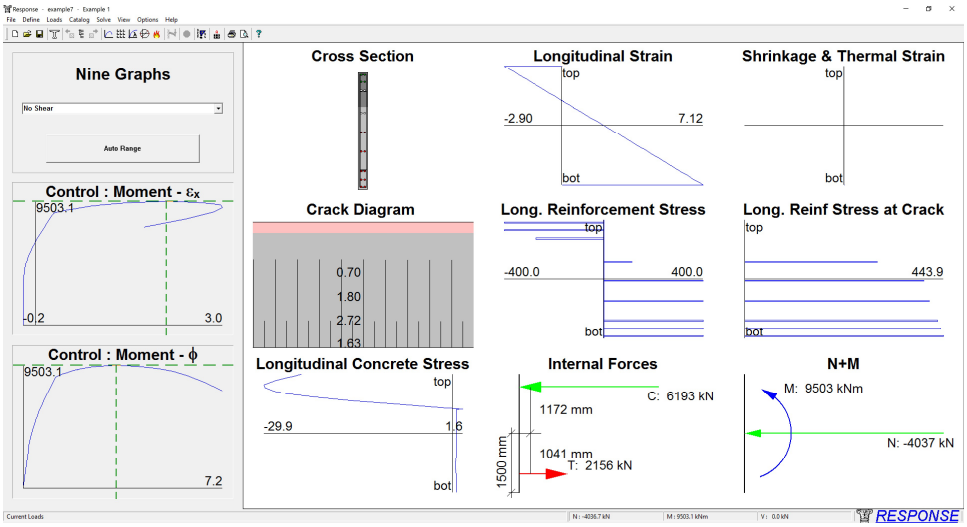

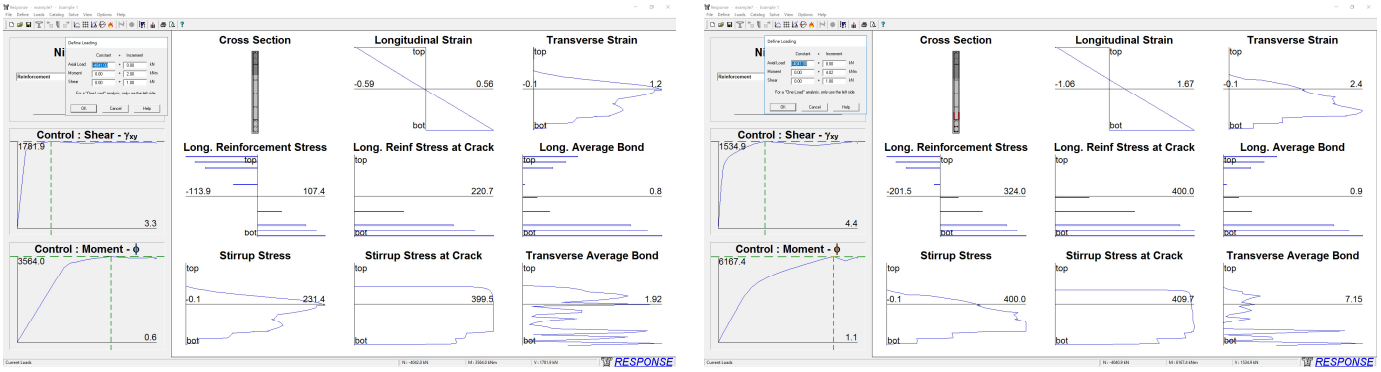

Figure A-13 Response 2000 - Rectangular wall (boundary elements) Example 7

Example 8

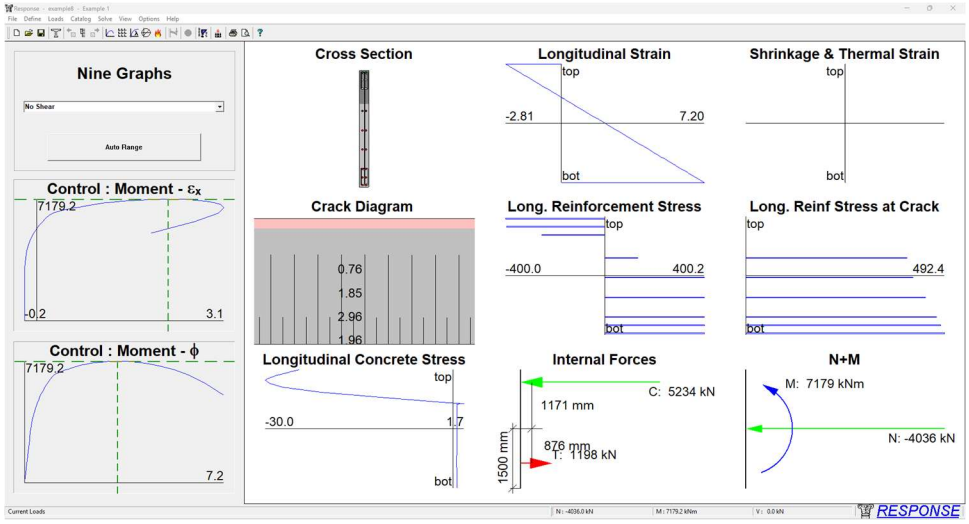

The neutral depth its 843mm (C/L = 0.281)

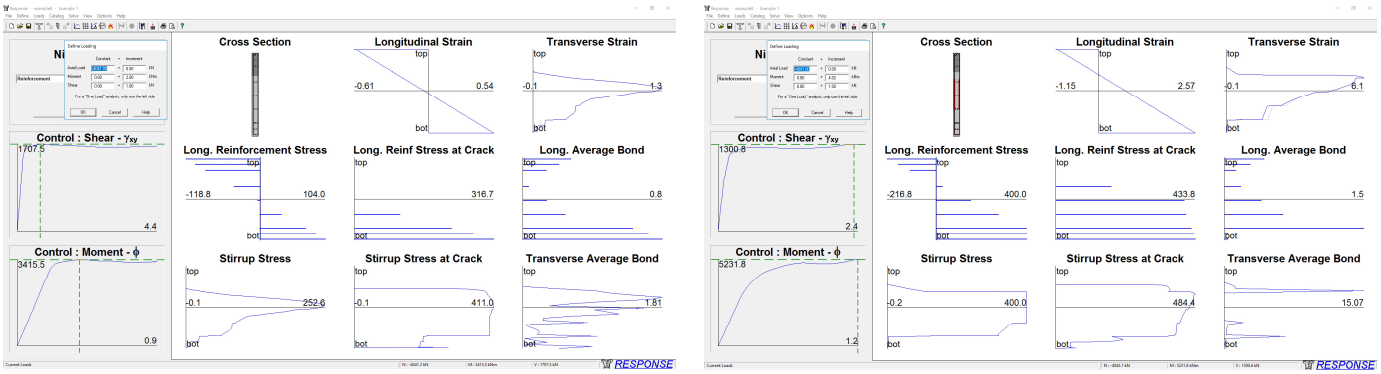

Figure A-14 Response 2000 - Rectangular wall (boundary elements) Example 8

Example 9

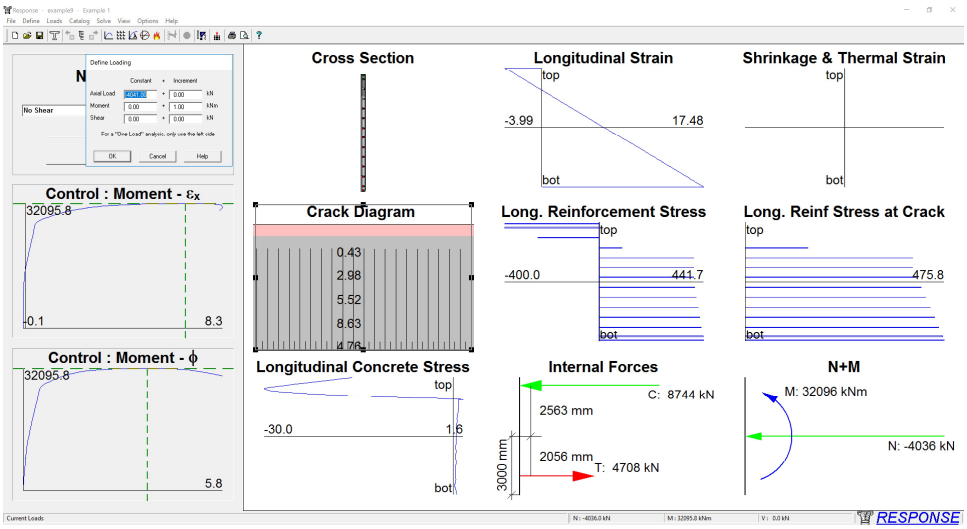

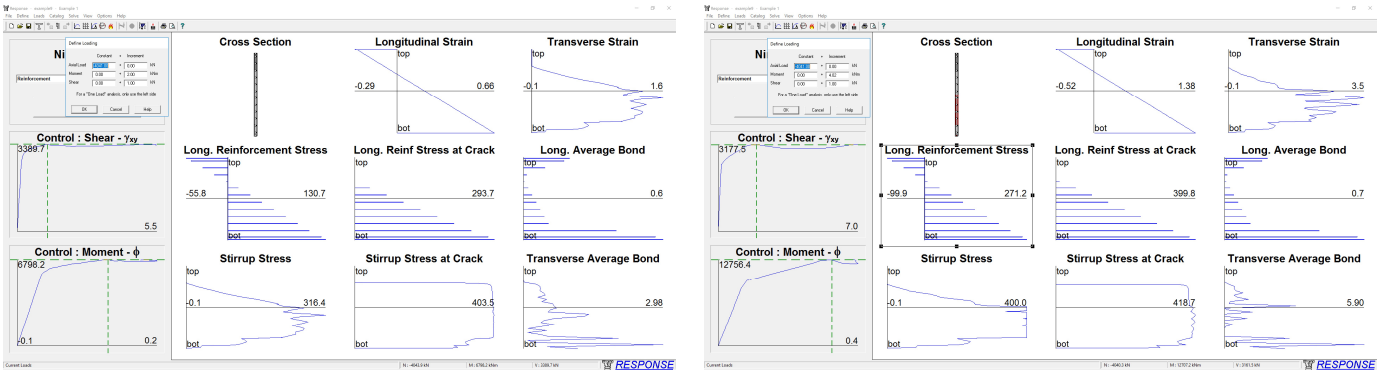

Figure A-15 Response 2000 - Rectangular wall (boundary elements) Example 9

Example 1

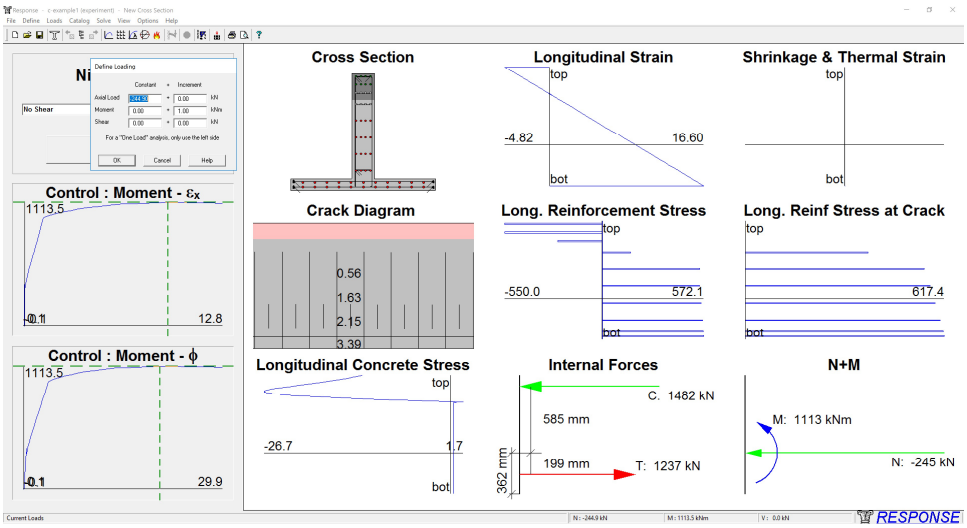

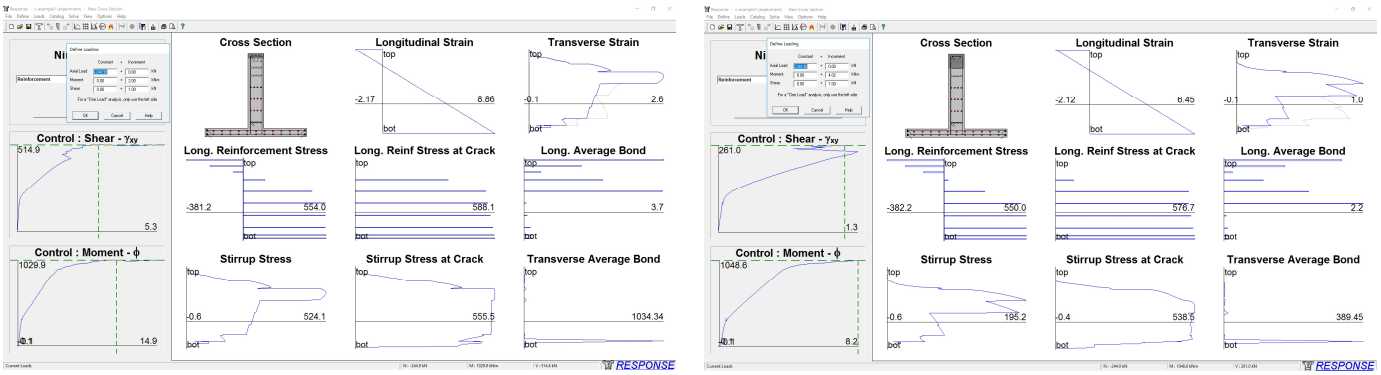

Figure A-16 Response 2000 - T-shaped wall (boundary elements) Example 1

Calculate C - Neutral axis

E_{steel}	2E+05	Mpa
F_y	550	Mpa
F_c	27	Mpa
$E_{concr.}$	23383	Mpa
n	8.55	

ε_T	0.00275
ε_c	0.0030

L_w	1.30	m	$A_{g(C)}$	0.32	m^2
L_f	1.05	m	$X_{centroid\,(c)}$	0.6883	m
t_w	0.10	m	C_1	289.5	mm
t_f	0.10	m	2(C)(t_f)	57897	mm^2
Cover	25	mm	$L_w{*}t_w{*}\{(C-t_w)+(t_w/2)\}$	8.4E+06	mm^3

C/L	0.276	
$A_{g(S)}$	0.0284	m^2
$L^*A_{g(S)}$	0.0166	m^3
C	289.4	mm

$A_{g(C+S)}$	0.3484	m^2
$X_{centroid\,(c+s)}$	0.3799	m
ρv	1.09%	

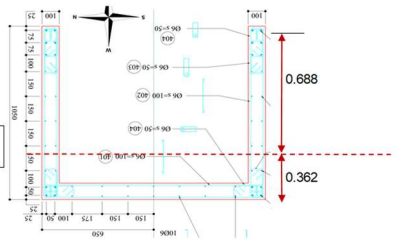

M = 1361 Kn*m

	Reinf	X(mm)	Flange 1 D(mm)	Flange 1 Area (mm^2)	Web	Web D (mm)	Web D (mm)	Web Area (mm^2)	Flange 2 D (mm)	Flange 2 Area (mm^2)	Steel Area (mm^2)	Compresion A' (mm^2)	Compresion (n-1)*A'	Compresion (n-1)*A'*d'	Tension A_t (mm^2)	Tension n^*A_t	Tension $n^*A_t{*}d$	Moment (kn*m) d (mm)	M steel	M concrete
		1050.0									*3498.2*		*11769.8*	*1442754.1*		*16593*	*15144553*		*724*	*637*
1	1	25	2	12	226.2	0	8	0	6	0.0	2	12	226.2	452.4	452	3417	85426					663	165.0	
2	2	100	2	12	226.2	0	8	0	6	0.0	2	12	226.2	452.4	452	3417	341705					588	146.4	
3	3	175	2	12	226.2	0	1	0	1	0.0	2	12	226.2	452.4	452	3417	597984					513	127.7	
4	4	275	2	8	100.5	0	1	0	1	0.0	2	8	100.5	201.1	201	1519	417639					413	45.7	
5	5	425	2	6	56.5	0	1	0	1	0.0	2	6	56.5	113.1				113	967	411128		263	-16.4	
6	6	575	2	6	56.5	0	1	0	1	0.0	2	6	56.5	113.1				113	967	556232		113	-7.0	
7	7	725	2	6	56.5	0	1	0	1	0.0	2	6	56.5	113.1				113	967	701336		-37	2.3	
8	8	875	2	8	100.5	0	1	0	1	0.0	2	8	100.5	201.1				201	1720	1504782		-187	20.6	
9	9	975	2	9	127.2	7	9	0	6	445.3	2	9	127.2	699.8				700	5986	5835899		-287	110.4	
10	10	1025	2	9	127.2	7	9	0	6	445.3	2	9	127.2	699.8				700	5986	6135176		-337	129.6	

Example 2

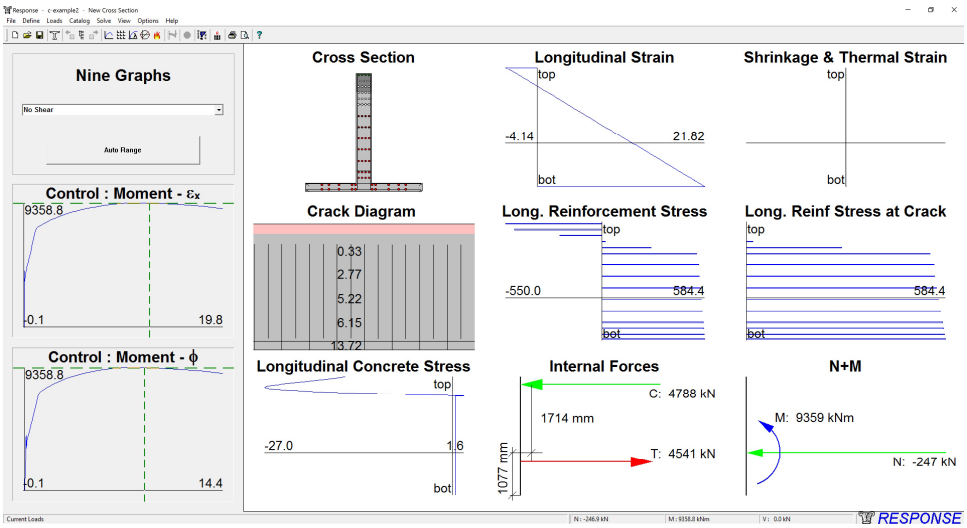

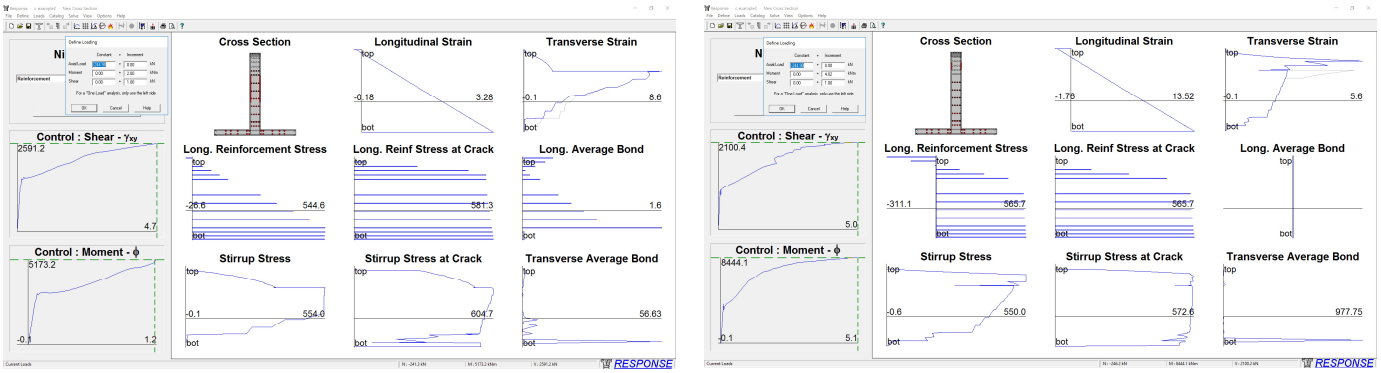

Figure A-17 Response 2000 - T-shaped wall (boundary elements) Example 2

Calculate C - Neutral axis

E_{steel}	200000	Mpa
F_y	550	Mpa
F'_c	27	Mpa
E_{conc}	23382.69	Mpa
n	8.55	

ε_t	0.00275
ε_c	0.0030

L_w	3.00	m	$A_{b(C)}$	1.72	m^2	
L_f	3.00	m	$X_{centroid\ (c)}$	1.9233	m	
t_w	0.20	m	C_1	639.3	mm	
t_f	0.20	m	2(C)(t_f)	255720	mm^2	
Cover	25	mm	L_w*t_w*{(C-t_w)+(t_w/2)}	8.2E+07	mm^3	

C/L	0.213	
$A_{b(S)}$	0.0871	m^2
L'$A_{b(S)}$	0.1373	m^3
C	639.1	mm

$A_{b(C+S)}$	1.8071	m^2
$X_{centroid\ (c+s)}$	1.1009	m
ρv	0.614%	

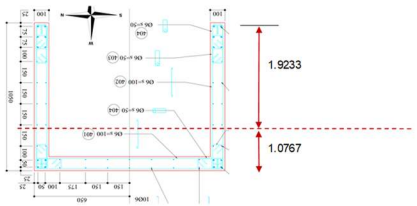

M = 11834 Kn*m

Reinf	X(mm)	Flange 1 D(mm)	Flange 1 Area (mm^2)	Web	Web D (mm)	Web	Web D (mm)	Web Area (mm^2)	Flange 2	Flange 2 D (mm)	Flange 2 Area (mm^2)	Steel Area (mm^2)	Compresion A' (mm^2)	Compresion (n-1)*A'	Compresion (n-1)*A'*d'	Tension A_t (mm^2)	Tension n*A_t	Tension n*A_t*d	Moment (kn*m) d (mm)	Moment (kn*m) M steel	Moment (kn*m) M concrete
	2985.0											10555.8		24299.0	6439239.6		62770.9	130899885		3588	8246.1
1	40	2	16	402.1	0	8	0	6	0.0	2	16	402.1	804.2	804	6075	242990				1883	833
2	190	2	16	402.1	0	8	0	6	0.0	2	16	402.1	804.2	804	6075	1154203				1733	767
3	340	2	16	402.1	0	8	0	6	0.0	2	16	402.1	804.2	804	6075	2065416				1583	700
4	490	2	16	402.1	0	8	0	6	0.0	2	16	402.1	804.2	804	6075	2976630				1433	634
5	640	2	16	402.1	0	8	0	6	0.0	2	16	402.1	804.2				804	6879	4402561	1283	-568
6	790	2	16	402.1	0	8	0	6	0.0	2	16	402.1	804.2				804	6879	5434412	1133	-501
7	1080	2	10	157.1	0	8	0	6	0.0	2	10	157.1	314.2				314	2687	2902079	843	-146
8	1370	2	10	157.1	0	8	0	6	0.0	2	10	157.1	314.2				314	2687	3681341	553	-96
9	1660	2	10	157.1	0	8	0	6	0.0	2	10	157.1	314.2				314	2687	4460603	263	-45
10	1950	2	10	157.1	0	8	0	6	0.0	2	10	157.1	314.2				314	2687	5239865	-27	5
11	2240	2	10	157.1	0	8	0	6	0.0	2	10	157.1	314.2				314	2687	6019127	-317	55
12	2520	2	16	402.1	0	10	0	6	0.0	2	16	402.1	804.2				804	6879	17335085	-597	264
13	2670	2	16	402.1	0	10	0	6	0.0	2	16	402.1	804.2				804	6879	18366935	-747	330
14	2820	2	16	402.1	6	10	0	6	471.2	2	16	402.1	1275.5				1275	10910	30765262	-897	629
15	2960	2	16	402.1	6	10	0	6	471.2	2	16	402.1	1275.5				1275	10910	32292615	-1037	727
	3000																				

Example 3

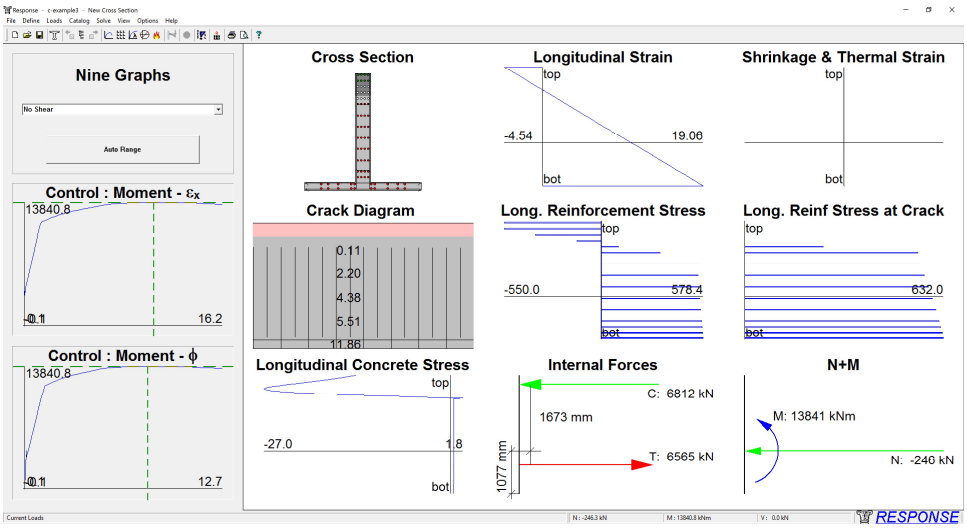

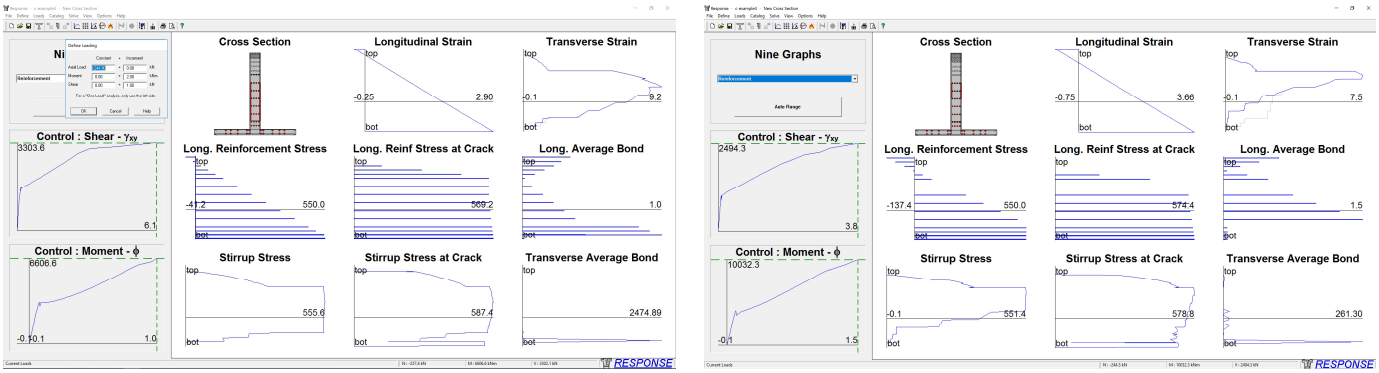

Figure A-18 Response 2000 - T-shaped wall (boundary elements) Example 3

Calculate C - Neutral axis

E_{steel}	200000	Mpa
F_y	550	Mpa
F'_c	27	Mpa
$E_{concr.}$	23382.69	Mpa
n	8.55	

ε_T	0.00275
ε_c	0.0030

L_w	3.00	m	$A_{g(C)}$	1.72	m^2
L_f	3.00	m	$X_{centroid\,(c)}$	1.9233	m
t_w	0.20	m	C_t	756.9	mm
t_f	0.20	m	2(C)(t_f)	302760	mm^2
Cover	25	mm	$L_w{*}t_w{*}\{(C-t_f)+(t_f/2)\}$	1.1E+08	mm^3

C/L	0.252	
$A_{g(S)}$	0.1499	m^2
$L{*}A_{g(S)}$	0.2279	m^3
C	756.6	mm

$A_{g(C+S)}$	1.8699	m^2
$X_{centroid\,(c+s)}$	1.1123	m
pv	1.070%	

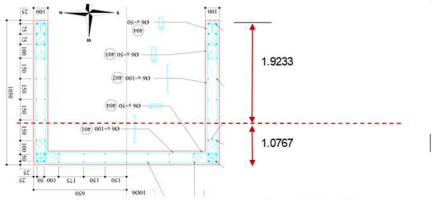

Reinf	X(mm)	Flange 1			Web				Flange 2			Steel	Compresion			Tension			M = 18033 Kn*m Moment (kn*m)		
		D(mm)		Area (mm^2)		D (mm)		D (mm)	Area (mm^2)		D (mm)	Area (mm^2)	Area (mm^2)	A' (mm^2)	(n-1)*A'	(n-1)*A'*d'	A_t (mm^2)	n*A_t	n*A_t*d	d(mm)	M steel	M concrete
													18409.7		57425.4	19524640.0		92436.6	20835597		8587	9446.1
1	40	2	22	760.3	0	8	0	6	0.0	2	22	760.3	1520.5	1521	11485	459403				1883	1575	
2	190	2	22	760.3	0	8	0	6	0.0	2	22	760.3	1520.5	1521	11485	2182166				1733	1450	
3	340	2	22	760.3	0	8	0	6	0.0	2	22	760.3	1520.5	1521	11485	3904928				1583	1324	
4	490	2	22	760.3	0	8	0	6	0.0	2	22	760.3	1520.5	1521	11485	5627690				1433	1199	
5	640	2	22	760.3	0	8	0	6	0.0	2	22	760.3	1520.5	1521	11485	7350453				1283	1073	
6	790	2	22	760.3	0	8	0	6	0.0	2	22	760.3	1520.5				1521	13006	10274434	1133	-948	
7	1080	2	12	226.2	0	8	0	6	0.0	2	12	226.2	452.4				452	3869	4178994	843	-210	
8	1370	2	12	226.2	0	8	0	6	0.0	2	12	226.2	452.4				452	3869	5301131	553	-138	
9	1660	2	12	226.2	0	8	0	6	0.0	2	12	226.2	452.4				452	3869	6423268	263	-66	
10	1950	2	12	226.2	0	8	0	6	0.0	2	12	226.2	452.4				452	3869	7545405	-27	7	
11	2240	2	12	226.2	0	8	0	6	0.0	2	12	226.2	452.4				452	3869	8667543	-317	79	
12	2520	2	22	760.3	0	10	0	6	0.0	2	22	760.3	1520.5				1521	13006	32774145	-597	499	
13	2670	2	22	760.3	0	10	0	6	0.0	2	22	760.3	1520.5				1521	13006	34724987	-747	624	
14	2820	2	22	760.3	6	10	0	6	471.2	2	22	760.3	1991.8				1992	17036	48042305	-897	982	
15	2960	2	22	760.3	6	10	0	6	471.2	2	22	760.3	1991.8				1992	17036	50427384	-1037	1136	
	3000																					

Example 4

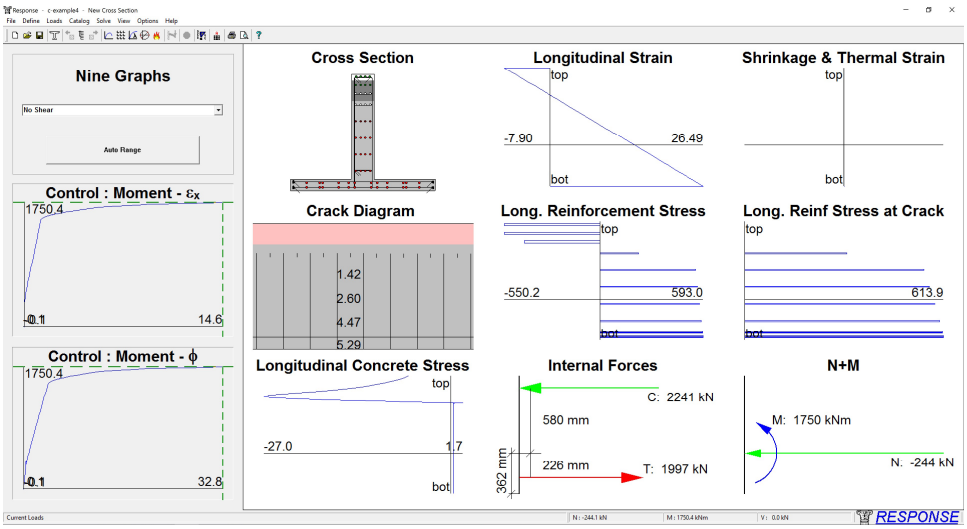

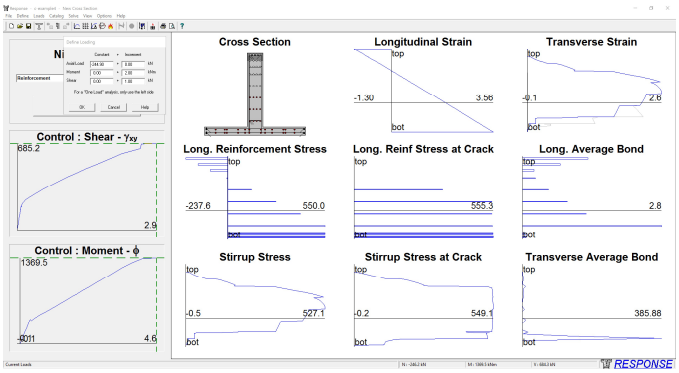

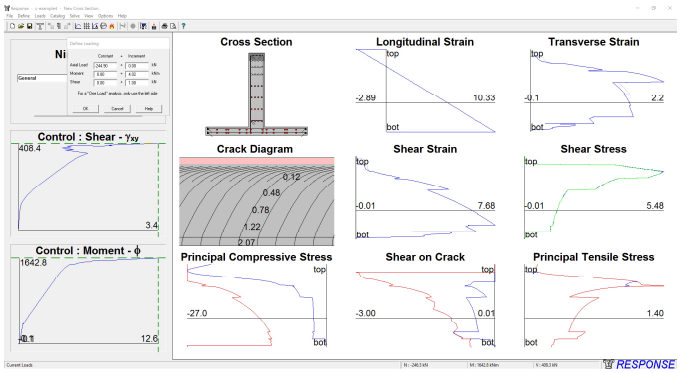

Figure A-19 Response 2000 - T-shaped wall (boundary elements) Example 4

Calculate C - Neutral axis

E_{steel}	2E+05	Mpa
F_y	550	Mpa
F_c	27	Mpa
$E_{concr.}$	23383	Mpa
n	8.55	

ε_t	0.00275
ε_c	0.0030

L_w	1.30	m	$A_{g(C)}$	0.32	m^2
L_f	1.05	m	$X_{centroid\,(c)}$	0.6883	m
t_w	0.10	m	C_1	331.0	mm
t_f	0.10	m	2(C)(t_f)	66192	mm^2
Cover	25	mm	$L_w{*}t_w{*}\{(C-t_w)+(t_w/2)\}$	1.1E+07	mm^3

C/L	0.315	
$A_{g(S)}$	0.0523	m^2
$L^{*}A_{g(S)}$	0.0283	m^3
C	330.9	mm

$A_{g(C+S)}$	0.3723	m^2
$X_{centroid\,(c+s)}$	0.3868	m
ρv	2.03%	

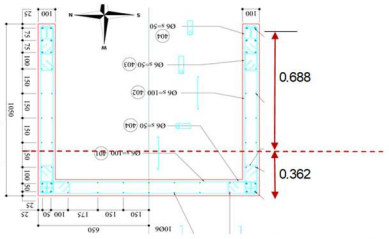

M = 2201 Kn*m

Reinf	X(mm)	Flange 1			Web					Flange 2			Steel	Compresion			Tension			Moment (kn*m)		
			D(mm)	Area (mm^2)		D (mm)		D (mm)	Area (mm^2)		D (mm)	Area (mm^2)	Area (mm^2)	A' (mm^2)	(n-1)* A'	(n-1)* A'*d'	A_t (mm^2)	$n^{*}A_t$	$n^{*}A_t{*}d$	d (mm)	M steel	M concrete
	1050.0												*6509.4*		*25438.0*	*2959069.8*		*26871*	*25301829*		*1497*	*704*
1	25	2	18	508.9	0	8	0	6	0.0	2	18	508.9	1017.9	1018	7688	192209				663	371.3	
2	100	2	18	508.9	0	8	0	6	0.0	2	18	508.9	1017.9	1018	7688	768836				588	329.3	
3	175	2	18	508.9	0	1	0	1	0.0	2	18	508.9	1017.9	1018	7688	1345463				513	287.4	
4	275	2	10	157.1	0	1	0	1	0.0	2	10	157.1	314.2	314	2373	652561				413	71.4	
5	425	2	6	56.5	0	1	0	1	0.0	2	6	56.5	113.1				113	967	411128	263	-16.4	
6	575	2	6	56.5	0	1	0	1	0.0	2	6	56.5	113.1				113	967	556232	113	-7.0	
7	725	2	6	56.5	0	1	0	1	0.0	2	6	56.5	113.1				113	967	701336	-37	2.3	
8	875	2	10	157.1	0	1	0	1	0.0	2	10	157.1	314.2				314	2687	2351221	-187	32.3	
9	975	2	18	508.9	8	6	0	6	226.2	2	18	508.9	1244.1				1244	10641	10374932	-287	196.2	
10	1025	2	18	508.9	8	6	0	6	226.2	2	18	508.9	1244.1				1244	10641	10906980	-337	230.4	
	1050																					

Example 5

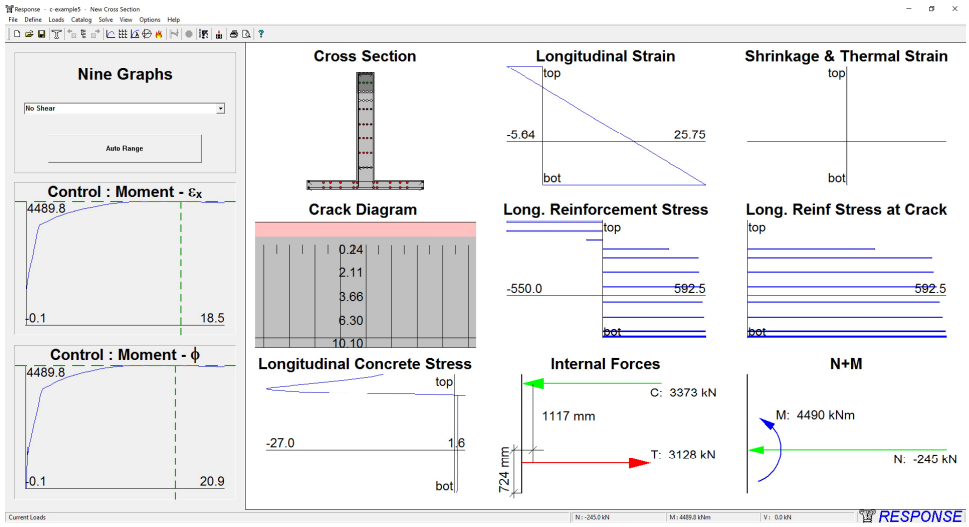

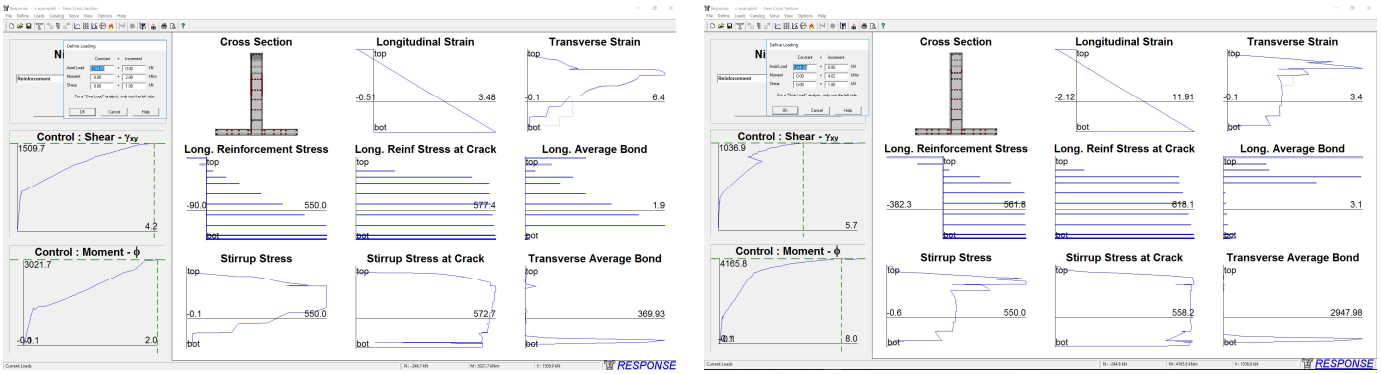

Figure A-20 Response 2000 - T-shaped wall (boundary elements) Example 5

Calculate C - Neutral axis

E_{steel}	200000	Mpa
F_y	550	Mpa
F'_c	27	Mpa
$E_{conc.}$	23382.69	Mpa
n	8.55	

ε_t	0.00275
ε_c	0.0030

L_w	2.00	m	$A_{w(C)}$	0.855	m^2
L_f	2.00	m	$X_{centroid(c)}$	1.2759	m
t_w	0.15	m	C_t	477.0	mm
t_f	0.15	m	2(C)(t_f)	143100	mm^2
Cover	25	mm	L_w*t_w*{(C-t_w)+(t_f/2)}	3.4E+07	mm^3

C/L	0.239	
$A_{g(C)}$	0.0733	m^2
L*$A_{g(C)}$	0.0690	m^3
C	476.8	mm

$A_{g(C+s)}$	0.9283	m^2
$X_{centroid(c+s)}$	0.7413	m
ρ_V	1.054%	

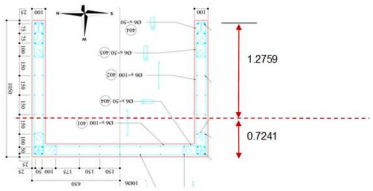

Reinf	X(mm)	Flange 1 D(mm)	Flange 1 Area (mm^2)	Web D (mm)	Web D (mm)	Web Area (mm^2)	Flange 2 D (mm)	Flange 2 Area (mm^2)	Steel Area (mm^2)	Compresion A' (mm^2)	Compresion (n-1)*A'	Compresion (n-1)*A'*d'	Tension A_t (mm^2)	Tension n*A_t	Tension n*A_t*d
	2000.0								9010.1		28475.4	5125574.0		44821.0	63912915
1	30	2	20	628.3	0	1	0	1	0.0	2	20	628.3	1256.6	1257	9492	284754			
2	180	2	20	628.3	0	1	0	1	0.0	2	20	628.3	1256.6	1257	9492	1708525			
3	330	2	20	628.3	0	1	0	1	0.0	2	20	628.3	1256.6	1257	9492	3132295			
4	480	2	20	628.3	0	1	0	1	0.0	2	20	628.3	1256.6				1257	10748	5159252
5	630	2	8	100.5	0	1	0	1	0.0	2	8	100.5	201.1				201	1720	1083443
6	880	2	8	100.5	0	1	0	1	0.0	2	8	100.5	201.1				201	1720	1513380
7	1130	2	8	100.5	0	1	0	1	0.0	2	8	100.5	201.1				201	1720	1943318
8	1380	2	8	100.5	0	1	0	1	0.0	2	8	100.5	201.1				201	1720	2373256
9	1630	2	8	100.5	0	1	0	6	0.0	2	8	100.5	201.1				201	1720	2803193
10	1875	2	18	508.9	6	10	0	6	471.2	2	18	508.9	1489.1				1489	12737	23881692
11	1975	2	18	508.9	6	10	0	6	471.2	2	18	508.9	1489.1				1489	12737	25155382
	2000																		

M = 5699 Kn*m

d(mm)	Moment (kn*m) M steel	M concrete
	2705	2993.9
1246	861	
1096	757	
946	654	
796	-550	
646	-71	
396	-44	
146	-16	
-104	12	
-354	39	
-599	491	
-699	573	